

Dissertation  
submitted to the  
Combined Faculties for the Natural Sciences and for Mathematics  
of the Ruperto-Carola University of Heidelberg, Germany  
for the degree of  
Doctor of Natural Sciences

Put forward by  
Vikas Joshi M.Sc. (Physics)  
Born in: Tanakpur, Uttarakhand, India  
Oral examination: 6-February-2019





# Reconstruction and Analysis of Highest Energy $\gamma$ -Rays and its Application to Pulsar Wind Nebulae

Referees: Prof. Dr. Jim Hinton  
Prof. Dr. Stefan Wagner



## Abstract

The High Altitude Water Cherenkov (HAWC)  $\gamma$ -ray observatory detects cosmic- and  $\gamma$ -rays in the TeV energy range. HAWC was recently upgraded with a sparse detector array (the outrigger array), which increases the instrumented area by a factor of 4-5 and will improve the sensitivity at energies greater than 10 TeV. This thesis consists of a number of contributions towards the improvement of the performance of HAWC at the highest energies and the study of a prominent high energy source, 2HWC J2019+367. To decide on components of the outrigger array, simulation input is provided. A new Monte Carlo template-based reconstruction method for air shower arrays is developed. It reconstructs the core location and energy of  $\gamma$ -ray showers. The goodness of fit of the method is utilised to separate the cosmic- and  $\gamma$ -ray showers. This method significantly improves the HAWC shower reconstruction and combines the reconstruction of HAWC and the outrigger array. In-depth spectral and morphological studies of 2HWC J2019+367 are performed. 2HWC J2019+367 shows a hint of energy-dependent morphology. A new HAWC source is discovered in the vicinity associated with VER J2016+371. The preferred direction of the X-ray and TeV emission indicates their association, and their combined spectral modelling show that 2HWC J2019+367 is likely to be the TeV pulsar wind nebula of PSR J2021+3651.

## Zusammenfassung

Das High Altitude Water Cherenkov (HAWC)  $\gamma$ -Strahlen-Observatorium weist kosmische Strahlung und  $\gamma$ -Strahlung im Energiebereich von TeV nach. HAWC wurde kürzlich um ein dünn besetztes Detektorfeld (Outrigger Array) erweitert, welches die instrumentierte Fläche um einen Faktor 4-5 vergrößert und die Sensitivität bei Energien über 10 TeV verbessern wird. Diese Arbeit umfasst eine Reihe von Beiträgen zur Verbesserung der Empfindlichkeit von HAWC bei den höchsten Energien, sowie eine Untersuchung einer bedeutenden Hochenergiequelle, 2HWC J2019+367. Simulationsergebnisse werden genutzt, um Komponenten für das Outrigger Array zu wählen. Eine neue Rekonstruktionsmethode für Luftschauder-Detektorfelder basierend auf Monte-Carlo Templates wird entwickelt. Sie rekonstruiert das Zentrum und die Energie von  $\gamma$ -Schauern. Die Fitqualität der Methode wird zur Unterscheidung von kosmischer und  $\gamma$ -Strahlung benutzt. Diese Methode verbessert die Schauer-Rekonstruktion von HAWC signifikant und kombiniert die Rekonstruktion von HAWC und des Outrigger Arrays. Tiefgehende spektrale und morphologische Untersuchungen von 2HWC J2019+367 werden durchgeführt. 2HWC J2019+367 zeigt Hinweise auf eine energieabhängige Morphologie. Im Verlauf der Untersuchungen wurde eine neue HAWC-Quelle in der zu VER J2016+371 gehörenden Umgebung entdeckt. Die Vorzugsrichtung der Röntgen- und TeV-Strahlung deutet auf eine Verbindung der Quellen hin und ein kombiniertes spektrales Modell beider Quellen zeigt, dass es sich bei 2HWC J2019+367 höchstwahrscheinlich um den TeV Pulsarwind-Nebel von PSR J2021+3651 handelt.



*To my family and friends*



# Contents

<b>Contents</b>	<b>i</b>
<b>List of Figures</b>	<b>v</b>
<b>List of Tables</b>	<b>ix</b>
<b>1 Introduction to <math>\gamma</math>-Ray Astronomy</b>	<b>1</b>
1.1 The Non-thermal Universe . . . . .	1
1.2 Cosmic Rays . . . . .	3
1.2.1 Acceleration Mechanisms . . . . .	4
1.2.2 Sites of CR Acceleration . . . . .	6
1.3 $\gamma$ -Ray Astronomy . . . . .	7
1.3.1 $\gamma$ -Ray Emission Mechanisms . . . . .	7
1.3.1.1 Bremsstrahlung . . . . .	8
1.3.1.2 Inverse Compton Scattering . . . . .	9
1.3.1.3 Synchrotron Radiation . . . . .	10
1.3.1.4 Pion Decay . . . . .	11
1.3.2 Known Source Types of VHE $\gamma$ -rays . . . . .	11
1.3.2.1 Pulsars and Pulsar Wind Nebulae . . . . .	11
1.3.2.2 Supernova Remnants . . . . .	12
1.3.2.3 Binary Systems . . . . .	12
1.3.2.4 Active Galactic Nuclei . . . . .	12
1.3.2.5 Starburst Galaxies . . . . .	12
1.3.2.6 Gamma-Ray Bursts . . . . .	13
1.4 Detection Techniques . . . . .	13
1.4.1 Space-Based Instruments . . . . .	13
1.4.2 Ground-Based Experiments . . . . .	14
1.4.2.1 Extensive Air Showers . . . . .	15
1.4.2.2 Cherenkov Radiation . . . . .	17
1.4.2.3 Imaging Atmospheric Cherenkov Telescopes . . . . .	18
1.4.2.4 EAS Particle Detector Arrays . . . . .	20

## CONTENTS

---

<b>2</b>	<b>The HAWC <math>\gamma</math>-Ray Observatory</b>	<b>23</b>
2.1	Water Cherenkov Detectors (WCDs)	24
2.2	Photomultiplier Tubes	25
2.3	Data Acquisition System	26
2.4	Calibration System	27
2.5	Simulations	27
2.6	Air Shower Reconstruction	28
2.6.1	Core Reconstruction	29
2.6.2	Direction Reconstruction	32
2.6.3	$\gamma$ -Hadron Separation	33
2.7	Reconstruction Strategy	34
2.8	Analysis Cuts	35
2.9	Point Spread Function	35
2.10	Detector Response Function	37
2.11	HAWC Sky-maps	37
2.12	HAWC Sensitivity and Science Case	37
<b>3</b>	<b>HAWC High Energy Upgrade</b>	<b>41</b>
3.1	Motivation for Outriggers	41
3.2	Outrigger Array Description	42
3.3	Toy Model for a WCD	44
3.4	Simulations for the Outriggers	45
3.4.1	Air Shower Simulations	46
3.4.2	Detector Simulations	46
3.5	Analysis of Simulations	49
3.5.1	Single Tank Trigger Probability	49
3.5.1.1	Number of Tanks Triggered for Real Outrigger Layout	51
3.5.2	Time Resolution of the Shower Front	52
3.5.3	Signal Amplitude Study	55
3.6	Analysis of Impact on Air Shower Reconstruction	56
3.6.1	Core Estimation Using Outriggers	57
3.6.2	Analytical Estimation of Angular Resolution	59
3.7	Conclusions	62
<b>4</b>	<b>A Template-based <math>\gamma</math>-ray Reconstruction Method for Air Shower Arrays</b>	<b>63</b>
4.1	Introduction	63
4.2	General Considerations	65
4.2.1	Ambiguity Between Primary Energy and $X_{\max}$	65
4.2.2	Signal Free Detectors	65
4.2.3	Logarithmic Signal Amplitude	66
4.3	Likelihood Function	67
4.4	Air Shower and Detector Simulations	69
4.5	Template Generation	69



## CONTENTS

---

4.5.1	Binning Scheme . . . . .	70
4.5.2	Smoothing . . . . .	70
4.5.3	Interpolation . . . . .	70
4.6	Fitting Procedure . . . . .	70
4.6.1	First Pass . . . . .	71
4.6.2	Second Pass . . . . .	72
4.6.3	Examples . . . . .	73
4.7	Binning Optimisation . . . . .	73
4.8	Performance on Simulations . . . . .	75
4.8.1	Core Resolution . . . . .	77
4.8.2	Energy Resolution and Bias . . . . .	79
4.8.3	Gamma-Hadron Separation . . . . .	80
4.9	Performance on Crab Nebula Data . . . . .	81
4.10	Application to Mixed Detector Arrays . . . . .	87
4.11	Conclusion and Prospects . . . . .	90
<b>5</b>	<b>Introduction to Pulsar Wind Nebulae</b> . . . . .	<b>93</b>
5.1	Stellar Remnants . . . . .	93
5.2	Pulsars . . . . .	95
5.3	Pulsar Models . . . . .	96
5.3.1	Spin-Down Luminosity . . . . .	96
5.3.2	Age of the System . . . . .	97
5.3.3	Surface Magnetic Field Strength . . . . .	98
5.3.4	Time Evolution of Pulsar Parameters . . . . .	98
5.3.5	Distance to the Pulsar . . . . .	99
5.4	Pulsar Magnetosphere and $\gamma$ -ray Emission . . . . .	99
5.5	Pulsar Wind Nebulae . . . . .	101
5.5.1	Formation and Evolution . . . . .	101
5.5.2	Relic Nebula . . . . .	103
5.6	Multi-wavelength Emission from PWNe . . . . .	104
5.7	PWN Modelling . . . . .	106
<b>6</b>	<b>Spectral and Morphological Studies of 2HWC J2019+367</b> . . . . .	<b>109</b>
6.1	Introduction . . . . .	109
6.2	Reconstructed Datasets . . . . .	113
6.2.1	Energy Estimators . . . . .	114
6.2.2	Quality Cuts . . . . .	114
6.2.3	Binning . . . . .	115
6.3	Slice Profiling Tool . . . . .	116
6.4	Systematic Studies . . . . .	117
6.4.1	Data and Simulation Comparison . . . . .	117
6.4.2	Declination Dependence . . . . .	119
6.4.3	Energy Band Definition . . . . .	121

## CONTENTS

---

6.5	2HWC J2019+367 and its Field of View . . . . .	124
6.6	Energy-Dependent Morphology . . . . .	126
6.7	Morphological and Spectral Fit . . . . .	130
6.7.1	Single Source Fit . . . . .	130
6.7.2	Joint Source Fit . . . . .	133
6.8	Multi-wavelength Data . . . . .	137
6.9	Spectral Modelling . . . . .	138
6.9.1	Model Considerations . . . . .	139
6.9.2	One Zone Model . . . . .	142
6.9.3	Two Zone Model . . . . .	144
6.10	Discussion . . . . .	146
6.11	Conclusions . . . . .	149
<b>7</b>	<b>Conclusion</b>	<b>153</b>
<b>A</b>	<b>Appendix</b>	<b>157</b>
	<b>References</b>	<b>167</b>
	<b>Acronyms</b>	<b>173</b>
	<b>Units</b>	<b>177</b>
	<b>Prefixes</b>	<b>177</b>

# List of Figures

1.1	The electromagnetic spectrum. . . . .	2
1.2	The Cosmic-Ray (CR) spectrum as a function of energy-per-nucleus. . . . .	3
1.3	Schematic diagram of the diffusive shock acceleration. . . . .	5
1.4	The Hillas plot. . . . .	7
1.5	Schematic of different channels of $\gamma$ -ray production. . . . .	9
1.6	The 3FGL Catalogue. . . . .	14
1.7	$\gamma$ /hadron shower schematics. . . . .	15
1.8	MC simulations of $\gamma$ /proton shower. . . . .	16
1.9	Cherenkov radiation. . . . .	18
1.10	Schematic of the two ground-based detection techniques of EAS. . . . .	19
1.11	The TeVCat catalogue. . . . .	20
2.1	The HAWC $\gamma$ -Ray Observatory. . . . .	24
2.2	HAWC WCDs. . . . .	24
2.3	HAWC PMTs. . . . .	26
2.4	Schematic of an EAS. . . . .	28
2.5	The different functional shapes for HAWC core fitter. . . . .	29
2.6	Charge distribution and LDF of $\gamma$ -ray event. . . . .	30
2.7	The arrival time distribution of the candidate $\gamma$ -ray. . . . .	32
2.8	Charge distribution and LDF of CR data event. . . . .	33
2.9	HAWC PSF derived from simulations. . . . .	36
2.10	HAWC sensitivity. . . . .	38
3.1	Fully deployed outrigger array. . . . .	42
3.2	The main array and outrigger tank. . . . .	43
3.3	The schematic of the column layout. . . . .	47
3.4	The realistic outrigger layout. . . . .	48
3.5	The square grid outrigger layout. . . . .	49
3.6	One PE trigger probability, tank colours are black and white. . . . .	50
3.7	One PE trigger probability, tank colours are black and mirror. . . . .	51
3.8	One PE trigger probability, only 10 TeV all tank colors. . . . .	52
3.9	The number of outriggers got triggered, tank color black. . . . .	52
3.10	The number of outriggers got triggered, tank color white. . . . .	53
3.11	Time resolution black tanks. . . . .	53

## LIST OF FIGURES

---

3.12	Time resolution ratio, white/black tanks. . . . .	54
3.13	Time resolution ratio, mirror/black tanks. . . . .	54
3.14	The average number of PE, black and white tank for 3" PMT. . . . .	55
3.15	The average number of PE, black and white tank for 8" PMT. . . . .	56
3.16	The average number of PE for 3" PMT with black and mirror tank. . . . .	56
3.17	The average number of PE for 8" PMT with black and mirror tank. . . . .	57
3.18	Core resolution outrigger-like array. . . . .	58
3.19	Schematic for the analytical calculation of angular resolution. . . . .	59
3.20	Core resolution vs. angular resolution, fixed zenith angle. . . . .	60
3.21	Core resolution vs. angular resolution, different zenith angles. . . . .	61
4.1	$N_{pe}$ as a function of the impact distance. . . . .	66
4.2	Probability density distribution of the observed $N_{pe}$ at distance $r$ . . . . .	67
4.3	The distribution of Likelihood as a function of the number of tanks hit. . . . .	69
4.4	A typical template histogram. . . . .	71
4.5	Energy and $X_{max}$ guess templates. . . . .	72
4.6	Likelihood surface example events, MC and Crab data, main array. . . . .	74
4.7	LDF and PDF template corresponding the MC and data event for main array. . . . .	75
4.8	$X_{max}$ binning optimisation. . . . .	76
4.9	$r$ binning optimisation. . . . .	76
4.10	Energy binning optimisation. . . . .	77
4.11	Result core resolution plot main array. . . . .	78
4.12	Result energy reconstruction matrix. . . . .	79
4.13	Result energy resolution plot. . . . .	80
4.14	The GoF distributions of the likelihood fit method. . . . .	81
4.15	GoF simulation and data comparison. . . . .	82
4.16	$\gamma$ -ray efficiency and hadron rejection power. . . . .	83
4.17	Excess count profiles in $\mathcal{B}$ 0 to 9 on Crab data, main array only. . . . .	85
4.18	Performance plots on Crab data, main array only. . . . .	86
4.19	Likelihood surface example events MC and Crab data, with outriggers. . . . .	88
4.20	LDF and PDF template for the MC and data event, with outriggers. . . . .	89
4.21	Result core resolution plot, outriggers improvement. . . . .	90
5.1	The fate of the stars. . . . .	94
5.2	Chandra image of composite SNR G21.5-0.9. . . . .	95
5.3	Schematic of a pulsar and its magnetosphere. . . . .	97
5.4	Schematic showing the wind zone model. . . . .	100
5.5	A schematic of a composite SNR. . . . .	102
5.6	Relic nebula examples. . . . .	103
5.7	Schematic showing the different regions of PWN emission. . . . .	104
5.8	A composite image of the Crab nebula. . . . .	105
5.9	The observed spectrum (by different instruments) of the Crab nebula. . . . .	107
6.1	The excess count map of MGRO J2019+37 region observed by VERITAS. . . . .	110

## LIST OF FIGURES

---

6.2	The spectrum of VER J2019+368 measured by VERITAS. . . . .	111
6.3	MGRO J2019+37 region observed by VERITAS in two energy bands. . . . .	112
6.4	Occupied bins for GP and NN energy sky-maps. . . . .	115
6.5	Example of slice profiling for the HAWC Crab data. . . . .	116
6.6	PSF' as a function of $\mathcal{B}$ bins, Crab data and simulations, for GP. . . . .	118
6.7	PSF' as a function of $\mathcal{B}$ bins, Mrk421 data and simulations, for GP. . . . .	119
6.8	PSF' as a function of $\mathcal{B}$ bins, Crab data and point source at J2019+367, for GP. . . . .	120
6.9	PSF' and Signal/Noise as a function of $\mathcal{B}$ bins in energy bands. . . . .	122
6.10	Selected bins in energy bands for GP and NN energy sky-maps. . . . .	123
6.11	PSF' obtained in energy bands in the excluded and selected 2D energy and $\mathcal{B}$ bins. . . . .	124
6.12	2HWC J2019+367 in HAWC sky-maps. . . . .	125
6.13	2HWC J2019+367 in HAWC energy-skymaps above 56 TeV. . . . .	126
6.14	Schematic of the slice overlaid on 2HWC J2019+367. . . . .	127
6.15	The slice profiles for 2HWC J2019+367 in different energy bands. . . . .	128
6.16	2HWC J2019+367 size in different energy bands. . . . .	129
6.17	Size vs. distance to the pulsar PSR J2021+3651 in different energy bands. . . . .	129
6.18	Residual maps after the fitting a 2D Gaussian morphology. . . . .	132
6.19	SEDs obtained for 2HWC J2019+367. . . . .	134
6.20	Residual maps after the joint fitting of 2HWC J2019+367. . . . .	136
6.21	Schematic of the observations performed by Suzaku. . . . .	137
6.22	Suzaku soft and hard band intensity maps. . . . .	138
6.23	Pulsar luminosity and B-field time evolution. . . . .	140
6.24	The radiation field model used for 2HWC J2019+367 analysis. . . . .	141
6.25	One zone spectral modelling of 2HWC J2019+367. . . . .	142
6.26	The effect of birth period ( $P_0$ ) in the devised model. . . . .	143
6.27	The effect of pulsar braking index ( $n$ ) in the devised model. . . . .	144
6.28	Two zone spectral modelling of 2HWC J2019+367. . . . .	145
6.29	Composite image of 2HWC J2019+367 emission region ini multi-wavelengths. . . . .	148
A.1	Excess count profiles in $\mathcal{B}$ 0 to 9 on Crab data, including off-array events. . . . .	159
A.2	Performance plots on Crab data, including off-array events. . . . .	160
A.3	PSF' as a function of $\mathcal{B}$ bins, Crab data and simulations, for NN. . . . .	161
A.4	PSF' as a function of $\mathcal{B}$ bins, Mrk421 data and simulations, for NN. . . . .	162
A.5	PSF' as a function of $\mathcal{B}$ bins, Crab data and point source at J2019+367, for NN. . . . .	163
A.6	One zone model: spin-down power evolution and injected particle spectrum. . . . .	164
A.7	One zone model: B-field evolution. . . . .	164
A.8	One zone model: evolved particle spectrum. . . . .	165
A.9	Two zone model: spin-down power evolution and injected particle spectrum. . . . .	165
A.10	Two zone model: B-field evolution. . . . .	166
A.11	Two zone model: evolved particle spectrum. . . . .	166



# List of Tables

1.1	Domains of the $\gamma$ -ray astronomy depending on the energy ranges. . . . .	8
2.1	Different steps in the HAWC event reconstruction. . . . .	35
2.2	The HAWC standard analysis cuts defined over analysis bins ( $\mathcal{B}$ ). . . . .	36
3.1	Different WCD components and layouts used for the outrigger simulations. . . . .	46
4.1	The binning definition of the MC dataset to produce the templates. . . . .	70
4.2	The analysis cuts for the LH method, main array events only. . . . .	84
6.1	Definition of energy bands with their corresponding energy ranges. . . . .	121
6.2	Selection of $\mathcal{B}$ bins in energy bands. . . . .	123
6.3	Result of different morphology and spectral assumptions for 2HWC J2019+367. . . . .	131
6.4	Results from the joint fit of 2HWC J2019+367. . . . .	135
6.5	Parameters of the model presented in Figure 6.25. . . . .	143
6.6	Comparison of PSR J2021+3651 and PSR B1823-13. . . . .	146
A.1	The analysis cuts for the LH method, including off-array events. . . . .	157
A.2	CORSIKA simulation input card, for outrigger simulations. . . . .	158





# 1

## Introduction to $\gamma$ -Ray Astronomy

The study of the universe in the realm of astrophysics relies largely on the observation of the photons in the Electromagnetic (EM) spectrum, which spans over a very wide range of energies. Depending on the energy of the EM photon, it is divided into different fields of study as shown in Figure 1.1. EM radiation emission processes are either thermal or non-thermal in nature. The traditional astronomy deals mainly with the thermally emitted photons by hot objects that can emit photons up to few hundreds of keV in most extreme conditions. However, to produce higher energy  $\gamma$ -ray photons, the non-thermal processes are required. This is because to produce them thermally, the temperature of the black-body would need to be close to that present at the early stages of the Big Bang.

### 1.1 The Non-thermal Universe

The study of the non-thermal universe started with the discovery of Cosmic-Rays (CRs) by Victor Hess (Hess 1912), for which he was awarded the 1936 physics Nobel prize. Hess made a series of balloon flights and measured an increase in the density of ionised particles with altitude. He observed an initial decrease in the rate of ionisation with increasing altitude, however, it started to increase beyond  $\sim 1$  km. Therefore, the source of this ionising radiation (later called as CRs) was attributed to be outside the Earth's atmosphere. Modern instruments have observed CRs up to  $\sim 10^{20}$  eV energy. Alongside CRs, the by-products of non-thermal processes are observed in the whole EM spectrum, spanning from radio to Very High Energy (VHE)  $\gamma$ -rays.

To understand the evolution of the universe the study of the non-thermal phenomena is very crucial, as non-thermal radiations contribute equally towards the total energy of the universe as the thermal radiations. The highest known energies carried by CRs also provide the possibility to

# 1. INTRODUCTION TO $\gamma$ -RAY ASTRONOMY

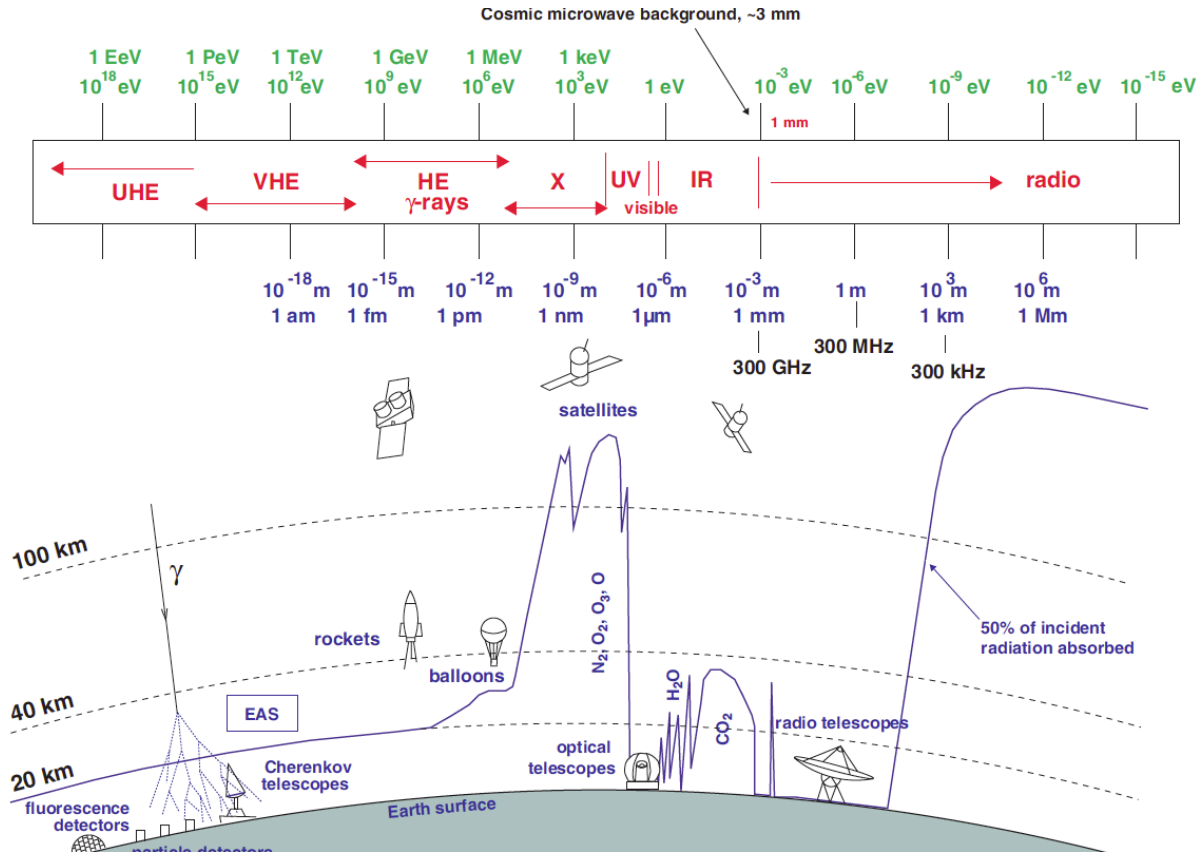


**Figure 1.1:** The electromagnetic spectrum and the different levels of the atmosphere where they get fully absorbed. The different ranges of EM radiation are labelled in red. The Figure is taken from (Wagner 2006).

explore the fundamental physics beyond the current reach of the man-made accelerators. Since CRs are charged particles, they are deflected by the randomly oriented magnetic fields present in the galactic and inter-galactic medium before reaching to Earth. Therefore, their arrival directions cannot be used to point back their source. However, for CRs exceeding the  $\sim$ EeV energies, their trajectories are not bent for distances of tens of Mpc. Nonetheless, the study of CRs can give us information about the composition, energy spectrum and possible anisotropies for the highest energy ones.

To study the acceleration sites of these CRs one has to rely on the neutral particles which are not deflected by magnetic fields.  $\gamma$ -rays and neutrinos are such particles which are produced as the by-products of CRs. Neutrinos interact with other particles only through weak-interactions with a very small cross-section and are therefore very difficult to detect. Nevertheless, it is to be noted that a considerable improvement on the neutrino astronomy is being made in recent times (Ahlers & Halzen 2018; Aartsen et al. 2017). Further, in this chapter, I will give a brief introduction to CRs. Afterwards, I will give a relatively more detailed description of  $\gamma$ -ray astronomy, since it is the area of study of this thesis.

## 1.2 Cosmic Rays

Ever since the discovery of Victor Hess of CRs, numerous efforts have been made to understand the nature and origin of this radiation. Following Victor Hess' discovery, the corpuscular nature of CRs was found (Bothe & Kolhörster 1929), making clear that they are not a new kind of radiation but rather charged particles coming from the outer atmosphere. Later, in 1938 Pierre Auger showed that CRs can initiate Extensive Air Showers (EASs) of secondary particles extending hundreds of meters on the ground and concluded that the primary particle should have  $\sim$ PeV energies. By observing the EAS or through the direct detection of CRs by several experiments,

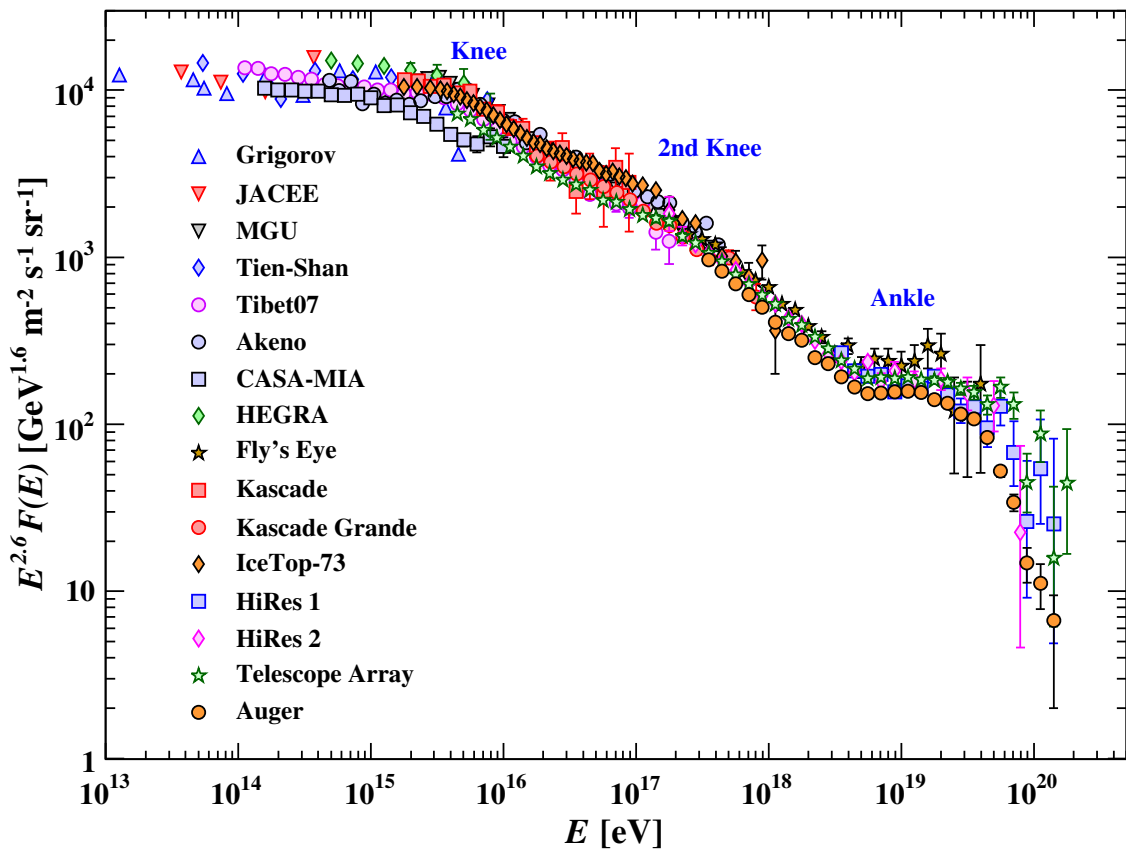


**Figure 1.2:** The Cosmic-Ray (CR) spectrum as a function of energy-per-nucleus, observed from earth compiled using several experiments. Major features are shown such as the knee, 2<sup>nd</sup> knee, and the ankle. The figure is taken from (Tanabashi et al. 2018).

the all-particle spectrum of CRs has been measured over 12 decades in energy. The lowest energy CRs ( $< 1$  GeV) are generally thought to be generated by the solar flares, because the solar magnetic field blocks most of the particles coming from outside the solar system.

Above that, it shows several interesting features as shown in Figure 1.2. From 100 GeV to 5 PeV, the CR spectrum can be described by a power-law with index  $\Gamma$  of  $\sim 2.7$ . The PeV region is also well known as the knee of the spectrum where the transition in the spectrum occurs. The

exact location of the knee is also dependent on the particle species as particles with the higher charge peaks at the higher energies. Up to the knee, the origin of CRs is believed to be of galactic origin and are also associated with objects such as Supernova Remnants (SNRs) being their origin. However, CRs  $> 10^{15}$  eV energies cannot be confined by the magnetic fields and length scales of galactic objects and therefore are able to escape. CRs flux between  $\sim 5$  PeV and 0.1 EeV follows a power-law of spectral index  $\Gamma$  of  $\sim 3.0$ . It is believed to be the transition region from galactic to the extra-galactic origin. From 0.1 EeV to 5 EeV, the spectral index again steepens to a value of  $\Gamma = 3.3$ , this feature is known as the 2<sup>nd</sup> knee. It is associated with the transition to heavier primaries (Tanabashi et al. 2018). The spectral index  $\Gamma$  again hardens above 5 EeV up to 40 EeV to a value of  $\sim 2.6$ . This transition around 5 EeV is also known as the ankle of the spectrum. The origin of these highest energy CRs is most likely to be extra-galactic in nature. However, it is to be noted that the exact location of these above-mentioned transitions and their origin is still under debate as it also depends on the mass composition of the CRs spectrum. The spectrum has a severe cut-off above 40 EeV. One of the explanations given for this cut-off is the so-called Greisen-Zatsepin-Kuzmin (GZK) cut-off (Greisen 1966),(Zatsepin & A. Kuzmin 1966). This is because of the interaction of CRs with the Cosmic Microwave Background (CMB), which limits the maximum distance that can be travelled by CRs of energies  $> 10^{20}$  eV to be 50 Mpc. The cut-off occurs at around 50 EeV for protons, however, for heavier nuclei, it might be at higher energies.

### 1.2.1 Acceleration Mechanisms

To account for the high energies of the observed CRs, astrophysical acceleration mechanisms are needed. CRs are relativistic charged particles, accelerated to the high energies in extreme astrophysical environments in the universe. The acceleration of CRs is generally explained by the repeated crossing of charged particles in astrophysical shocks. It was proposed by Fermi in (Fermi 1949), depending on the properties of moving plasma the two processes known as *first* and *second order* Fermi acceleration are defined. The *first order* Fermi acceleration is also known as the *diffusive shock acceleration*.

Diffusive shock acceleration involves the propagation of strong shocks in the interstellar medium. The shocks can be defined as non-linear disturbances in the medium that transfer energy and momentum to the particles. In Figure 1.3, the downstream, upstream and shock front region are shown. It also shows the scenarios of the rest frame being the shock front, upstream and downstream regions. The shock front defines the boundary of the shock. The downstream is the shocked part of the medium, while upstream is the region where the shock has not interacted with the medium yet. Taking the reference frame of the shock front, it can be seen that the upstream approaches with a speed  $U$  towards the shock. One can apply the mass continuity equation at the shock front as  $\rho_1 v_1 = \rho_2 v_2$ , where,  $\rho_1$ ,  $\rho_2$  and  $v_1$ ,  $v_2$  being the mass densities and velocities of the upstream and downstream respectively. Let us assume the shock front is in fully ionised monotonic gas. Therefore the specific heat capacity ( $\gamma$ ) of the medium is  $5/3$ . In strong shocks, the compression factor results in  $\rho_2/\rho_1 \approx (\gamma + 1)/(\gamma - 1) = 4$ . Therefore, one would get  $v_2 = v_1/4 = U/4$ . From the rest frame of upstream, the downstream would approach the shock with speed  $|v_1 - v_2| = 3U/4$ . This would be the same while going to the rest frame of downstream,

## 1. INTRODUCTION TO $\gamma$ -RAY ASTRONOMY

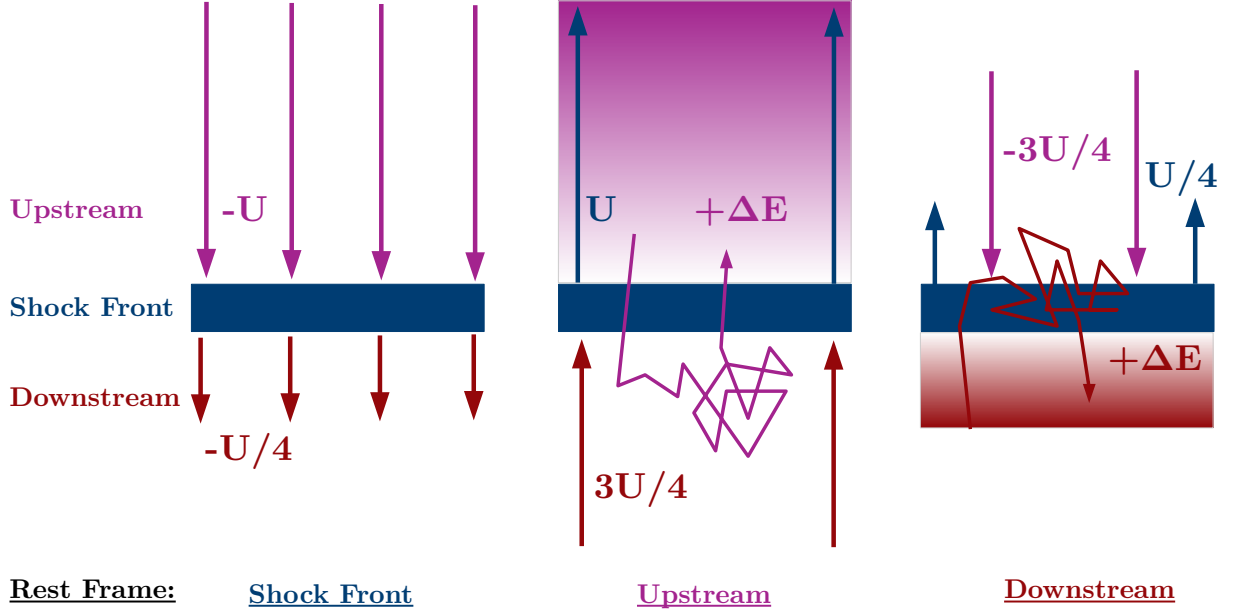


**Figure 1.3:** Schematic diagram of the diffusive shock acceleration. Upstream and downstream show the shocked and yet to be shocked part of the medium. Left panel: the shock front frame, the upstream and downstream are moving with velocity  $U$  and  $U/4$  respectively. Middle panel: the upstream frame, the shock front is moving with a velocity of  $3U/4$ . Right panel: the downstream frame, the shock is moving with a velocity of  $3U/4$ . The figure is adapted from (Funk 2005).

where the upstream would be seen as approaching with a speed of  $3U/4$ . In this case, the particle will always gain energy while crossing the shock-front from upstream to downstream or vice versa. It can be shown that during a round trip around the shock front the particle will gain the energy as:

$$\left\langle \frac{\Delta E}{E} \right\rangle = \frac{4V}{3c}, \quad (1.1)$$

where  $V = 3U/4$  is the velocity of the gas approaching the particle.

After each crossing, the average energy of the particle can be defined as  $\langle E \rangle = \beta \langle E_0 \rangle$ , where  $\langle E_0 \rangle$  is the initial energy and  $\beta$  is a dimensionless constant. Let us define the probability of the particle remaining in the system after each crossing is  $P$ . Taking into account the instabilities in the medium and the magnetic fields, which allow the particles to cross the shock several times, therefore, if the particle crosses the shock  $k$  times the final average energy becomes  $\langle E \rangle = \beta^k \langle E_0 \rangle$  and number of particles remaining in the system will be  $N = P^k N_0$ . Where  $N_0$  is the initial number of particles. Combining these two relations one can obtain the number of particles remaining in the system after  $k$  crossing with energy  $E$  as:

$$\frac{\ln(N/N_0)}{\ln(\langle E \rangle / \langle E_0 \rangle)} = \frac{\ln P}{\ln \beta}, \quad (1.2)$$

Using the above equation one can obtain the following power-law equation (1.3):

$$N(E)dE \propto E^{-1+\ln P/\beta} dE. \quad (1.3)$$

The value of  $\beta$  can be obtained as  $1 + U/c$  using equation (1.1). It can be calculated that the number of particles crossing the shock front with relativistic speeds is  $nc/4$ , where  $c$  is the velocity of light and  $n$  is the number density of particles. It can be seen from Figure 1.3 that the number of particles advected away in the downstream region would be  $nU/4$ . Therefore the probability of escaping the system is  $U/c$  and hence the probability of remaining in the system would be  $P = 1 - U/c$ . Putting the values of  $\beta$  and  $P$  back in equation (1.3), one would get the power law index of -2 for non-relativistic shocks, where  $U \ll c$ .

It can be seen by equation (1.1) that the gain in energy is proportional to the velocity of the shock, this is why the process is called *first order* Fermi acceleration. However, in the case of *second order* Fermi acceleration, the gain in energy is proportional to the square of the velocity of the shock. This is due to the interaction of the charged particles with a moving magnetised cloud. More details can be found in (Longair 2011).

## 1.2.2 Sites of CR Acceleration

CRs can be accelerated via the Fermi mechanism as described in section 1.2.1 in various known astrophysical environments. The main requirement here is that the particle's Larmor radius of gyration in the magnetic fields present around these sources cannot exceed the physical size of the source, otherwise, the particle would not be confined anymore. The Larmor radius is defined as the radius of the circular motion of a charged particle in a uniform magnetic field. The maximum attainable energy ( $E_{\max}$ ) by these particles in this scenario is given by the following equation

$$E_{\max} = Ze\beta cBL, \quad (1.4)$$

where the particle of charge  $Ze$  is moving with velocity  $\beta c$  in a magnetic field of  $B$  of an object of length scale  $L$ . For given source properties, heavier nuclei can be accelerated to higher energies than lighter nuclei. It is observed that the highest energy CR spectrum is likely to be dominated by heavier nuclei (Ave et al. 2003). In Figure 1.4, the so-called ‘‘Hillas plot’’ is shown, which is a handy tool to characterize the candidates to accelerate CRs. It displays the various acceleration sites and their magnetic fields as a function of physical size. It also shows lines for required  $B$  and  $L$  to accelerate particles to 100 EeV and 1 ZeV energies. The 1 ZeV line is shown for protons and 100 EeV is for Iron nuclei. Sources lying above the specified energy line are able to accelerate CRs to that energy. Although, not all the source types are suitable for the acceleration of the highest energy CRs, however, they can contribute towards different energy ranges of the all-particle CR spectrum as it extends for more than 10 order of magnitude in energies. The sources can be divided into two main categories namely galactic and extragalactic. The main galactic sources are SNRs, Pulsar Wind Nebulae (PWNe), Pulsars, Binary systems, and young stars. The  $E_{\max}$  reachable by the galactic sources is a matter of debate, however, they can significantly contribute until the PeV energies of the CR spectrum. The highest energy part of the CR spectrum is believed to be due to sources of extragalactic origin. The proposed sources of extragalactic origin are Active Galactic Nuclei (AGN), starburst galaxies, cluster of galaxies and Gamma-Ray Bursts (GRBs).

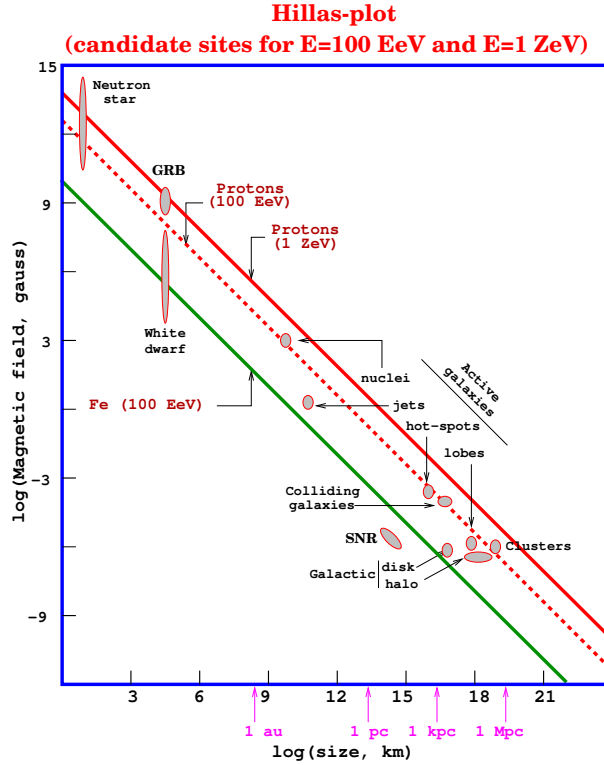


**Figure 1.4:** The Hillas plot (Hillas 1984): magnetic field vs. typical size of various potential sites of astrophysical particle acceleration. The different lines indicate the energy reachable for the given particle species as a function of source size and its magnetic field. The source above the lines fulfils this criterion. The figure is taken from (Fraschetti 2008).

## 1.3 $\gamma$ -Ray Astronomy

Previously, I introduced the production and acceleration of CRs in extreme astrophysical environments. CRs detected at Earth have lost the directional information while travelling through the magnetic field present in the galactic and extragalactic medium. However, through the interaction of CRs (charged particles) with the ambient medium, high energy  $\gamma$ -rays are also produced.  $\gamma$ -rays are not deflected by the magnetic fields as they are neutral particles. Therefore, the directional information about the source location is intact. Hence,  $\gamma$ -rays serve as excellent messengers to study the source environments of the highest energy accelerator sites in the universe.  $\gamma$ -rays cover a large part of the EM-spectrum starting from  $\sim 1$  MeV until the highest energies (see Figure 1.1). Depending on the energy, the observed  $\gamma$ -rays can be divided into the following domains (see Table 1.1). The work presented in this thesis is concerned to the VHE domain.

### 1.3.1 $\gamma$ -Ray Emission Mechanisms

$\gamma$ -rays are produced through the interaction of the high-energy charged particles with the different media in the universe. The nature of this interaction can differ, depending on the CR particle

Energy domain	Energy range
Low Energy (LE)	1 MeV to 30 MeV
High Energy (HE)	30 MeV to 50 GeV
Very-High Energy (VHE)	50 GeV to 100 TeV
Ultra-High Energy (UHE)	100 TeV to 100 PeV
Extremely-High Energy (EHE)	>100 PeV

**Table 1.1:** Domains of the  $\gamma$ -ray astronomy depending on the energy ranges.

type and the available medium, resulting in different  $\gamma$ -ray emission mechanisms. Understanding the emission mechanism is crucial because it can provide information about the origin, type, and propagation of CRs in the ambient medium. CRs can be hadronic or leptonic in nature. Therefore, the dominant  $\gamma$ -ray emission processes are divided into two scenarios namely hadronic and leptonic emission. The emission mechanism depends on the type of media where the interaction occurs. The media can be matter, radiation fields, or magnetic fields. The  $\gamma$ -ray production through a leptonic scenario occurs mainly through Bremsstrahlung, synchrotron, and Inverse Compton scattering processes. A hadronic scenario occurs mainly through pion decay. These pions are created in CR collisions. All of these scenarios of  $\gamma$ -ray production are depicted in Figure 1.5 and will be discussed below. More details can be found in (Blumenthal & Gould 1970; Longair 2011; Aharonian 2004).

### 1.3.1.1 Bremsstrahlung

Electrons get decelerated while passing near atomic nuclei and ions (see Figure 1.5 upper left panel). The energy lost in deceleration creates a  $\gamma$ -ray photon, this emission process is known as “Bremsstrahlung” or braking radiation. The Bremsstrahlung energy loss rate of electrons can be written as:

$$-\frac{dE_e}{dt} = \frac{cm_p n}{X_0} E_e, \quad (1.5)$$

where  $E_e$  is the electron energy,  $m_p$  is the proton mass,  $c$  is the speed of light and  $n$  is the number density of the ambient gas. The radiation length ( $X_0$ ) is a characteristic of a material and is defined as the mean distance over which ultra-relativistic electron loses  $1/e$  of its energy through Bremsstrahlung. For electrons of energy  $E_e$ , the lifetime due to Bremsstrahlung losses is defined as:

$$\tau_{\text{br}} = \frac{E_e}{-dE_e/dt} \approx 4 \times 10^7 (n/\text{cm}^{-3})^{-1} \text{yr}. \quad (1.6)$$

As it can be seen from equation (1.5) the energy loss rate is proportional to  $E_e$ , the lifetime ( $\tau_{\text{br}}$ ) is independent of electron energy. Therefore, we can see that Bremsstrahlung losses would not change the shape of the injected electron spectrum. As the energy loss rate is directly proportional to the ambient gas density, therefore Bremsstrahlung becomes particularly important in



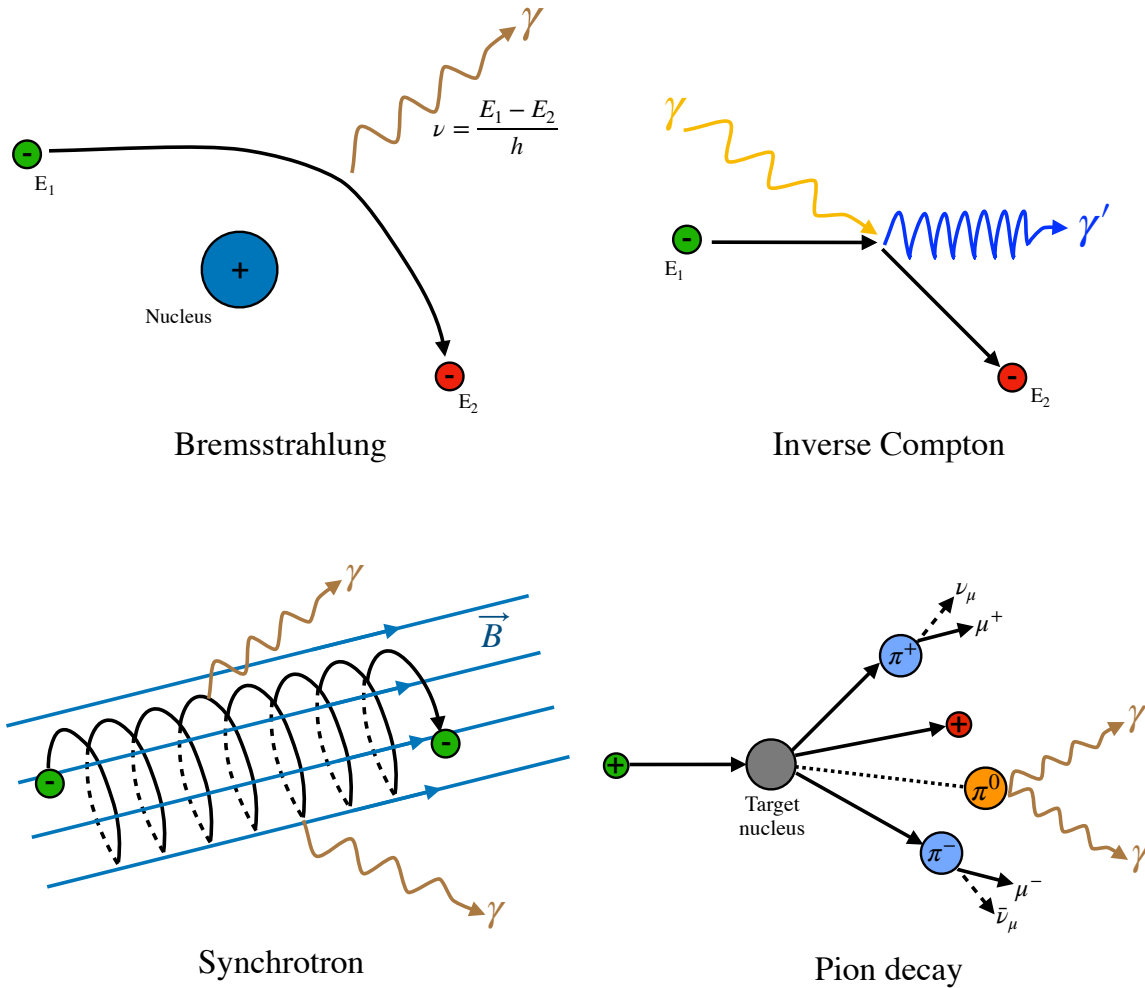


**Figure 1.5:** Schematic of different channels of  $\gamma$ -ray production. The figure is adapted from (Lopez-Coto 2015).

the dense gaseous regions for  $\gamma$ -ray production. Bremsstrahlung-produced  $\gamma$ -rays have energies of MeV, however, with higher energy CRs, VHE  $\gamma$ -rays can be produced.

### 1.3.1.2 Inverse Compton Scattering

In a leptonic scenario for  $\gamma$ -ray production, the VHE  $\gamma$ -ray photons are mainly produced by Inverse Compton (IC) scattering. IC scattering occurs when a low energy photon is up-scattered by an ultra relativistic electron and therefore gains energy. The schematic of the IC scattering is shown in the upper right panel of Figure 1.5.  $\gamma$ -rays are produced when highly energetic electrons up-scatter the ambient radiation field photons. In an astrophysical context, the target ambient fields usually consist the Cosmic Microwave Background (CMB) radiation, Infrared (IR) radiation produced by the dust of the interstellar medium and optical photons from the

starlight. The scattering cross-section of the IC process ( $\sigma_{\text{IC}}$ ) can be defined as a function of electron energy  $E_e$  and the initial photon energies of  $\omega_0 = h\nu$  by defining a term  $\epsilon_0 = \omega_0/E_e$  as shown in Klein-Nishina (KN) formula:

$$\sigma_{\text{IC}} = \frac{3\sigma_T}{8\epsilon_0} \left[ \left( 1 - \frac{2}{\epsilon_0} - \frac{2}{\epsilon_0^2} \right) \ln(1 + 2\epsilon_0) + \frac{1}{2} + \frac{4}{\epsilon_0} - \frac{1}{2(1 + 2\epsilon_0)^2} \right], \quad (1.7)$$

where  $\sigma_T$  is the Thompson scattering cross-section, which can be defined as  $\sigma_T = (8\pi/3)r_e^2 \approx 6.65 \times 10^{-25} \text{cm}^2$ ,  $r_e$  is the classical electron radius. The rest frame electron energy  $E_e = m_e c^2$ , where  $m_e$  is the rest mass of the electron and  $c$  is the speed of light. Depending on the energy of the electron and the photon the IC scattering is divided into two regimes. For non-relativistic electron energies, where  $\epsilon_0 \ll 1$ , is known as the Thompson regime. At the highly relativistic electron energies, where  $\epsilon_0 \gg 1$ , is known as the KN-regime.

The electron energy-loss rates by IC scattering in the Thompson regime can be written as:

$$-\frac{dE_e}{dt} = \frac{4}{3}\sigma_T c U_{\text{rad}} \left( \frac{v^2}{c^2} \right) \gamma^2, \quad (1.8)$$

where  $U_{\text{rad}}$  is the density of the ambient radiation fields and  $\gamma$  is the Lorentz factor of the moving electron with velocity  $v$ . The energy loss rate using equation (1.8) can be solved in terms of  $E_e$  and is  $\propto E_e^2$  in the Thompson regime. A similar expression can be obtained for KN regime where the electron energy loss rate is independent of  $E_e$ . The lifetime due to IC losses  $\tau_{\text{IC}} = \frac{E_e}{-dE_e/dt}$  is  $\propto 1/E_e$  in the Thompson regime and  $\propto E_e$  in the KN regime. Therefore, in the Thompson regime, the higher energy electrons cool down faster than the lower energy ones.

The maximum energy reached by the scattered photon can be approximated as  $E_{\text{max}} \approx 4\gamma^2 E_\gamma$ , where  $E_\gamma$  is the energy of the parent photon. In the Thompson regime, the spectral shape of the emitted photon and parent photons is similar. However, in the KN regime emitted photons suffer a very sharp cut-off. It is worth to mention that, although protons can also up-scatter the ambient photon fields via IC scattering, the relative rate of proton interaction is suppressed by a factor of  $(m_e/m_p)^4$ , where  $m_p$  is the rest mass of the proton.

### 1.3.1.3 Synchrotron Radiation

When an electron moves in a magnetic field it get accelerated. It traces a spiral around the magnetic field lines as shown in a schematic diagram in the lower left panel of Figure 1.5. The spiral motion is due to the perpendicular component of electron's velocity to the magnetic field lines. Due to the circular motion, the electrons are accelerated and produce an electromagnetic radiation known as *Synchrotron radiation*. Similarly, while instead of moving around the magnetic field lines the electrons move along the curved magnetic field lines and therefore get accelerated and emit electromagnetic radiation, this phenomenon is called *Curvature radiation*.

The average electron energy-loss rate due to synchrotron radiation is given as:

$$-\frac{dE_e}{dt} = \frac{4}{3}\sigma_T c U_{\text{mag}} \left( \frac{v^2}{c^2} \right) \gamma^2, \quad (1.9)$$

## 1. INTRODUCTION TO $\gamma$ -RAY ASTRONOMY

---

where  $U_{\text{mag}} = B^2/2\mu_0$  is the energy density of the ambient magnetic field ( $B$ ), where  $\mu_0$  is the permeability of the free space. The remaining symbols are the same as in equation (1.8). It can be obtained that the lifetime due to synchrotron losses is  $\tau_{\text{syn}} = \frac{E_e}{-dE_e/dt}$  is  $\propto 1/E_e$ , similar to the IC losses in the Thompson regime. Therefore, with increasing energy of electron, the cooling timescales will decrease. From equation (1.9) and (1.8) one can see that the emitted photon flux due the synchrotron and IC scattering hold the following relation shown in equation (1.10), which is very useful to estimate magnetic field energy density in a given astrophysical environment.

$$\frac{F_{\text{syn}}}{F_{\text{IC}}} = \frac{U_{\text{mag}}}{U_{\text{rad}}}, \quad (1.10)$$

where  $F_{\text{syn}}$  and  $F_{\text{IC}}$  is the integrated photon flux due to synchrotron and IC emission.

### 1.3.1.4 Pion Decay

In a hadronic scenario of  $\gamma$ -ray production, the main mechanism is the neutral pion decay. Pions are produced as the by-products of the proton-proton or proton-nuclei collisions. Hadronic CR travelling through the dense regions of Interstellar Medium (ISM) gives rise to this possibility. In this process, both charged and neutral pions are produced. The production of the charged pions ( $\pi^+$ ,  $\pi^-$ ) and the neutral pion ( $\pi^0$ ) happens with the same probability. Charged pions further decay into muons and neutrinos. However,  $\pi^0$  decay most probably into producing a photon pair as  $\pi^0 \rightarrow \gamma + \gamma$ . The schematic diagram of the  $\pi^0$  decay is shown in the lower right panel of Figure 1.5. The threshold energy required by the protons to produce  $\pi^0$  is given as:

$$E_{\text{th}} = 2m_{\pi^0}c^2 \left(1 + \frac{m_{\pi^0}}{4m_p}\right) \approx 280\text{MeV}. \quad (1.11)$$

The rest mass ( $m_{\pi^0}$ ) is 134.9 MeV and the mean lifetime  $\tau = 8.4 \times 10^{-17} s$ .  $m_p$  is the rest mass of the proton. As the protons producing the pions are relativistic in nature and therefore are highly energetic, the decay of the  $\pi^0$  produced in this process leads to the production of VHE  $\gamma$ -rays. A characteristic of the  $\pi^0$  decay and hence the hadronic  $\gamma$ -ray production is known as the ‘‘pion bump’’ in the GeV-TeV range of the resulting  $\gamma$ -ray spectrum.

### 1.3.2 Known Source Types of VHE $\gamma$ -rays

Sources of several kinds emitting in VHE  $\gamma$ -rays have been observed. They are also associated with the sources of CR acceleration as explained in Section 1.2.2. I have discussed in Section 1.3.1, the different ways of  $\gamma$ -ray emission and their association with the CRs. Broadly they can be divided into two categories: galactic and extragalactic. In Galactic sources, we have mainly pulsars and PWNe, SNRs and binary systems. Extragalactic sources mainly consist of AGN, starburst galaxies and GRBs.

#### 1.3.2.1 Pulsars and Pulsar Wind Nebulae

In certain cases of massive star explosion through Supernova (SN), the remaining product can become a pulsar and PWNe. A pulsar is rotating and highly magnetised Neutron Star (NS).

Particles can get accelerated in certain parts of the NS magnetosphere and therefore emit in VHE  $\gamma$ -rays (Aliu et al. 2008). The rotational energy of pulsars is mainly lost through the  $e^\pm$  wind production. The  $e^\pm$  wind interacts with the ISM and generates a shock acceleration scenario, where VHE  $\gamma$ -rays can also be produced mainly through the leptonic scenario. More details on pulsar and PWNe are given in Chapter 5 and in the reference therein. A detailed case study of the source 2HWC J2019+367, a PWN candidate, will be discussed in Chapter 6.

### 1.3.2.2 Supernova Remnants

Massive stars end their life through SN explosions. The material ejected by the SN explosion expands over a period of time and interacts with the ISM creating a shock front where CRs are accelerated. The accelerated CRs produce VHE  $\gamma$ -rays and are thought to be of hadronic origin. A more detailed description of SNe and SNRs is given in Section 5.1. The detailed reviews on this topic can be found in (Gaisser et al. 1998; Naito & Takahara 1994).

### 1.3.2.3 Binary Systems

Although, there are many binary star-systems in the galaxy, however, only a handful are known to emit in VHE  $\gamma$ -rays. Five previously known systems are (PSR B1250-63, LS 5039, LS I +61 303, HESS J0632+057, HESS J1018-589) and one new system recently discovered by High Altitude Water Cherenkov (HAWC) observatory is SS 443 ((Abeysekara et al. 2018b)). Mostly, in these cases, the system consists of a heavy and compact object such as NS or black hole and a massive star. One of the explanations of the  $\gamma$ -ray emission is the accretion of mass from the companion massive star into the compact object also known as the micro-quasar scenario. In this case, a jet is formed, where the particles get accelerated and therefore also produce VHE  $\gamma$ -rays. In another scenario, the pulsar winds interact with the winds of the massive star and shock develops, where the particle acceleration happens. More details can be found in the review (Dubus 2013).

### 1.3.2.4 Active Galactic Nuclei

AGN are the galaxies, where the central nucleus is brighter than the rest of the galaxy and hosts a Super Massive Black Hole (SMBH). Collimated jets of relativistic charged particles coming out of the central region has been observed in the past. These highly energetic charged particles produce non-thermal emission in radio to  $\gamma$ -rays. Depending on the viewing angle they are divided into different categories such as Blazars, radio galaxies, Quasars and BL Lac's. More details can be found in reviews (Fabian 2012; Netzer 2015).

### 1.3.2.5 Starburst Galaxies

Galaxies with exceptionally high star-formation rate are named as starburst galaxies. Due to high star formation rate, the rate of SN explosions is high, providing a high CR density. These CRs produce VHE  $\gamma$ -ray emission. Further details can be found in Ohm (2016) and in the references therein.

### 1.3.2.6 Gamma-Ray Bursts

GRBs are extremely energetic  $\gamma$ -ray outbursts of extragalactic origin. They can last from tens of millisecond to several hours. They are categorised as short duration ( $< 2$  s) and long duration ( $> 2$  s). The origin of these two categories is believed to be a merger of two compact objects and hyper-nova explosion of a very massive star respectively. The emission occurs promptly in soft  $\gamma$ -rays and then later an afterglow emission which is observed in all wavelengths. More details on GRBs can be found in (Kumar & Zhang 2015; Piran 2004).

## 1.4 Detection Techniques

The current detection techniques in  $\gamma$ -ray astronomy can be broadly divided into two main categories: space-based and ground-based. As shown in Figure 1.1  $\gamma$  rays cover a wide part of the EM spectrum. Earth's atmosphere is not transparent to  $\gamma$  rays, therefore the direct detection is only possible with space-based instruments. However, the size of the space-based instruments is small due to the hosting constraints put by the satellites. The power-law behaviour of the observed  $\gamma$  rays of an index around -2, makes the statistics scarce as we go higher in energy. Therefore, the small size and hence lower effective area (about  $1\text{m}^2$ ) of the space-based instruments are only suitable for  $\gamma$  rays of MeV-GeV energy range. To observe  $\gamma$  rays above GeV energies, the indirect detection techniques from the ground are utilised. They reach a large effective area to be able to detect lower fluxes at higher energies. In this thesis, one of the ground-based detector, the HAWC observatory is used, therefore I will give a short introduction to space-based instruments and then will lead to a more detailed introduction to ground based instruments.

### 1.4.1 Space-Based Instruments

Observation of  $\gamma$ -rays using space-based instruments started in 1961 with Explorer 11, which observed  $\gamma$ -rays photons coming from all directions (Kraushaar & Clark 1962). Later with the launch of Small Astronomy Satellite 2 (SAS-2) (Warren 1990) in 1972 and COS-B satellite (Swanenburg 1981) in 1982 the first detailed view of the  $\gamma$ -ray Universe was observed. In 1991, the Energetic Gamma-Ray Experiment Telescope (EGRET) was launched, which was one of the instruments carried by the Compton Gamma-Ray Observatory (CGRO). It was sensitive to  $\gamma$ -rays in the MeV-GeV energy range and detected 270 sources between 0.1 to 10 GeV energies (Hartman et al. 1999).

Later in 2008, the Fermi  $\gamma$ -ray telescope was launched which hosts two different detectors, the Large Area Telescope (LAT) and the Gamma-ray Burst Monitor (GBM). Fermi-LAT is an imaging, wide Field of View (FOV) ( $\sim 2$  sr), high-energy  $\gamma$ -ray telescope. The size its aperture is about  $\sim 1\text{m}^2$ . It is sensitive in the energy range of 0.2 to 500 GeV. In the energy range of 0.03 to 300 GeV, the photon material interactions are dominated by electron-positron pair production. Therefore, pair production is used to detect and reconstruct the direction of  $\gamma$ -rays and a calorimeter is used for energy reconstruction. This kind of detector is consists of a *converter*, a *tracker* and a *calorimeter*. The converter converts the incoming  $\gamma$ -ray photon into electron-positron pairs, which are then tracked by the tracker in order to estimate the direction and energy

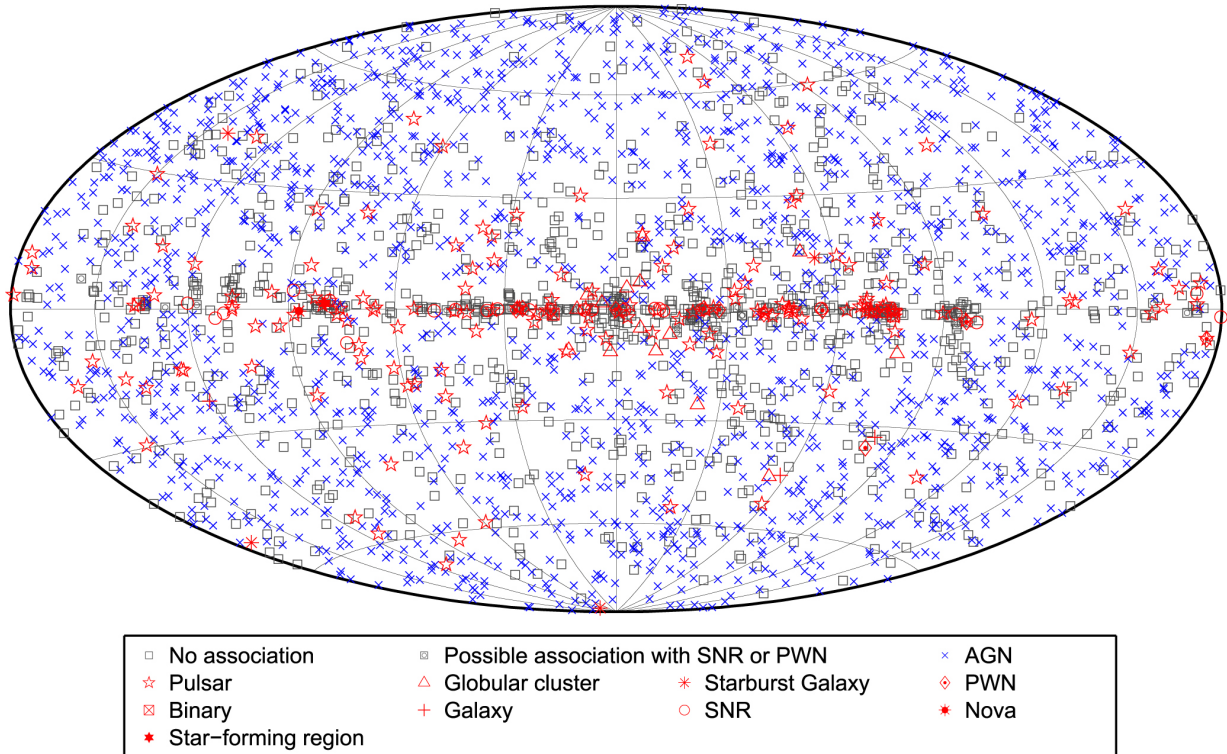


**Figure 1.6:** The 3FGL Catalogue. The coordinates are galactic. Figure is take from (Acero et al. 2015)

loss of the process. The calorimeter is used to absorb the produced leptons completely to estimate the remaining energy and hence improving the energy estimation. For background rejection, it uses an *anti-coincidence* system to veto the background events generated by the charged CRs. The angular resolution of Fermi-LAT is about  $3.5^\circ$  at 300 MeV and goes to  $< 1.5^\circ$  at  $> 10$  GeV and it can scan the full sky in 3 hours. The energy resolution of Fermi-LAT is about  $< 10\%$ . In Figure 1.6 the third Fermi-LAT catalogue sources are shown. Various different types of sources are detected with a total of 3033 sources (Acero et al. 2015). More details can be found in (Zanin 2011; Ayala Solares 2017) and the references therein.

## 1.4.2 Ground-Based Experiments

To observe the  $\gamma$ -ray above tens of GeV energies, indirect methods are used.  $\gamma$ -rays do not penetrate the Earth's atmosphere, however, the primary particle of  $\gamma$ - or cosmic-ray interact with the nuclei present in the earth's atmosphere and generate a cascade of secondary particles. This cascade process leads to the development of the so-called Extensive Air Shower (EAS), which can be detected by the detectors placed on the ground. The detected EAS is then reconstructed using different methods to determine the type, energy, and direction of the primary particle.

1.4.2.1 Extensive Air Showers

By the interaction of the primary particle in the Earth’s atmosphere, the secondary particles can be produced with several different mechanisms. The first interaction usually occurs at an altitude of around 15-30 km. The mechanism of the first interaction is primarily determined by the type of the primary particle.

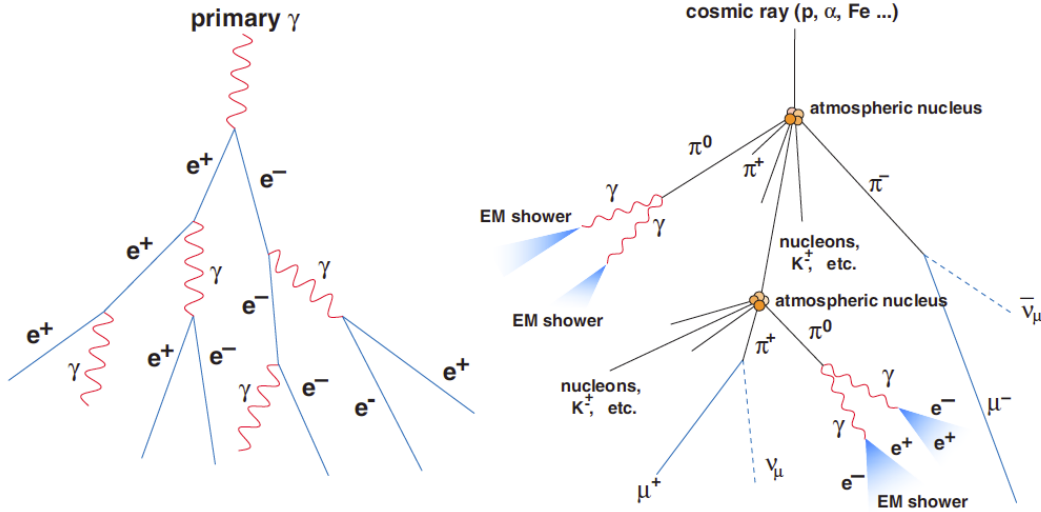


**Figure 1.7:** Left:  $\gamma$ -ray induced air shower. Right: CR (hadron) induced air shower. Figure is taken from (Wagner 2006).

The EM showers are initiated by  $\gamma$ -ray photons or leptons (mostly electrons). Both of which are similar in nature the main difference is the height of the first interaction in the atmosphere. The initial development stages of the EM air showers are dominated by pair-production, Bremsstrahlung and in the later stages by ionisation. The schematic of a  $\gamma$ -ray induced air shower is shown in the left panel of Figure 1.7. For pair production to occur, the energy of the primary photon has to be larger than the sum of the rest-mass energy of the electron-positron pair,  $E_\gamma > 2 \times (m_e c^2) = 1.022 \text{ MeV}$ . Where,  $E_\gamma$  is the energy of the  $\gamma$ -ray photon and  $m_e$  is the rest-mass of the electron. The secondary photons in the EM showers are produced through Bremsstrahlung (see Section 1.3.1.1). For a given medium, the characteristic length scale over which the electron will lose  $1/e$  of its energy through Bremsstrahlung is known as the *radiation length* ( $X_0$ ) of the medium. It is also the  $7/9$  of the mean free path for pair production. For the Earth’s atmosphere the value of  $X_0 = 37.15 \text{ g/cm}^2$  (Grieder 2010).

The first theory of showers induced by fast electrons was given by (Bhabha & Heitler 1937). Later, a simple model of shower development is given (Matthews 2005) with three basic assumptions:

- ⊙ The length scales due to Bremsstrahlung and pair-production are equal.
- ⊙ Bremsstrahlung and pair-production are the two dominant processes.



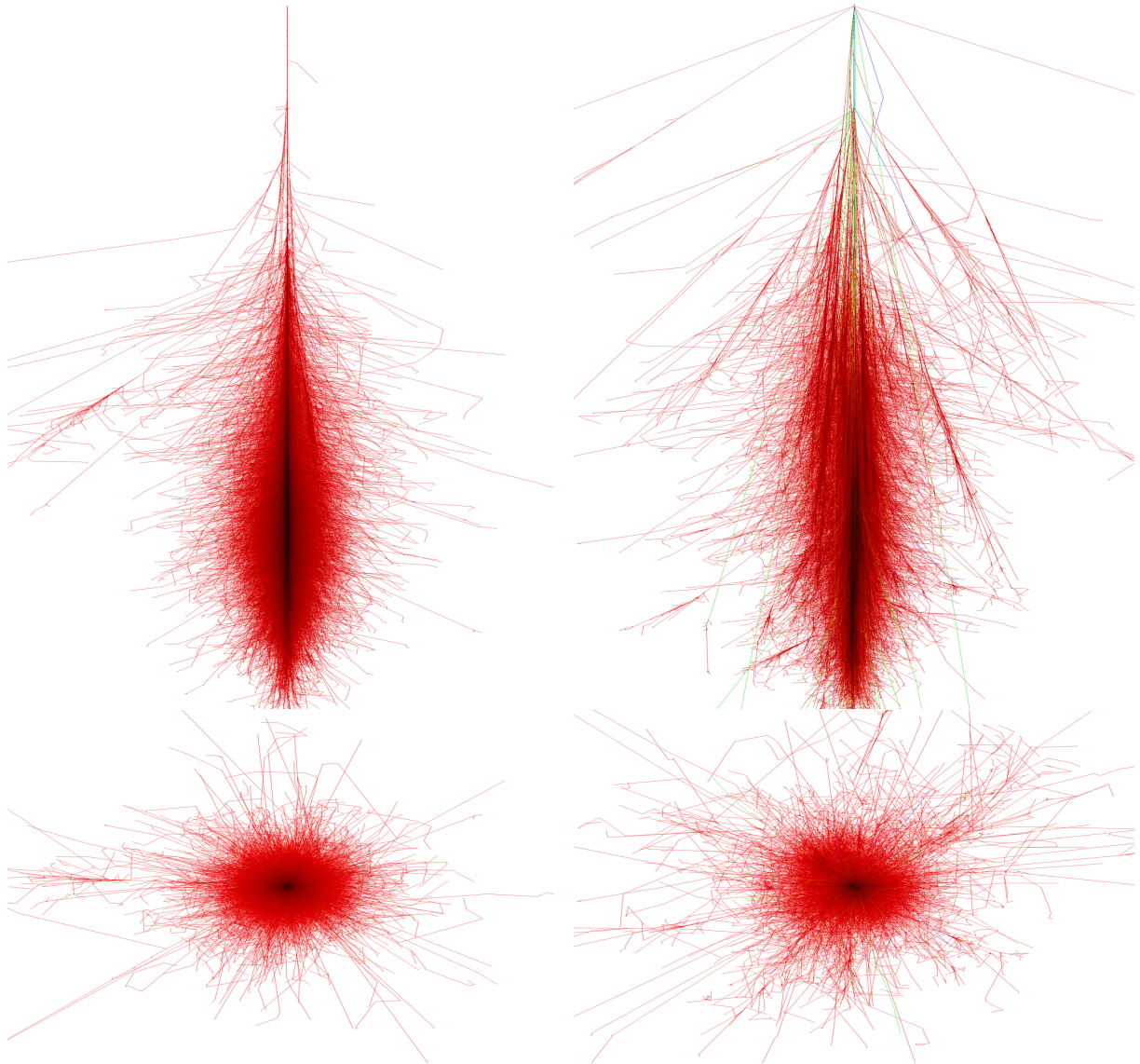


**Figure 1.8:** MC simulations of 1 TeV  $\gamma$ -ray and proton shower. Upper left panel:  $\gamma$ -ray shower particle tracks. Lower left panel: same shower as above in the transversal plane. Upper right panel: Proton shower particle tracks. Lower right panel: same shower as above in the transversal plane. The red colour lines represent the EM part of the shower. In the proton shower, The green and blue lines show muons and hadrons respectively. Images are taken from (Heck et al. 1998).

⊙ The distribution of energy among secondary particles is equal in each step.

Using this model,  $E_0$  being the primary energy, the number of particles at a travelled distance of  $x$  is given as  $N(x) = 2^{x/X_0}$  and each of these particles has an energy of  $E(x) = E_0 2^{-x/X_0}$ . The number of secondary particles increases till a certain depth in the atmosphere, where it reaches a



## 1. INTRODUCTION TO $\gamma$ -RAY ASTRONOMY

---

maximum, also known as the depth of the shower maximum ( $X_{\max}$ ), which can be estimated as:

$$X_{\max} = X_0 \frac{\ln E_0/E_c}{\ln 2}, \quad (1.12)$$

where  $E_c \sim 80$  MeV is the critical energy. At this energy the losses due to Bremsstrahlung and ionisation are equal. After reaching the  $X_{\max}$  the shower size starts to decrease owing to the ionisation losses.

For hadron initiated showers, the main difference is that it is dominated by strong interactions. The primary particle in this case, interact with the nuclei present in the Earth's atmosphere and produce mesons (mostly pions (90 %) and kaons (10 %)) and some light baryons ( $p$ ,  $\bar{p}$ ,  $n$ ,  $\bar{n}$ ). The charged pions decay into muons and neutrinos ( $\pi^+ \rightarrow \mu^+ + \nu_\mu$ ;  $\pi^- \rightarrow \mu^- + \bar{\nu}_\mu$ ). The neutral pions which are 1/3 of the total pions, decay into  $\gamma$  photons ( $\pi^0 \rightarrow \gamma + \gamma$ ). The charged pions have a significantly larger lifetime of  $2.6 \times 10^{-8}$  s compared to the lifetime of neutral pions of  $0.8 \times 10^{-16}$  s. The muons produced by charged pions can later decay into electrons and neutrinos ( $\mu^+ \rightarrow e^+ + \nu_e + \bar{\nu}_\mu$ ;  $\mu^- \rightarrow e^- + \nu_\mu + \bar{\nu}_e$ ), however, for muons decay dominates over the ionisation-losses. Therefore, they produce the penetrating part of the shower which can be detected on the ground directly. The  $\gamma$ -ray produced by neutral pions can start individual sub-showers, which follows the shower development as of an EM shower described previously.

There are certain differences in the EM or hadron induced air showers, which are used by the ground-based detectors to separate one from the other. The EM showers are more compact and more symmetrically distributed around the shower development axis. While the hadron induced air showers are more dispersed, due to the larger transverse momentum imparted to the secondary particles during their production. Additionally, muons produced in hadron induced showers gives distinct feature in the detected air shower which is utilised to  $\gamma$  from hadron showers. Figure 1.8 shows the Monte Carlo (MC) simulations of two EASs for the same primary energy of  $\gamma$ -ray and proton. It can be seen that the proton-induced air shower is more disperse than the  $\gamma$ -ray induced one. More details can be found in (Grieder 2010; Longair 2011).

Now I will discuss two techniques for the detection of EASs: Imaging Atmospheric Cherenkov Telescopes (IACTs) and EAS particle detector arrays. However, before that a brief introduction to the Cherenkov radiation is required as the IACTs and some of the EAS detector array techniques rely on the detection of the Cherenkov radiation.

### 1.4.2.2 Cherenkov Radiation

When a charged particle passes through a dielectric medium (such as water or air) with a speed higher than the speed of light in that medium, it produces the Cherenkov radiation. This effect was discovered by Pavel Cherenkov (Cherenkov 1934), for which he was awarded the 1958 physics Nobel Prize. A moving charged particle would cause a net polarisation in a dielectric medium because the surrounding atoms and molecules will move in order to compensate for its presence. Therefore a net dipole field arises, which get relaxed when the particle has passed, through a dipole transition emitting the EM radiation.

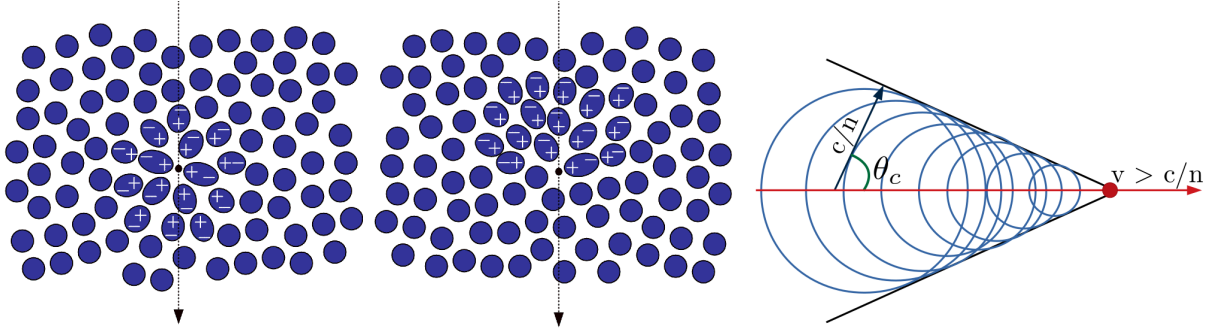


**Figure 1.9:** Schematics of polarisation of molecules while non-relativistic and relativistic charged particle travelling through a dielectric medium are shown in the left and middle panel respectively. Schematic diagram showing the production of Cherenkov light and the geometric expansion of the wavefront.

There are two scenarios of emitting this EM radiation. For a charged particle travelling non-relativistically the EM radiation will be produced from all parts of the particle track incoherently as shown in the left panel of Figure 1.9, therefore, no Cherenkov radiation is produced. However, for charged particles travelling faster than the speed of light in the medium, the radiation from different parts of the particle track adds coherently using Huygens construction. It is shown in the middle panel of Figure 1.9 and in the right panel, the schematic of the Huygens construction is shown. It can be seen from the geometric representation of the Huygens construction that the constructive interference creates a conical wavefront of EM radiation. Given the speed of light in the vacuum is  $c$  the refractive index of the medium is  $n$  and the velocity of the particle is  $v$ . The coherent wavefront will propagate in the medium with speed  $c/n$  with an angle  $\theta_c = c/vn$  with respect to the velocity vector. For water  $n = 1.33$ , which corresponds to  $\theta_c = 41.2^\circ$ , given  $v > c/n$ . The threshold energy ( $E_{\min}$ ) to produce Cherenkov radiation for a particle of mass  $m_0$  can be written as:

$$E_{\min} = \gamma_{\min} m_0 c^2 = \frac{m_0 c^2}{\sqrt{1 - n^{-2}}}. \quad (1.13)$$

where  $\gamma_{\min}$  is the Lorentz factor of the moving charged particle. It can be seen that the  $E_{\min}$  is lower for lighter particles, therefore, the Cherenkov radiation production is dominated by them. The number of Cherenkov photons produced at a wavelength  $\lambda$ , by an ultra-relativistic particle while travelling a length  $X$  in a given dielectric medium is described by the Frank-Tamm formula:

$$\frac{d^2 N}{dx d\lambda} = 2\pi\alpha Z^2 \lambda^{-2} \left( 1 - \frac{1}{\beta^2 n^2(\lambda)} \right), \quad (1.14)$$

where  $\alpha \approx 1/137$  is the fine structure constant and  $Z$  is the charge of the particle. It also describes the peak of the Cherenkov radiation, which lies in the range of blue to ultraviolet wavelengths.

### 1.4.2.3 Imaging Atmospheric Cherenkov Telescopes

The charged particles in EAS produce Cherenkov light (see Section 1.4.2.2) while passing through the atmosphere. A Cherenkov light pool is created by the whole EAS on the ground with a radius

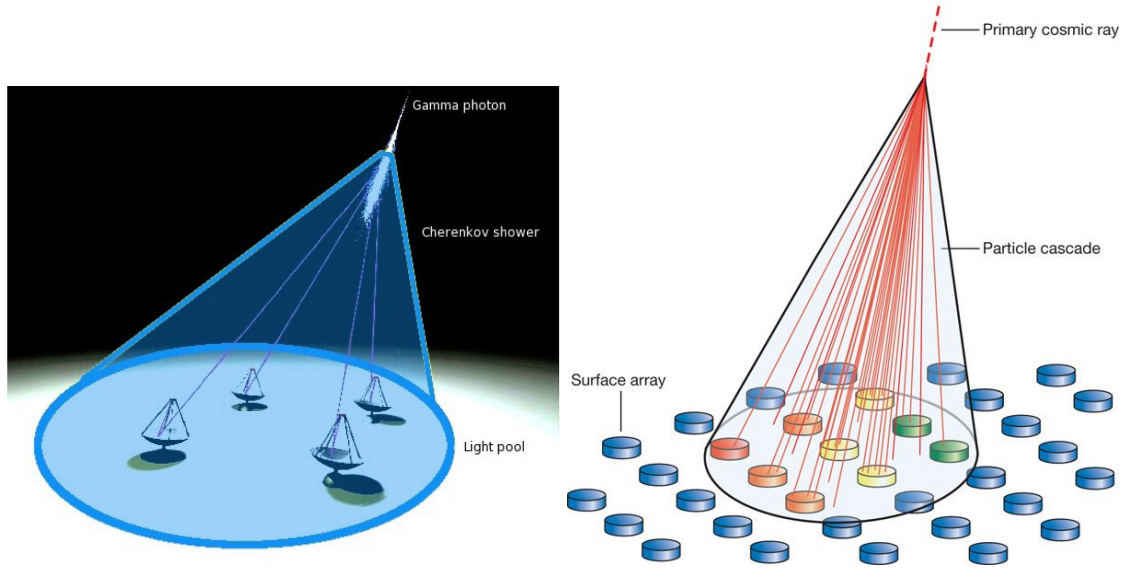


**Figure 1.10:** Schematic of the two ground-based detection techniques of EAS. On the left, the IACT technique, to detect the Cherenkov light pool produced in the atmosphere by EASs using an imaging telescope. On the right, the EAS particle detector array, which detects the secondary particles of EASs. The Figure is taken from (Bauleo & Rodriguez Martino 2009).

of  $\sim 120$  m. A schematic of an IACT and the Cherenkov light pool created by an EAS is shown on the left panel of Figure 1.10. The part of the light pool collected by the telescope on the ground is focused on a  $\sim 3$ - $5^\circ$  diameter FOV stereoscopy camera. The camera consists of a set of Photo-Multiplier Tubes (PMTs) (see Section 2.2). The image of the EAS recorded by the camera is reconstructed to estimate the shower properties.

The technique of IACTs started with the Whipple telescope, which detected the Crab Nebula as the first source emitting in VHE  $\gamma$ -rays (Weekes et al. 1989). It was further developed by the second generation IACTs, Cherenkov Array at Themis (CAT) (Barrau et al. 1997), Collaboration of Australia and Nippon for a Gamma-Ray Observatory in the Outback (CANGAROO), (Tanimori et al. 1998) and High Energy Gamma-Ray Astronomy (HEGRA) (Aharonian et al. 2000), also detecting a ten of VHE  $\gamma$ -ray sources mostly bright galactic sources and nearby AGN. Significant improvement was made with the third generation of IACTs in the early 2000's (Aharonian et al. 2008), with High Energy Stereoscopic System (HESS) (Hinton 2004) in the southern hemisphere, Major Atmospheric Gamma Imaging Cherenkov Telescopes (MAGIC) (Cortina 2005) and Very Energetic Radiation Imaging Telescope Array System (VERITAS) (Krennrich et al. 2004) in the northern hemisphere. These new generation telescopes have lowered the energy threshold to few tens of GeV and improved the flux sensitivity an order of magnitude. They have detected more than 200 galactic and extragalactic sources. To further advance the field of  $\gamma$ -ray astronomy using IACTs, the Cherenkov Telescope Array (CTA) observatory is under development. It will cover the whole sky with two parts of the observatory in the northern and southern hemisphere (Acharya et al. 2013). It will improve the sensitivity an order of magnitude compared to the current IACTs and will also significantly increase the energy range (10 GeV to 100 TeV)

of observation.

#### 1.4.2.4 EAS Particle Detector Arrays

In this technique, EASs are detected using an array of particle detectors deployed over a large area ( $\mathcal{O} > 10^4 \text{ m}^2$ ). The particle detector array is used to detect the secondary particles of the EAS. Therefore, these arrays are deployed at high altitudes in order to be close to the depth of the shower maximum ( $X_{\text{max}}$ ) of the shower. A schematic of the technique is shown in the right panel of Figure 1.10.

The main techniques to detect the secondary particles are either using scintillation counters or by using Water Cherenkov Detectors (WCDs). In the first, PMTs detect the light from scintillation, while in the second, they detect the Cherenkov light produced by the secondary particles in water. The time and charge information of the signal observed by the PMTs is then utilised to estimate the shower properties. Tibet AS- $\gamma$  experiment (Amenomori et al. 2015) is one such kind of scintillator based detector array. There are also other particle detection techniques such as the usage of Resistive Plate Chambers (RPCs), which are utilised to detect EASs and proven to be successful, an example of this being the ARGO-YBJ experiment (Bartoli et al. 2013) (Bartoli et al. 2015). The first generation example of WCD based technique is the Multiple Institution Los Alamos Gamma Ray Observatory (MILAGRO) (Dingus et al. 2000) (Abdo et al. 2007b). The second generation WCDs based EAS particle detector array is the HAWC  $\gamma$ -ray Observatory (Abeysekara et al. 2013). HAWC has already shown several exciting results since the full deployment of the observatory in March 2015 and is the instrument used in this thesis. In the Chapter 2, the description of the observatory will be given more detail.

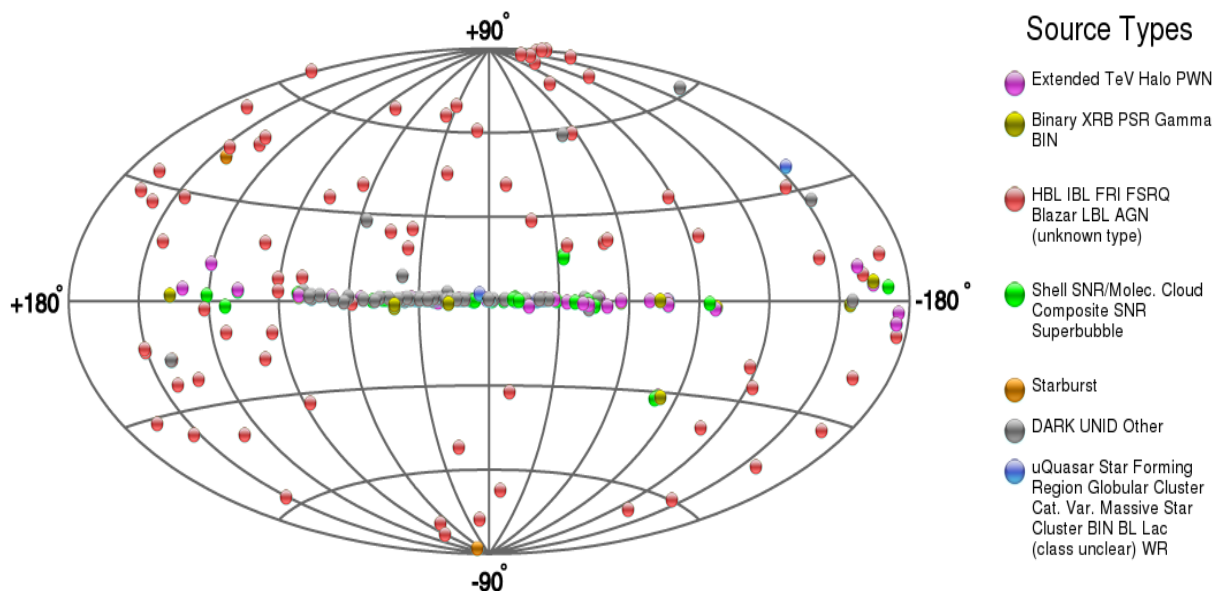


**Figure 1.11:** The TeVCat catalogue for energies above  $> 50 \text{ GeV}$ . The coordinates are galactic. The Figure is taken from <http://tevcat.uchicago.edu> in October 2018 which is based on the concept of (Wakely & Horan 2008).

## 1. INTRODUCTION TO $\gamma$ -RAY ASTRONOMY

---

Both of the ground-based detection techniques explained in Section 1.4.2.3 and 1.4.2.4 are complementary to each other. In the VHE range, IACTs are suitable for few tens of GeV to tens of TeV, whereas EAS particle detector arrays are competent at few TeV to few hundreds of TeV. The angular resolution and energy resolution of IACTs is better than the EAS arrays, therefore, being more suited for spectral and morphological studies. However, IACTs are optical instruments and can only operate in dark nights or moderate moonlight, while EAS arrays have no such limitation and have almost  $\sim 100\%$  duty cycle, making them ideal instruments for surveying purposes. The pointing capability of IACTs is ideal for deep observations, but their FOV is limited, on the other hand, the wide FOV of EAS arrays is better for the observation of extended sources. In conclusion, both the techniques are important to observe the different aspects of the VHE  $\gamma$ -ray sky. In Figure 1.11, the source population detected to date by ground-based experiments (IACTs and EAS arrays) is shown. It can be seen that there is a wide variety of objects in the detected source population, however, a large number of them are still unidentified. Nevertheless, the rich source population detected by ground-based detection techniques is the evidence of their success.



# 2

## The HAWC $\gamma$ -Ray Observatory

The High Altitude Water Cherenkov (HAWC)  $\gamma$ -ray observatory (Abeysekara et al. 2013) is a second generation ground-based Water Cherenkov Detector (WCD) array. It is located at Sierra Negra in the state of Puebla in central Mexico ( $18^{\circ} 59'41''$  N,  $97^{\circ} 18'30.6''$  W) at 4100 m above sea level (a.s.l.). The array is composed of 300 WCDs encompassing an area of 22000 m<sup>2</sup>. It is sensitive to  $\gamma$  rays and CRs in an energy range of a few hundreds of GeV to  $\sim 100$  TeV energies. It has a large instantaneous FOV of  $\sim 2$  sr and covers the declination band of  $-24^{\circ}$  to  $64^{\circ}$ . HAWC covers two thirds of the sky every day and observes half of the galactic plane with the galactic center being close to the horizon. The duty cycle of HAWC is  $> 95\%$ .

On the right panel of Figure 2.1, the shower size as a function of atmospheric depth travelled by the shower is shown. It can be seen that the shower size increases until a certain depth in the atmosphere and then starts to decrease. The atmospheric depth corresponding to the maximum shower size is known as the  $X_{\max}$  (see discussion in Section 1.4.2.1). The altitude of HAWC corresponds to 630 g/cm<sup>2</sup> in the atmospheric depth, which also corresponds to 17 radiation lengths in the atmosphere. It can be seen that HAWC is significantly closer to  $X_{\max}$  compared to the MILAGRO experiment, this is the main reason for better sensitivity achieved by HAWC. However, the ideal scenario to observe the maximum number of particles would be at the height of 5400 m.

In the left panel of Figure 2.1, a picture of HAWC observatory is shown. The comparatively larger building outside the array is the utility building, which also hosts the water filtration facility for the HAWC WCDs. The white building in the center is the counting-house, where the calibration and data acquisition system (DAQ) is situated.





**Figure 2.1:** Left panel: shower size as a function of the depth travelled in the atmosphere and height a.s.l.. Right panel: The complete HAWC  $\gamma$ -Ray Observatory. Showing all the WCDs, the counting-house at the center and the utility building at the bottom left corner. The plot on the left panel is taken from (BenZvi 2018).

## 2.1 Water Cherenkov Detectors (WCDs)

The base design of a WCD unit in HAWC is a cylindrical corrugated steel tank of 7.3 m diameter and 5 m in height and is illustrated in Figure 2.2. On the top, it is covered by a protective

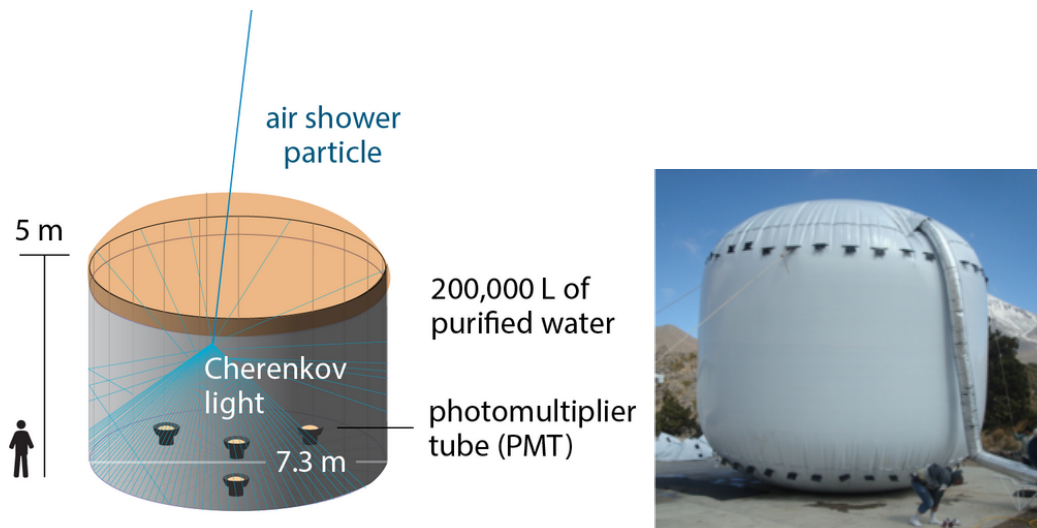


**Figure 2.2:** Left panel: Schematic of a HAWC WCD, showing an incoming particle and four upward facing PMTs to detect the produced Cherenkov light. Right panel: An inflated bladder. It is white from outside but it is black on the inside.



## 2. THE HAWC $\gamma$ -RAY OBSERVATORY

---

canvas dome supported by a robust steel frame to prevent accumulation of snow and rain. It consists of a light-tight plastic liner (or bladder) filled with  $\sim 200,000$  litres of purified water, which corresponds to a water height of 4.5 m. The inner surface of the bladder is black. At the bottom, it has four upward facing high quantum efficiency Photo-Multiplier Tube (PMT)s (see Section 2.2), one 10" Hamamatsu R7081-MOD PMT at the center and three 8" Hamamatsu R5912 PMTs spaced  $120^\circ$  apart at 1.8 m from the center.

The secondary particles from a particle air shower mainly consist of  $e^\pm$ ,  $\gamma$ , and muon ( $\mu$ ) (see Section 1.4.2.1). These secondary particles enter into WCDs and produce Cherenkov light (see Section 1.4.2.2), which is then detected by the PMTs. Water is an excellent medium with a high refractive index to facilitate the Cherenkov light production by relativistic charged particles. The water is purified to increase the attenuation length up to  $\sim 10$  m for the wavelengths detectable by the PMTs (300 nm to 500 nm). The water level of  $\sim 4$  m ensures that the electromagnetic component of the air shower will lose all their energy before reaching the bottom of the tanks and hence creating a uniform light pool. While mostly muons will reach the bottom of the tank and produce light along their full track length. This further helps in separating  $\gamma$  from hadron induced EAS.

The modular structure of the HAWC WCDs makes them optically isolated from each other, which has two benefits. Firstly, it helps in dealing with them separately in the construction phase or for maintenance. Secondly, it aids in the identification of the local variations in the observed particle air shower, which provides a strong  $\gamma$ -hadron separation power (more details in Section 2.6.3).

### 2.2 Photomultiplier Tubes

Photomultiplier tubes (PMTs) are extremely sensitive devices for detecting photons. They are sensitive to single photons and have a very fast response time of tens of nanoseconds. The working of PMT utilises the basic principle of the photo-electric effect. In HAWC, we use 8" Hamamatsu R5912 and 10" Hamamatsu R7081-02 PMT. The 8" PMTs were inherited from the MILAGRO experiment. In Figure 2.3 (left panel) the PMTs used in HAWC array are shown.

The working of a PMT can be described by the right panel of Figure 2.3. When a Cherenkov photon hits the photo-cathode of the PMT it can produce a photo-electron (PE) via the photo-electric effect. This ejected PE then accelerates to the first dynode where it ejects more electrons. This process continues till the last dynode, increasing in number at each dynode depending on the voltage applied. In the end, at the anode, the resulting signal is measured. The gain of the PMT is defined as the ratio of the mean integrated output from a single incident photon to the fundamental charge of an electron. The value of the gain depends on the number of dynodes and the applied high voltage (HV). In our case, both of the PMT types have 10 stage dynode chain and are operated at  $\sim 1700$  V. However, the exact value of the HV applied to each channel is tuned in order to match the gain of all PMTs thereby producing uniform electronics response. The average gain of  $1.6 \times 10^7$  is designed to give very good charge resolution for single PE signals.

The probability of a photon entering the photo-cathode and in turn producing a certain signal



**Figure 2.3:** Left panel: PMTs used in HAWC (left: 10", right: 8"). Right panel: Schematic diagram of a typical PMT. The PMT schematic is taken from (Wood 2018).

can be characterized by the quantum efficiency (QE) of the given PMT. The QE depends on factors like the photo-cathode material, wavelength of the incident light, location of the impinging photon on the photo-cathode and the landing of the PE on the first dynode. Therefore, calculation of the QE is a difficult process. Usually, the quoted values from the manufacturer are taken. The manufacturer-quoted peak QE for the R5912 PMT is  $\sim 25\%$ , and  $\sim 40\%$  for the R7081-02 PMT. More details can be found in (Wood 2018).

### 2.3 Data Acquisition System

The DAQ is located in the counting-house (see Fig. 2.1 central white building). More than 180 m length of RG59 coaxial cable runs from here to connect each PMT. It carries HV to all the channels and brings back the observed signals from them to the counting-house. The PMT signals are then processed using custom-made front-end boards (FEBs). The signals are amplified, shaped and discriminated using threshold definitions of 20 mV and 50 mV. The timings at which the pulsed signals from the PMTs crosses each threshold are recorded using CAEN VX1190A time-to-digital-converter (TDC) modules with a precision of 100 ps. Depending on the threshold crossed by the observed signal (20 mV or 50 mV), it is characterised as low or high time-over-threshold (ToT) hit. The ToTs are used to infer the signal size and hence the observed number of PEs. For further processing, the data is then sent to the computing farm.

HAWC has two DAQ systems referred to as main and scaler. The main DAQ system records individual air shower events. It utilises the TDCs and reads out PMT signals within a  $2 \mu\text{s}$  window once a trigger condition is met. The trigger threshold is 28 PMTs in a sliding time window of 150 ns. The trigger rate of HAWC is about 25 kHz. The signals from the PMTs are then digitised for further reconstruction of the air shower events. The scaler DAQ system counts the number of

signals in each PMT within 10 ms window. It is utilised to monitor transient  $\gamma$ -ray events, flaring AGN, GRBs, and fluctuations in cosmic ray rate from solar activity. In this thesis, I will only be using the data recorded by the main DAQ. More details on the HAWC DAQ system can be found in (Wisher 2016; Wood 2018).

### 2.4 Calibration System

Recording a triggered air shower event precisely requires a proper calibration of the observed signals. In HAWC, the signal is the electrical signal measured by the deployed PMTs in each tank. It is then sent to the central counting house using the coaxial cables. To ensure a well-calibrated signal, various measures are taken, i.e. equal cable length to connect each PMT to the counting-house and similar gain for each PMT. Later, the observed signal can be affected by the water level and quality of water within a tank. The water quality affects the attenuation of the emitted Cherenkov light and hence changing the signal amplitude. In order to take care of all these issues, an in-house calibration system is deployed. It consists of a known input light source (laser), optical filters and optical fibres which connect it to each of the WCDs. The optical filters can attenuate the signals from the light source in a range of six orders of magnitude. The light from the laser, attenuated by the optical filters (to control the intensity) travels to each WCD. It enters from the top of each WCD and is scattered using an optical diffuser to illuminate all channels within a WCD. The properties of the light entering each channel are well known, therefore it is utilised to calibrate the measured PMT signals. More details on HAWC calibration can be found in (Zhou 2015; Ayala Solares 2017).

### 2.5 Simulations

To study the performance of the various reconstruction algorithms the simulation of air showers in combination with the detector response is needed. The HAWC simulations can be divided into two parts: air shower and detector simulations. For both of these, standard simulations packages used in the community are utilised. For the simulation of air shower the COsmic Ray Simulations for KAscade (CORSIKA) package (v7.4000) (Heck et al. 1998) is used. Using the CORSIKA package, primary particle are propagated in the atmosphere and the secondary particle distribution at the HAWC altitude is obtained. Later, to simulate the detector a dedicated software package based on Geant4 (v4.10.00) (Agostinelli et al. 2003) simulations is used and is referred to as HAWCSim. The observed particles on the ground are propagated through HAWC WCDs to produce Cherenkov photons. The Cherenkov photons are detected using the simulated PMTs. In which, the quantum efficiency (QE) of the PMT, the uncertainty in the logarithm of the detected charge and the single PE noise are taken into account. The QE of the PMTs in simulations is tuned to vertical muon data. The vertical muons pass through the HAWC WCDs mostly to its entire depth and lose energy with almost constant rate, therefore, behave like a constant light source. After this stage, the simulated air showers are reconstructed the same way as data. In this thesis, I will use the HAWC simulations in Chapters 3 and 4. More details can be

found in (Abeysekara et al. 2017; Hampel-Arias 2017).

## 2.6 Air Shower Reconstruction

The reconstruction of an EAS consists of estimating the core location, the direction, the energy and type of the primary particle. HAWC employs two reconstruction chains: first is the online reconstruction at the HAWC site, and second is the offline reconstruction. The online reconstruction is performed on site to get preliminary results in order to identify transient events. In offline reconstruction, more sophisticated algorithms are used to better reconstruct the air shower properties to produce official data products of HAWC such as the HAWC sky maps. In this section, I will describe the reconstruction of core and direction, and the  $\gamma$ /hadron separation strategies used in HAWC. In this thesis, in Chapter 4, a new reconstruction method to perform the core and energy reconstruction, and  $\gamma$ -hadron separation will be discussed in more detail. Using this new method the combined event reconstruction of the HAWC main array and its high energy upgrade with a sparse outrigger array will also be discussed.

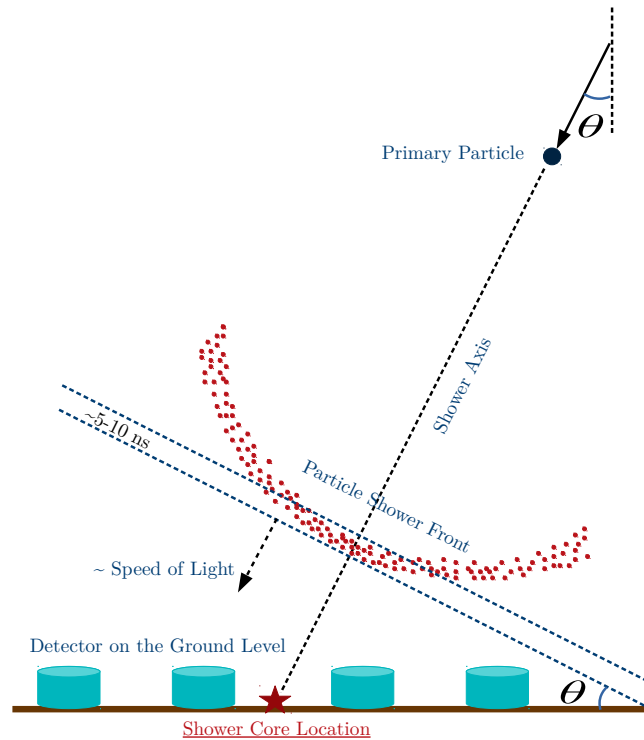


**Figure 2.4:** Schematic of an EAS. The primary particle interacts in the Earth’s atmosphere and creates a shower of secondary particles as shown in the particle shower front. The impact point of the shower axis on the ground is the core location shown with the red star. The incoming zenith angle is  $\theta$ . The figure is adapted from (Hampel-Arias 2017).

### 2.6.1 Core Reconstruction

A proper estimation of the core of an EAS is crucial to determine the direction and energy of the primary particle. As described in section 1.4.2.1 the secondary particles in an EAS are concentrated near to the shower development axis. Therefore, at the intersection of the shower axis and the ground the maximum shower energy is deposited, this location is defined as the core of an EAS (see Figure 2.4). The evolution of the air shower around the shower axis differ depending on the type of the primary particle. This property of EAS development is used to perform the  $\gamma$ /hadron separation. Therefore, an accurate estimation of the core location is important in air shower reconstruction.

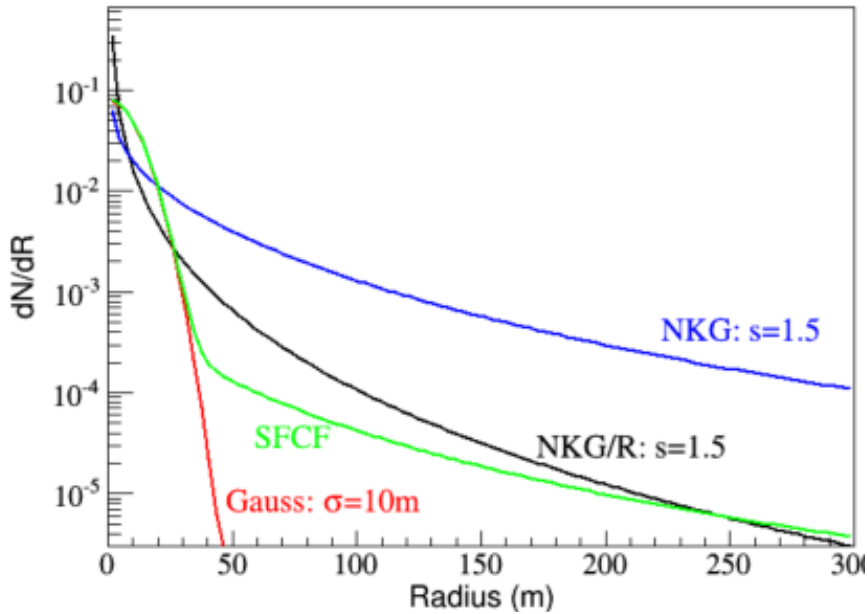


**Figure 2.5:** The different functional shapes used for fitting the observed LDF of an air shower event in HAWC. The Gaussian function falls off too fast going away from the core. The NKG function is too steep near to the core, therefore very computing intensive to converge. Where  $s = 1.5$  denotes the shower age (see text for explanation). The hybrid of both of these two is SFCF which is presently being used for determining the core location in HAWC. The Figure is taken from internal HAWC document (Braun 2016).

Before using a computing intensive algorithm to obtain the core location, a simple estimate of the core location is performed using the center of mass (COM) of the measured charge in different PMTs. The COM estimate is used as a first guess for the more advanced core fit algorithms.

In HAWC, several different functional shapes have been tested to describe the observed lateral distribution function (LDF) of an observed air shower event. The LDF of an air shower event describes the observed charge distribution as a function of distance from the shower axis (impact distance) ( $r$ ). Using a  $\chi^2$  minimisation algorithm, the expected charge  $Q_i$  and measured charge  $q_i$  distributions are compared and minimised in order to find the core location. Where suffix  $i$

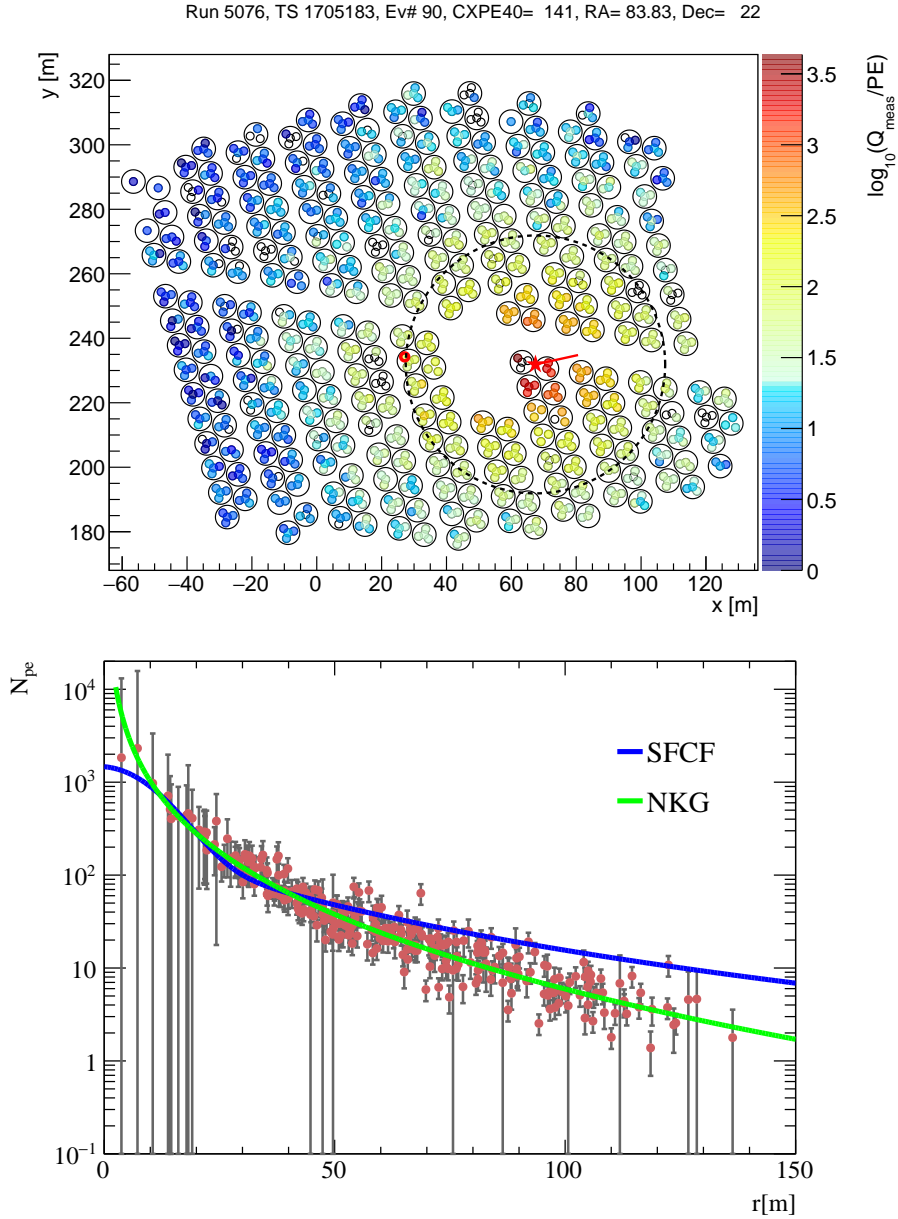


**Figure 2.6:** Top panel: the observed charge distribution of a candidate  $\gamma$ -ray data event coming from the vicinity of the Crab Nebula. Bottom panel: the observed LDF of the event shown above with the SFCF and NKG functional fit.

represents a given PMT. In the very early days, a simple Gaussian function was used, although it was simpler and faster, however, it preferred the tails of the LDF to be inside the array and therefore worsen the core estimation for partially contained events. Later the Nishimura-Kamata-Greisen (NKG) and  $\text{NKG}/r$  functions were used which are widely known to describe the LDFs of EM-induced air showers. However, it became too computationally intensive mainly because of

## 2. THE HAWC $\gamma$ -RAY OBSERVATORY

---

the cusp-like shape near to the core, which required many iterations to converge the fit. Therefore, a hybrid function was devised, which is currently being used, named as Super Fast Core Fit (SFCF). It is motivated by the NKG-function and a Gaussian function. All of these functional shapes are depicted in Figure 2.5. The functional shape of the SFCF is shown in equation (2.1).

$$Q_i = A \left( \frac{1}{2\pi\sigma^2} \exp\left(\frac{-|\mathbf{x} - \mathbf{x}_i|^2}{2\sigma^2}\right) + \frac{N}{\left(0.5 + \frac{|\mathbf{x} - \mathbf{x}_i|}{R_{\text{Mol}}}\right)^3} \right) \quad (2.1)$$

where  $\mathbf{x}$  and  $\mathbf{x}_i$  represent the core location and the location of the PMT respectively.  $A$  is the overall amplitude.  $\sigma$  is the width of the Gaussian distribution and  $N$  is the normalisation of the NKG distribution's tail.  $\sigma$  and  $N$  are fixed to a value of 10 and  $5 \times 10^{-5}$  respectively.  $R_{\text{Mol}}$  is the Molière radius, which can be calculated as:

$$R_{\text{Mol}} = X_0 \frac{E_s}{E_c \rho}, \quad (2.2)$$

where  $X_0$  is the radiation length in Earth's atmosphere it has a value of 36.08 g/cm<sup>2</sup>.  $E_c$  is the critical energy as defined in section 1.4.2.1 and has a value of  $\sim 84$  MeV.  $E_s$  is the scattering energy of electrons which has a value of 21 MeV.  $\rho$  is the density of the atmosphere at the height of HAWC it has a value of  $7 \times 10^{-4}$  g/cm<sup>3</sup>. Plugging in all these numbers back in equation (2.2) one gets the value of Molière radius at the HAWC altitude is  $\sim 124$  m.

The  $\chi^2$  to minimise can be written as:

$$\chi^2 = \sum_{i=1}^{N_{\text{PMT}}} \frac{(q_i - Q_i)^2}{Q_i + \delta q_i^2}, \quad (2.3)$$

where  $\delta q_i$  is the uncertainty in the estimated charge, which is derived from calibrations. PMTs measure charge in PEs, that are governed by Poissonian statistics, and the uncertainty in the expected charge is  $\sqrt{Q_i}$ . Hence, the total uncertainty is calculated as the quadrature sum of the uncertainties in the measured and expected charges.

In the NKG-function there is a parameter known as the shower age parameter ( $S_{\text{NKG}}$ ), which is a measure to estimate the shower development stage. The value of  $S_{\text{NKG}}$  typically lies between 0 and 2. It takes the value of 1 at the shower maximum, whereas the value of 0 and 2 are corresponding to the initial and end stages ( $\mathcal{O} \approx 1$  particle) of the shower development. To calculate  $S_{\text{NKG}}$  the NKG-function is fitted to the measured LDF with the core location fixed which is estimated by the SFCF, therefore there are only two parameters left to fit.  $S_{\text{NKG}}$  and the amplitude. This way all the parameters in the NKG-function are determined which describes the LDF of a given air shower event. In the top panel of Figure 2.6, the observed charge at different PMTs is shown for a candidate  $\gamma$ -ray event coming from the vicinity of the Crab Nebula. In the bottom panel of Figure 2.6, the observed LDF is fitted with SFCF and also the NKG-functional shape is shown as described above. More details can be found in (Abeysekara et al. 2017; Hampel-Arias 2017; Ayala Solares 2017).



## 2.6.2 Direction Reconstruction

To reconstruct the direction of an incident air shower's primary particle, the arrival timing information of the PMT hits are used. The shower front can be imagined as a thin disk of secondary particles travelling at approximately the speed of light  $c$ . The thickness of the shower front is  $\sim 5$  ns (see Figure 2.4). Depending on the incoming direction of the shower front the different PMTs are hit at different times. In Figure 2.7, the arrival time distribution of the shower front is shown for the candidate Crab Nebula  $\gamma$ -ray event shown in Figure 2.6. It can be seen that the shower front arrives on the right part of the image relative to the left part. The relative time between the different PMT hit is used to produce the shape of the shower front. The shower front is then fitted with a plane. The fit is performed using  $\chi^2$  minimisation with each PMT is weighted by its measured charge to obtain the incoming direction of the primary particle in the local sky.

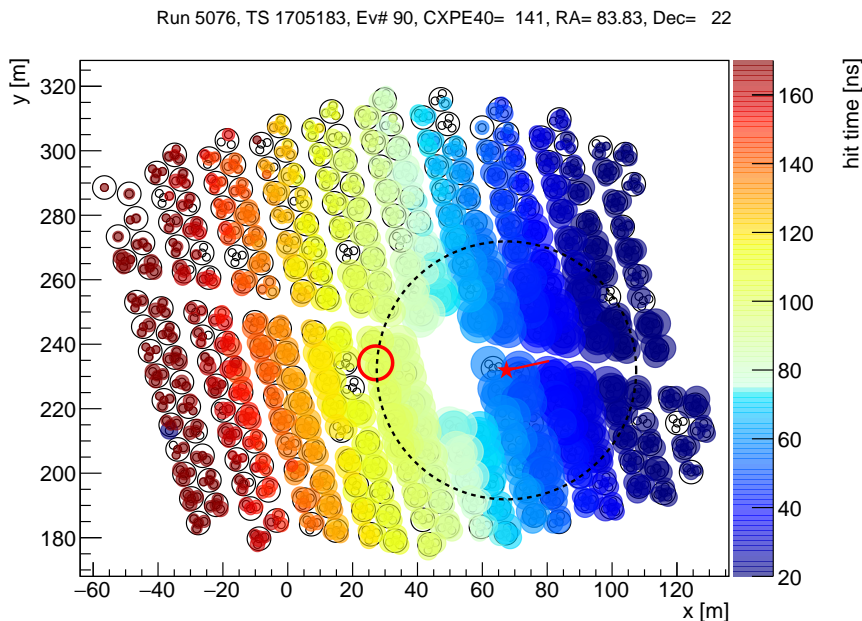


**Figure 2.7:** The arrival time distribution of the candidate  $\gamma$ -ray Crab data event shown in Figure 2.6. This distribution is fitted with a plane to reconstruct the shower arrival direction.

However, the observed shower front is not flat but curved. It is mainly because of the following two effects: firstly, the particles near the core have maintained their directionality more than the particles away from the core. The particles away from the core are multiply scattered, which leads to a wider disk. Secondly, larger PMT hits are detected before than the smaller hits, this effect becomes prominent at the tail of the shower front because it is mainly dominated by smaller hits. These two effects are taken into account in the observed timings as corrections and are subtracted from the signal times. The corrected shower front is then fitted with a plane as described before. More details can be found in (Abeysekara et al. 2017).



### 2.6.3 $\gamma$ -Hadron Separation

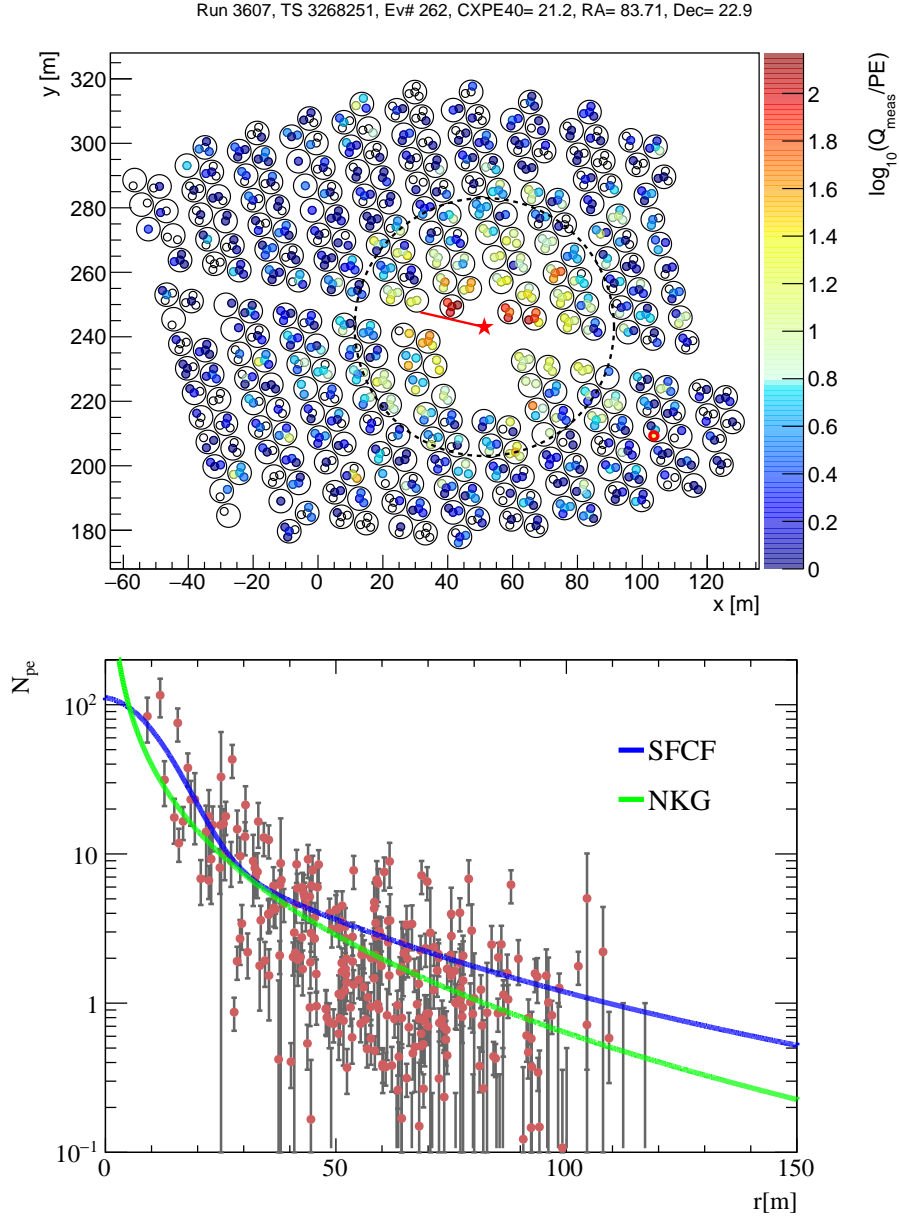


**Figure 2.8:** Top panel: the observed charge distribution of a candidate CR data event coming from the vicinity of the Crab Nebula. Bottom panel: the observed LDF of the event shown above with the SFCF and NKG functional fit.

CRs are the major background in the observation of  $\gamma$ -rays. Therefore, an effective  $\gamma$ -hadron separation strategy is required. As described in Section 1.4.2.1, the EM and hadron induced air showers have certain features which makes them distinguishable. The observed LDF of hadron

induced air showers are more clumpy around the shower axis in comparison to the  $\gamma$ -ray induced air showers. Figure 2.8 shows for a candidate CR event coming from the vicinity of the Crab Nebula. In the top panel, relatively higher charge hits are observed at different locations away from the shower core. In the bottom panel, the observed LDF of this event is shown, with fitted functional shapes of SFCF and NKG. Comparing this CR event with the  $\gamma$ -ray event shown in Figure 2.6 it can be seen that the observed LDF is more dispersed in the case of the CR event. This behaviour is mainly due to the following two effects: firstly, an isolated PMT can be by a muon, which produce a large signal in a tank. Secondly, hadronic showers can be branched in to several sub-showers, which were initiated in the later shower development phase.

To capture these features, two variables are defined in HAWC air shower reconstruction, named as *Compactness* and *Parameter for Identifying Nuclear Cosmic-rays (PINC)*. The first variable compactness ( $\mathcal{C}$ ) is defined as:

$$\mathcal{C} = \frac{N_{\text{hit}}}{\text{CxPE}_{40}}, \quad (2.4)$$

where  $N_{\text{hit}}$  is the number of hit PMTs and  $\text{CxPE}_{40}$  is the largest charge measured outside a circle of 40 m from the shower core. The  $\mathcal{C}$  takes smaller values for hadron induced air showers since they are likely to get an isolated large hit.

The second variable PINC ( $\mathcal{P}$ ) is defined as a  $\chi^2$  formula:

$$\mathcal{P} = \frac{1}{N} \sum_{i=0}^N \frac{(\log_{10} q_i - \langle \log_{10} q_i \rangle)^2}{\sigma_{\log_{10} q_i}^2}, \quad (2.5)$$

where  $q_i$  is the measured charge at a given PMT  $i$ .  $\langle \log_{10} q_i \rangle$  is expected charge, obtained by defining an annulus of 5 m centred at the shower core, and averaging the measured charge in all the containing PMTs in that annulus, which also contains the given PMT  $i$ . The  $\sigma_{\log_{10} q_i}^2$  is the corresponding uncertainty which is calculated by using a strong  $\gamma$ -ray sample obtained from the vicinity of the Crab Nebula. The value of  $\mathcal{P}$  describes the smoothness of the observed LDF, therefore, it is expected to have lower values of  $\mathcal{P}$  for  $\gamma$ -ray showers than hadron showers. More details can be found in (Abeysekara et al. 2017; Ayala Solares 2017).

## 2.7 Reconstruction Strategy

For an event to be reconstructed there are different hit selections that are made at different stages of the reconstruction procedure. Not all the recorded hits by the DAQ for a given air shower event are taken into account. Only the hits which are within a window of -150 and +400 ns of the trigger time are considered during the reconstruction. Additionally, hits are removed if they occur just after a high-charge hit because they might come from an after-pulse, or if they can not be calibrated properly because of saturation of the PMT. The only PMTs that are taken into account in the reconstruction are those which were not vetoed by calibration problems, were available before seeing the air shower event, and were not removed because of any of the selection cuts. There are certain steps taken in the event reconstruction in a sequential order to obtain the final reconstructed dataset which are summarised in Table 2.1.

## 2. THE HAWC $\gamma$ -RAY OBSERVATORY

---

Step	Hit Selection Description
COM core reconstruction	As before
SFCF core reconstruction (first pass)	As before
Direction reconstruction (first pass)	As before
SFCF core reconstruction (second pass)	Hits within 50 ns of first pass plane
Direction reconstruction (second pass)	Hits within 50 ns of first pass plane
Compactness	Hits within 20 ns of second pass plan
PINC	Hits within 20 ns of second pass plan

**Table 2.1:** The different steps in the HAWC event reconstruction to obtain the final reconstructed dataset.

The reconstruction of a more accurate core and direction is performed iteratively. This is because an accurate core estimation is crucial for direction reconstruction. After event geometry reconstruction, Compactness, and PINC information is added to the reconstructed dataset with the hits and information related to the detector status. More details can be found in (Abeysekara et al. 2017).

### 2.8 Analysis Cuts

To exclude events from the reconstructed dataset where the detector was unstable because of maintenance and other reasons, only the events where at least 800 PMTs were taking data and at least 90% of those were considered during the reconstruction are used. The remaining dataset is binned in nine analysis bins ( $\mathcal{B}$ ) which correspond to a certain fraction of the HAWC PMTs which observed a non-zero signal also called as fraction of PMTs hit ( $f_{\text{hit}}$ ).

The  $f_{\text{hit}}$  corresponds to the shower size, therefore it is used as a simple energy estimator. Increasing shower size corresponds to larger energy. Larger  $f_{\text{hit}}$  showers contain more information, which improves the shower reconstruction. It leads to better background rejection power with increasing  $f_{\text{hit}}$ . The background rejection parameters, PINC and Compactness are optimised in each  $\mathcal{B}$  bin data from the direction of the Crab Nebula to obtain the highest significance with additional condition of at least 50%  $\gamma$ -ray efficiency. The definition of the  $\mathcal{B}$  bins and optimised cuts for the reconstructed data are summarised in Table 2.2. For more details refer to (Abeysekara et al. 2017; Abeysekara et al. 2017b).

### 2.9 Point Spread Function

The Point Spread Function (PSF) is a measure of the accuracy of direction reconstruction. The PSF of HAWC is approximated as a sum of two two-dimensional (2D) Gaussian and is written as:

$$\text{PSF}_{\text{HAWC}} = \alpha G_1(\psi) + (1 - \alpha)G_2(\psi), \quad (2.6)$$

$\mathcal{B}$	$f_{\text{hit}}$	PINC ( $\mathcal{P}$ ) Maximum	Compactness ( $\mathcal{C}$ ) Minimum
1	6.7 - 10.5%	<2.2	>7.0
2	10.5 - 16.2%	3.0	9.0
3	16.2 - 24.7%	2.3	11.0
4	24.7 - 35.6%	1.9	15.0
5	35.6 - 48.5%	1.9	18.0
6	48.5 - 61.8%	1.7	17.0
7	61.8 - 74.0%	1.8	15.0
8	74.0 - 84.0%	1.8	15.0
9	84.0 - 100.0%	1.6	3.0

**Table 2.2:** The analysis cuts defined over analysis bins ( $\mathcal{B}$ ) which correspond to a certain fraction of the available PMTs that observed a non-zero signal ( $f_{\text{hit}}$ ). The PINC and Compactness cuts, which determines the background rejection are optimised on the Crab data for statistical significance.

where  $\psi$  is the angle difference between the true and reconstructed direction of the incoming particle.  $G_i$  represents the normalised Gaussian distribution and parameter  $\alpha$  is used to describes its weight. The functional shape shown in equation (2.6) have highly coupled parameters. Therefore, the angular resolution is described in the traditional way as 68% containment radius ( $\psi_{68}$ ) of the resultant fit of this functional shape. In Figure 2.9 it is shown for  $\mathcal{B}$  bin 3 and 8 respectively for declination band from  $21.5^\circ$  to  $22.5^\circ$ .

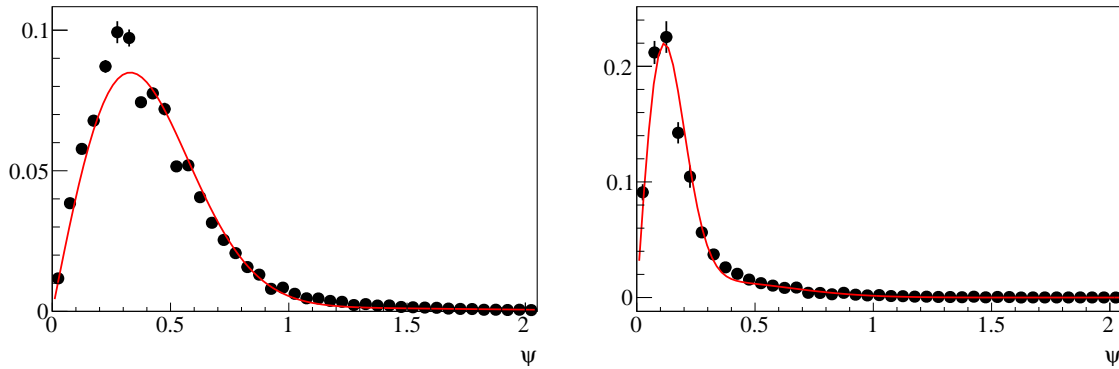


**Figure 2.9:** PSF derived from simulations for  $\mathcal{B}$  bin 3 and 8 in the left and right panel respectively for declination band of  $21.5^\circ$  to  $22.5^\circ$ . The angular resolution is  $\psi_{68}$  is the 68% containment radius of the fitted function (see equation 2.6) shown in red.

The PSF depends on the declination because the shower size changes depending on the arrival direction of the incoming particle. To predict the PSF at other declinations simulations are used. However, relying on simulation to predict the PSF at different declinations other than the Crab Nebula declination, the agreement of angular resolution between the Crab Nebula data and simulated Crab-like source is needed. Therefore the good agreement is verified as is shown in Figure 9 of Abeysekara et al. (2017).

### 2.10 Detector Response Function

The detector response function is comprised of the HAWC PSF at different declinations for each  $\mathcal{B}$  bin. Using the HAWC detector response function one can simulate an expected source for given source parameters at different declinations. A source hypothesis obtained using the detector response function together with the estimated background is compared to the observed data in order to calculate its test statistics (TS) using a likelihood approach, more details are described in Section 6.7, where I will use it to study the morphological and spectral behaviour of 2HWC J2019+367. The background calculation is described in the next Section.

### 2.11 HAWC Sky-maps

The reconstructed HAWC data in the defined analysis bins ( $\mathcal{B}$ ) is utilised to make event and background maps. The HAWC event sky-maps are produced by projecting the event reconstructed arrival direction on the sky in the equatorial coordinate system. To produce the background maps the direct integration method developed by MILAGRO experiment (Atkins et al. 2003) is used. In which, the isotropic distribution of reconstructed events is obtained using the events which have passed the background rejection cuts. The asymmetric angular response of the detector and the variation in the all-sky rate is taken into account while producing the background maps. Certain regions of the sky which consist of bright  $\gamma$ -ray sources such as the Crab Nebula, Markarions, Geminga regions and  $\pm 3^\circ$  region around the inner galactic plane are masked while estimating the background in order to avoid a bias.

For the production of the maps, the Hierarchical Equal Area isoLatitude Pixelization of a sphere (HEALPix) scheme is used (Górski et al. 2005). In which, the sphere is divided into 12 base pixels and each of them is subdivided into a grid of  $N_{\text{side}} \times N_{\text{side}}$ . In the official HAWC catalogue (Abeysekara et al. 2017b)  $N_{\text{side}} = 1024$ . This way, for each  $\mathcal{B}$  bins, one event and background map is generated. Together with the HAWC detector response function, these maps are then used to derive the science results. More details can be found in (Abeysekara et al. 2017b).

### 2.12 HAWC Sensitivity and Science Case

The differential point source sensitivity of HAWC, derived from the detector simulation to Crab-like sources at the declination of the Crab Nebula is shown in Figure 2.10. The sensitivity of HAWC depends on the declination of the source. The best sensitivity of HAWC is achieved for sources transiting through the zenith which is  $19^\circ$  for HAWC. It decreases for sources at large zenith angles because the incoming shower has to travel through more atmosphere before reaching the detector.

HAWC has the best sensitivity at the highest energies. The 507 days of HAWC sensitivity surpasses above IACT sensitivity of 50 hours above 10 TeV energies for a Crab-like source. It is evident from the sensitivity compared to other existing experiments, HAWC compliments observations by the IACTs and satellite experiments.

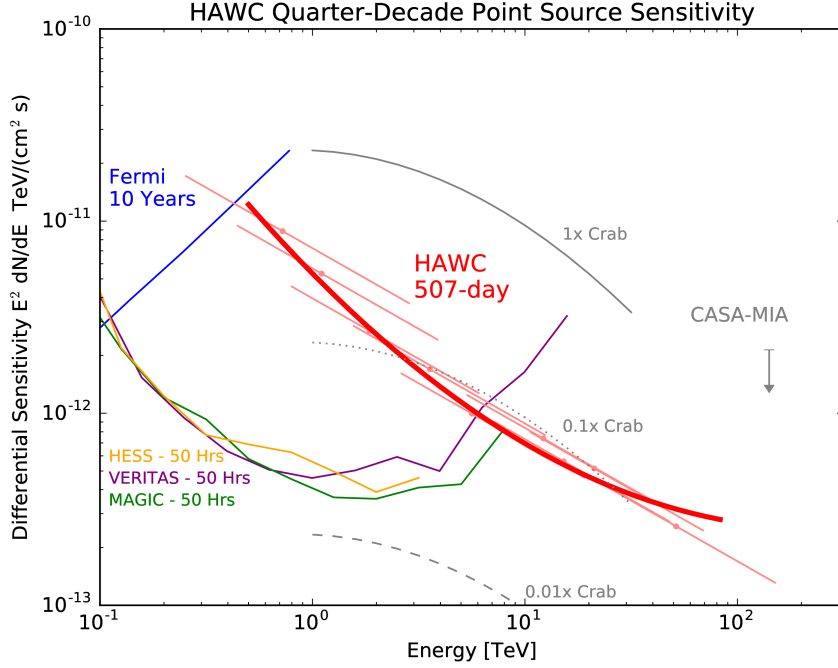


**Figure 2.10:** The quasi-differential sensitivity of HAWC as a function of  $\gamma$ -ray energy. The Figure is taken from (Abeysekara et al. 2017)

The HAWC catalogue (Abeysekara et al. 2017b) with 507 days of data has a total of 39 sources. The source population is comprised of point-like and extended sources of galactic and extragalactic origin. Most of these can be associated with already known sources, which includes the source categories of PWNe, SNRs and blazars. The remaining 23 of them have no firm association yet, which provides an excellent opportunity for HAWC to investigate them in more details. For instance, the shape of the  $\gamma$ -ray energy spectra of these sources might reveal the particle population at the acceleration site being leptonic or hadronic dominant. In addition, the extended sources allow us to probe the propagation mechanisms and the magnetic fields in the vicinity of the local environment. One such example is 2HWC J2019+367, which is an extended  $\gamma$ -ray source observed above 30 TeV energies by HAWC. Regardless of previous studies, the nature of the source remains to be unidentified, I will present the results from its spectral and morphological studies using HAWC data in Chapter 6 of this thesis.

In addition, extended objects like the Fermi Bubbles (Abeysekara et al. 2017a) have their own importance in the understanding of galactic  $\gamma$ -ray emission. Given wide field of view, high and consistent duty cycle and connectivity to the real-time alert system involving instruments from all the energy ranges, HAWC is an excellent instrument to study the most violent environments of the universe such as GRBs (Alfaro et al. 2017) and flaring AGN (Abeysekara et al. 2017). Apart from  $\gamma$  rays, HAWC detects CR as well throughout its energy range. Utilizing the cosmic-ray data the study of large and small-scale cosmic-ray anisotropy (Abeysekara et al. 2018a) is performed and the all-particle CR spectrum (Alfaro et al. 2017) is measured.

## 2. THE HAWC $\gamma$ -RAY OBSERVATORY

---

Finally, HAWC data is also used to probe new physics topics, such as dark matter. Dark matter particle masses of  $\sim 1$  TeV can be probed indirectly from their corresponding  $\gamma$ -ray emission from the low luminosity and high mass/light ratio galaxies (Albert et al. 2018b) (Albert et al. 2018a).





# 3

## HAWC High Energy Upgrade

The High Altitude Water Cherenkov (HAWC)  $\gamma$ -ray observatory has been recently upgraded with a sparse array of small Water Cherenkov Detector (WCD)s (see Section 2.1) (the outrigger array) around the main HAWC array and will start its science operation towards the end of the year 2018 (see Figure 3.1). In this chapter, I will explain the motivation behind the high energy upgrade of HAWC and the work done in the early days (starting from the fall of the year 2015) of the planning of the upgrade. This work has mainly contributed towards the simulation input to the planning of the upgrade, in order to make certain decisions for the outrigger components such as Photo-Multiplier Tube (PMT) size, the properties of the outrigger WCDs and the separation between them. The results of the work have been published in (Joshi 2017).

### 3.1 Motivation for Outriggers

The footprint of the shower on the ground is inherently dependent on the primary particle energy and on the altitude of the detector plane. At HAWC altitude, the footprint of the shower at around  $\sim 10$  TeV primary particle energy becomes comparable to the total instrumented area. Therefore, most of the showers at these energies are not well-contained within the array. Although the HAWC main array still has enough information to perform gamma-hadron separation, direction reconstruction, and shower size estimation, the shower reconstruction suffers due to the large uncertainty in the core location. To tackle this issue, it was decided to construct an outrigger array (Joshi & Jardin-Blicq 2017) around the main HAWC array. Using the outrigger array, it will be possible to better constrain the core location, so that the shower reconstruction can be improved. It will lead to an increased number of well-reconstructed showers above multi-TeV energies. Hence, it will improve the sensitivity of HAWC at those energies. One such outrigger

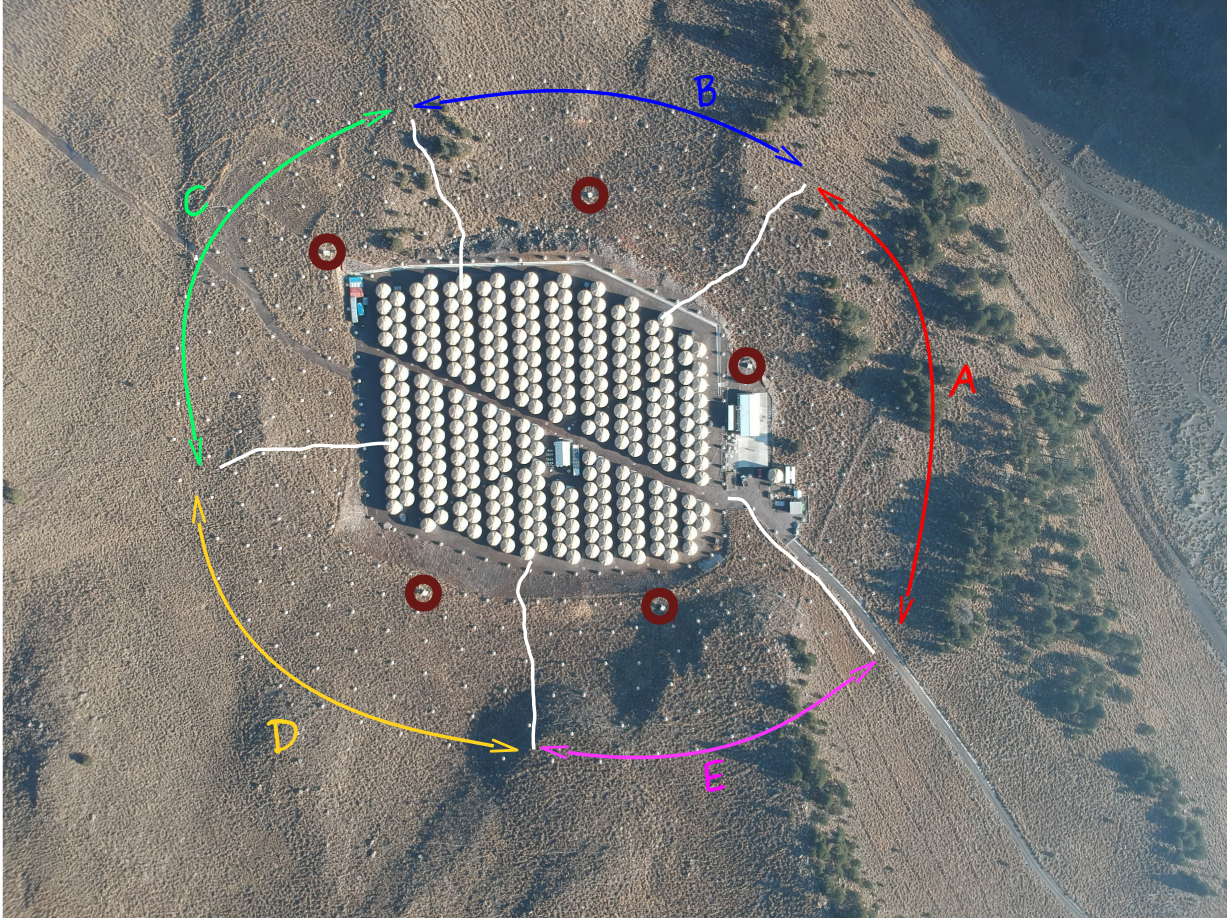


**Figure 3.1:** Fully deployed outrigger array (small tanks) around the main HAWC array. The white lines show the different sections (A, B, C, D, and E) of the outrigger array. The dark red circles show the node locations hosting the trigger and readout electronics for respective outrigger section.

array for MILAGRO instrument has already shown its effectiveness by dramatically increasing its sensitivity at the highest energies.

## 3.2 Outrigger Array Description

HAWC outrigger array consists of 345 cylindrical tanks of diameter 1.55 m and height 1.65 m. Each with one 8" PMT anchored at the bottom of the tank (see Figure 3.1 and 3.2). The outrigger array is deployed in a concentric circular symmetric way around the main array. The outrigger array increases the instrumented area of HAWC by a factor of 4-5. The outriggers are mutually separated from each other by 12 to 18 m. The smaller size and larger separation of the outrigger WCDs are prompted by the fact that there are a lot of particles and consequently bigger signals present near to the core of a big shower. For trigger and readout purpose, the outrigger array is divided into 5 sections of 70 outriggers each, connected to a node with equal



### 3. HAWC HIGH ENERGY UPGRADE

---

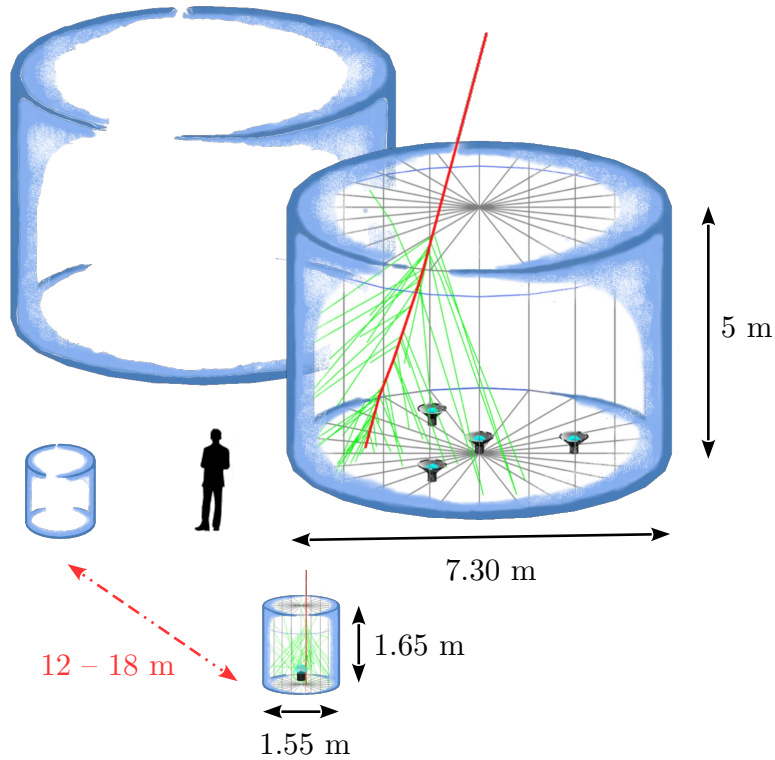


**Figure 3.2:** Top Panel: A real image of the main array (big) and outrigger (small) tank. Bottom panel: Schematics of the main array and outrigger tank as shown in the top panel with the number of PMTs and dimensions. The red line shows a particle coming inside the tank and producing Cherenkov light.

cable lengths. Each node hosts the power supply and the trigger, readout, and calibration system for the corresponding section. Hereafter in this chapter, I will show the simulation results to motivate the choice of some of the components of the outrigger array.

### 3.3 Toy Model for a WCD

In this section, I discuss a toy model to get a crude estimation of the number of photo-electrons ( $N_{pe}$ ) observed in a WCD, at a given distance from the shower axis (impact distance) ( $r$ ) for an Electromagnetic (EM) shower. Defining a toy model first before doing a full simulation is helpful in getting the approximate values of the simulation parameters. In this case, it is used to calculate the expected  $N_{pe}$  in an outrigger-like WCD at HAWC altitude for vertical 10 TeV  $\gamma$ -ray showers.

For the outrigger array, vertical 10 TeV  $\gamma$ -ray showers are an appropriate choice to study certain aspects. This is because showers larger than 10 TeV energy are not fully contained in the main HAWC array and therefore, the outriggers start becoming useful in containing those big showers. Additionally, the vertical 10 TeV showers correspond to much higher energy showers with increasing zenith angles. It is because the number of particles observed at the HAWC altitude decreases to approximately 1/2 with zenith angle  $30^\circ$  and 1/10 with zenith angle  $45^\circ$ . To perform this calculation the following steps are taken for the given Extensive Air Shower (EAS) properties:

- ⊙ Calculation of the total number of  $e^\pm$  at a certain depth in the atmosphere ( $X$ ).
- ⊙ Used the Nishimura-Kamata-Greisen (NKG) formula (Kamata & Nishimura 1958), to obtain the density of  $e^\pm$  at a given  $r$  and at a specific  $X$ .
- ⊙ Cherenkov yield of PEs in water as a function of depth travelled by the particle in the water tank.
- ⊙ Estimated the effect of WCD tank and PMT properties.

Let's define a depth in the atmosphere scaled with its radiation length  $X_0$  as  $t$  using equation (3.1). One can use equation (3.2) to estimate the number of particles produced at a given,  $t$ , by a particle of initial energy,  $E_0$ . Where  $E_c$  is the critical energy of the given medium, at which the losses due to Bremsstrahlung and ionisation are equal (see Section 1.4.2.1).

$$t = \frac{X}{X_0}, \quad (3.1)$$

$$N_e(E_0, t) = \frac{0.31}{\sqrt{t_{\max}}} \exp[t(1 - 1.5 \ln S_{\text{NKG}})], \quad (3.2)$$

$$\text{where } t_{\max} = \ln\left(\frac{E_0}{E_c}\right), \quad (3.3)$$

$$\text{and the age parameter } (S_{\text{NKG}}) = \frac{3t}{t + 2t_{\max}}. \quad (3.4)$$

For this calculation, without taking into account the atmospheric profile, we can treat  $X_0$  and  $E_c$  as constants with values  $X_0 = 36.08 \text{ g/cm}^2$  and  $E_c = 84 \text{ MeV}$  for the Earth's atmosphere (Nakamura et al. 2010). For a 10 TeV EM shower and at the HAWC altitude of  $X = 630 \text{ g/cm}^2$ , the obtained value of the number of particles produced is  $N_e = 5105$

### 3. HAWC HIGH ENERGY UPGRADE

---

At a distance  $r$ , the density function for the number of particles produced can be described by the NKG function in a simplified form as:

$$\rho_e = \frac{N_e}{\pi r_m^2} \frac{\Gamma(4.5 - S_{\text{NKG}})}{\Gamma S_{\text{NKG}} \Gamma(4.5 - 2S_{\text{NKG}})} \left(\frac{r}{r_m}\right)^{S_{\text{NKG}}-2} \left(1 + \frac{r}{r_m}\right)^{S_{\text{NKG}}-4.5}, \quad (3.5)$$

where  $S_{\text{NKG}}$  is the age parameter and  $r_m$  is the Molière radius. Using the equation (3.4) with radiation length ( $X_0 = 36.08 \text{ g/cm}^2$ ) and critical energy ( $E_c = 84 \text{ MeV}$ ), the resulting value of  $S_{\text{NKG}} = 1.3$ . The value used for the Molière radius is  $= 124 \text{ m}$  (see Section 2.6.1). Using these values at  $r = 20 \text{ m}$  in equation (3.5), the calculated value of observed particle density was  $\rho_e = 0.7 \text{ particles/m}^2$ .

Cherenkov yield can be defined as the number of Cherenkov photons produced per particle ( $e^\pm$ ), when the particle travels through a medium (water). The particle will lose energy mainly because of ionization. For electrons, the rate of losing energy with length travelled in water is  $\sim 2 \text{ MeV/cm}$ , which corresponds to a Cherenkov yield of  $\sim 300$  Cherenkov photons per particle (see equation (1.14)). Assuming the particle has an initial energy equal to the critical energy  $84 \text{ MeV}$ , when it enters into the tank's water surface, the depth multiplication factor becomes  $84/2$  per particle.

To calculate the effect of the WCD geometry, I used two PMT sizes 3" (7.62 cm) and 8" (20.32 cm), with a typical quantum efficiency of 25% (see Section 2.2). The diameter of the simulated tank is 155 cm. I calculated the area ratio of PMT and tank's bottom surface and multiplied it by the PMT's efficiency. The obtained factors for the 3" and 8" PMTs are:

$$\odot 3'' = 2.4 \times 10^{-3} \times 0.25$$

$$\odot 8'' = 1.7 \times 10^{-2} \times 0.25$$

By multiplying the above value in both the cases (3" and 8" PMTs) with the radial density of particles ( $\rho_e$ ), Cherenkov yield and depth multiplication factor, one can estimate the number of PEs which can be detected with specified water tank dimensions and PMT sizes. The obtained values for 3" and 8" PMT are as follows:

$$\odot \text{Number of PEs produced for } 3'' = 5.$$

$$\odot \text{Number of PEs produced for } 8'' = 37.$$

It can be seen that the expected number of PEs for a 3" PMT is very low, therefore to increase it, one can explore the possibility to make the WCD walls more reflective using wall colours other than black. A detailed simulation on this aspects will be discussed in later sections.

## 3.4 Simulations for the Outriggers

After having the crude estimation of the  $N_{pe}$ , which can be observed in an outrigger-like WCD, I performed detailed simulations to study the effect of different WCD's properties on the working of the outrigger array. The simulation chain is divided into two parts: air shower simulations and the detector simulations.

### 3.4.1 Air Shower Simulations

To generate the particle air shower simulations, I used CORSIKA air shower simulation package (Heck et al. 1998), which is widely used in the community.  $\gamma$ -ray air showers with energies 1, 3, 10, 30 and 50 TeV were generated with a zenith angle of  $0^\circ$  at the HAWC altitude of 4100 m. All the input parameters given for the CORSIKA air shower simulation are described in the example input card in Table A.2. In the example input card, the main parameters which were modified according to the required properties of the needed simulations are shown in bold characters.

### 3.4.2 Detector Simulations

In order to generate the detector simulations, a GEANT4 based HAWC detector simulation package (Agostinelli et al. 2003) named HAWCSim is used. After using the CORSIKA air shower simulation package, which tracks the shower development through the atmosphere until the HAWC altitude; the secondary particles of the shower are propagated through the WCDs using the HAWCSim simulation framework. More details on the HAWC simulations can be found in Section 2.5. At this step, detector characteristics are applied. I have defined detector components with their properties and different detector layouts. The tank types, PMTs and detector layouts used are summarised in Table 3.1. A more detailed description of each component is given later in the section.

Component	Types
Inner wall colours	Black, White, and Mirror
PMT sizes	3" and 8"
Array layouts	Column, Realistic, and Square Grid

**Table 3.1:** Different WCD components and layouts used for the outrigger simulations.

**Tank Properties:** The tanks used for HAWC outriggers are ROTOPLAS commercial water storage tanks of volume  $2500 \text{ m}^3$ . By default, they have a black painted interior. The geometry of the outrigger tank is given below:

- ⊙ Diameter = 1.55 m
- ⊙ Height = 1.65 m
- ⊙ Thickness = 0.6 cm
- ⊙ Water Height = 1.25 m

As described in Table 3.1, three tank types are simulated that are dubbed as: black, white and mirror. From now on I will refer to the wall colour/coating only from inside of the tank. This is because we are only interested in the light distribution inside the WCD.

### 3. HAWC HIGH ENERGY UPGRADE

---

- ⊙ **Black Tanks:** All the three sections of the tanks, which are the bottom lining, wall lining, and cover lining are Polypropylene. Polypropylene has a defined reflectivity of 10% at a wavelength range from 275 to 650 nm.
- ⊙ **White Tanks:** Only the wall lining is Tyvek and the rest of the bottom and cover linings are Polypropylene. Tyvek have a defined reflectivity of ~90%. The diffusivity of the reflection ( $\sigma_\alpha$ ) has a value of 0.17.
- ⊙ **Mirror Tanks:** A reflectivity of 100% for the full wavelength range of 275 to 650 nm. In this case, the wall lining is mirror and the top and bottom are black. For mirror tanks, to make them perfect reflectors the value of the diffusivity of the reflection ( $\sigma_\alpha$ ) is 0.00.

**PMT Characteristics:** The PMT sizes of 3" and 8" were simulated. The simulated PMT was the 8" Hamamatsu R5912 (see Section 2.2). To obtain the 3" PMT the observed  $N_{pe}$  from the 8" PMT were scaled down.

**Layouts:** To study the effect of different tank wall colours and PMT sizes on the observed signal, I have performed the detector simulation for two different layouts namely column and realistic layout. Another layout named as square grid layout was simulated to perform the preliminary study of the core estimation for an outrigger-like array. For all three layouts, the outrigger tanks were used. The description of the layouts are as follows:

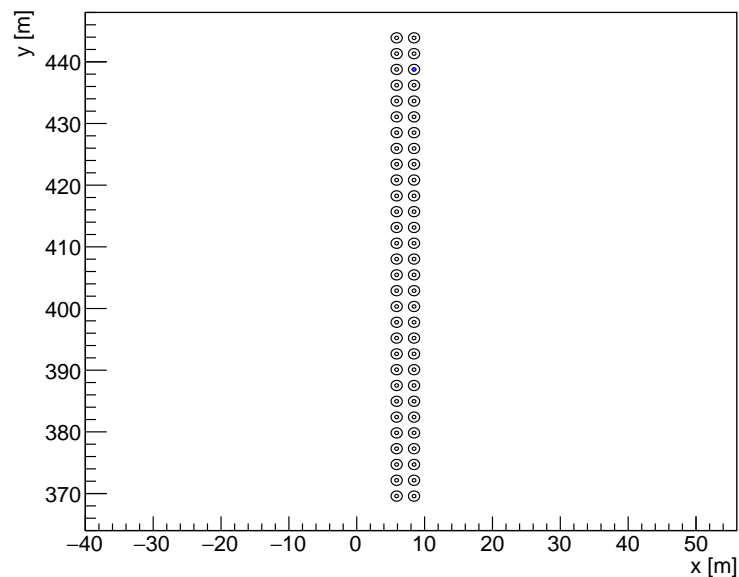


**Figure 3.3:** The schematic of the column layout. The big circles represent the outrigger tanks and the small circles inside represents the PMT. The separation between two tanks in one given column, as well as the separation between two columns, is 1 m. The orientation of the of the layout is parallel to the geomagnetic field at the HAWC site.

- ⊙ **Column Layout:** I defined a column layout using the outrigger tanks. In Figure 3.3, the schematic of the column layout is shown. It has in total 160 outrigger tanks arranged in

two columns, each with 80 tanks. The separation between the two outrigger tank columns and also the separation between two tanks in one column is 1 m. The layout is parallel to the geomagnetic field at the HAWC site. All the showers ( $\sim 10000$  for each energy) with energies 3, 10, 30 and 50 TeV were thrown at the center of the array with zenith angle  $0^\circ$ . The PMTs used are 3" and 8" with tank colour combination of black, white and mirror.

A column layout is an excellent option for the studies involving the observed signal's amplitude distribution as a function of distance from the shower core. The definition of the two columns provides the ability to study the fluctuations in the timing of the observed signals at same the distance to the shower axis.

- ⊙ **Realistic Layout:** It consists of 350 outrigger tanks. They are distributed as shown in Figure 3.4 with small dots in concentric circles with the main HAWC array in the center. They have a variable separation distance between 12 and 18 m. It is called realistic because

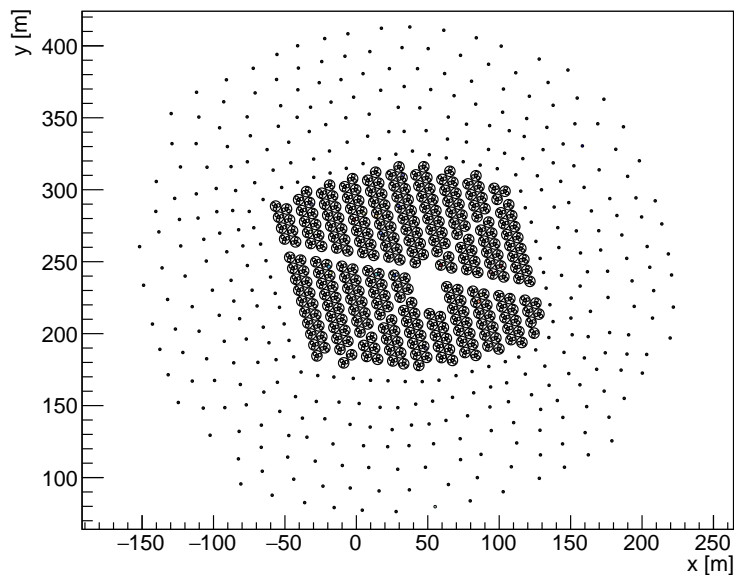


**Figure 3.4:** The realistic outrigger layout around the main HAWC array. The main HAWC array is at the center with big circles representing big tanks. The surrounding small dots represent the outrigger tanks.

it is close to the real outrigger array. The realistic outrigger layout is appropriate to study the number of triggered outriggers.

- ⊙ **Square Grid Layout:** It consists of 400 outrigger tanks distributed in a square grid with its unit cell's side dimension of 12 m, as shown in Figure 3.5. The separation of 12 m is similar to the typical separation of outriggers in realistic outrigger layout. This layout will only be used later in Section 3.6.1.



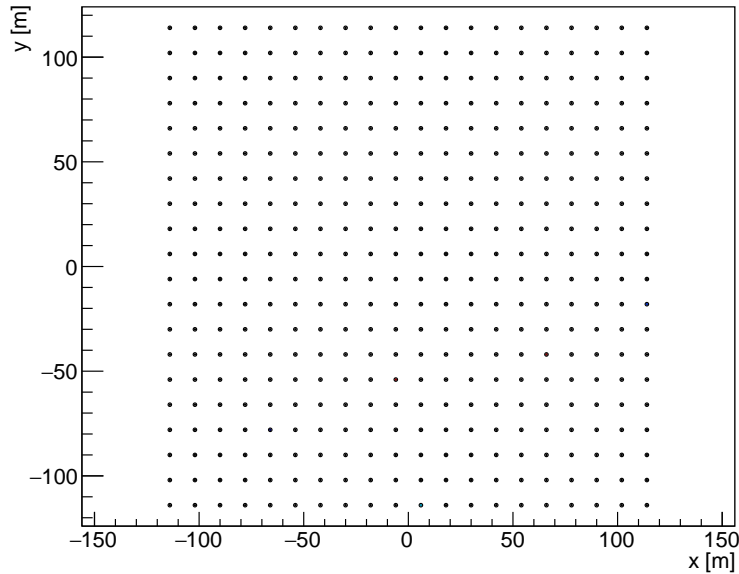


**Figure 3.5:** The square grid outrigger layout. The dots represent the outriggers. The separation between two outriggers in a row or in a column is 12 m.

## 3.5 Analysis of Simulations

### 3.5.1 Single Tank Trigger Probability

To get an estimate for a good separation distance between the outrigger tanks, the study of single tank trigger probability as a function of distance from the shower axis (impact distance) ( $r$ ) is useful. To obtain the at least one PE trigger probability profile, I used Column layout shown in Figure 3.3. The simulated energies are 3, 10, 30 and 50 TeV with zenith angle  $0^\circ$ . All the showers were thrown at the center of the array with PMT sizes 3" and 8" and tank colours black, white and mirror. In Figures 3.6 and 3.7, the profiles of all the energies with 3" and 8" PMTs and different tank colour combinations attached with corresponding probability ratio profiles are shown. In Figure 3.8, only the 10 TeV energy is shown because it is the most relevant energy for outriggers in the case of zenith angle  $0^\circ$  as explained in Section 3.3.

The main conclusions which can be drawn from the Figure 3.8 are: by looking at the distance where the probability is 50% of getting at least one PMT with a charge  $\geq 1$  PE, one could estimate the adequate separation between the outrigger tanks. From Figure 3.8 for 10 TeV showers, it can be seen that it is 30, 35 and 37 m from the shower core in the case of a 3" PMT, and with an 8" PMT it increases to 43, 50 and 53 m for black, white and mirror tank respectively. Within the above-mentioned distances from the shower core, the probability increases with 20% in the case of white tanks with respect to black tanks, and furthermore, it increases  $\sim 5\%$  from white to mirror tanks.

Additionally, one can use the other energies: 3, 30 and 50 TeV with different colour options represented in Figure 3.6 and 3.7 to look at the behaviour of the probability of getting at least one PMT with charge  $\geq 1$  PE. These plots also tell about the saturation distance (probability =

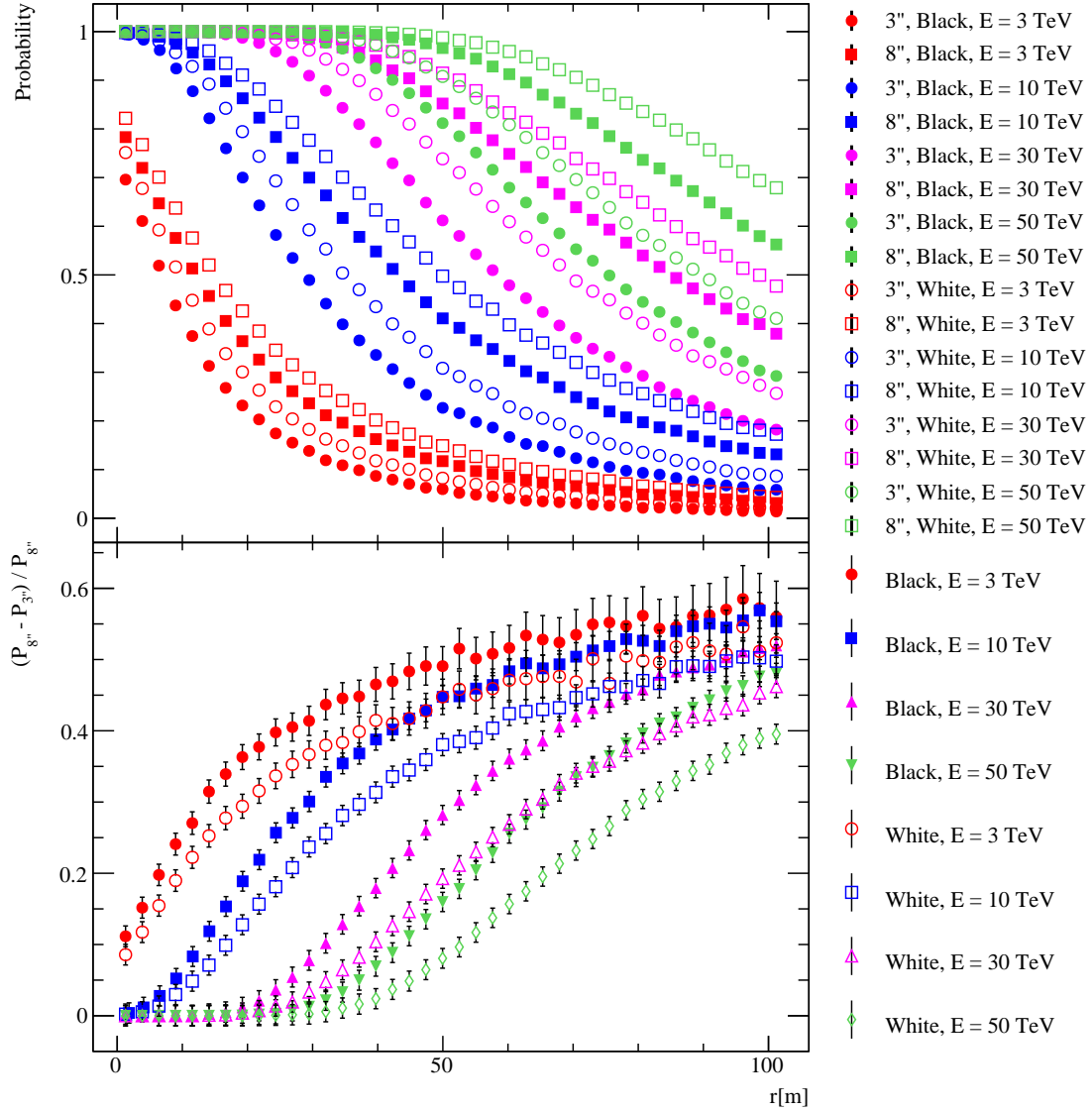


**Figure 3.6:** Top: at least one PE trigger probability profiles with energies 3, 10, 30 and 50 TeV. The tank colours are black and white. Bottom: the ratio of the difference in probability ( $P$ ) for 8'' and 3'' PMTs with probability for 8'' PMT as a function of  $r$ .

1) from the shower core, which is approximately 12m, 25m and 40m for the energies 10, 30 and 50 TeV respectively. By looking at the probability ratio plots Figure 3.6 and 3.7, one can deduce the gain in the probability with an 8'' PMT with respect to a 3'' PMT for different energies and wall colour combinations. It is  $\sim 30\%$  at 10 TeV energy with all the tank colors at an approximate distance of 1/2 trigger probability.

### 3. HAWC HIGH ENERGY UPGRADE

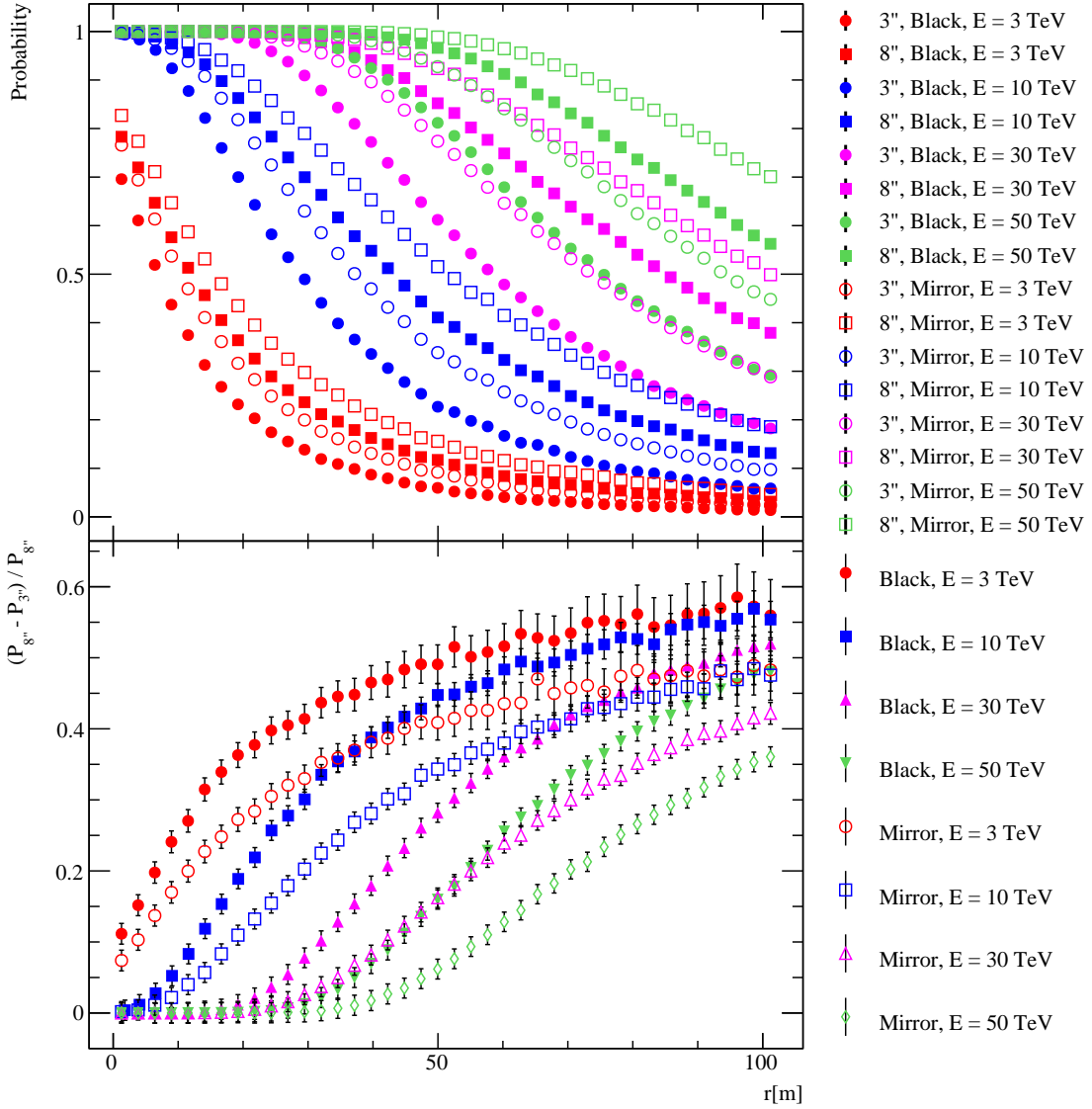


**Figure 3.7:** Top: at least one PE trigger probability profiles with energies 3, 10, 30 and 50 TeV. The tank colours are black and mirror. Bottom: the ratio of the difference in probability ( $P$ ) for 8'' and 3'' PMTs with probability for 8'' PMT as a function of  $r$ .

#### 3.5.1.1 Number of Tanks Triggered for Real Outrigger Layout

By using the probability profiles from the previous study, one can estimate the number of tanks triggered on the real outrigger layout. I used the trigger probability profile for 10 TeV energy, as shown in Figure 3.8. The probability profile is then convolved with the real outrigger layout, as shown in Figure 3.4, with simulated shower cores uniformly distributed over the instrumented area.

It can be concluded from the two-dimensional profiles of the number of tanks ( $N_{\text{Trig}}$ ) with at least one PE trigger (Figure 3.9 and 3.10), that we get approximately  $\sim 20$  and  $\sim 25$  tanks hit for

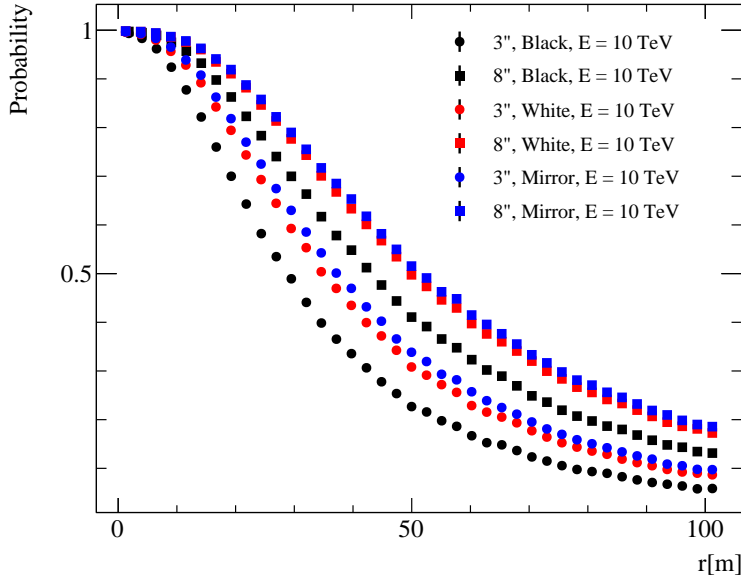


**Figure 3.8:** At least one PE trigger probability profiles as a function of  $r$  for energy ( $E$ ) 10 TeV, tank wall colours black, white and mirror and PMTs 3'' and 8''.

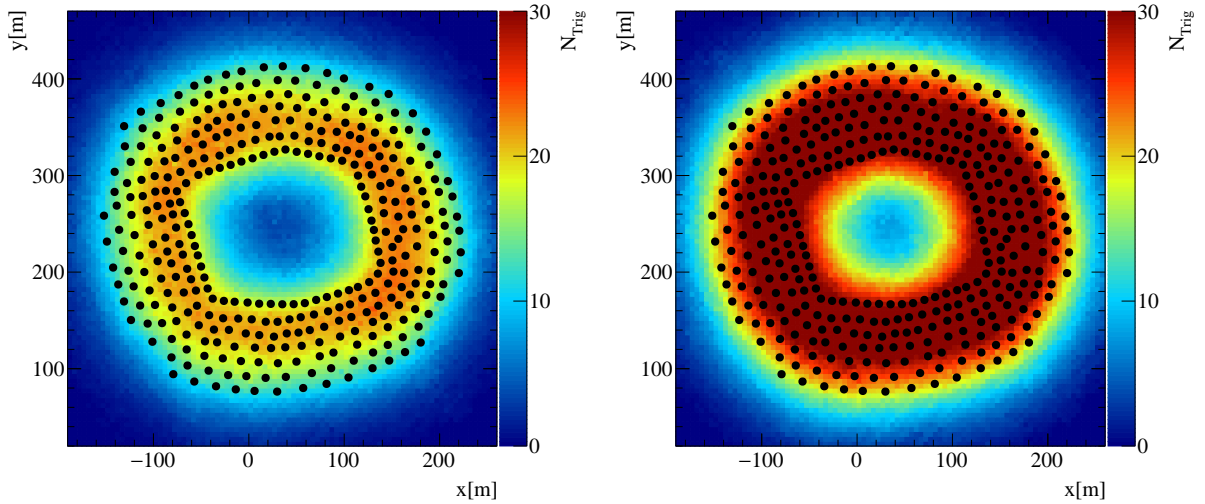


**Figure 3.9:** The number of outriggers (shown as black dots) got triggered ( $N_{\text{Trig}}$ ) with at least one PE for energy 10 TeV and tank wall colour black: 3'' PMT (left), 8'' PMT (right).

3'' and 8'' PMTs respectively with black tanks. Similarly, we get  $\sim 25$  and  $\sim 30$  tanks for 3'' and 8'' PMT respectively for the white tanks.

### 3.5.2 Time Resolution of the Shower Front

To study the shower fluctuations and therefore the time resolution, the arrival time of the first PE is extracted for the left tank ( $t_L$ ) and for the right tank ( $t_R$ ) for each tank pair of the column layout

### 3. HAWC HIGH ENERGY UPGRADE

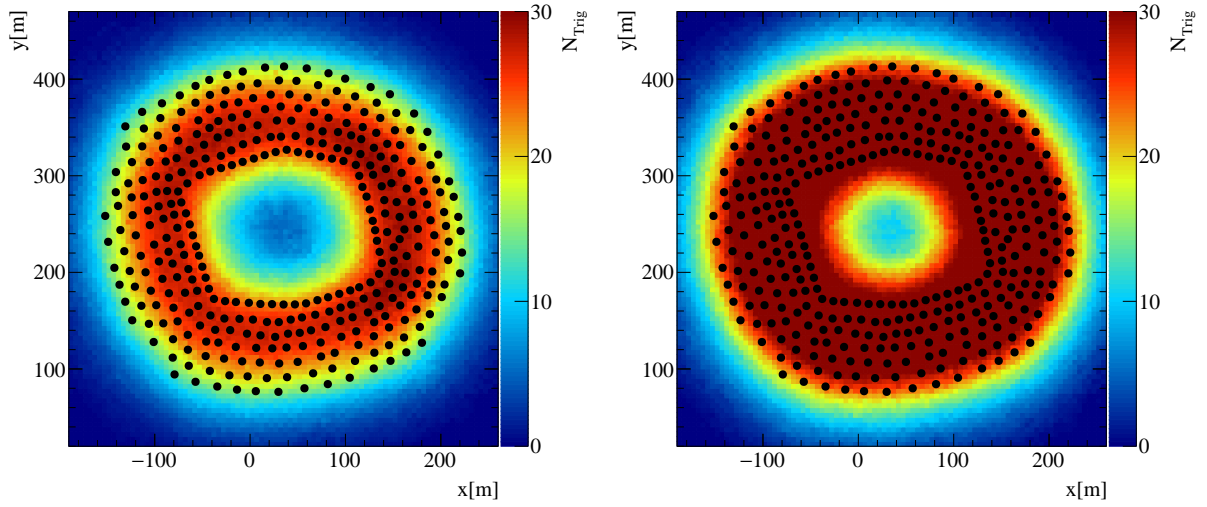


**Figure 3.10:** The number of outriggers (shown as black dots) got triggered ( $N_{\text{Trig}}$ ) with at least one PE for energy 10 TeV and tank wall colour white: 3'' PMT (left), 8'' PMT (right).

as shown in Figure 3.3. By using these two time values one can calculate the time difference

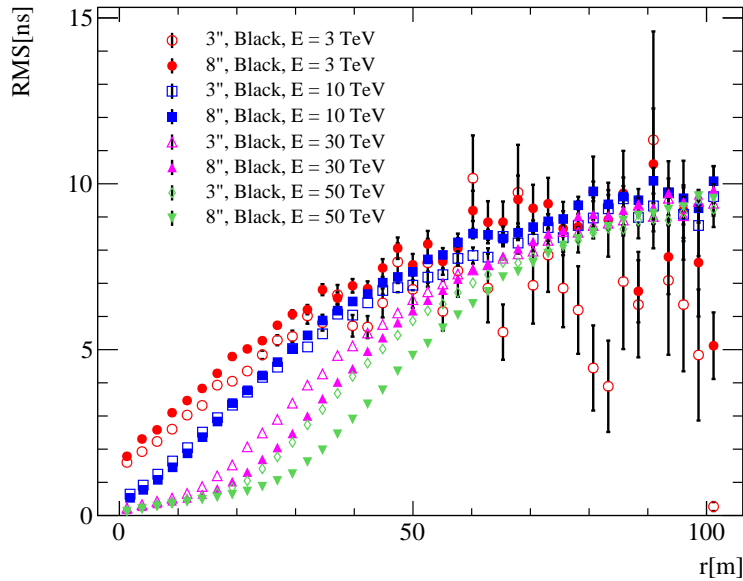


**Figure 3.11:** The RMS of  $\Delta t$  distribution as a function of distance from the shower core ( $r$ ) for 3'' and 8'' PMT with black tanks and for different energies ( $E$ ). Here  $\Delta t$  is the time difference of the first observed PE in left and right tanks of a given tank pair at  $r$ .

( $\Delta t = t_L - t_R$ ). The distribution of  $\Delta t$  for a given energy results in a Gaussian distribution. The Root Mean Square (RMS) of such a distribution gives the information about the inherent shower fluctuations in the timing of the shower arrival. Figure 3.11, shows the RMS as a function of  $r$  for 3'' and 8'' PMTs for black tanks. It can be seen that the difference in RMS for 3'' and 8'' PMTs for energy 10 TeV is almost the same, and for other energies, it is approximately less than

1 ns. Therefore, it can be concluded that the effect of the different PMT sizes for a given tank configuration is marginal.

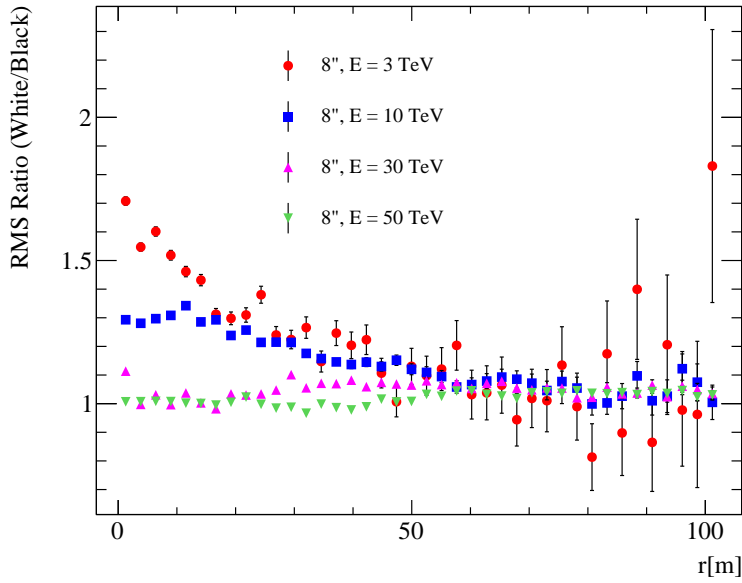


**Figure 3.12:** RMS (as defined in Figure 3.11) ratio for white/black tank wall colours for 8” PMT and for different energies ( $E$ ) as a function of  $r$ .

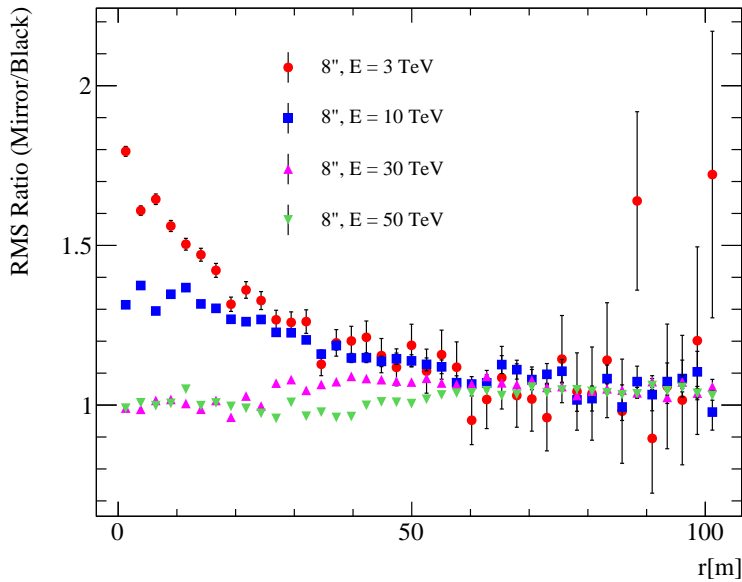


**Figure 3.13:** RMS (as defined in Figure 3.11) ratio for mirror/black tank wall colours for 8” PMT and for different energies ( $E$ ) as a function of  $r$ .

However, from the RMS ratio plots shown in Figure 3.12 and 3.13 for white/black and mirror/black tanks respectively, it can be concluded that the ratio increases by more than 20% for

energies (3 and 10 TeV), in both the cases. This is due to the higher reflectivity of white and mirror tanks in comparison to black tanks. The Cherenkov photons can reflect multiple times on the white and mirror walls before arriving at the PMT, and therefore loses significantly in the arrival timing of the first PE.

### 3.5.3 Signal Amplitude Study

The signal amplitude at a given distance from the shower axis (impact distance) ( $r$ ) is a good measure to study the saturation and to estimate the variation in the observed  $N_{pe}$ s. The saturation of PMTs have an adverse effect on the shower reconstruction. This is because, due to saturation, the real signal amplitude information is lost. Avoiding saturation for a given detector configuration while maximising the signal amplitude is favourable to improve the shower reconstruction.

In order to estimate this, the study of averaged  $N_{pe}$  as function of  $r$  was performed. The results are shown in Figures 3.14, 3.15, 3.16 and 3.17. The PMT options are 3" and 8" with

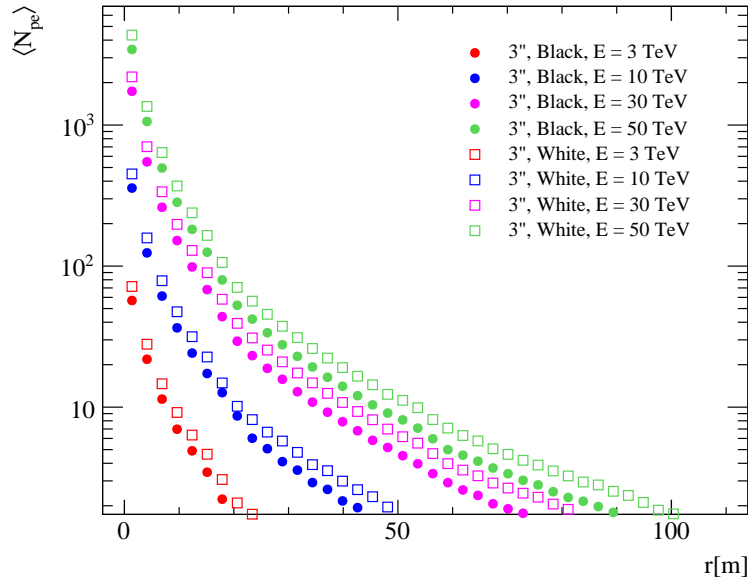


**Figure 3.14:** The average number of PE ( $\langle N_{pe} \rangle$ ) for 3" PMT with black and white tank wall colours as a function of  $r$  for different energies ( $E$ ).

the tank colours black, white, and mirror. From the plots of Figure 3.14, 3.15, 3.16 and 3.17, it can be concluded that the observed  $N_{pe}$ s increased by a factor of 10 while going from 3" to 8" PMTs, which is expected due to the bigger size of the PMT. The increase in the observed  $N_{pe}$ s while going from black to white or mirror colour is  $\approx 20\%$ . The 8" Hamamatsu R5912 saturates at around few thousands of PEs. Therefore, by evaluating the above-mentioned plots, it can be concluded that for  $> 10$  TeV showers, the required separation between the outrigger tanks should be more than 10 m in order to avoid saturation of a significant number of PMTs.

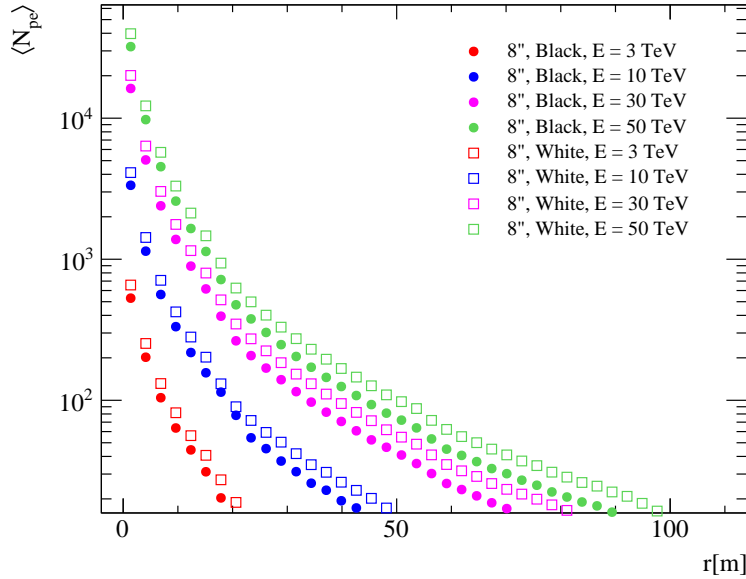


**Figure 3.15:** The average number of PE ( $\langle N_{pe} \rangle$ ) for 8" PMT with black and white tank wall colours as a function of  $r$  for different energies ( $E$ ).

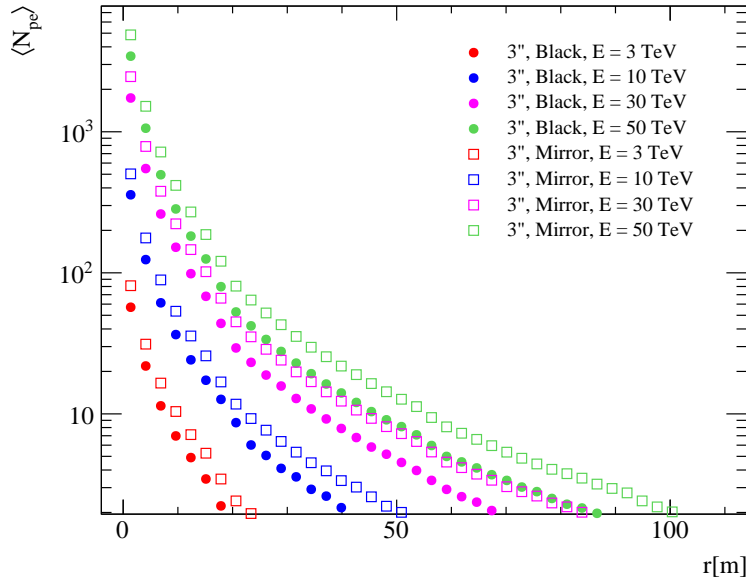


**Figure 3.16:** The average number of PE ( $\langle N_{pe} \rangle$ ) for 3" PMT with black and mirror tank wall colours as a function of  $r$  for different energies ( $E$ ).

### 3.6 Analysis of Impact on Air Shower Reconstruction

To perform the air shower reconstruction using the outrigger array, and to incorporate the reconstruction of the outrigger array with the main array, the air shower reconstruction of HAWC (see Sections 2.6 and 2.7) needs to be upgraded. This gave us an opportunity to explore the possibility for a new air shower reconstruction method for EAS arrays, which improves the reconstruction



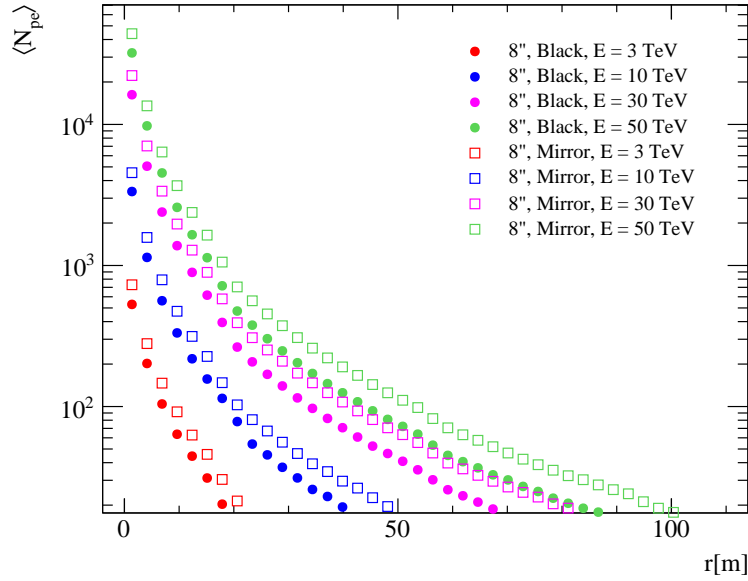


**Figure 3.17:** The average number of PE ( $\langle N_{pe} \rangle$ ) for 8" PMT with black and mirror tank wall colours as a function of  $r$  for different energies ( $E$ ).

and can combine the reconstruction of different particle detector type arrays. Therefore, a new MC template-based  $\gamma$ -ray reconstruction method is devised, which uses a likelihood approach to combine the reconstruction from different detector type arrays. A brief idea of this approach is that it uses a probabilistic model to describe the LDF of the observed particle air shower. The model consists of MC simulation based templates, which contain the information of observed  $N_{pe}$ s as a function of  $r$  for  $\gamma$ -ray induced air showers. The templates are binned in shower properties such as energy,  $X_{max}$  and zenith angle. Utilizing this model with a likelihood approach, one can get the estimate of the core and energy of the primary particle. I will go into details of this method in Chapter 4. In the following, I show the impact of such an approach in estimating the core location with an example of an outrigger-like array. Further, I will analytically show the expected angular resolution for a given core resolution for the outrigger array.

### 3.6.1 Core Estimation Using Outriggers

To study the core resolution achievable by the outrigger array, I have tested the aforementioned MC template-based method for an outrigger-like array (the square grid array). The square grid layout is explained in 3.4.2. To obtain the model for the likelihood method using MC simulations, I have simulated the previously defined column layout because it captures the LDF of a given air shower. A test sample is simulated using the square grid layout. The following are the simulations characteristics for the column layout to generate the MC templates and for the square grid layout to generate the test sample:

- ⊙ Energy range: 300 GeV to 300 TeV, with a spectrum of  $E^{-2}$ .
- ⊙ Zenith angles: 0, 15, 30 and 45°.

- ⊙ Azimuth angle range: 0 to 360°.
- ⊙ Only  $\gamma$ -rays are simulated.

The showers were uniformly distributed over the centre cell of the column layout and over the whole area of the square grid layout.

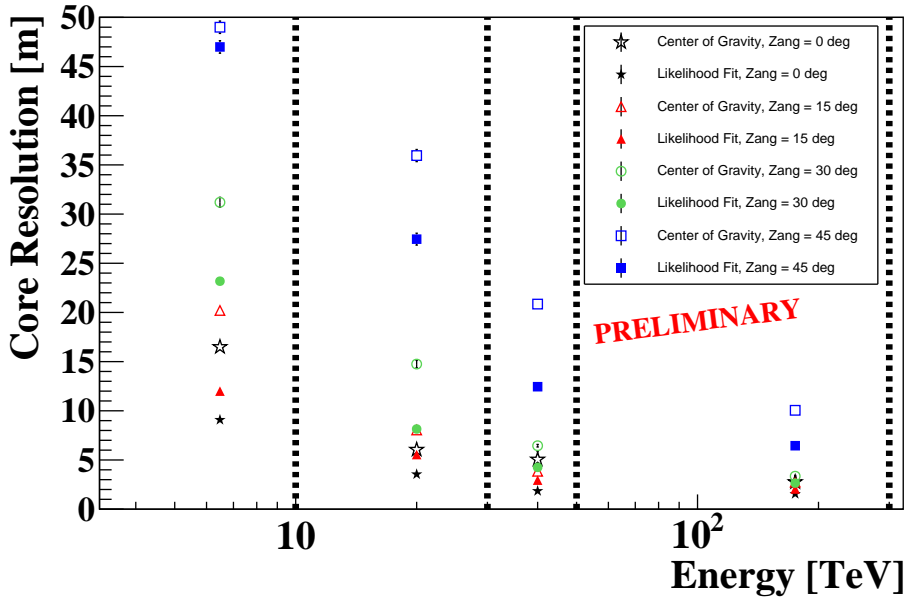


**Figure 3.18:** Core resolution as a function of simulated  $\gamma$ -ray energy. The simulated energy range is divided into four bins shown by the vertical dashed black lines. The core resolution is shown for the center of gravity estimate and for the likelihood fit method. The core resolution is defined as the 68% containment radius of the distribution of the distance between the reconstructed and true shower core. The core resolution points are put in the middle of the given energy range. The core resolution for other zenith angles (Zang) is also shown. The Figure is taken from (Joshi 2017).

In Figure 3.18 the core resolution obtained by this new method is shown. The core resolution is defined as the 68% containment radius of the distribution of the distance between the reconstructed and true shower core. For reference, the core resolution of a simple center of gravity estimate of the observed number of PE on different detector units is also shown. It is evident that the likelihood fit method always performs better than the center of gravity estimate. The core resolution is shown for different zenith angles (Zang) divided into four energy ranges. The core resolution points are put in the middle of the given energy range. The core resolution starts improving while going from lowest energy bin to the higher energy bins as expected. It can be observed that for energies higher than 10 TeV and for lower zenith angles, by just using the outrigger-like array, one can achieve a core resolution of  $\sim 5$  m. Although the separation of the outriggers are 12 m and the tank size is considerably smaller than the main array, it is promising to see an expected core resolution of  $\sim 5$  m. It will be shown in Section 4.10 that the results obtained here with a basic implementation using a square grid layout are in agreement with a more mature study performed on the real outrigger layout.

### 3.6.2 Analytical Estimation of Angular Resolution

Using the estimate of the core resolution for an outrigger-like array, it is interesting to evaluate the expected improvement in the angular resolution. For this study, I performed an analytical estimation of angular resolution as a function of core resolution.

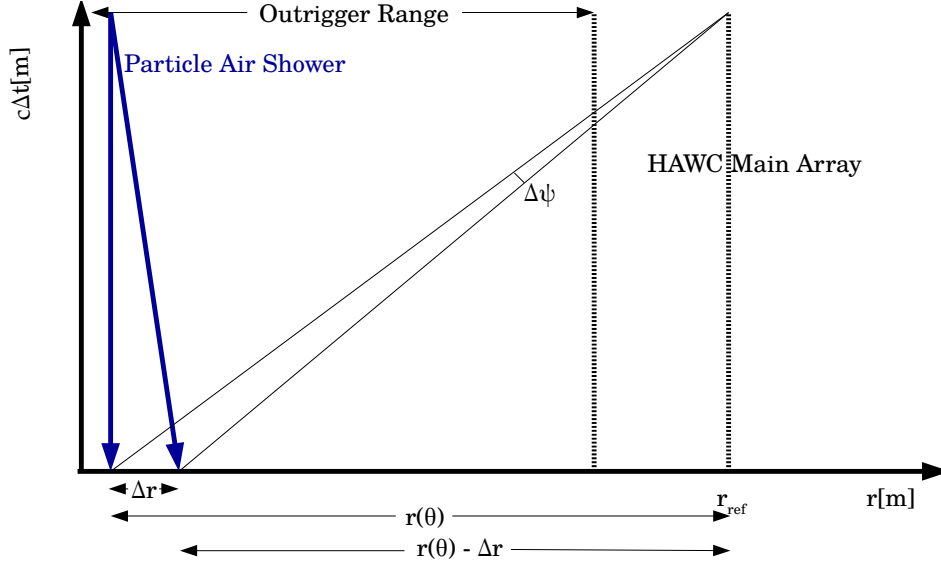


**Figure 3.19:** Schematic for the analytical calculation of angular resolution ( $\Delta\psi$ ) vs. core resolution ( $\Delta r$ ). Here  $\theta$  is the zenith angle.  $\Delta t$  represents the time difference of the shower front arrival at two given points on the ground.  $r_{\text{ref}}$  is a reference point in the main array from where the distance of the shower core is calculated.  $c$  represents the speed of light in vacuum.

In Figure 3.19, the idea behind the analytical calculation is shown. For a given air shower with its core on the outrigger array, and the core resolution due to the outrigger array, ( $\Delta r$ ), the corresponding estimate for the angular resolution would be ( $\Delta\psi$ ). To estimate the angular resolution apart from the  $\Delta r$ , one needs to know the time difference ( $\Delta t$ ) corresponding to the resolution in core location. The value of  $\Delta t$  is inherently dependent on the curvature of the shower front. If one can estimate the curvature of the shower front, then it is straightforward to estimate the time delay between the observation of the signal for given two points on the shower front. In HAWC, we have a shower front curvature model, which is dependent on the observed charge  $N_{\text{pe}}$  at a given  $r$ . The curvature model is defined as:

$$t(N_{\text{pe}}, r) = t_{\text{norm}}(N_{\text{pe}}, r) - \left( \frac{7.2 \times 10^{-2}}{\text{ns/m}} \right) r + \left( \frac{4.5 \times 10^{-4}}{\text{ns/m}^2} \right) r^2, \quad (3.6)$$

where  $t_{\text{norm}}$  is the normalisation factor determined by using the simulations. Although it is to be noted that this curvature model is defined for the HAWC main array. Nevertheless, as an initial step for angular resolution estimation for the outrigger array, it can be used in a pragmatic approach.

Using this model, one can calculate the time difference  $\Delta t$ . For given values of  $\Delta r$  and  $\Delta t$ , one can calculate the value of  $\Delta\psi$  with a simple geometrical calculation. In the schematic, I only

show it for the vertical showers but, it can be generalised for other zenith angles ( $\theta$ ) as shown below. Let us define two new variables  $l$  and  $l'$  as:

$$l = \sqrt{(ct)^2 + (r \cos \theta)^2}, \quad (3.7)$$

$$l' = \sqrt{\Delta r^2 + l^2 - 2r \cos \theta \Delta r}, \quad (3.8)$$

$$\text{so that, } \Delta\psi = \frac{\cos^{-1}(l'^2 + l^2 - \Delta r^2)}{2l'l} \text{ radian,} \quad (3.9)$$

where  $c$  is the speed of light and  $t$  is the same as in equation (3.6).

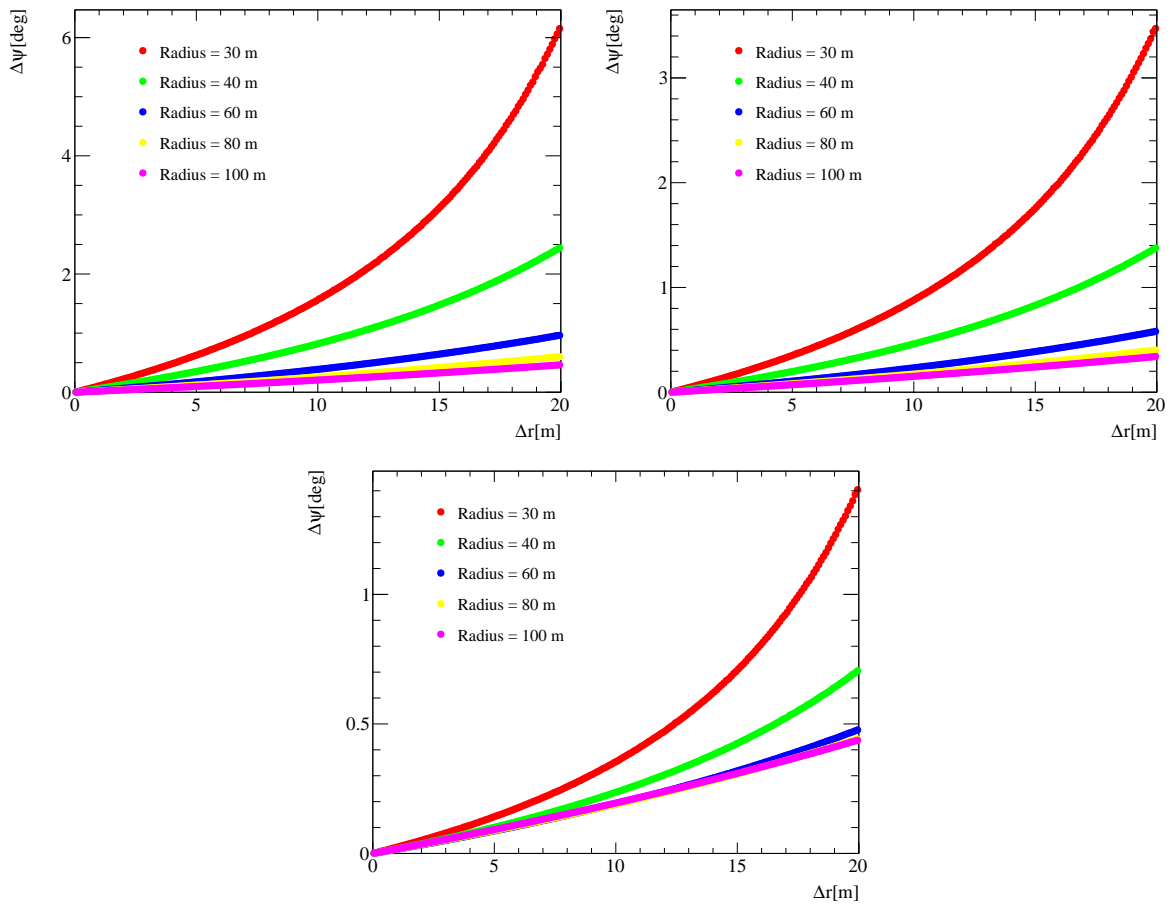


**Figure 3.20:** Core resolution ( $\Delta r$ ) vs. angular resolution ( $\Delta\psi$ ) for a fixed value of zenith angle of the incoming shower as  $0^\circ$ . The top left, top right, bottom left and bottom right plots are corresponding to the values of an observed  $N_{pe}$  of 10, 100, and 1000 respectively. The radius is calculated from the centre of the main array. Note the scales on the y-axis are different in each figure.

There are three free parameters  $r$ ,  $\theta$  and the observed  $N_{pe}$ . The results are shown in two sets of plots. In Figure 3.20, the  $\theta$  is fixed to  $0^\circ$  and  $r$  is varied for a given  $N_{pe}$  signal. In each of these plots the change in angular resolution is shown as a function of the core resolution between 0 to 20 m. It can be seen that when the core moves towards the outrigger array, while going

### 3. HAWC HIGH ENERGY UPGRADE

from 30 m to 80 m from the center of the main array; the core resolution achieved by outriggers start playing a crucial role and the angular resolution starts to improve. By looking at Figure 3.15, for  $> 10$  TeV showers, the observed average  $N_{pe}$  is about a few hundreds at 20 m from the core location. Therefore, from corresponding figures of 100 and 1000  $N_{pe}$ , at a radius of  $\sim 80$  m from the centre of the main array with a given core resolution of 5 to 10 m, one would expect an angular resolution of about  $0.1$  to  $0.2^\circ$  for vertical showers.

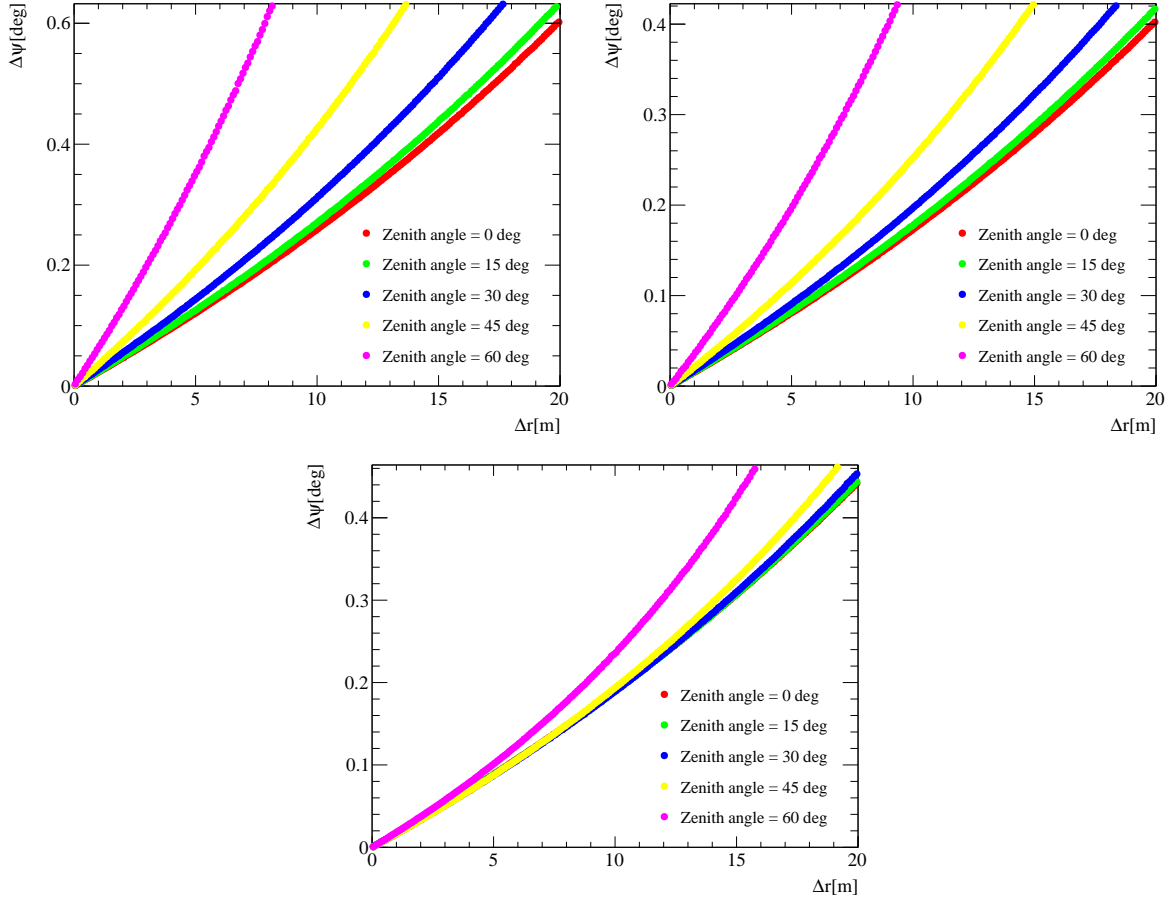


**Figure 3.21:** Core resolution ( $\Delta r$ ) vs. angular resolution ( $\Delta\psi$ ) for a fixed value of  $r$  as 80 m. The top left, top right, bottom left and bottom right plots are corresponding to the values of an observed  $N_{pe}$  of 10, 100, and 1000 respectively. In each plot, the different curves represent the different zenith angle of the incoming shower. Note the scales on the y-axis are different in each figure.

In Figure 3.21,  $r$  is fixed to 80 m, which is similar to the distance of the outrigger array from the center of the HAWC main array. In this case, by varying  $\theta$  and  $N_{pe}$  values, one can obtain the profiles for angular resolution, corresponding to the core resolution. It can be seen that at large zenith angles, the angular resolution starts to become worse as expected. However, at an observed  $N_{pe}$  value of 100 and 1000 (similar to the previous case), it can be seen that until a zenith angle of  $45^\circ$ , one could get an angular resolution of  $0.1$  to  $0.2^\circ$ , for a core resolution of 5 to 10 m. Although, this is a simplified analytical approach to estimate the expected angular

resolution, due to the outriggers; nevertheless, the obtained results give us some insight into the expected improvements.

### 3.7 Conclusions

In this chapter, I introduced the concept of the HAWC high energy upgrade with a sparse outrigger array. Different Photo-Multiplier Tubes (PMTs), tank wall colours, and detector layouts using the outrigger tanks were simulated to decide the suitable components. Using the results shown in Sections 3.5.1, 3.5.2 and 3.5.3, one can conclude the following:

It is expected to see around 20-30 outriggers triggered if the separation between them is about 15-25 m in all design choices at 10 TeV energies for vertical showers. To avoid saturation of a significant number of PMTs the separation should be larger than 10 m in case of an 8" PMT for 10 TeV showers. The 8" PMT produces  $\sim 10$  times more PEs than a 3" PMT with a 30% higher trigger probability. Using the white/mirror-walled tank, one could get 20-25% more PEs than the black walled tank. However, one would lose significantly in timing information, by about more than 20%. Therefore, using an 8" PMT with a black tank wall colour and a 10-20 m separation between the tanks, one could get enough PEs, with a sufficient number of triggered outriggers without losing considerably in the timing information while avoiding saturation of a significant number of PMTs. In the real outrigger array, the 8" PMTs are being used with black wall colour tank, which was based on these simulation results. The separation of the outrigger tanks is 12 to 18 m.

The deployment of the outrigger array was finished in August 2018. It has started taking the first data. Further checks and developments are currently ongoing. To combine the reconstruction for the outrigger array with the one for the main array, a new Monte Carlo (MC) template-based reconstruction method is devised. It showed promising results on the core resolution of  $\sim 5$  m above 10 TeV energies for low zenith angle showers, by just using an outrigger-like array. Using a crude analytical approach for the outrigger array, the expected angular resolution of 0.1 to 0.2° was estimated, for 5 to 10 m of core resolution for showers  $> 10$  TeV energy and zenith angles  $< 45^\circ$ . In the next Chapter 4, I will describe the working of the new MC template-based reconstruction method for air shower arrays. As an example, I will demonstrate its performance for the HAWC main array and combined with the outrigger array.

# 4

## A Template-based $\gamma$ -ray Reconstruction Method for Air Shower Arrays

In this chapter, I introduce a new Monte Carlo (MC) template-based reconstruction method for air shower arrays (see Section 1.4.2.4), with a focus on shower core and energy reconstruction of  $\gamma$ -ray induced air showers. The algorithm fits an observed lateral amplitude distribution of an Extensive Air Shower (EAS) (see Section 1.4.2.1) against an expected probability distribution using a likelihood approach. A full MC air shower simulation in combination with the detector simulation is used to generate the expected probability distributions. The goodness of fit (GoF) can be used to discriminate between  $\gamma$ -ray and hadron induced air showers. As an example, this method is applied to the High Altitude Water Cherenkov (HAWC)  $\gamma$ -ray Observatory (see Chapter 2) and its recently installed high-energy upgrade with a sparse outrigger array (see Chapter 3). The performance of this method and the applicability to air shower arrays with mixed detector types makes it a promising reconstruction approach for current and future instruments. The results and performance of this method have been published in (Joshi et al. 2018).

### 4.1 Introduction

Extensive Air Shower (EAS) detector arrays take advantage of their large collection area on the ground to detect the secondary particles generated by the interaction of a primary particle in the Earth's atmosphere. The estimation of EAS properties is performed by measuring the lateral distribution function (LDF) and the arrival time distribution of the secondary particles. Here, I demonstrate a method to estimate properties of the EAS that can be derived from the information in LDF. The LDF of an EAS describes the observed number of particles at a given distance from

#### 4. A TEMPLATE-BASED $\gamma$ -RAY RECONSTRUCTION METHOD FOR AIR SHOWER ARRAYS

---

the shower axis (impact distance) ( $r$ ). By using the LDF information the shower impact point on the ground and energy of the primary particle can be estimated.

Traditionally, the LDF is fitted with a functional shape, which is typically derived empirically to describe on average the features of the distribution. Typically, the parameters of these functions cannot directly be associated with the air shower properties. A widely used functional shape is the Nishimura-Kamata-Greisen (NKG) functions (Kamata & Nishimura 1958) (Greisen 1960). In addition to the shape of the distribution, also the fluctuations need to be taken into account in the fitting procedure. Fluctuations in observed signal amplitude arise from detector response and fluctuations in particle densities, both of which might not be trivial to parametrize. This makes the fit results from these approaches to depend on the actual type of the detector, in turn making the combined fitting of EASs with a mixed array of particle detectors challenging.

To address these problems, I present a MC template-based likelihood fit method for  $\gamma$ -ray induced EASs observed with an array of particle detectors. This method can in principle be extended to air showers induced by other Cosmic-Ray (CR) particles, however, here the focus is on the application of this method in  $\gamma$ -ray astronomy. The template-based fit procedure for  $\gamma$ -ray induced EAS was pioneered for the Cherenkov Array at Themis (CAT) telescope (Barrau et al. 1998; Le Bohec et al. 1998) and further improved and re-implemented in the HESS telescopes (de Naurois & Rolland 2009). A more mature version of this approach based on MC templates known as Image Pixel-wise Fit for Atmospheric Cherenkov Telescopes (ImPACT) (Parsons & Hinton 2014) is used in Imaging Atmospheric Cherenkov Telescopes IACTs such as HESS and has shown its effectiveness (Hinton 2004). Another example of template-based likelihood fitting of EAS was recently developed to obtain CR energy for observations made with the HAWC  $\gamma$ -ray Observatory. It has been applied to obtain the all-particle CR energy spectrum recently published in (Alfaro et al. 2017).

The MC template-based likelihood fit method presented here is applicable for EAS detector arrays and reconstructs the shower core and the energy of VHE  $\gamma$ -ray showers. In addition, the quality of the fit can be used to discriminate between EAS induced by  $\gamma$ -rays or hadronic particles. The nature of likelihood fitting makes it straightforward to combine measurements of different detector types in the same fit algorithm. The MC template-based likelihood fit method employs no approximations apart from the EAS simulation and the detector model itself, which is inevitable in a model-based fitting procedure. Due to the lack of hadronic interaction,  $\gamma$ -ray induced EASs can be modelled more reliably than nuclei. In addition, a prior unknown composition of the flux of subatomic nuclei makes the phase-space to be covered by the EAS templates significantly larger and therefore the fitting procedure more complex.

This approach can be used in general for air shower arrays. As a proof of the concept I demonstrate its usability for HAWC  $\gamma$ -ray Observatory (Abeysekara et al. 2013) and to its high-energy upgrade consisting of a sparse array of smaller water Cherenkov detectors (Joshi & Jardin-Blicq 2017). It is applicable to the current (Tibet AS- $\gamma$  Experiment (Amenomori et al. 2015) and ARGO-YBJ (Bartoli et al. 2015)) and future observatories (LHAASO (Di Sciascio 2016) and a next-generation observatory to be built in the Southern Hemisphere (Ohnishi et al. 2017; Becherini et al. 2017; Conceição et al. 2017; Di Sciascio et al. 2017; Schoorlemmer et al. 2017)). A method like this one is a robust approach to perform the combined reconstruction for mixed type particle detector arrays (in this case HAWC and its high energy upgrade with a sparse array).



## 4.2 General Considerations

Before going into details on the method, I discuss in this section the general considerations that lead to this particular implementation. As an illustration, the simulations for the HAWC array are used, of which the details are given in Section 4.4. However, the discussion in this section applies to all type of particle detectors.

### 4.2.1 Ambiguity Between Primary Energy and $X_{\max}$

The LDFs measured by EAS detector arrays exhibit large fluctuations, due to the fact that they are observed at a particular developmental stage of the EAS. The intrinsic uncertainty in the first interaction of the primary particle gives rise to different observed LDFs for the same primary particle properties. As we are using the HAWC WCDs (see Section 2.1) for illustration, the LDFs are measured using the observed  $N_{\text{pe}}$  (for more details see Section 4.4). In Figure 4.1 averaged LDFs for  $\gamma$ -ray induced EAS are shown for vertical showers. The averages are calculated over

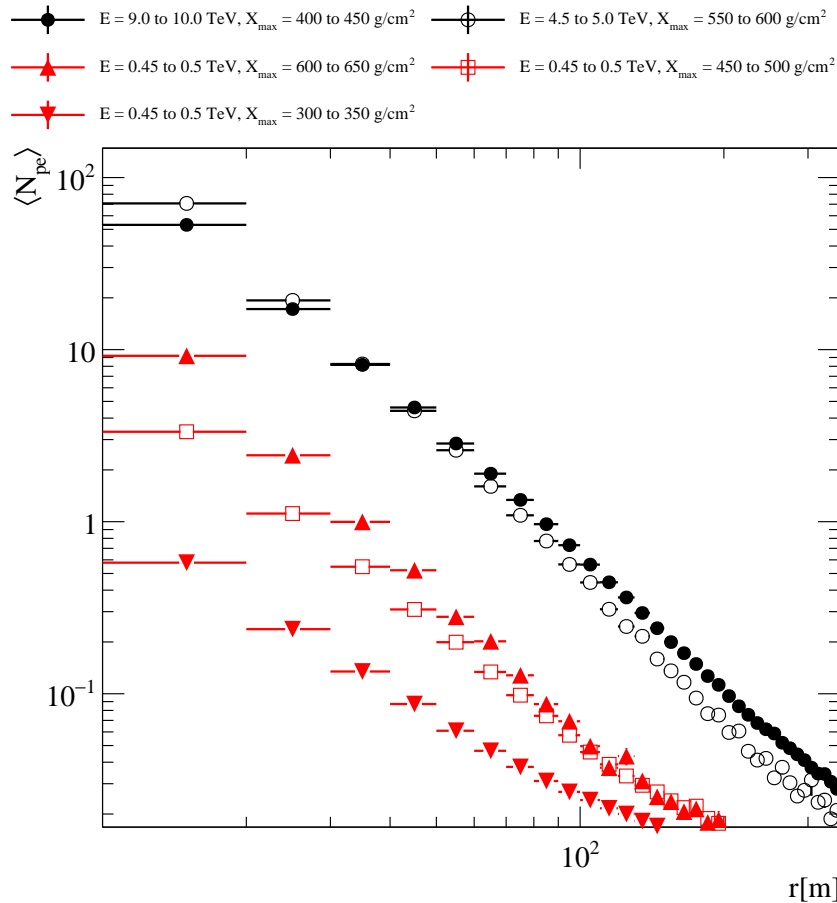


**Figure 4.1:** Average of observed  $N_{\text{pe}}$  as a function of the impact distance  $r$ . Figure reproduced from (Joshi et al. 2018).

EASs initiated with the same energy of the primary  $\gamma$ -rays that have similar shower development. These curves are shown to illustrate some complications that arise when using LDFs to deduce the properties of the primary particle. The black curves show the example of matching LDFs combination for multi-TeV  $\gamma$ -rays, in which, the energies are two-fold apart and the difference in  $X_{\max}$  values is  $150 \text{ g/cm}^2$ . The red curves show that for sub-TeV  $\gamma$ -rays for a fixed value of energy of the primary particle with increasing  $X_{\max}$  the averaged LDFs of the showers shifts significantly to the higher PE values, which again might lead to ambiguity in determining the primary particle energy. It is not likely to break this ambiguity completely, however by guiding the fit procedure the ambiguity can be significantly reduced. The way it is implemented will be discussed in Section 4.6.

### 4.2.2 Signal Free Detectors

The LDF has a long tail in which typically only a fraction of the detectors will have a signal, in Figure 4.1 this corresponds to the distances at which the value of  $\langle N_{\text{pe}} \rangle < 1 \text{ PE}$ . It can be seen that

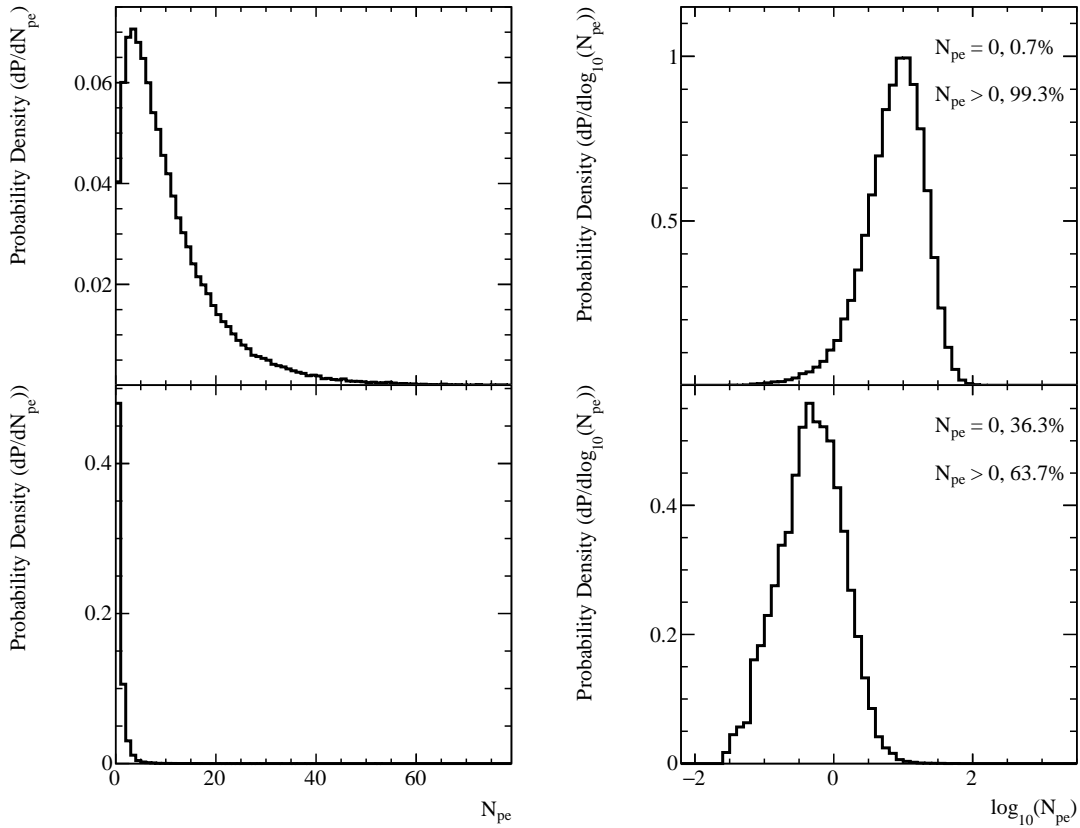


**Figure 4.2:** This plot includes vertically simulated EASs between 4.5 and 5.5 TeV. The top left panel shows the probability density distribution of the observed  $N_{\text{pe}}$  at an impact distance of 20 m and the right panel shows it for  $\log_{10}(N_{\text{pe}})$ . The bottom panel (left and right) show the same as above at an impact distance of 80 m. Figure reproduced from (Joshi et al. 2018).

there actually is some information in the tail of distribution that can break the aforementioned ambiguity, therefore it is desirable to maximise the information in the fit which includes the measurement of zeros. In Figure 4.2 the probability density distributions of observing a certain  $N_{pe}$  at impact distances of  $\sim 20$  m and  $\sim 80$  m are shown. We see that the probability of observing zero PE signal increases from 0.7% to 36.3% at impact distances of  $\sim 20$  m to  $\sim 80$  m. In a likelihood-based method, it is straightforward to add the LDF of the signal free detectors to the likelihood function.

### 4.2.3 Logarithmic Signal Amplitude

Since the underlying physical processes that lead to the particle densities observed at the ground are partially multiplicative in nature, fluctuations are typically easier described in log-space. This is illustrated in Figure 4.2, in which, the left panels show the amplitude distribution in a linear scale, while the figure on the right shows them on log-scale. It can be observed, by transforming to log-space the effect of the long-tails in the amplitude are significantly reduced. Additionally, small signal distributions can be described with similar binning as that of large signals, making the generation of template distributions for the likelihood fit significantly easier in log-space. The observed zero PE signal is stored at a low negative value in the log-space, which is lower than the small non-zero PE signal observed in the log-space.

## 4.3 Likelihood Function

Due to the aforementioned reasons, as an alternative to a semi-analytical model dependent fit, an MC template-based likelihood fit method is presented. It automatically takes into account all the fluctuations and gives a complete picture of the model in a probabilistic way, with only the assumption that the MC model and the detector simulations are accurate enough.

In Figure 4.4, one of such MC templates which describes the probability of an observed LDF of a  $\gamma$ -ray shower for given shower parameters is shown. These templates are generated by binning the simulated MC dataset in Energy ( $E$ ),  $X_{max}$ , and zenith angle ( $\theta$ ) bins. One such three-dimensional bin contains one such template, further binned in the logarithm of the observed  $N_{pe}$  ( $\log_{10}(N_{pe})$ ) and the impact distance of the PE signal  $r$  bins. However, it is to be noted that the observed signal does not necessarily have to be observed PE. For different particle detection techniques, the nature of the observed signal may vary. The function to be minimised in the fit procedure is defined as the negative log-likelihood

$$\log L = -2 \sum_i \log(F(S_i, r_i, X_{max}, E|\theta, \phi)), \quad (4.1)$$

where function  $F$  gives the probability of a given detector unit observing signal ( $S_i$ ) situated at an impact distance of ( $r_i$ ) for a  $\gamma$ -ray shower of energy ( $E$ ), ( $X_{max}$ ), zenith angle ( $\theta$ ) and azimuth angle ( $\phi$ ). For HAWC WCD technique,  $S_i$  term is replaced with  $\log_{10}(N_{pe})_i$ . Distance  $r_i$  is defined as the perpendicular distance to the shower axis as:

$$r_i = [(x_i - x_c)^2 + (y_i - y_c)^2 - \sin^2 \theta \{(x_i - x_c) \cos \phi + (y_i - y_c) \sin \phi\}^2]^{1/2}, \quad (4.2)$$

#### 4. A TEMPLATE-BASED $\gamma$ -RAY RECONSTRUCTION METHOD FOR AIR SHOWER ARRAYS

---

with  $x_i, y_i$  and  $x_c, y_c$  representing the coordinates of the different detector units and the location of the shower core in the detector plane respectively. The calculation of  $r_i$  in shower frame, as shown in equation (4.2) contains the information of the core coordinates on the ground.

For a given EAS, one can get the log-probability for all detector units using the previously defined templates. Summing-up the log-probability of all detector units gives the likelihood of the given set of values of the parameters. As we are using negative log-likelihood, by minimising the likelihood ( $L$ ) one obtains the best fitting values at the minimum value of  $L$ , the value of  $x_c$  and  $y_c$  give the estimated shower core coordinates,  $E$  gives the estimated primary  $\gamma$ -ray energy, and  $X_{\max}$  gives the depth of the shower maximum.

It is straightforward to extend this formalism for a mixed type particle detector array. One can define the likelihood function as defined in equation (4.1) for the different type of detector arrays and then summing them will give the total likelihood function (see equation (4.3)) for the combined detector array

$$L_{\text{total}} = L_{\text{type}_1} + L_{\text{type}_2} + L_{\text{type}_3} + \dots, \quad (4.3)$$

where  $L_{\text{type}_i}$  tells the likelihood of detector type  $i$  and it can be described as in equation (4.1) with the corresponding probability function  $F_{\text{type}}$ .

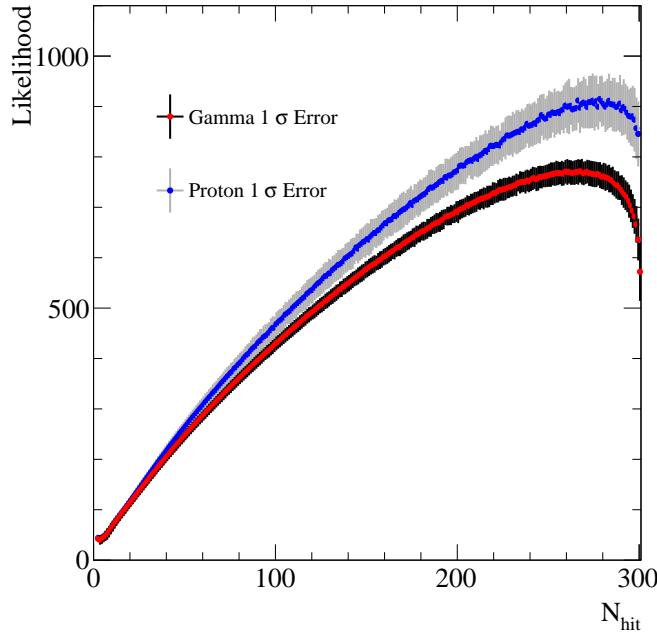


**Figure 4.3:** The distribution of Likelihood as a function of the number of tanks hit ( $N_{\text{hit}}$ ) of the HAWC main array. It is shown for Gammas and Protons, the points show the mean value  $\langle L \rangle$  and the error bars represent the  $1 \sigma$  width of the distribution for a given value of  $N_{\text{hit}}$ .

To assess the quality of the likelihood fit, a goodness of fit (GoF) is constructed. The GoF value can be used to identify events on which the fit method failed. Further, it can also be used to deliberately separate the model behaviours which are different than the model for the fit method itself. In this case, the model is defined for the  $\gamma$ -ray induced air showers, and the other models

are the LDFs of a hadron induced air showers. The GoF is defined by modelling the mean and the uncertainty of the likelihood value as a function of observed tank hits of the array. For a given value of the tanks hits of the array, the resultant distribution for the likelihood values results in a Gaussian-like distribution. Therefore, a Gaussian is fitted to the likelihood distribution for a given value of the tank hits, the mean  $\langle L \rangle$  and  $\sigma$  of the Gaussian are used to define the GoF in the following way:

$$\text{GoF} = \frac{L_{\text{Fit}} - \langle L \rangle}{\sigma}. \quad (4.4)$$

In Figure 4.3 the obtained  $\langle L \rangle$  one  $\sigma$  width of the fitted Gaussian to the likelihood distribution for  $\gamma$  and proton showers is shown as function of  $N_{\text{hit}}$ . It can be seen that the resultant distribution starts to separate significantly above a 100 tanks hit.

## 4.4 Air Shower and Detector Simulations

Detailed MC simulations are needed in order to generate the MC based templates. To simulate the interactions in the atmosphere induced by the  $\gamma$ -ray, the CORSIKA package (v7.4000) (Heck et al. 1998) is used, which provides us with secondary particles tracks at the ground level. To obtain the LDF-templates, a large statistic set of simulations in the energy range between 0.3 and 300 TeV and with an  $E^{-2}$  energy spectrum is simulated. The zenith angles ( $\theta$ ) of these  $\gamma$ -rays were distributed uniformly in  $\cos \theta$  within the range  $0^\circ < \theta < 45^\circ$ .

The results in this chapter are shown for the HAWC  $\gamma$ -ray observatory. Therefore, the LDF of an EAS is obtained from the charge, expressed in the  $N_{\text{pe}}$ , observed at each PMT. The detector response, including interactions of secondary particles in the WCDs, Cherenkov light production (see Section 1.4.2.2), propagation, and detection by PMTs are modelled using a dedicated software package based on Geant4 (v4.10.00) (HAWCSim) (Agostinelli et al. 2003). A more detailed description of the HAWC simulations can be found in Section 2.5 and in the references therein.

## 4.5 Template Generation

In this section, the different steps in the procedure to generate MC based templates using the simulation dataset defined in Section 4.4 are explained.

### 4.5.1 Binning Scheme

The dataset described in Section 4.4 is binned in  $E$ ,  $X_{\text{max}}$  and  $\theta$  bins. The binning of the parameter phase-space has been optimised as a compromise between the size of the dataset and the achievable resolution on the fit parameters. The optimisation procedure is described in section 4.7, the resulting binning scheme is summarised in Table 4.1.

Each combination of  $E$ ,  $X_{\text{max}}$  and  $\theta$  bin contains a probability distribution function (PDF) as shown in Figure 4.4, for the probabilistic description of an observed lateral amplitude distribution

## 4. A TEMPLATE-BASED $\gamma$ -RAY RECONSTRUCTION METHOD FOR AIR SHOWER ARRAYS

Parameter	Range	Bin size	Number of bins	Description
$\theta$	0 to $45^\circ$	0.06	5	equally spaced in $\cos \theta$
$E$	0.3 to 300 TeV	0.1	30	equally spaced in $\log_{10}(E/\text{GeV})$
$X_{\text{max}}$	150 to 750 $\text{g}/\text{cm}^2$	50 $\text{g}/\text{cm}^2$	12	The statistics is limited
$\log_{10}(N_{\text{pe}})$	-4 to 8	0.1	120	-
$r$	0 to 500 m	2 m	250	-

**Table 4.1:** The binning definition of the MC dataset to produce the templates.

of a  $\gamma$ -ray shower. The PDFs are stored as 2D histograms with  $\log_{10}(N_{\text{pe}})$  on one axis and  $r$  on the other.

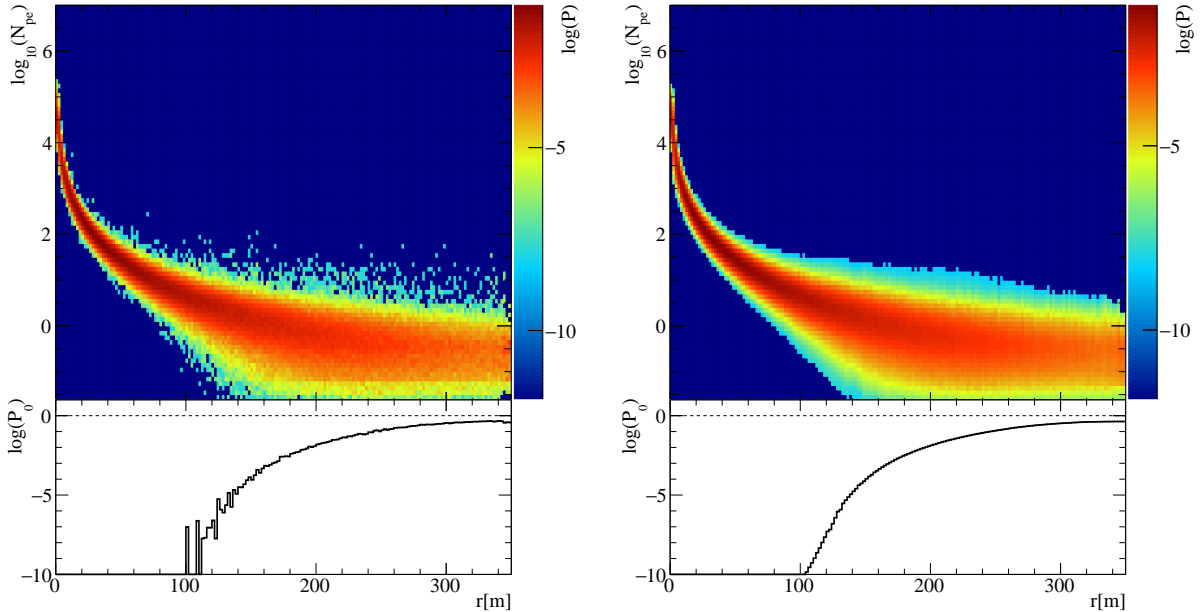


**Figure 4.4:** A typical template histogram for  $X_{\text{max}}$  bin 500 to 550  $\text{g}/\text{cm}^2$ , energy bin  $\sim 59$  to  $\sim 75$  TeV and zenith angle bin 19 to 28 degree. It shows the probability (P) distribution as a function of  $\log_{10}(N_{\text{pe}})$  and impact distance  $r$ . The z-axis shows the probability in logarithmic scale. The left panel shows the template histogram before smoothing and the right one after smoothing. The histograms attached below show the probability ( $P_0$ ) of observing a zero PE signal as a function of  $r$ . Figure reproduced from (Joshi et al. 2018).

### 4.5.2 Smoothing

Since the MC simulation chain is very computationally intensive, generating enough MC statistics to populate the whole phase-space of EAS parameters is not practical. Therefore, there are very rarely or unpopulated bins that occur particularly in the edges of the phase-space which con-

tain little statistics. These bins might introduce unwanted artefacts in the templates that might influence the fits. To reduce the impact of these bins, the PDFs are smoothed using a Gaussian distributed weighted sum for a given bin in a given direction ( $r$  or  $\log_{10}(N_{pe})$ ). Figure 4.4 shows one such profile before and after smoothing.

### 4.5.3 Interpolation

It is essential to make the likelihood surface smooth specifically for a multidimensional fitting procedure such as this case. A three-dimensional grid interpolation over the parameters (i.e.  $E$ ,  $X_{max}$  and  $r$ ) is used to obtain the probability of a given signal at a given impact distance. This probability is then used in the likelihood fit procedure to calculate the likelihood value.

## 4.6 Fitting Procedure

As described in Section 4.3, we get the likelihood function by combining the probabilities of observing  $\log_{10}(N_{pe})$  at a given distance  $r$  for given values of  $E$ ,  $X_{max}$  and  $\theta$  of the primary particle at different detector units. In this section, I will further describe the details of the likelihood fit method itself explaining the various measures which are taken to aid the fit method to find the global minimum. The fitting is performed using the widely-used MINUIT (James & Roos 1975) minimisation algorithm.

We have four parameters  $E$ ,  $X_{max}$ ,  $x_c$  and  $y_c$  to fit simultaneously for a given information of shower arrival direction. In order to guide the minimisation process, the following strategy is applied. The reconstruction of the direction is not part of this method, however, it is needed to select the right lookup table and to transform the detector locations into the plane perpendicular to the shower axis. For direction reconstruction, a curved shower front fit which is used within the HAWC software framework is used as input to the method (see Section 2.6.2). The reconstructed direction together with the calculated center of mass (COM) of the amplitude of the signals provides the starting point of the fit procedure (see Section 2.6.1).

### 4.6.1 First Pass

In the first pass of the method, three starting values for the minimisation procedure, based on the calculated COM are tried. First being the COM estimate itself, which in the case of a shower core inside the array should provide a starting point close the global minimum. In order not to get stuck in a local minimum, the minimisation procedure is performed at two additional starting ( $X,Y$ ) locations. These trials are defined in the direction of the COM estimate with respect to the centre of the array, which is an educated guess of the true location of the shower core. The second trail is just outside the array, while another one is placed at a significant distance from the array.

To start the minimisation with a reasonable value of  $E$  the information of the number of detectors that got at least a single PE hit ( $N_{hit}$ ) is used as a function of the distance of the core location from the centre of the array. Using the distribution shown in Figure 4.5 (left panel),

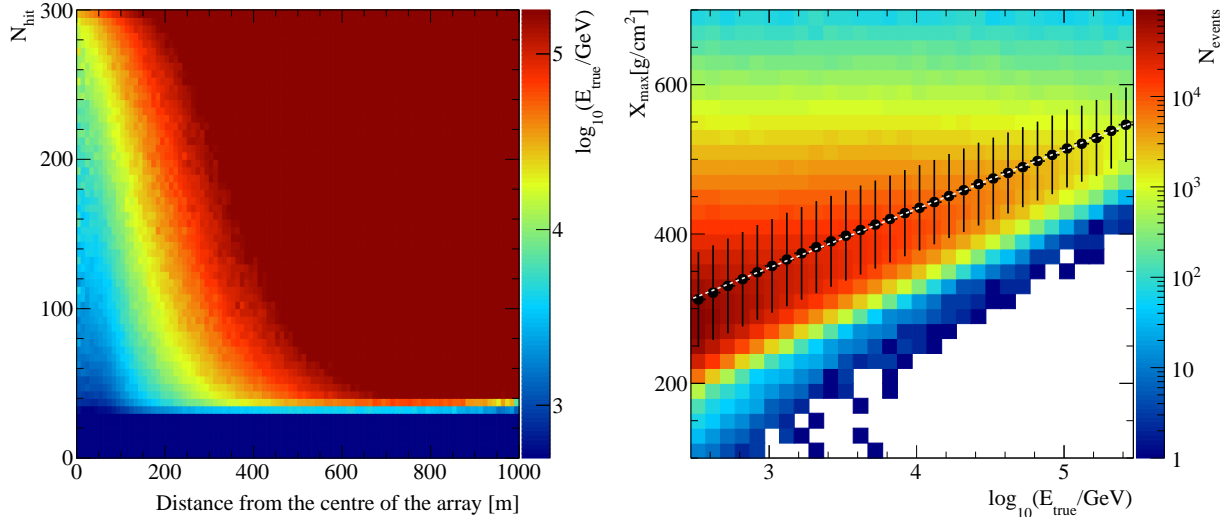


**Figure 4.5:** The left panel shows the relation between the number of tanks got at least a single PE hit and the distance of the shower core from the centre of the array. The true energy ( $E_{\text{true}}$ ) of the primary  $\gamma$ -ray photon is shown on the z-axis. The right panel is showing the relation between the  $E_{\text{true}}$  and the true  $X_{\text{max}}$ . The white dashed line shows the functional relation. The z-axis shows the number of shower events ( $N_{\text{events}}$ ). Figure reproduced from (Joshi et al. 2018).

one can estimate the energy of a given shower by using the value of the observables  $N_{\text{hit}}$  and the distance of the trial core from the centre of the array.  $E_{\text{true}}$  denotes the simulated energy of the primary  $\gamma$ -ray photon.

As explained in Section 4.2, one of the challenges is finding the global minimum while there are ambiguities in LDF for different values of  $X_{\text{max}}$  and shower energy. Therefore, in the first pass of the fit procedure, the linear relation between  $E_{\text{true}}$  and the average value of  $X_{\text{max}}$  is enforced (see Figure 4.5 (right panel)). To reduce the total computation time, the number of iterations of the minimiser is limited to 10 for each of the three starting points. From the three resulting minimum likelihood values, the smallest value is selected and the corresponding fit parameters are used as the starting point in the second pass of the fit method.

## 4.6.2 Second Pass

The results of the first pass of the fit-procedure are passed to the direction-reconstruction method, which can get a more accurate estimate of the direction now that it has a better knowledge of the shower core location. The results from the direction-reconstructor are used, together with the location of the shower core as the starting point for the next pass. In this pass, the constrained on the relation between  $X_{\text{max}}$  and  $E_{\text{true}}$  is no longer enforced and the maximum number of iterations of the minimiser is increased to 40. Typically the fit procedure converges on the best fitting parameters before reaching the maximum number of iterations. The reconstructed core now can further be used to improve the direction-reconstruction.



### 4.6.3 Examples

In the top panel of Figure 4.6, one typical example MC event of the  $\gamma$ -ray reconstructed energy of  $\sim 17$  TeV is shown. The 2D projection of the likelihood surface shows the contours in different

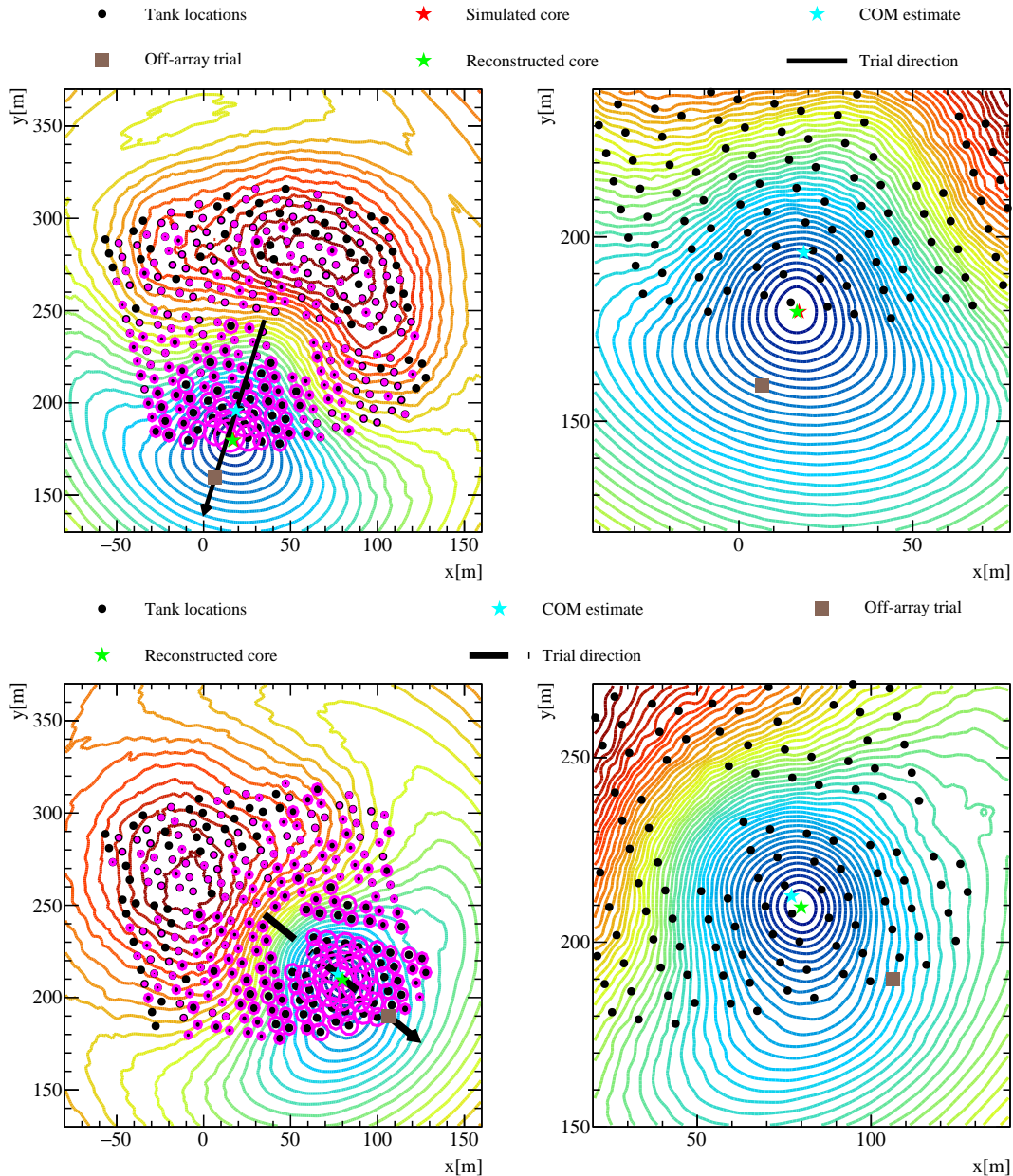


**Figure 4.6:** The figure on the right is the zoom in version of the figure on the left around the reconstructed core. Top panel: an example MC event. The likelihood surface contours from blue to red colour show the minimum to maximum respectively. The magenta circles over the tanks show the relative charge observed between the different tanks. Bottom panel: similar to the top panel a  $\gamma$ -ray like data event coming from the vicinity of the Crab Nebula is shown. The top panel of the Figure is reproduced from (Joshi et al. 2018).

#### 4. A TEMPLATE-BASED $\gamma$ -RAY RECONSTRUCTION METHOD FOR AIR SHOWER ARRAYS

---

colours. The contour colour scale varies from red to blue indicating the maximum to minimum of the likelihood surface respectively. The red colour star shows the true (simulated) core location. The COM location is shown with the cyan colour star. The magenta colour circles over the tanks denote the relative charge observed between the tanks. The off-array trial direction and one such trial is also shown. The green colour star shows the reconstructed core as the best fit result which falls in the prominent minimum shown with blue coloured contours of the likelihood surface. It can be seen that the method converged to very close to the true core location. Similarly, in the bottom panel, an example of real  $\gamma$ -ray like data event of reconstructed energy  $\sim 17$  TeV is shown, which is selected after hadron rejection cuts (see Section 2.8) from the direction of the Crab Nebula. It can be seen that the reconstructed core coincides with the global minimum of the likelihood surface.

In the left panel of Figure 4.7, the LDF of the example MC  $\gamma$ -ray shower discussed above and the template PDF corresponding to the best fit parameter values are shown. The black dots represent the tank locations and observed signal and the dashed line show the observed zero PE. Similarly, in the right panel of Figure 4.7, the best fitting template PDF and LDF of the Crab Nebula data event described above are shown.

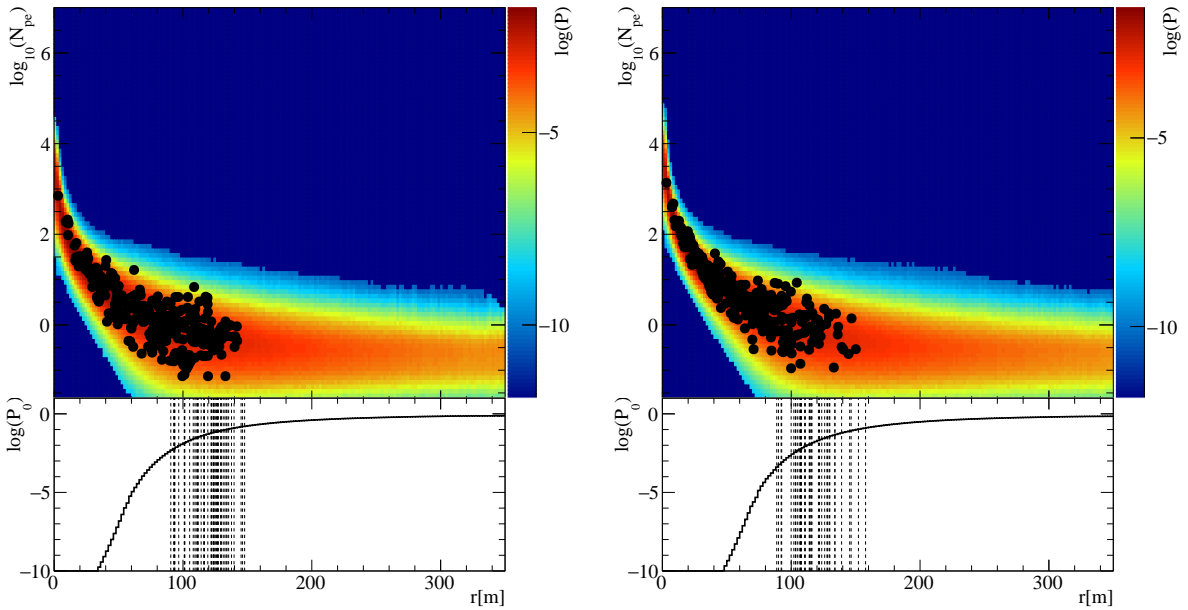


**Figure 4.7:** The LDF and PDF template corresponding to the event in Figure 4.6 with true energy  $\sim 16$  TeV, reconstructed energy of  $\sim 17$  TeV and true  $X_{max} \sim 400$  g/cm<sup>2</sup>, reconstructed  $X_{max} \sim 423$  g/cm<sup>2</sup> and zenith angle  $\sim 20.76^\circ$  for the MC event (left panel). One similar Crab data event is also shown (right panel) with the reconstructed energy of  $\sim 17$  TeV,  $X_{max} \sim 424$  g/cm<sup>2</sup> and zenith angle  $\sim 4.03^\circ$ . The black dots show the LDFs for non-zero  $N_{pe}$  and observed zeros are shown as the dashed lines on the histogram below with their corresponding probability. Figure reproduced from (Joshi et al. 2018).

## 4.7 Binning Optimisation

Deciding the bin size for different fit parameters to make the templates is a crucial step. On one hand, too fine binning can be very computing intensive for making the templates and performing the fit, while on the other hand, too coarse binning affects the smoothness of the likelihood function and hence will decrease the achievable resolutions of the fitted parameters.

To find an optimal bin size for each parameter, templates of varying bin sizes are created for a given parameter while fixing the others. Typically, reducing the bin size in a parameter will improve the resolution and reduce the bias up to a point where binning is not the dominant effect on parameter estimation any-more.

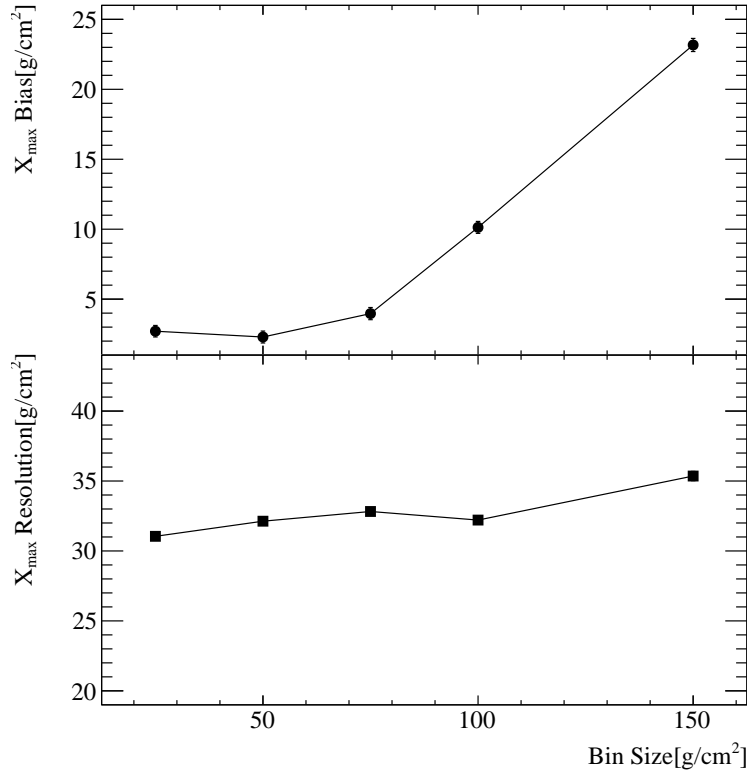


**Figure 4.8:**  $X_{\max}$  bias ( $\langle X_{\max,\text{reco}} - X_{\max,\text{true}} \rangle$ ) and  $X_{\max}$  resolution ( $\text{RMS}(X_{\max,\text{reco}} - X_{\max,\text{true}})$ ) shown as a function of bin size of  $X_{\max}$ . Figure reproduced from (Joshi et al. 2018).

Firstly, by fixing the shower energy at 10 TeV, the binning in  $X_{\max}$  and  $r$  is optimised. Energy 10 TeV is chosen as it is a rather central value in the sensitivity of air shower detector arrays like HAWC, however, it is to be noted that the procedure of optimisation can be repeated at different energies.

The Figure 4.8 shows the case of varied bin sizes (25, 50, 75, 100 and 150 g/cm<sup>2</sup>) of  $X_{\max}$  and fixed bin size of energy to 0.1 in  $\log_{10}(E/\text{GeV})$  and core distance to 2 m. While fitting  $X_{\max}$ , the other two parameters are fixed to their simulated values and only  $X_{\max}$  is the free parameter. As  $X_{\max}$  is also dependent on energy, only 10 TeV energy showers were used.

#### 4. A TEMPLATE-BASED $\gamma$ -RAY RECONSTRUCTION METHOD FOR AIR SHOWER ARRAYS

---

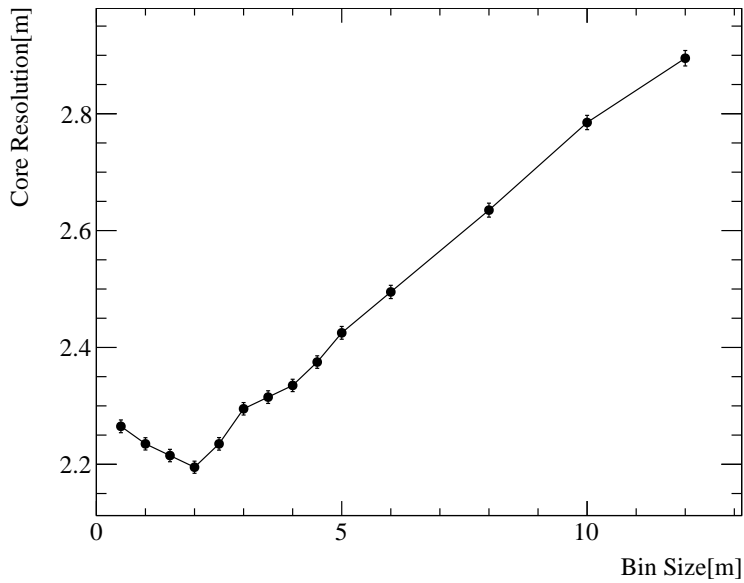


**Figure 4.9:** Core resolution (68% containment radius) versus varying bin size of distance from the shower core. Figure reproduced from (Joshi et al. 2018).

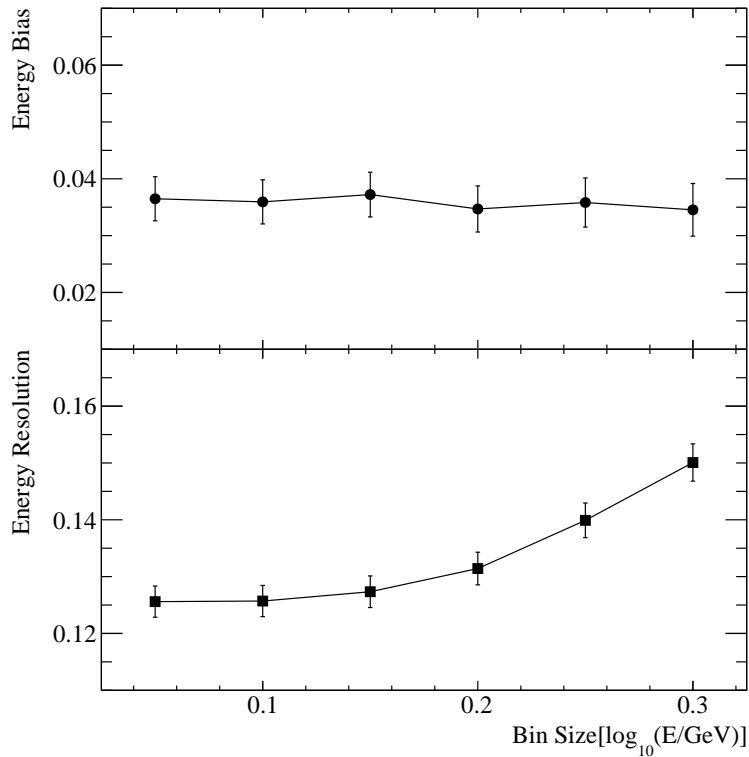


**Figure 4.10:** Fractional energy bias (top) and energy resolution (bottom) versus bin size of true energy of the  $\gamma$ -ray photon. Figure reproduced from (Joshi et al. 2018).

Figure 4.8 shows the  $X_{\max}$  bias and  $X_{\max}$  resolution as a function of  $X_{\max}$  bin size.  $X_{\max}$  bias and  $X_{\max}$  resolution are the mean and RMS of  $X_{\max,\text{reco}} - X_{\max,\text{true}}$  distribution, which is approximately a Gaussian. Reducing the bin size below  $50 \text{ g/cm}^2$  seems not to improve resolution and bias any further, therefore it is chosen as the optimal value.

The procedure was repeated for the  $r$  binning. Figure 4.9 shows that the optimal bin size at 10 TeV energy is 2 m. The points for a given bin size represents the core resolution (68% containment radius) of the corresponding core (true) - core (reco) distribution.

To optimise the  $E$  bin size, the procedure was again repeated for creating the templates, but for the test sample, an energy range instead of only 10 TeV energy was taken in order to escape the discreteness in the  $\log_{10}(E_{\text{reco}}) - \log_{10}(E_{\text{true}})$  distribution. From the fit output for the energy range, the 10 TeV bin is taken, which includes some nearby energies and makes the distributions smooth. By looking at Figure 4.10, 0.1 in  $\log_{10}(E/\text{GeV})$  seems to be the best choice.

## 4.8 Performance on Simulations

The performance of the fit method is first assessed using MC simulations for the HAWC array. The test simulation data set has the same ranges for the parameters  $E$ ,  $X_{\max}$  and  $\theta$  as of the simulation dataset for generating the MC templates which are described in Section 4.4. To have events of a reasonable size, an additional condition is applied that at least 10% of the available channels should have observed a signal.

The performance on the core and energy reconstruction and gamma-hadron separation are shown. The performance on  $X_{\max}$  is not shown because it was found to be dominated by the used prior relation between  $X_{\max}$  and  $E$  as described in Section 4.6. However, it is to be noted that the template binning and fitting in  $X_{\max}$  is crucial in order to partially break the ambiguity in  $X_{\max}$  and energy as discussed in Section 4.2.1.

### 4.8.1 Core Resolution

The core resolution is defined as 68% containment radius of the distribution of the distance between the reconstructed and true shower core. In Figure 4.11, the core resolutions for the SFCF method (present core fit method employed in HAWC) and for the likelihood (LH) method are shown. The SFCF method is a model based fit method, which utilises a hybrid function of a NKG-like and Gaussian function for the description of the observed LDF of an EAS. Its working is explained in Section 2.6.1 in more details. For both the methods, the core resolution is shown for the true core of the showers falling inside (on-array, solid markers) and outside (off-array, hollow markers) the array. Off-array is defined as a radially symmetric area, which is 50% as of the area of the main array.

For the on-array events, at energies  $<10$  TeV, the LH method has a core resolution of  $\sim 18$  m at energy 0.3 TeV which further improves to  $\sim 3$  m for energies  $>10$  TeV. The improvement in this energy range is about 3 fold compared to the SFCF. It is because of two main reasons. First, for the low energy events, there are a lot of zero PE signals, which are properly accounted for in the LH method. Second, the uncertainty in the observed LDFs is large in this low energy range,

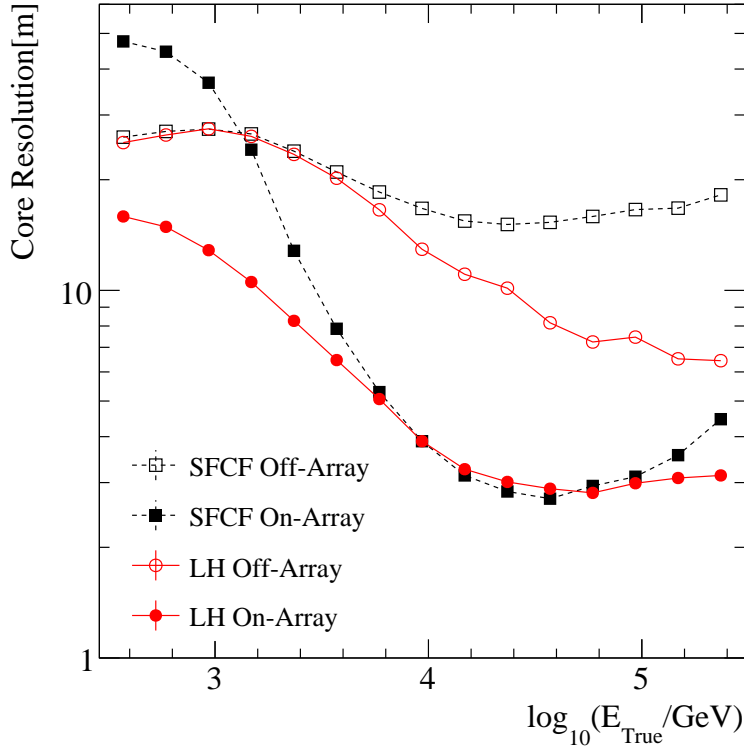


**Figure 4.11:** Core resolution (68% containment radius) shown as a function of the true energy of the  $\gamma$ -ray photon. Here SFCF and LH represent the HAWC present core estimator and the likelihood fit method respectively. Off and On-Array stands for the true core of the shower falling inside and outside the array respectively.

and the LH method captures it properly in a probabilistic way. Both of these measures are very hard to take care of in a model-dependent fit method such as SFCF. At the energies  $>10$  TeV, the footprint of the shower becomes comparable to the instrumented area of HAWC. Therefore most of the WCDs observe PEs. The observed  $N_{\text{pe}}$  also increases, in turn, the uncertainty in the LDFs decreases. Therefore, the LH method and SFCF performs in a similar way.

For the off-array events, in the energy range of 0.3 to 3 TeV, both the methods perform in a similar way with a core resolution of  $\sim 30$  m. For the low energy off-array events, the uncertainties in the observed LDF is large, and only the tail of the LDF is observed. Therefore it is likely for the LH method to get stuck into a local minimum. However, for energies  $>10$  TeV, one starts observing the advantages of the LH method, where it has a core resolution of  $\sim 20$  m at 10 TeV, which further improves to  $\sim 7$  m at 300 TeV. This is again a  $\sim 3$  fold improvement compared to the SFCF. This is because, for the off-array events, one starts observing zero PE signals, as the shower footprint is not well contained within the array. Additionally, only the tail of the LDF is observed, which has large uncertainties even for high energy events. Both of these issues are accounted for in the LH method.

### 4.8.2 Energy Resolution and Bias

In Figure 4.12 the distribution of reconstructed energy versus true energy is shown. The z-axis shows the number of shower events. The figure shows the strong correlation between reconstructed and true energy.

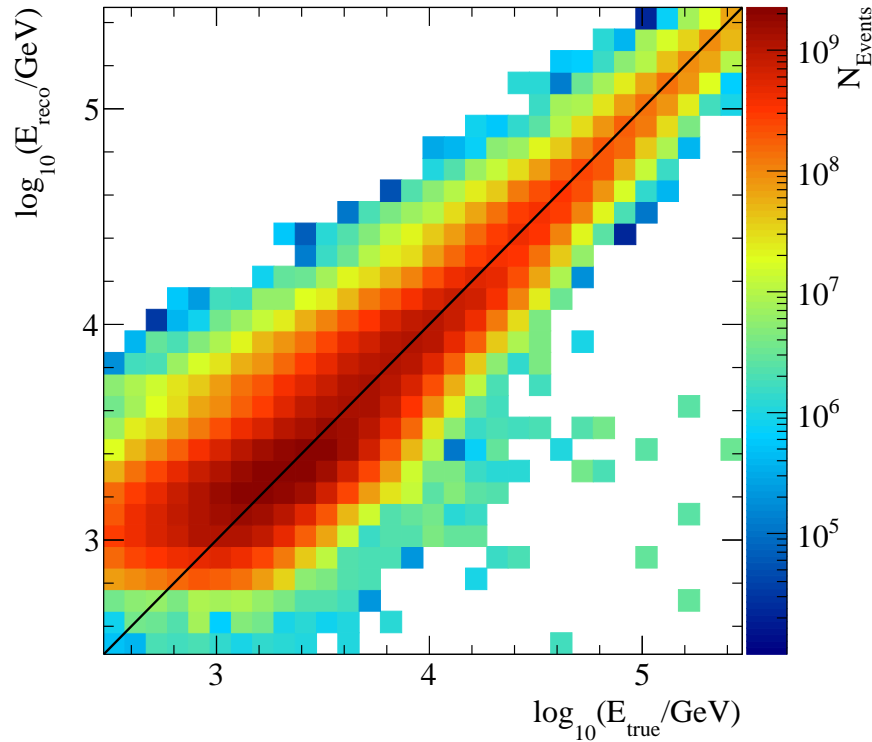


**Figure 4.12:** Distribution of reconstructed  $\gamma$ -ray photon energy versus true  $\gamma$ -ray photon energy. The z-axis shows the number of  $\gamma$ -ray events. Figure reproduced from (Joshi et al. 2018).

The performance of the energy reconstruction can be evaluated by the fractional deviation ( $\log_{10}(E_{\text{reco}}) - \log_{10}(E_{\text{true}})$ ) of the reconstructed energy with respect to the true energy. The deviation of the mean of the fractional deviation distribution from zero (see Figure 4.13 (top panel)) is the bias in the energy reconstruction. Similarly, the RMS can be understood as the energy resolution (see Figure 4.13 (bottom panel)). The energy bias is large at the low energies but converges to zero at energies  $>4$  TeV, which indicates the stable region of the energy reconstruction. The bottom panel of Figure 4.13 shows the energy resolution of the likelihood fit method, which starts at  $\sim 50\%$  for low energies and drops down to  $\sim 25\%$  at the highest energies. Such energy resolution is very promising for EAS arrays like HAWC.

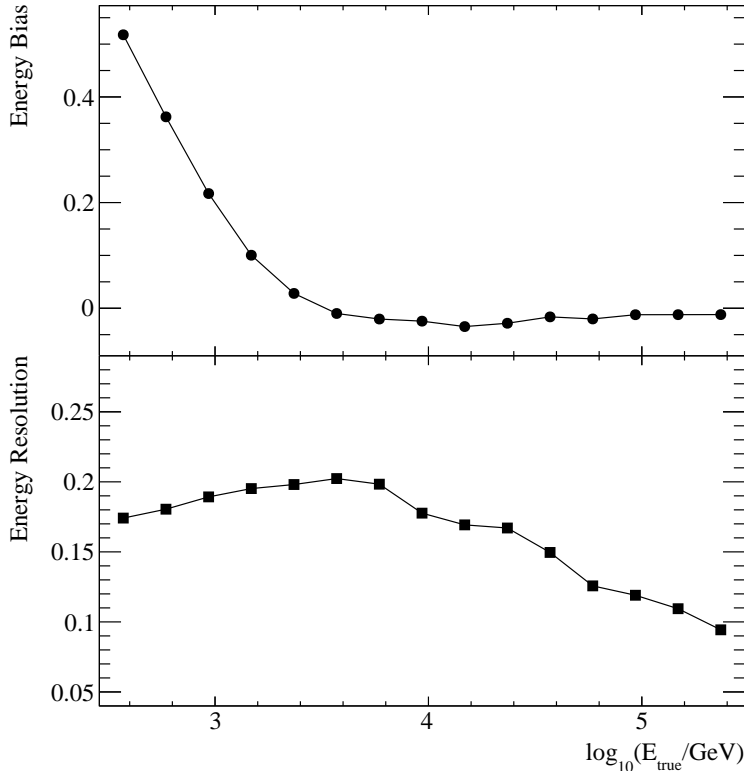


**Figure 4.13:** Fractional energy bias (top) and energy resolution (bottom) as a function of true  $\gamma$ -ray photon energy. Figure reproduced from (Joshi et al. 2018).

### 4.8.3 Gamma-Hadron Separation

The concept of the goodness of fit (GoF) is explained in Section 4.3. To demonstrate the gamma-hadron separation power, the GoF distributions for the simulated MC air showers are shown. Figure 4.14 exhibits the GoF distributions as a function of observed percentage hits (percent number of detector units) of the HAWC array. It shows the most probable value of the GoF distribution with 68% and 95% containment. The distributions for simulations of  $\gamma$ -ray and proton induced air showers are presented. For the higher mass hadrons, one would expect even more diverge distribution of the GoF from the  $\gamma$ -ray induced air showers.

It is evident from the GoF distribution of  $\gamma$ -ray and proton induced air showers that it starts showing a separation power for as low as  $\sim 20\%$  of the percentage hits of the array and the separation power increase with event size. At the highest energies a slight decrease in separation power can be seen, which might be due to saturation effects of the detector.



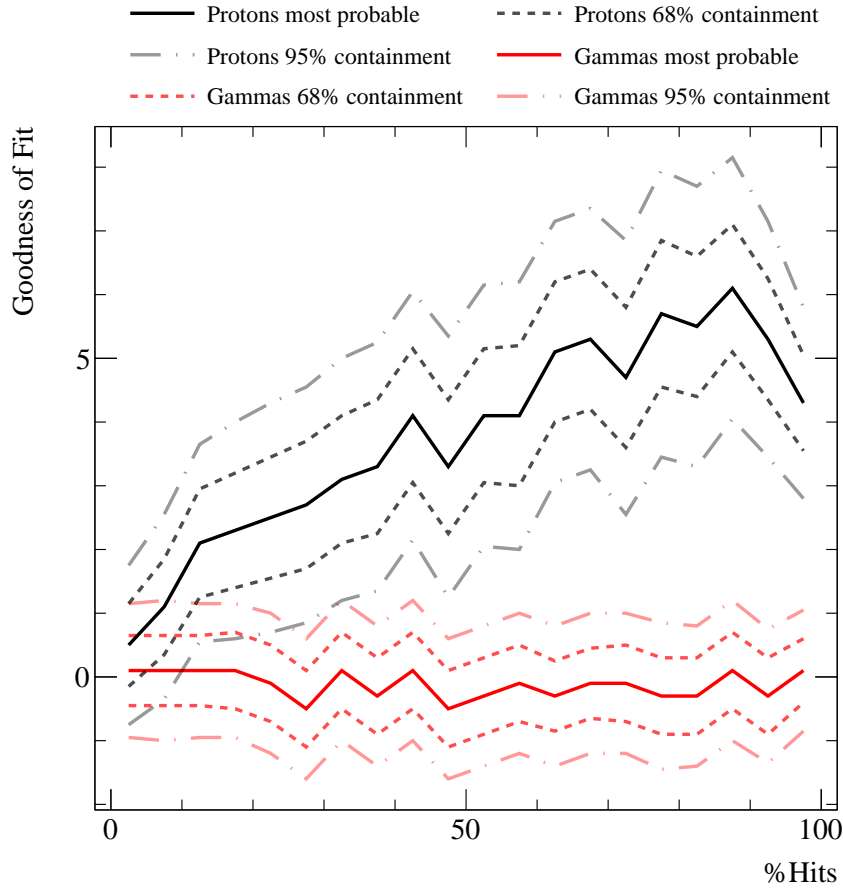


**Figure 4.14:** The GoF distributions of the likelihood fit method for simulated  $\gamma$ -ray and proton induced air shower are shown in red and black respectively. It shows the most probable value of GoF with 68% and 95% containment as a function of percentage hits of the HAWC main array. Figure reproduced from (Joshi et al. 2018).

## 4.9 Performance on Crab Nebula Data

From the performance results of the LH method in simulations, it can be seen that the LH method improves the core resolution significantly in comparison to the SFCF method. Therefore to evaluate the immediate impact of the better core reconstruction on the reconstruction of HAWC, a small subset of data which only includes the Crab Nebula transit is used. For brevity, I will refer to the Crab Nebula as Crab from hereafter. However, before making the comparison between the standard HAWC reconstruction (using SFCF method) and the LH method following considerations need to be addressed. First, because the LH method is heavily dependent on the MC simulation, the agreement between simulations and data needs to be verified. Second, the  $\gamma$ -hadron separation parameters, PINC and Compactness, as defined in Section 2.6.3 depend intrinsically on the core location. Therefore, to perform the  $\gamma$ -hadron separation using the LH method on the reconstructed Crab data in the  $\mathcal{B}$  bins (see Section 2.8), the PINC and Compactness cuts need to be optimised. Additionally, with the LH method, the GoF parameter provides the  $\gamma$ -hadron

separation power. Therefore, it is worthwhile to take GoF into account together with PINC and Compactness in the optimisation of the new cuts. To proceed further, two datasets were reconstructed. The first dataset for checking the agreement between simulation and data and for optimising the cuts, and second dataset as an independent dataset, to compare the performance between the standard HAWC reconstruction and the LH method. The duration of the first dataset is a half year of 2016 and the second dataset is the full year of 2017.

Using the first dataset, in Figure 4.15, the comparison of the GoF distributions of  $\gamma$ -ray like events obtained from the simulated and observed Crab data is shown for the HAWC main array. The simulation of a Crab-like source is done by re-weighting of the reconstructed MC simulation

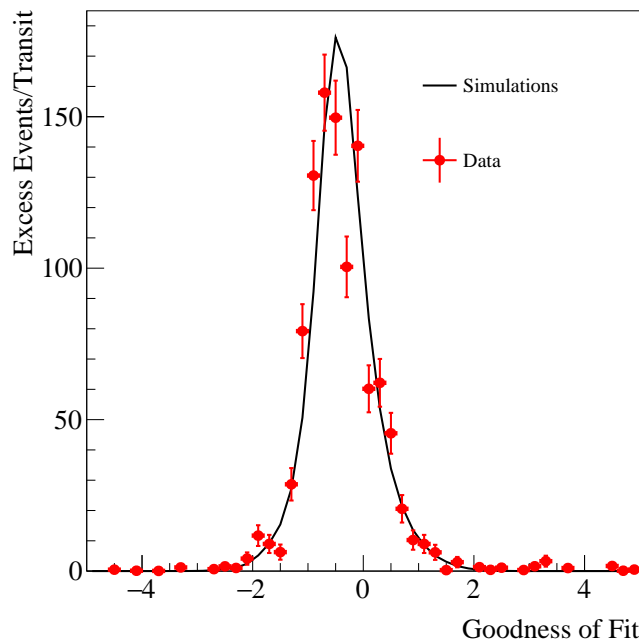


**Figure 4.15:** The excess events per transit as a function of GoF is shown for a simulated and observed crab data in black and red colour respectively.

dataset. To calculate the observed excess from the Crab, a  $0.5^\circ$  on and off regions were defined in the vicinity and away from the Crab respectively. Events from all the  $\mathcal{B}$  bins were combined together to check the overall agreement in data and simulations for the GoF distributions. The overall agreement tells that the GoF distribution range is consistent in data and simulations, which is useful to optimise the cuts. However, it is to be noted that in individual  $\mathcal{B}$  bins the distribution between simulations and data might differ. Nevertheless, efforts are being made to improve the simulations in order to better match them with the observed data. It can be seen from Figure 4.15 the GoF distributions in data and simulation agree reasonably well.

Therefore in the next step, using the first dataset, the  $\gamma$ -hadron separation parameters: PINC, Compactness, and GoF are optimised to obtain the highest statistical significance on the Crab. Similar to standard optimised cuts a 50%  $\gamma$ -ray efficiency requirement is imposed. The cuts are optimised in same nine  $\mathcal{B}$  bins in order to finally make the sky-maps same as for the standard HAWC reconstruction as described in Sections 2.8 and 2.11. It is decided to only take

#### 4. A TEMPLATE-BASED $\gamma$ -RAY RECONSTRUCTION METHOD FOR AIR SHOWER ARRAYS

---

into account the events which are reconstructed on the HAWC array, as this improves the PSF significantly. Therefore, an additional cut is applied to select only those events which are reconstructed on the HAWC main array. However, I also performed the same studies (shown later in this Section) for combining events reconstructed outside the array until a circular symmetric area 50% of that of the main HAWC array. Events only until a circular symmetric area of 50% were taken into account because for areas bigger than that the reconstruction degrades significantly. I will refer to these additional results as “including the off-array events”, the related results are in the appendix A. I will refer to the results on “including the off-array events” accordingly while discussing the results for the events reconstructed on the array.

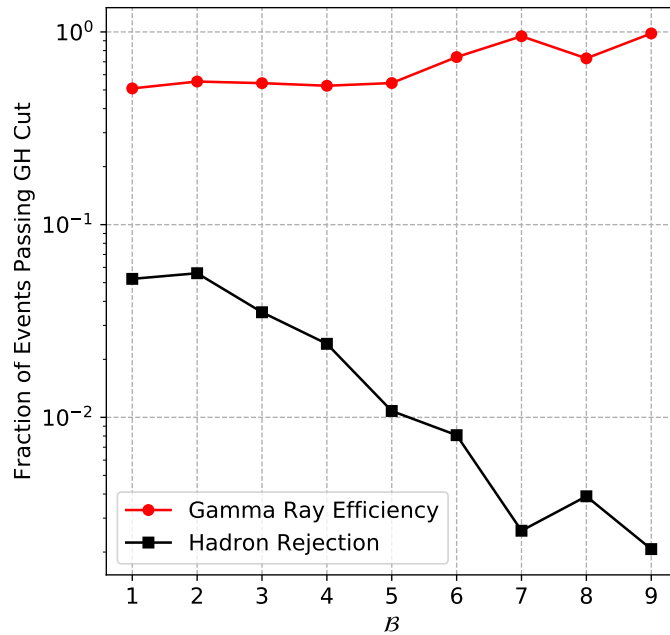


**Figure 4.16:**  $\gamma$ -ray efficiency and hadron rejection power as a function of  $\mathcal{B}$  bins obtained for LH method after optimising the cuts.

In Figure 4.16, the obtained  $\gamma$ -ray efficiency and hadron rejection power is shown as a function of the  $\mathcal{B}$  bins. It can be seen that the  $\gamma$ -ray efficiency satisfies the imposed condition of 50%  $\gamma$ -ray efficiency in all the  $\mathcal{B}$  bins. The hadron rejection power is calculated using the off-Crab regions of radius  $1^\circ$ . The average of the observed counts is calculated with and without  $\gamma$ /hadron separation cuts in those off-regions. The ratio of these two tells us the hadron rejection power. The obtained optimised cuts for the LH method are shown in Table 4.2 (optimised cuts including the off-array events are shown in Table A.1).

The year 2017 dataset was reconstructed with both the (SFCF and LH) methods. The optimised cuts for standard HAWC reconstruction are the same as shown in Table 2.2. For the LH method, the optimised cuts shown in Table 4.2 are used. In both the cases, only the reconstructed events on the array were considered as described before. Finally, nine HAWC sky-maps as described in Section 2.11 were produced for both methods.

I have used the slice profiling tool as described in Section 6.3 to obtain the excess counts

#### 4. A TEMPLATE-BASED $\gamma$ -RAY RECONSTRUCTION METHOD FOR AIR SHOWER ARRAYS

$\mathcal{B}$	$f_{\text{hit}}$	PINC ( $\mathcal{P}$ ) Maximum	Compactness ( $\mathcal{C}$ ) Minimum	GoF Maximum
1	6.7 - 10.5%	<2.2	>7.0	2.5
2	10.5 - 16.2%	3.0	9.0	2.5
3	16.2 - 24.7%	1.5	15.85	2.5
4	24.7 - 35.6%	1.4	12.59	1.7
5	35.6 - 48.5%	1.4	15.85	1.5
6	48.5 - 61.8%	1.3	10.00	1.4
7	61.8 - 74.0%	1.2	12.59	3.2
8	74.0 - 84.0%	1.3	10.00	1.8
9	84.0 - 100.0%	1.3	5.01	5.0

**Table 4.2:** The analysis cuts for the LH method, defined over analysis bins ( $\mathcal{B}$ ), which correspond to a certain fraction of the available PMTs that observed a non-zero signal ( $f_{\text{hit}}$ ). The PINC, Compactness and GoF cuts, which determines the background rejection are optimised on the Crab data for highest statistical significance.

profiles. The defined slice is centred at the location of the Crab and has a width of  $1^\circ$  and length of  $6^\circ$ . The orientation of the slice on the sky-map does not matter for point sources, therefore, it is kept aligned to the equal longitude lines. In Figure 4.17, the excess count profiles obtained for the SFCF and LH are shown in black and red colour respectively. The different bins are annotated in respective panels. The  $\mathcal{B} = 0$ , corresponds to the  $f_{\text{hit}}$  4.4 to 6.7% and contain small events and are usually not reconstructed well.  $\mathcal{B} = 0$  also set limits on HAWC reconstruction in the lower energy range, therefore it is not considered in the HAWC analysis. Consequently, the optimised cuts tables are only shown for  $\mathcal{B}$  bins 1 to 9. The excess count profiles in each  $\mathcal{B}$  bin is fitted with a Gaussian. By looking at the error bars of the excess count profiles it is evident that in the case of reconstruction using the LH method the background is reduced significantly. In most of the  $\mathcal{B}$  bins, the number of excess counts obtained and the width of the fitted Gaussian is rather similar between the two methods. Similar results were obtained by including the off array events and are shown in Figure A.1. The  $1\sigma$  width of the fitted Gaussian is used as an equivalent measure to the PSF and will be denoted by  $\text{PSF}'$  from hereafter.

In Figure 4.18 top panel, the number of excess and background counts obtained using the slices profiles from Figure 4.17 are shown in the left and right respectively. It can be seen that the obtained number of excess counts are similar for both the methods, however, it is to be noted that the number of background counts is reduced significantly in most of the bins for the LH method. This might be due to the additional GoF cut, which improves the  $\gamma$ -hadron separation and excludes badly reconstructed events. Additionally, for the shower falling outside the array, SFCF has a tendency to push the off-array events on the array. This might be because of the hybrid nature of the SFCF function which includes a Gaussian component near to the core location. As discussed in Section 2.6.1 the Gaussian component prefers the reconstruction of the events on the array. These additional real off array showers which has been wrongly reconstructed on the array introduce additional background for the SFCF method.

#### 4. A TEMPLATE-BASED $\gamma$ -RAY RECONSTRUCTION METHOD FOR AIR SHOWER ARRAYS

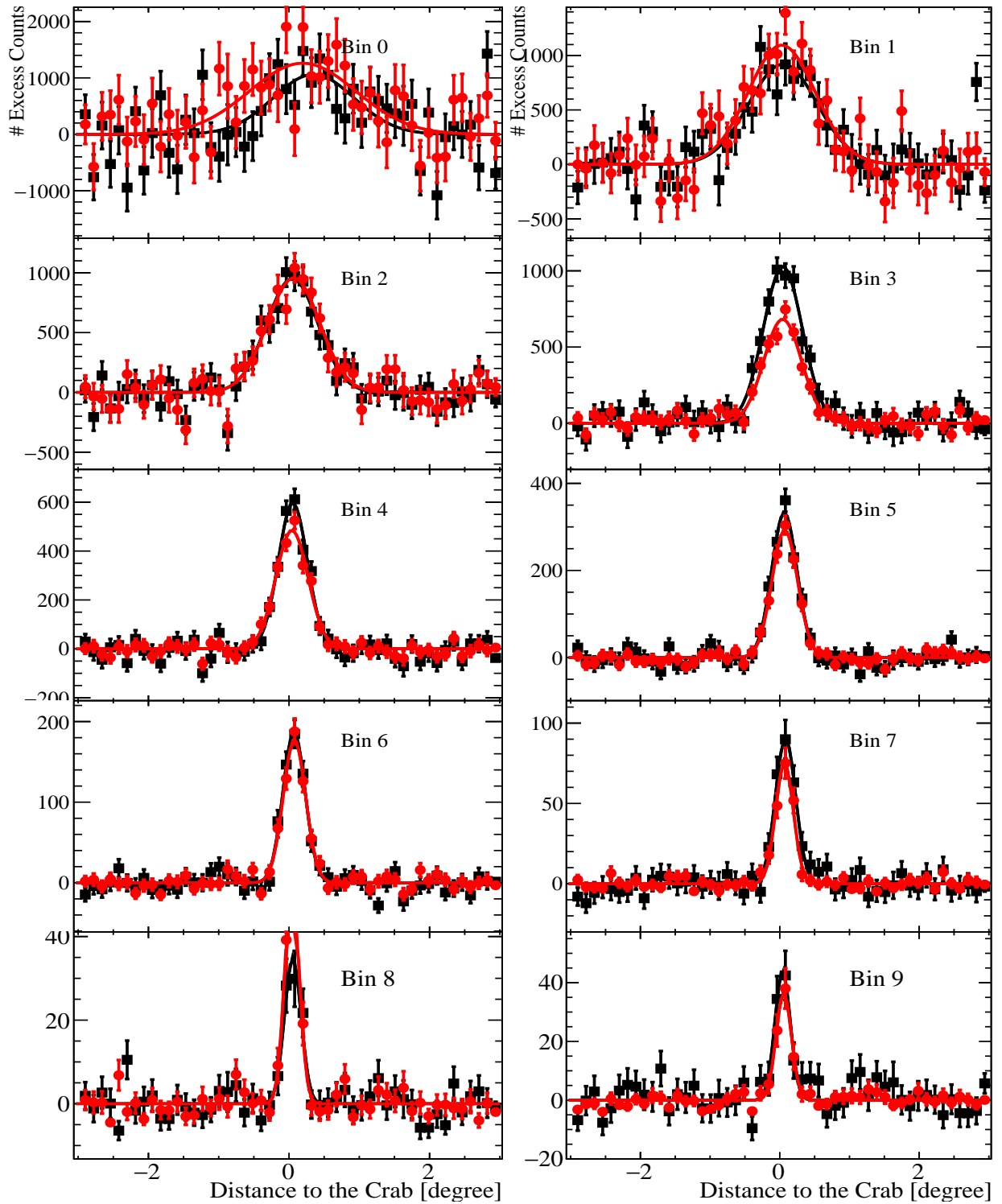


**Figure 4.17:** Excess count profiles in  $\mathcal{B}$  0 to 9 on Crab data. The reconstructed data using the LH and SFCF methods are shown in red and black colours respectively. The excess count profiles are fitted with a Gaussian in both the cases. The location of the Crab is at 0 on the X-axis.

#### 4. A TEMPLATE-BASED $\gamma$ -RAY RECONSTRUCTION METHOD FOR AIR SHOWER ARRAYS

Whereas, the LH method does not show this problem as it reconstructs the off array events better in comparison to the SFCF method as shown in Figure 4.11. The corresponding results by including the off-array events are shown in the top panel of Figure A.2.

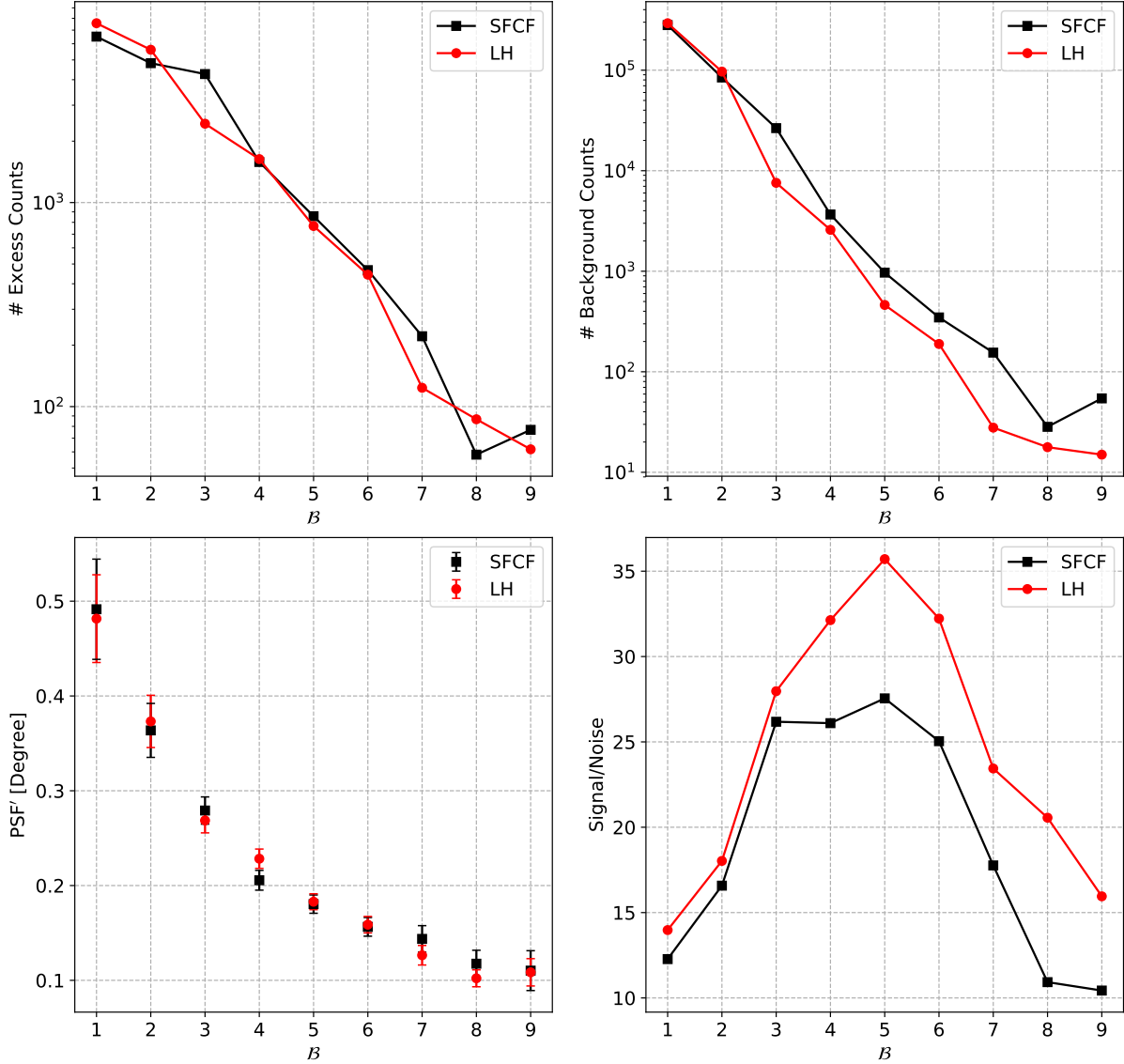


**Figure 4.18:** The results are shown for the Crab data using the slice profile analysis as described in the text. SFCF is the standard core fit method used in HAWC and LH stands for the new likelihood method. Top panel: excess counts (left) and background counts (right) as a function of  $B$  in  $1\sigma$  region of the fitted Gaussian to the slice profiles. Bottom panel: PSF' (left),  $1\sigma$  width of the fitted Gaussian and signal to noise ratio (right) in that region (right) as a function of  $B$  bin.

In Figure 4.18 bottom panel, the  $1\sigma$  width of the fitted Gaussian is shown in the left panel which is denoted as PSF'. It is an equivalent measure of the PSF. It can be seen that in both the cases the results are similar. This might be due the on array selection of the reconstructed events,

for which, the reconstruction in both cases is similar. This can also be seen from the results from simulations as shown in Figure 4.11, where the core resolution is rather similar above few TeV energies. In the bottom right panel of Figure 4.18, the signal to noise ratio calculated in the  $1\sigma$  width is shown. It can be seen that the LH method performs significantly better in comparison to the standard HAWC reconstruction using SFCF in all the  $\mathcal{B}$  bins. The improvement is  $\geq 20\%$  from  $\mathcal{B}$  bin 4 to 9. The main reasons for this improvement might be the better background rejection with additional GoF cut and better reconstruction of the core location. Similar results by including the off-array events are shown in the bottom panel of Figure A.2.

### 4.10 Application to Mixed Detector Arrays

In this section, I illustrate the applicability of this method for mixed detector type air shower arrays by using detector simulations for HAWC and its high-energy upgrade, the outrigger array (Joshi 2017; Joshi & Jardin-Blicq 2017). The detailed description of the outrigger array is given in Chapter 3. As explained in Section 4.3, it is straightforward to combine different detector types in the likelihood function.

In the top panel of Figure 4.19, an example is illustrated of the method applied to a simulated event with signals detected in both WCDs, the outriggers and the HAWC main array. It shows the likelihood contours and the reconstructed and true core for a simulated event located in the area instrumented by the outrigger array. For this event, the best fitting templates corresponding to the main array tanks and the outriggers are shown in the top panel of Figure 4.20 left and right panel respectively. In the case of the smaller outrigger detectors, the fluctuations in the particle density of the shower front become more prominent, which manifest in both larger amplitude fluctuations and more zero signal detectors. Nevertheless, it is not a problem for the template-based likelihood fit procedure, which combines these significantly different detector responses naturally to reconstruct the  $\gamma$ -ray properties.

Similarly, in the bottom panel of Figure 4.19, an example candidate  $\gamma$ -ray event coming from the vicinity of the Crab is shown. In the bottom panel of Figure 4.20, the corresponding LDF and PDF are shown. However, it is to be noted that the hit selection and more realistic outrigger simulation is still a work in progress. Therefore, this Crab event is selected using the existing criteria for the main array only. Nevertheless, it can be seen that the LH method reconstruct the event by fitting it to a PDF that closely represents the LDF of the observed data event.

In Figure 4.21, the expected improvement in the core resolution due to the outrigger array is shown as a function of true energy for the  $\gamma$ -ray induced air showers. To obtain the core resolution only the showers falling on the area of the Outrigger array are taken into account. The core resolution is defined as the same in Section 4.8.1. In order to have enough outrigger triggered, an additional condition of at least 4% of the Outrigger array trigger was applied. To evaluate the improvement due to the outrigger array, the comparison is shown between the reconstruction of the events falling on the area of the outrigger array with only HAWC main array using the SFCF and LH method, and with the using the HAWC main array and the Outrigger array combined for the LH method. It can be seen that the outrigger array improves the core resolution by  $\sim 3$  fold in comparison to SFCF above 1 TeV energies. Although it is to be noted that the LH method



#### 4. A TEMPLATE-BASED $\gamma$ -RAY RECONSTRUCTION METHOD FOR AIR SHOWER ARRAYS

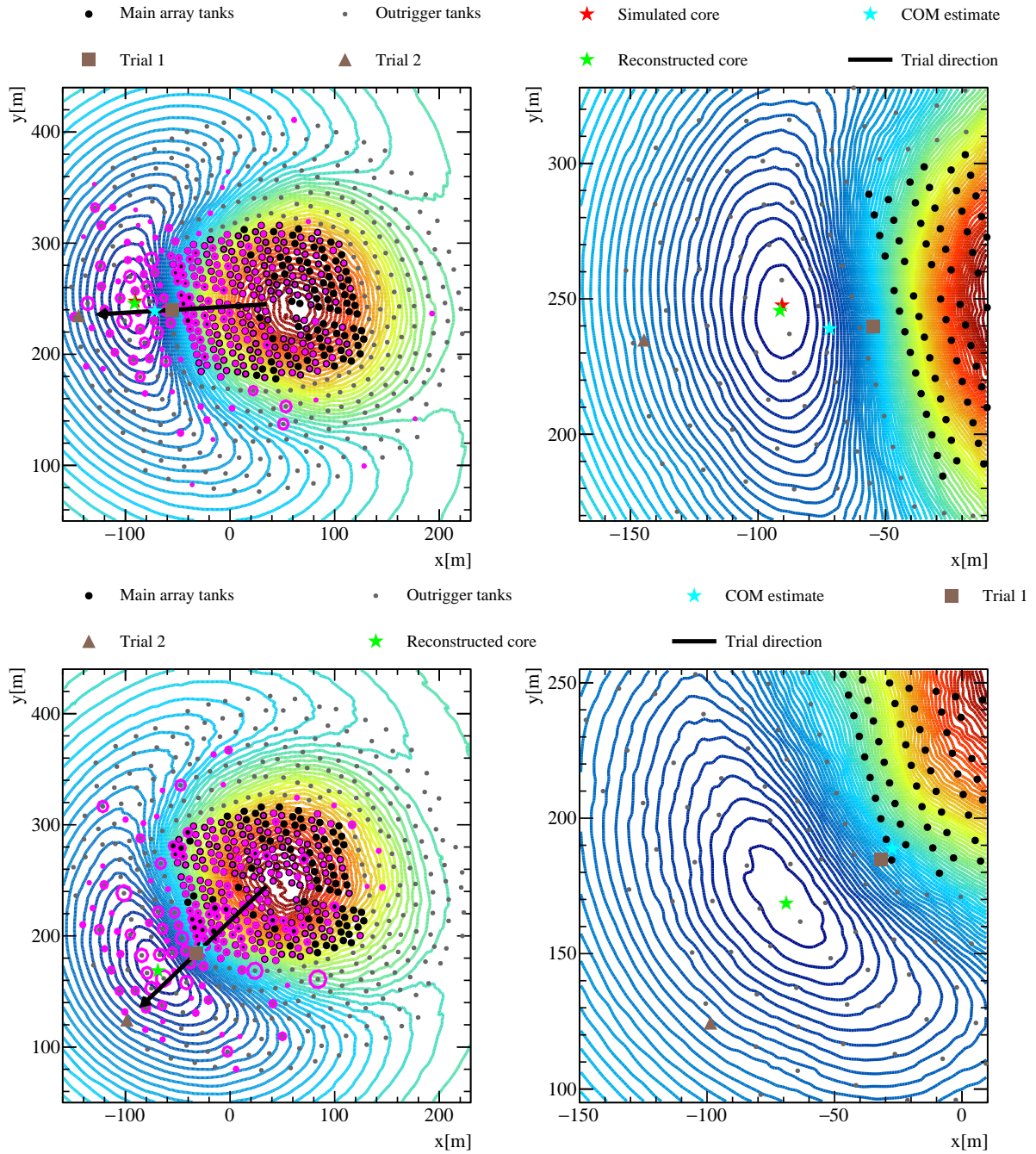


**Figure 4.19:** The Figure on the right is the zoom in version of the figure on the left around the reconstructed core. Top panel: the likelihood surface contours for an example simulated event are shown. Blue to red colour contours shows the minimum and the maximum of the surface respectively. The magenta circles over the tanks show the relative charge observed between the different tanks. Bottom panel: similar to the top panel a  $\gamma$ -ray like data event coming from the vicinity of the Crab Nebula is shown. The top panel of the Figure is reproduced from (Joshi et al. 2018).



#### 4. A TEMPLATE-BASED $\gamma$ -RAY RECONSTRUCTION METHOD FOR AIR SHOWER ARRAYS

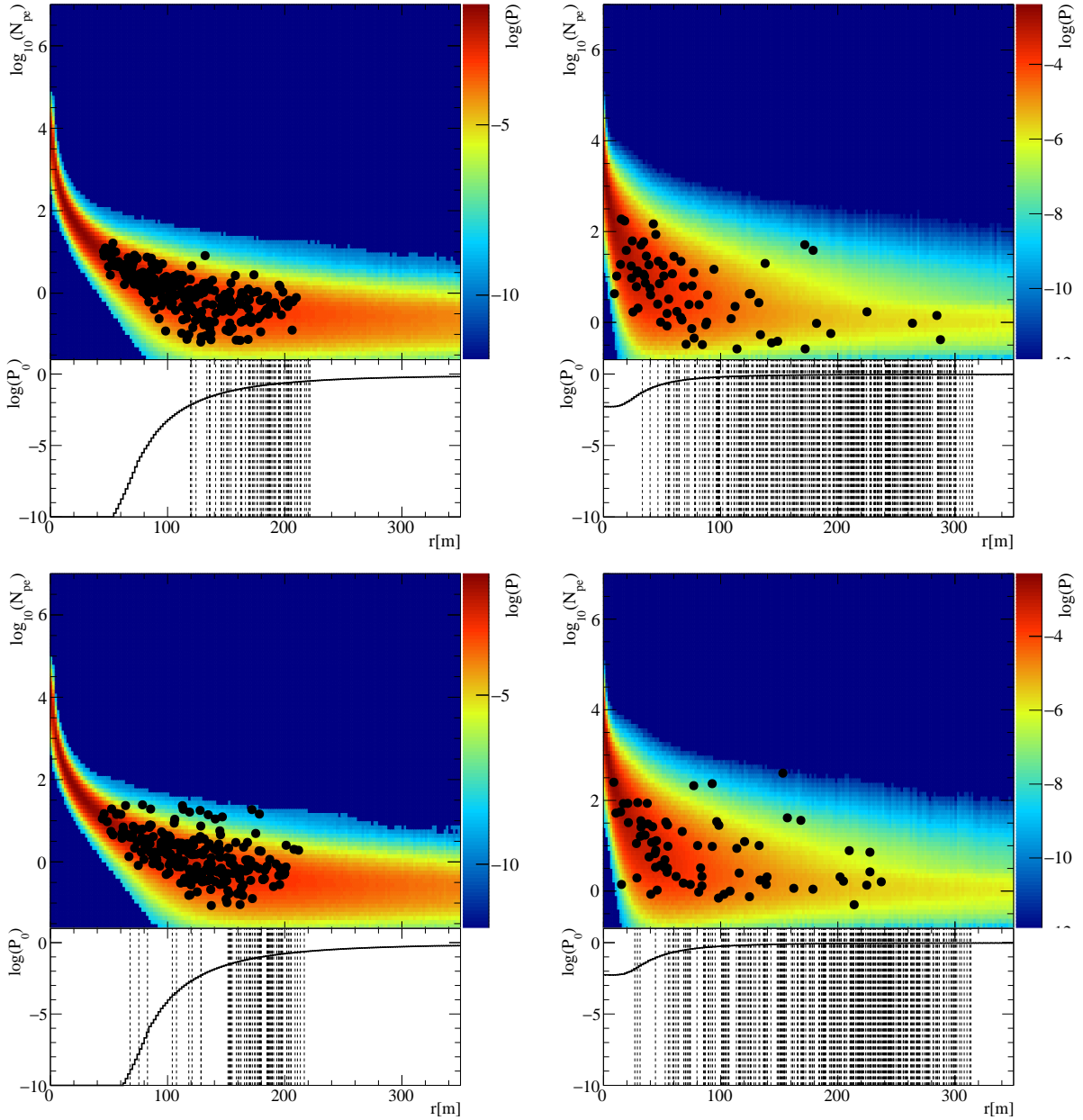


**Figure 4.20:** The LDF and PDF templates (main array tanks: left, outrigger tanks: right). Top panel: corresponding to the simulated event shown in the top panel of Figure 4.19, with true energy  $\sim 17$  TeV and reconstructed energy of  $\sim 21$  TeV and true  $X_{max} \sim 475$  g/cm<sup>2</sup> and reconstructed  $X_{max}$  of  $\sim 430$  g/cm<sup>2</sup> and zenith angle of 18.17°. Bottom panel: corresponding to the Crab data event shown in the bottom panel of Figure 4.19, with reconstructed energy  $\sim 27$  TeV  $X_{max} \sim 425$  g/cm<sup>2</sup> and zenith angle 16.08°. The black dots show the LDF for non-zero  $N_{pe}$  and observed zeros are shown as the dashed lines on the histograms below with their corresponding probability. The top panel of Figure is reproduced from (Joshi et al. 2018).

already performs better than the SFCE method even without using the outrigger array. However,

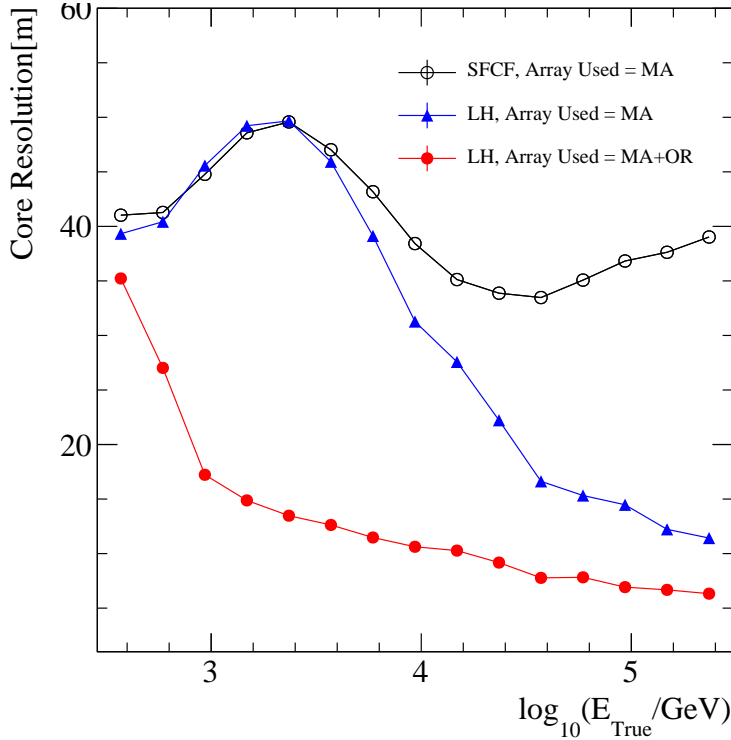


**Figure 4.21:** Core resolution (68% containment radius) shown as a function of the true energy of the  $\gamma$ -ray photon. Here SFCF and LH represent the HAWC present core estimator and this likelihood fit method respectively. The result is shown for the events falling on the Outrigger array only. Array used means the array used for reconstruction. MA and OR stand for the HAWC main array and outriggers respectively.

the core resolution improves further for the LH method while using the main array and outrigger array combined. The improvement is about 3 fold around 10 TeV energies and drops down to 2 fold at the highest energies. The core resolution obtained here is in agreement with the basic studies performed in Section 3.6.1 using a square grid layout in the early phase of the outrigger array planning. It is to be noted that comparing this core resolution to the one obtained for on array events using only HAWC main array as shown in Figure 4.11, one can see that it is very similar above 1 TeV energies. Therefore, the advantage of the outrigger array in improving the core resolution for the events falling outside the array is clear.

## 4.11 Conclusion and Prospects

In this chapter, I discussed the problems associated with a model-based air shower reconstruction approach using NKG-like functions and gave a better alternative to use a Monte Carlo (MC) template-based likelihood fit method. An MC template-based likelihood approach takes into account the uncertainties in the observed lateral distribution function (LDF) of particle air shower in a probabilistic way, therefore utilizes all the information available including signal-free detectors. In this work, this approach is used for the reconstruction of  $\gamma$ -ray induced air showers. Using

#### 4. A TEMPLATE-BASED $\gamma$ -RAY RECONSTRUCTION METHOD FOR AIR SHOWER ARRAYS

---

the LDF information, the core location and the energy of the primary  $\gamma$ -ray are estimated. In addition, the goodness of fit (GoF) of the method is used as a  $\gamma$ /hadron separator. The template-based likelihood fit approach allows us to incorporate mixed type particle detector arrays. This is shown for  $\gamma$ -ray air shower reconstruction using the HAWC main array combined with the outrigger array.

The performance of the method (likelihood (LH) method) is assessed using MC air shower simulations and the observed data on the Crab Nebula for the main array. In simulations, it is shown that the LH method improves the core resolution three-fold in the energy range  $< 10$  TeV for the showers falling on the array, and similarly, in the energy range  $> 10$  TeV for off-array showers. An energy resolution of  $\sim 50\%$  is achieved at energies  $< 10$  TeV, which further improves to  $\sim 25\%$  at the highest energies. The stable region of the energy reconstruction is  $> 7$  TeV energies. It is shown that the GoF of the method can be used as a  $\gamma$ /hadron separator when more than  $\sim 20\%$  of the array is hit for a given air shower.

New analysis cuts are obtained by optimising the  $\gamma$ /hadron separation (cuts) taking into account the new GoF parameter. The performance of the LH method is compared with the standard reconstruction on the significance and PSF on the Crab Nebula data. The performance on the PSF is rather similar, owing to the fact that only the events reconstructed on the HAWC main array are taken into account. However, the significance is improved by  $\geq 20\%$  from  $\mathcal{B}$  bins 4 to 9. The improvement might be due to the additional  $\gamma$ /hadron separation power and better reconstruction of the core location.

The agreement between the generated PDFs and observed LDFs for both types of detector arrays, i.e. main array and outrigger array, is shown. Using the LH method, the improvement in the core resolution due to the outrigger array is shown for the events falling on the outrigger array. The obtained core resolution is similar to the one for the on-array events above 10 TeV energies.

In principle, this method can be expanded for direction reconstruction by using the timing of the observed signals. Although I have shown its working only for  $\gamma$ -ray induced air showers, it might be possible to apply it to the reconstruction of other particle species. However, with the mixed composition of hadron-induced CR air showers and the uncertainty in the hadronic interaction models, it might be more challenging to obtain reconstruction with similar accuracy.

Currently, this method is in consideration for the reconstruction of the data. It can be applied to the archival data and to a new combined dataset taken with both the main array and the outrigger array. It is shown that the LH method already performs significantly better than the standard reconstruction. Nonetheless, it is worth to mention that, as the LH method is highly dependent on the MC simulations, with further improvements on the detector simulations the performance of the method will also improve.



# 5

## Introduction to Pulsar Wind Nebulae

In this chapter, I will give an introduction to PWNe to set the background for the studies done in this part of the thesis. I will talk about pulsars and the formation of PWNe. I will describe some of the relevant dynamical models of these objects. The emission mechanisms with an emphasis on  $\gamma$ -ray production will also be discussed.

### 5.1 Stellar Remnants

The fusion of elements (Hydrogen (H) into Helium (He)) within the cores of stars provide the necessary thermal energy and pressure to avoid the inward collapse due to their own gravity. This is the state of hydrostatic equilibrium, however, in a later stage, the supply of H dwindles, in turn, decreasing the fusion rate. Therefore eventually the star starts to contract to make the conditions favourable to start the fusion of heavier elements, i.e. He into Carbon (C) and Oxygen (O)). For the main sequence stars, the fate they see after their death depends on the mass of He cores and of the H envelopes (Heger et al. 2003). At this stage, if the star does not have enough temperature to fuse C and higher elements, further fusion stops, and the gravitational collapse takes over and contracts the star, in turn, releasing its gravitational potential energy. It also ignites the H shell burning around the core (Carroll & Ostlie 2006; Longair 2011). Different final states of the main sequence star as a function of their initial mass ( $M$ ) and metallicity is shown in Figure 5.1.

Stars with  $M < 9-10 M_{\odot}$  are likely to become red giants with an expanded and convective envelope. The envelope is finally lost in a series of shell flashes. Due to the Pauli exclusion principle, the electron degeneracy pressure supports the core from further collapse. However, it is only possible if the remaining core mass is  $< 1.4 M_{\odot}$ , known as the Chandrasekhar limit (Chandrasekhar 1931). The remnant is known as White Dwarf (WD), for example, the Sun will

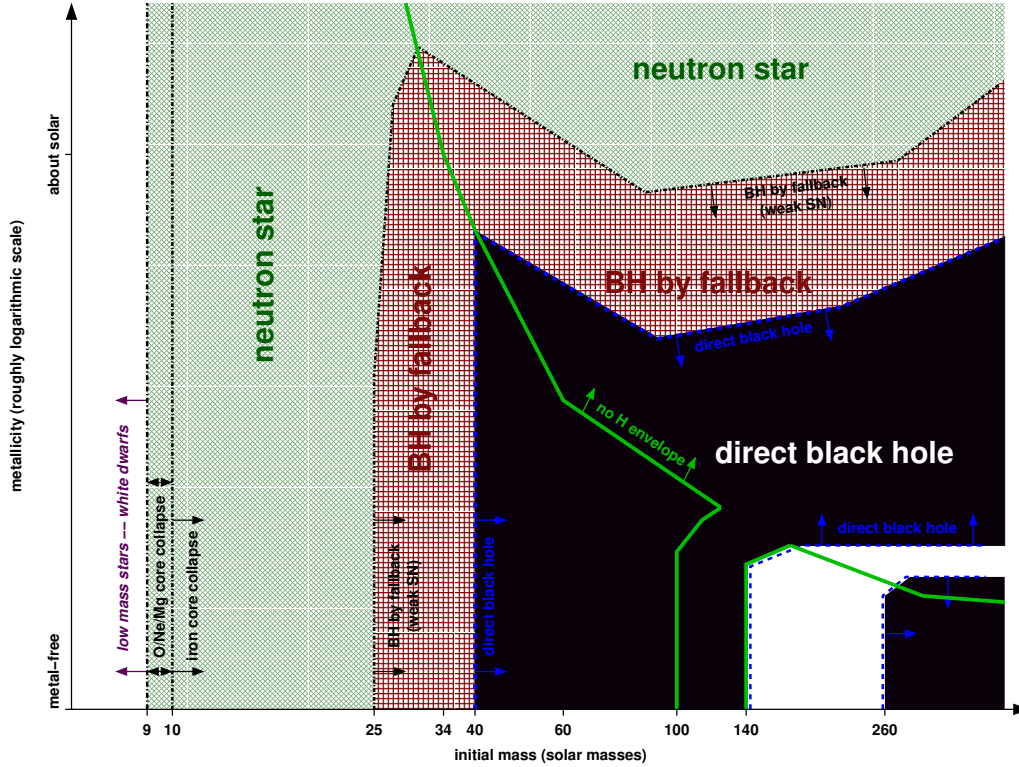


**Figure 5.1:** The fate of the stars as a function of their initial mass and metallicity. The diagram is taken from (Heger et al. 2003).

eventually become a WD.

For star mass  $9-10 M_{\odot} < M < 40 M_{\odot}$ , the fusion of heavier elements continues eventually leading to an Iron (Fe) dominated core. Further fusion of Fe core is not favourable as Fe has highest binding energy per nucleon. The photons produced in the earlier stages, disintegrate the heavy nuclei back into nucleons. The extremely dense core cannot be held by the electron degeneracy pressure, therefore the core starts to collapse. Electrons start to merge with protons creating neutrons and neutrinos ( $p^+ + e^- \rightarrow n + \nu$ ). Neutrinos carry away immense amount of energy, further supporting the inwards collapse as they have a low interactive rate and cause a Supernova (SN)-explosion. Now, there are two possibilities: first, for  $9-10 M_{\odot} < M < 25 M_{\odot}$ , the core predominantly consists of neutrons and therefore their degeneracy pressure comes into picture, which can hold the further core collapse and forms a Neutron Star (NS) (Gruppen 2005). Second, for  $25 M_{\odot} < M < 40 M_{\odot}$ , even the neutron degeneracy pressure is not capable of holding the core from further collapse, therefore a stellar mass Black Hole (BH) is formed.

For mass ranges  $40 M_{\odot} < M < 140 M_{\odot}$  or  $M > 260 M_{\odot}$ , the core is already so massive that no SN-explosion occurs, as a Black Hole (BH) is formed directly. Lastly, for the mass range  $140 M_{\odot} < M < 260 M_{\odot}$ ,  $\gamma$ -rays are produced and creates  $e^{\pm}$  pairs, which lead to a pressure

drop and results in a partial inward collapse. The partial collapse is followed by a thermonuclear explosion that disintegrate the star completely and no remnant is formed. More details can be found in (Heger et al. 2003).



**Figure 5.2:** Chandra image of composite SNR G21.5-0.9 (Matheson & Safi-Harb 2010). Young pulsar J1833-1034 (Gupta et al. 2005; Camilo et al. 2006) is shown at the center circularly surrounded by diameter  $\approx 1'.5$  PWN and diameter  $\approx 5'$  SNR shell.

In conclusion, the stellar remnants can be a WD, SN-explosion (with a NS or BH) or direct BH formation. After the SN-explosion, the ejected material interacts with the Interstellar Medium (ISM) and forms a Supernova Remnant (SNR). The SNRs can be divided mainly into three categories, namely *shell-like SNRs*, *plerions* and composite. Shell-like SNRs form a shell-like structure while interacting with the ISM. The *plerions* or *PWNe* are the objects which are centrally filled in all wavelengths and contain an object constantly injecting particles and energy. The *composite* system show both of these features. An example of such a composite system of SNR G21.5-0.9 (Matheson & Safi-Harb 2010) is shown in Figure 5.2, where a nicely circularly symmetric system of pulsar PSR J1833-1034 (Gupta et al. 2005; Camilo et al. 2006) is at the center surrounded by its PWN and SNR respectively. I will go into more details on the NS/pulsars and PWNe in the next sections, as I will be using this information in Chapter 6 to study 2HWC J2019+367 in a PWN scenario.

## 5.2 Pulsars

Present understanding of pulsars is that they are the rapidly rotating Neutron Star (NS). The birth of NS is briefly described in Section 5.1. The mass density of NS is similar to that of an atomic nucleus. NSs have a typically assumed radius of  $\sim 10$  km, density of ( $\rho$ )  $10^{17}$  kg/m<sup>3</sup> and mass

between 1.4 to 3  $M_{\odot}$ . During the formation of the NS, both the magnetic flux ( $\Phi_B = BR^2$ ) and angular momentum ( $L = I\omega$ ) are conserved. Where  $I$  is the moment of inertia,  $B$  is the magnetic field density,  $R$  is the radius of the object and  $\omega$  is rotation speed. Both,  $\omega$  and  $B$  are  $\propto 1/R^2$ . Due to the conservation of  $L$  and  $\Phi_B$  as the radius of the star decreases to form a NS, both  $\omega$  and  $B$  increases dramatically. Therefore, NS are highly magnetised and rapidly rotating objects with a period of 1 ms to 10 s. NS and its association with SN explosion was first postulated by (Baade & Zwicky 1934). However, the first detection of NS was as a pulsar by (Hewish et al. 1968).

Pulsars produce a pulsating signal by rotating their magnetic fields through space. The first detection of the pulsar was in the form of a periodic radio signal. The detected object was PSR J1919+21 with a period of 1.337 s. Back then, objects with such fast rotational speeds were unknown in astrophysics. The association of NS and a pulsar is explained by the observation of pulsars in the centres of SNRs and also at such high rotational speeds the object has to be as dense as a NS, otherwise it would disintegrate. Soon after the discovery of the first pulsar, a NS associated explanation of the central engine powering the Crab Nebula was given by (Pacini 1968). The explanation was given in the context of the magnetic dipole moment of a rotating NS. A loss in the rotational energy and therefore increase in the observed period was predicted. The prediction was soon after observed and confirmed by (Richards & Comella 1969).

### 5.3 Pulsar Models

The pulsed signal from pulsars is due to the misalignment of the magnetic field and the rotational axes. An electric field is generated at the surface of a pulsar by the rotating magnetic field, which in turn accelerate charged particles at the surface. The charged particles then move along the magnetic field lines and produce synchrotron and curvature radiation (see section 1.3.1.3). The emitted EM radiation (synchrotron and curvature) is beamed and polarised due to alignment to the magnetic field axis as the magnetic field is stronger in this direction. A schematic of pulsar magnetosphere is shown in Figure 5.3, where the pulsar rotational and magnetic field axis, magnetic field lines and different regions of EM radiation emission (will be discussed in more details in Section 5.4) are depicted.

#### 5.3.1 Spin-Down Luminosity

The spin-down luminosity of a pulsar is a measure of the energy loss rate of a pulsar. The pulsar slows down or loses its energy (mainly the rotational energy) in the form of EM emission or of high-energy particles. The rotational energy loss is primarily through the generation of relativistically moving and magnetised wind. It can be computed as a function of the pulsar period ( $P$ ), change in  $P$  with time ( $\dot{P}$ ) and the moment of inertia ( $I$ ) as (Gaensler & Slane 2006):

$$\dot{E} = -\frac{dE}{dt} \equiv 4\pi^2 I \frac{\dot{P}}{P^3} = I\Omega\dot{\Omega}, \quad (5.1)$$

where  $I$  is typically  $10^{45}$  g/cm<sup>2</sup> and the rotational angular frequency  $\Omega = \frac{2\pi}{P}$ . The value of  $\dot{E}$  for the observed pulsar population are in the range of  $10^{28}$  to  $10^{39}$  erg/s. For the Crab pulsar the



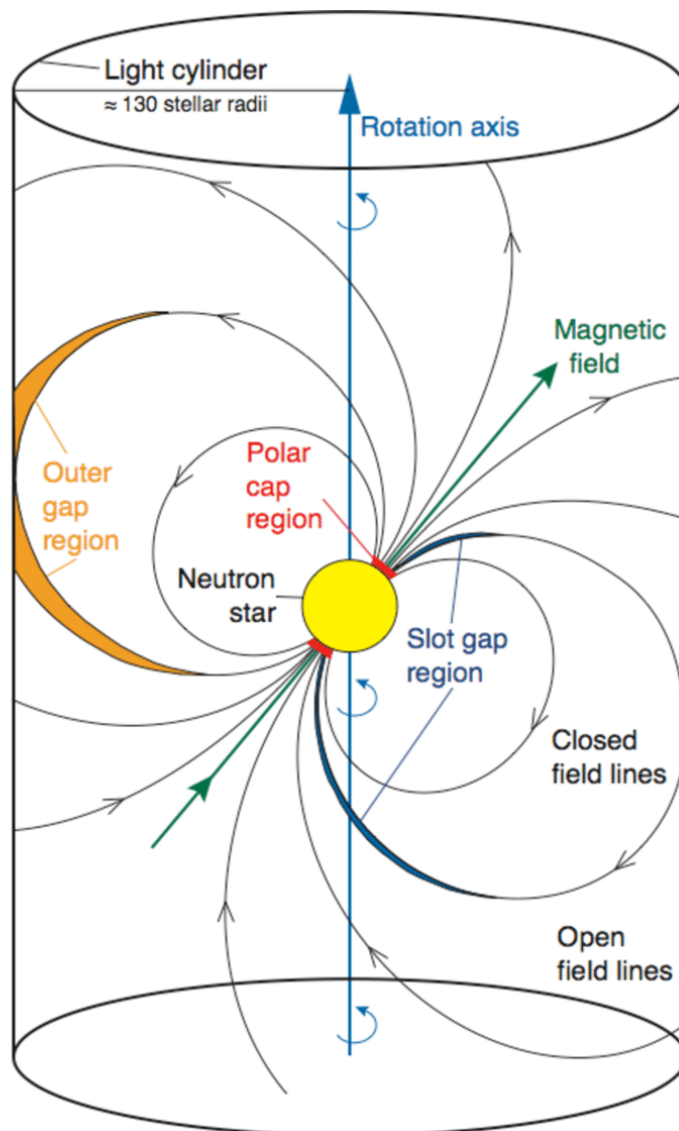


**Figure 5.3:** Schematic of a pulsar and its magnetosphere, with the magnetic field and rotational axes misaligned. The different regions of the Electromagnetic (EM) radiation production namely: polar cap, slot gap, and outer gap are shown. The co-rotating magnetic field lines with the light cylinder boundary are also depicted. The diagram is taken from (Aliu et al. 2008).

value of  $\dot{E}$  is  $\approx 5 \times 10^{38}$  erg/s and for the slowest known pulsar PSR J2144-3933 it is  $3 \times 10^{28}$  erg/s (Manchester et al. 2005). The PWNe are only created by pulsars with a  $\dot{E} \geq 4 \times 10^{36}$ .

### 5.3.2 Age of the System

The age of the pulsar can be calculated using the values of  $P$  and  $\dot{P}$ , which is subject to certain assumptions. If we assume that the pulsar spin-down from an initial period  $P_0$  such that  $\dot{\Omega} = -k\Omega^n$ . Where  $n$  is known as the “braking index” of the pulsar and  $k$  is a constant and can be

inferred as:

$$n = \frac{\Omega \ddot{\Omega}}{\dot{\Omega}^2} \quad (5.2)$$

Typically,  $n$  has a value between 2 and 3. The age ( $\tau$ ) of the pulsar can be inferred using the equation (5.3) (Manchester & Taylor 1977).

$$\tau = \frac{P}{(n-1)\dot{P}} \left[ 1 - \left( \frac{P_0}{P} \right)^{n-1} \right] \quad (5.3)$$

The initial period  $P_0$  is usually unknown. So, if we assume  $n = 3$  for the braking index which corresponds to purely magnetic dipole radiation and  $P_0 \ll P$ . The characteristic age ( $\tau_c$ ) of the pulsar is defined as:

$$\tau_c \equiv \frac{P}{2\dot{P}} \quad (5.4)$$

The assumption of  $P_0 \ll P$  is not specifically true for young pulsars. The other assumption being  $n = 3$ . That is why the value of  $\tau_c$  is usually an overestimation of the true age of the pulsar.

### 5.3.3 Surface Magnetic Field Strength

The surface magnetic field strength of a pulsar can be estimated using the value of  $P$  and  $\dot{P}$  as in equation (5.5) (Gaensler & Slane 2006).

$$B_p \equiv 3.2 \times 10^{19} (P\dot{P})^{\frac{1}{2}} \text{Gauss}, \quad (5.5)$$

The magnetic field inferred from equation (5.5) lies in a range of  $10^8$  to  $10^{15}$  Gauss.

### 5.3.4 Time Evolution of Pulsar Parameters

The parameters of the pulsar  $\dot{E}$ ,  $P$  and magnetic field ( $B$ ) also changes with time ( $t$ ). They are crucial to understanding the dynamical behaviour of the pulsar properties. If we assume, a pulsar begins its life with the initial values of period ( $P_0$ ), spin-down luminosity of ( $\dot{E}_0$ ) and magnetic field ( $B_0$ ) for a constant value of the braking index ( $n$ ), one gets the following equations 5.6 5.8 5.9 for the  $P$ ,  $\dot{E}$  and  $B$  evolution respectively with time (Pacini & Salvati 1973a; Gaensler & Slane 2006).

$$P(t) = P_0 \left[ 1 - \left( \frac{n-1}{2} \right) \frac{t}{\tau_c} \right] = P_0 \left( 1 + \frac{t}{\tau_0} \right)^{\frac{1}{n-1}} \quad (5.6)$$

Where

$$\tau_0 \equiv \frac{P_0}{(n-1)\dot{P}_0} = \frac{2\tau_c}{n-1} - t \quad (5.7)$$

represents the spin-down time-scale and  $t$  represent the present time.

$$\dot{E}(t) = \dot{E}_0 \left( 1 + \frac{t}{\tau_0} \right)^{-\frac{n+1}{n-1}}, \quad (5.8)$$

$$B(t) = B_0 \left( 1 + \frac{t}{\tau_0} \right)^\alpha, \quad (5.9)$$

where  $\alpha$  is the B-field parameter which usually takes a value of 0.5 (Venter & de Jager 2007).

### 5.3.5 Distance to the Pulsar

There are various different ways to estimate the distance to the pulsar. The most widely used one is the dispersion measurement (DM) method. Other methods involve the X-ray emission produced by the pulsar and there are also “pseudo distance” measurement using the pulsed  $\gamma$ -ray emission from the pulsar. The pulsed emission frequencies get dispersed over time while travelling from the pulsar location to the observer. The magnitude of dispersion is correlated to the free electron density ( $\rho_e$ ) in the line of sight. Therefore, with increasing distance and electron density the amount of experienced dispersion also increases. The DM is defined as:

$$\text{DM} = \int_0^d \rho_e dl, \quad (5.10)$$

where the integral is calculated over the electron density distribution along the line of sight over the path length travelled by light ( $l$ ) and the distance to the pulsar is  $d$ . However, the caveat to that is the free electron density ( $\rho_e$ ) in the line of sight is not known accurately, therefore the estimated distance using dispersion measurement can be far off the actual value.

## 5.4 Pulsar Magnetosphere and $\gamma$ -ray Emission

It can be seen using equation (5.5) that pulsar withholds a strong magnetic field. Therefore the rotating magnetic field generates a strong electric field on the surface of the NS. This electric field is strong enough to overcome the gravitational force at the surface. The interior body of a NS can be considered as a perfect conductor, therefore charges are built at the surface. The electric field is now able to pull the charged particles away from the surface (Goldreich & Julian 1969). These Charged particles are believed to initiate  $e^\pm$  cascades in the strong electric field and travel along the magnetic field lines, creating a particle plasma and forming the pulsar magnetosphere. The particle density in the pulsar’s magnetosphere, given by Goldreich-Julian density ( $\rho_{\text{GJ}}$ ) is defined as in equation (5.11) (Kirk et al. 2009).

$$\rho_{\text{GJ}} = \frac{\mathbf{\Omega} \cdot \mathbf{B}}{2\pi c} \quad (5.11)$$

Here,  $\mathbf{\Omega}$  is the angular speed and,  $\mathbf{B}$  is the strength of the magnetic field and  $c$  is the speed of light in vacuum.

The plasma of the charged particle’s is bound to co-rotates with the pulsar along the magnetic field lines. As the distance increases from the centre of the pulsar the speed of the particles also increases to be co-rotating with the pulsar. This distance then has to be limited by the maximum speed attainable by the particles, that is the speed of light. This builds a cylindrical boundary

around the pulsar of radius ( $R_L$ ), known as the *light cylinder*. It also sets the boundary of the magnetosphere from the center of the pulsar, the region beyond till the termination shock is then termed as the *wind zone*. The particle travelling along the open field lines can escape the magnetosphere to the wind zone while still retaining some of the magnetic field as shown in Figure 5.3.

The accelerated charged particles in the magnetosphere and beyond also emit pulsed  $\gamma$ -rays. The location of this emission is still a matter of debate with several models. However, the reasoning behind them argues the acceleration of the  $e^\pm$  by the strong electric fields generated in certain locations where the charged particle density is reduced. As shown in Figure 5.3 the main locations are the polar cap, slot gap, and outer gap regions.

In the polar cap model the emission region is explained to be at the poles and close to the surface ( $\sim 30$  km) of the NS. In this case, the strong acceleration of the charged particles near to the poles is responsible for the reduced particle density. The  $\gamma$ -rays produced by the curvature radiation of the  $e^\pm$  (Sturrock 1971; Arons & Scharlemann 1979). The slot gap model is similar to the polar cap model and considered to be an extension. In this case, the strong acceleration of the particles happens along the closed magnetic field lines but away from the poles. It creates a potential gap above the poles while approaching the last closed field lines (Scharlemann et al. 1978). This potential gap can generate EM cascades and hence  $\gamma$ -rays (Arons 1983).

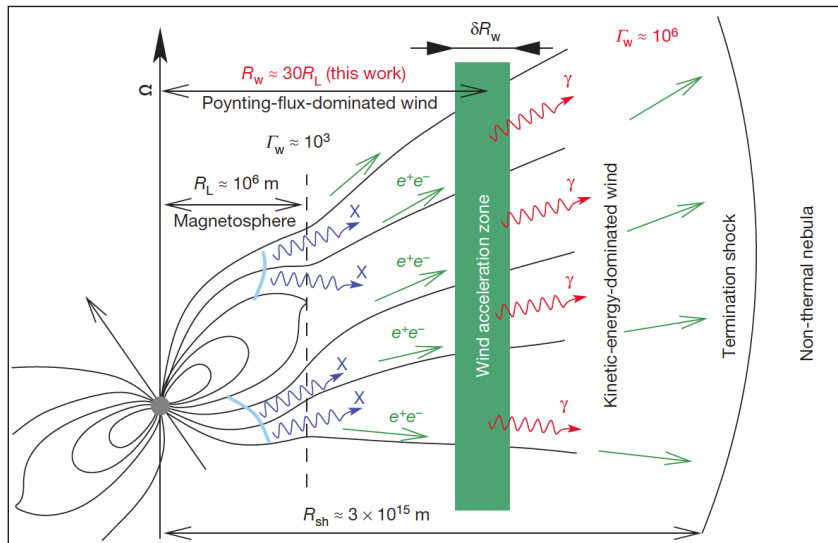


**Figure 5.4:** Schematic showing the wind zone model, X-ray coming from the magnetosphere is accelerating the  $e^\pm$  present in the wind zone. Which later emit  $\gamma$ -rays in the wind acceleration zone. The diagram is taken from (Aharonian et al. 2012).

In contrast to the polar cap and slot gap model, in the outer gap model the reduced particle density is achieved by the particle escape at the boundary of the light cylinder (Cheng et al. 1986) as shown in Figure 5.3. The  $e^\pm$  get accelerated due to the strong electric field present and emit  $\gamma$ -rays from the curvature radiation. The observations for the young pulsars is successfully explained using the outer gap model. The emission from the Crab pulsar is also explained by

adding IC scattering of the  $e^\pm$  pairs created by the  $\gamma$ -rays with the present radiation field density (Hirotani 2011, 2013), later producing higher energy  $\gamma$ -rays.

Finally, there is the wind zone model, in which, the emission region is proposed to be inside the wind zone (Kirk et al. 2002). The explanation given in this case is the VHE  $\gamma$ -ray emission due to the IC scattering of the X-ray photons with the  $e^\pm$  existing in the wind. These X-ray photons are the ones which are produced inside the magnetosphere and/or near to the pulsar. The range of wind zone emission region is thought to be between 20 to 50  $R_L$  with respect to the pulsar position (Aharonian et al. 2012). The schematic diagram is shown in Figure 5.4. More details can be found in (Kirk et al. 2009).

### 5.5 Pulsar Wind Nebulae

The class of cosmic objects which consists of magnetised particle winds generated by a central pulsar, radiating across the EM spectrum are known as the PWNe. The PWN of the Crab pulsar being the first such observed source, where the nebula was first presumed (Minkowski 1942; Pacini 1967) and later firmly associated with the observed pulsations from the central pulsar (Cocke et al. 1969; Staelin & Reifenstein 1968). To explain the observations the first attempts of the theoretical models was made by (Pacini & Salvati 1973b). Over the last several decades many such sources have been identified, making them the largest population of the galactic objects in TeV sky. But still, there remain many unresolved questions pertaining to the nature, formation, and evolution of these objects.

#### 5.5.1 Formation and Evolution

In Figure 5.5 a schematic of *composite systems* is shown, where the SNR contains a pulsar and its PWN. The SNR having the energy budget of  $\sim 10^{51}$  erg, much larger than that of a PWN over its lifetime  $\sim 10^{49}$  erg, does not get affected by the PWN significantly. However, the PWN evolution has a significant influence from the SNR.

After the SN explosion, the first stage is the *free expansion phase*, which lasts for about 1000-3000 yrs, Crab nebula being one such example. In this stage, both the SNR and the PWN expand freely. The SN ejecta moves outwards, shocking the ISM and forming the early stage of the SNR. The luminosity of the pulsar is constant and very high. The PWN starts forming from the supersonic particle wind coming out of the light cylinder to the wind zone. The wind zone medium has low density because of the evacuation of the material by the SNR. At the edge of the PWN, a thin shell of compressed material forms the termination shock. The expansion velocity of the SNR is  $\sim 50$ -300 km/s and that of the PWN is  $\sim 10^3$  km/s, both of which are very high compared to the kick velocity of the pulsar which is about  $\sim 10$  km/s. Therefore the pulsar remains roughly at the centre of the SNR (see Figure 5.2) (Bucciantini 2008). The spherically symmetric expansion of the PWN can be described from equation (5.12) (Chevalier 1977).

$$R_{\text{PWN}} \approx 1.5 \dot{E}_0^{\frac{1}{5}} E_{10}^{\frac{3}{10}} M_{\text{ej}}^{-\frac{1}{2}} t^{\frac{6}{5}} \quad (5.12)$$

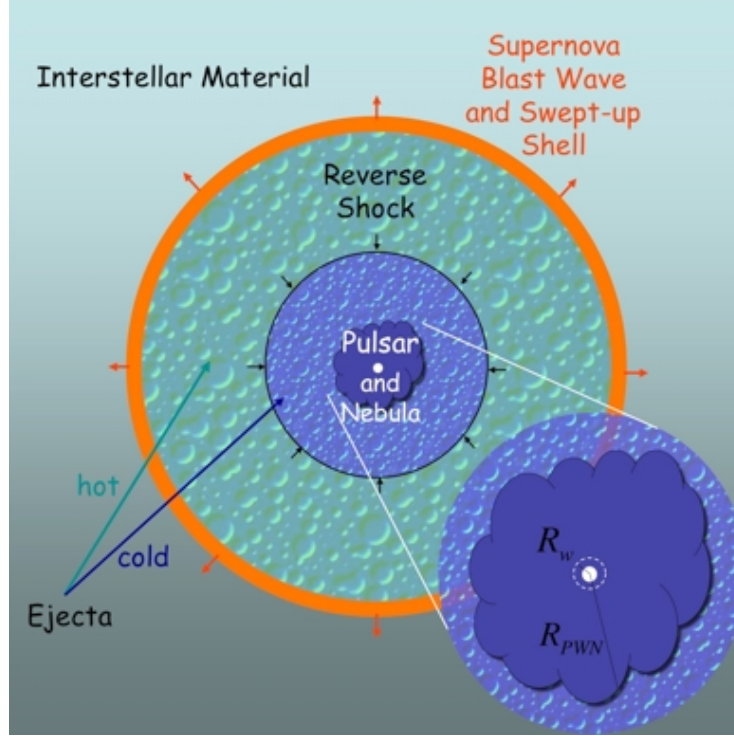


**Figure 5.5:** A schematic of a composite SNR showing the SNR boundary, the swept-up ISM shell, the central pulsar, and its PWN. The diagram is taken from (Gaensler & Slane 2006).

Where  $R_{\text{PWN}}$  is the radius of the PWN at time  $t$ ,  $E_{\text{SN}}$  and  $M_{\text{ej}}$  being the kinetic energy and the ejected mass released in the SN respectively. Solving this for a typical PWN give the value of the order of a few parsecs.

Next is the *Sedov-Taylor phase*, in which the SNR has now swept up significant mass equivalent to its own mass and the energy is conserved and is equally partitioned between kinetic and thermal contributions (Truelove & McKee 1999). Now, apart from the forward shock of the SNR, the reverse shock comes into the picture. The forward shock compress and heats the ambient gas and the reverse shock decelerates it and the instabilities are formed. Initially the reverse shock also moves forward but eventually, it starts moving inwards. It can reach the center of the SNR, in this case, the pulsar position in a time (see equation (5.13)) (Reynolds & Chevalier 1984).

$$t_{\text{Sedov}} \approx 7 \left( \frac{M_{\text{ej}}}{10M_{\odot}} \right)^{\frac{5}{6}} \left( \frac{E_{\text{SN}}}{10^{51} \text{ergs}} \right)^{-\frac{1}{2}} \left( \frac{n_0}{1 \text{cm}^{-3}} \right)^{-\frac{1}{3}} \text{ kyr} \quad (5.13)$$

The PWN collides with the reverse shock and it gets largely compressed, which increases the pressure and results in a sudden expansion. The system oscillates several times in this fashion and this phase is known as the *reverberation phase* lasting for about a few thousand years. It also increases the nebular magnetic field which synchrotron cool the highest energy electrons. The so-called Rayleigh-Taylor instabilities are also formed causing the filament-like structure and mixing of thermal and non-thermal material in the PWN. The existing proper pulsar motion

## 5. INTRODUCTION TO PULSAR WIND NEBULAE

makes the situation even more complex. The reverse shock collides with the PWN and owing to the asymmetrical nature of the PWN and of the reverse shock it can lead to highly distorted system morphology.

Finally, the reverberation phase ends and the supernova shock dissipates, the pulsar can form again a steadily expanding bubble. The new location of the PWN can be shifted because of the drift and asymmetric crushing effects as described before. It can produce a new PWN at the current location leaving behind a “relic PWN” (see Section 5.5.2).

After  $10^7$ - $10^8$  yrs, the last phase starts. The pulsar now has no more energy to power the PWN. Depending on the proper motion of the pulsar; if it is slow moving the PWN keep on growing adiabatically otherwise for the fast-moving pulsars they escape the original SNR position and form bow-shock nebulae, because of the interaction of the pulsar wind with the ISM. More details can be found in (Gaensler & Slane 2006) and the references therein.

### 5.5.2 Relic Nebula

As described above the relic nebulae are the one where the pulsar position is observed to be slightly shifted from the nebula. This is because the pulsar’s proper motion and has started forming a new nebula around its current position which it got after the reverberation phase has ended. Observationally, the relic nebulae are distorted radio PWN. The particles in the relic nebula have already synchrotron cooled, therefore reducing the X-ray emission. Although the X-ray emission can still be seen at the new location of the pulsar. The IC scattering continues to

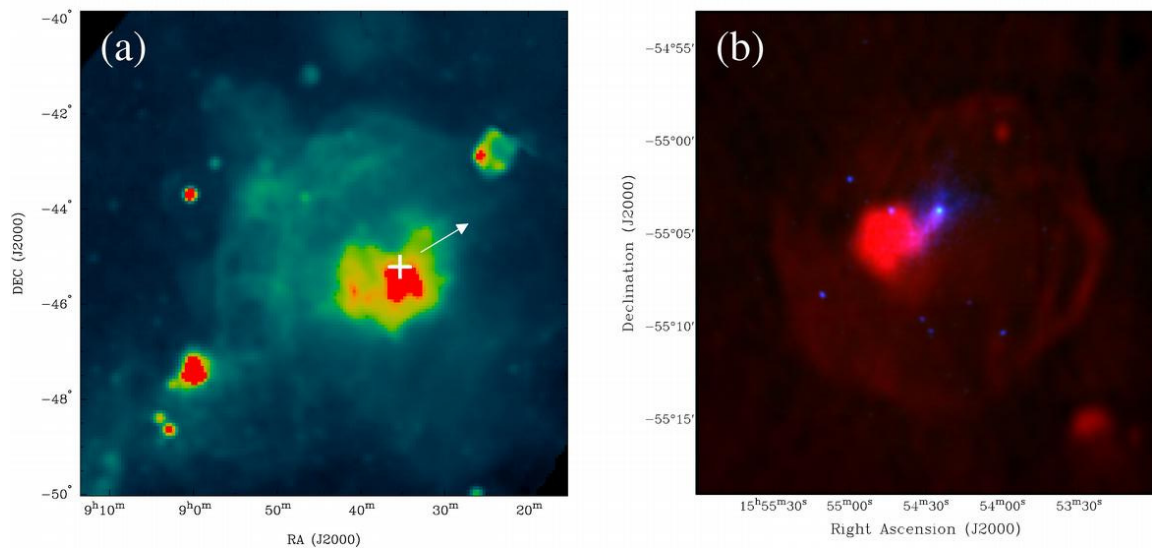


**Figure 5.6:** Left panel: Vela SNR in the radio band. The shell of the SNR and the PWN at the central part are shown. The cross indicates the location of the pulsar and the arrow is showing the direction of its proper motion. Right panel: showing the composite SNR G327.1-1.1. Radio shell SNR and PWN are shown in red the blue color is showing the X-ray emission of a yet undetected location of the pulsar. The diagram is taken from (Gaensler & Slane 2006).

take place because that typically requires less energetic particles than the synchrotron producing

X-rays. Therefore the size of the nebula in the TeV energies is larger than in the X-rays. However, given more time, the particles have travelled farther and have been cooled, even the TeV emission starts to diminish. It finally results in a large oddly shaped nebula with the pulsar being located at one side of it. In Figure 5.6 two examples of such systems are shown. More details can be found in (Mitchell 2016) and the references therein.

## 5.6 Multi-wavelength Emission from PWNe

When the pulsar wind interacts with the ISM it forms the termination shock, where injected particles coming from the wind zone can get accelerated to higher energy. These particles then produce radiative emission which can be divided into two categories: synchrotron and IC (see Sections 1.3.1.3 and 1.3.1.2). The synchrotron emission from PWNe ranges from radio to soft  $\gamma$ -rays. The IC emission covers the range of soft  $\gamma$ -rays till multi TeV energies. The different emission regions of a PWN are depicted in Figure 5.7.

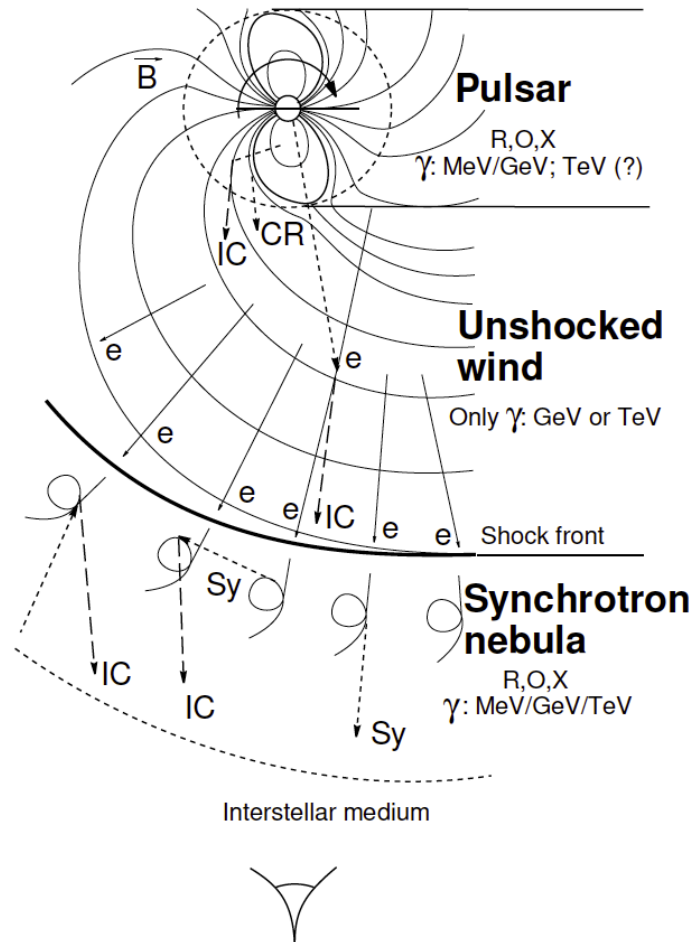


**Figure 5.7:** Schematic showing the different regions of PWN emission with corresponding mechanisms. The diagram is taken from (Aharonian et al. 2004).



## 5. INTRODUCTION TO PULSAR WIND NEBULAE

---

The synchrotron emission is characterised by the nebular magnetic field. A constant injection of particles from the pulsar to the termination shock can be defined as a power-law electron spectrum. While these electron travel through the magnetic field they are subject to the synchrotron cooling. The interplay between the strength of the magnetic field and the cooling causes a spectral break at the synchrotron emission. The spectral break frequency can be computed as in equation (5.14) (Ginzburg & Syrovatskii 1965).

$$\nu_b = 10^{21} \left( \frac{B_{\text{PWN}}}{10^{-6}\text{G}} \right) \left( \frac{t}{10^3\text{yrs}} \right)^{-2} \text{ Hz} \quad (5.14)$$

Where  $B_{\text{PWN}}$  is the nebular magnetic field and  $t$  is a given moment in time. The cooling time decides the size of the nebula at different frequencies. The cooling time is inversely proportional to the parent electron energy. From the synchrotron cross-section, we know that the frequency of the emitted photon  $\nu \propto E_e^2$  (see Section 1.3.1.3). So it can be concluded that the size of the nebula decreases with increasing frequency of the emitted photon (see Figure 5.8).



**Figure 5.8:** A composite image of the Crab nebula depicting X-ray (blue), optical (green) and radio (red). It can be seen that the size of the nebula decreases from radio to X-ray. The picture is taken from (Gaensler & Slane 2006).

The IC emission from a PWN is much larger in size than the synchrotron nebula. The IC scattering requires relatively lower energy electrons than for the synchrotron emission, which has longer cooling time-scales and hence can travel farther. The IC emission comes from all over the nebula. It occurs with the ambient photon density fields present as well as with the ones generated by the synchrotron emission. The former is mainly consist of CMB (uniformly

distributed), Far Infrared (FIR), IR, optical (present due to star-light and dust) and Ultraviolet (UV), latter additionally can contain X-ray (due to synchrotron emission).

The IC emission can range up to multi-TeV energies. The first PWN detected in TeV  $\gamma$ -rays is Crab Nebula (Weekes et al. 1989). Presently several other PWNe has been discovered. The TeV emission clearly indicates the presence of particles being accelerated to considerable energies. By the multi-wavelength studies of these sources, many interesting unresolved questions are being answered, such as the acceleration mechanisms of these particles, their propagation mechanisms and the magnetic and radiation field densities present in the vicinity etc. More details can be found in (Lopez-Coto 2015; Zanin 2011) and the references therein.

## 5.7 PWN Modelling

There are two main approaches to model the emission from PWNe, the Magnetohydrodynamic (MHD) and the energy-spectrum model. MHD models are proven to be suitable to study morphology. The energy spectrum models are utilized to describe the spectral behaviour. The MHD models are based on the relativistic description of the pulsar winds before and after the termination shock. The first attempt was made by (Rees & Gunn 1974) and the approach was further developed by (Kennel & Coroniti 1984). It assumes the simple spherical symmetry of the pulsar wind distributions. MHD models are able to explain the nebular size decrease with increasing frequency, the observed Rayleigh-Taylor instabilities and can also describe the steepness of the observed synchrotron spectrum. In later developments of the MHD approach, the photon fields were also taken into account to explain the IC emission.

The energy-spectrum modelling approach applies the time-dependent diffusion-loss equation for the evolution of the lepton population inside the PWN (Syrovatskii 1959). This lepton population interacts with the nebular magnetic and radiation fields and produces the photon spectrum. The one-dimensional energy spectral models do not take into account the energy-dependent morphology. Nevertheless, energy-spectrum models are proven to be successful in explaining the observed spectral behaviour over the entire energy range from the synchrotron to IC emission.

As described in Section 5.6, the PWNe show emission in a broad energy range and can be divided into two main parts: the synchrotron and IC emission. A typical example of the Crab Nebula spectrum is shown in Figure 5.9. The distinct synchrotron and IC peaks can be seen on the left and right side of the spectrum respectively. It can be seen that both the modelling approaches, MHD and energy-spectrum (in this case, with constant B-field) models describe the observed nebular emission in the whole energy range reasonably well.

On the far left side of the plot, the radio emission is shown. The radio synchrotron emission shows a power-law behaviour, with the radio flux  $S_\nu \propto \nu^\alpha$ . Where  $\nu$  is the frequency of the radio emission with a spectral index of  $\alpha$  which takes values in range of  $-0.3 \gtrsim \alpha \lesssim 0$ . The radio luminosity ( $L_R$ ) in a range of 100 MHz to 100 GHz are of the order of  $10^{34}$  erg/s. The conversion efficiency of pulsar  $\dot{E}$  to radio luminosity is of the order  $\eta_R \equiv L_R/\dot{E} \approx 10^{-4}$  (Frail & Scharringhausen 1997). There is an additional spectral feature at the IR frequencies as shown in Figure 5.9 with the dot-dashed line. It is explained with the galactic dust component emitting in FIR frequencies (Neugebauer et al. 1984). In the optical range, the emission flux also takes a

## 5. INTRODUCTION TO PULSAR WIND NEBULAE

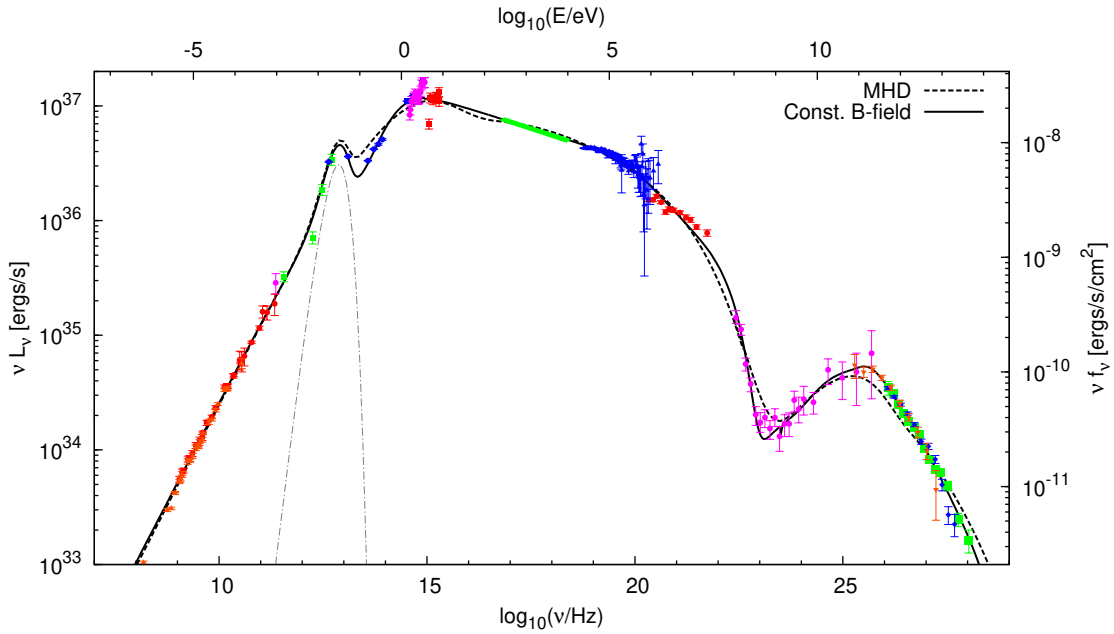


**Figure 5.9:** The observed spectrum (by different instruments) of the Crab nebula ranging from radio to tens of TeV  $\gamma$ -ray energies. Results from both the modelling approaches, MHD and spectral modelling (with constant B-field) are shown. The Figure is taken from (Meyer et al. 2010).

power law with typical spectral indices of  $-1$  to  $-0.5$ . Lastly, the X-ray synchrotron emission is well described by a power-law as  $N_E \propto E^{-\Gamma}$ . Where  $N_E$  is the photon flux at a given energy  $E$  and  $\Gamma$  is the spectral index. The value of  $\Gamma$  is typically  $\approx 2$ . The integrated X-ray luminosity in the range of  $0.5 - 10$  keV is typical of the order  $\eta_X \equiv L_X/\dot{E} \approx 10^{-3}$  (Becker & Truemper 1997).

In the IC emission regime, the spectral behaviour is well-modelled owing to the fact that the present radiation field densities are usually well known. The spectral shape is usually a power law, however, in some cases, it can take other shapes as log-parabola. At the highest energies where the KN-effect comes into picture, the IC flux can take a curved shape (see Section 1.3.1.2). The target radiation fields taken into account are usually CMB, IR, optical and synchrotron radiation present in the nebular region. The synchrotron radiation is responsible for the Synchrotron Self Compton (SSC) emission, which can have a dominant effect in IC emission in young systems. The CMB radiation is ambient present and therefore contributes the IC emission in the entire energy range. However, CMB plays a crucial role in the highest energies around  $100$  TeV. This is because at the highest energies the interaction between the electron population and radiation fields is mainly dominated by CMB. The IR and optical radiation fields are present due to dust and starlight respectively, both of which contribute to the IC emission. In star-forming regions, where the IR and optical radiation field densities are higher, they can contribute to the IC emission significantly. The IC emission is almost model-independent of the pulsar parameters, except for the young pulsars. However, it can be dominated by one or the other components of the IC emission depending on the specific system properties. More details can be found in (Meyer et al. 2010; Gaensler & Slane 2006; Lopez-Coto 2015; Zanin 2011) and in the references therein.



# 6

## Spectral and Morphological Studies of 2HWC J2019+367

2HWC J2019+367 is one of the most prominent high energy sources seen by HAWC in the Cygnus region. In HAWC dataset, it shows significant emission above 56 TeV reconstructed energy. 2HWC J2019+367 is the counterpart of VER J2019+368 in the HAWC sky-maps. In the previous works, it has been associated with the PSR J2021+3651 and its X-ray pulsar wind nebula. But still, the nature of the source remains unsettled, owing to its extended complex  $\gamma$ -ray emission region. In this Chapter, I introduce 2HWC J2019+367 and investigate its energy-dependent and overall morphology together with its spectrum. With these results, I perform the spectral modelling of 2HWC J2019+367 together with X-ray data to investigate the expected  $\gamma$ -ray pulsar wind nebula properties of the system.

### 6.1 Introduction

The Cygnus region is a prominent site of star formation. As a consequence, it is one of the brightest and most complex high energy emission region in our Galaxy. Star-forming regions contain a rich variety of potential particle accelerators such as pulsars, PWNe, SNRs, OB associations and Wolf-Rayet (WR) stars (Piddington & Minnett 1952; Uyaniker et al. 2001). The stellar remnant such as pulsars, PWNe and SNRs have been clearly associated with the VHE particle acceleration (Ginzburg & Syrovatskii 1964) (see Section 5.1). It is also suggested that star-formation can also generate ample kinetic power to accelerate particles up to very high energies through winds from WR and OB stars and from the binary and collective star systems, however, the observational evidence is still lacking (Lemoine-Goumard et al. 2011). In the past, the multi-wavelength

studies of the Cygnus region have been performed in radio, Infrared (IR), X-ray and multi-TeV  $\gamma$ -rays. The region is observed as the brightest diffuse  $\gamma$ -ray source in the northern hemisphere in GeV (Hunter et al. 1997) and multi-TeV energies (Aliu et al. 2014).

Several bright and extended TeV  $\gamma$ -ray sources in the vicinity of the Cygnus region have been identified in the observations of the MILAGRO observatory (Abdo et al. 2007a). The brightest source in the region is MGRO J2019+37 with a measured flux of about 80% of the Crab Nebula flux at 20 TeV (Abdo et al. 2012). MGRO J2019+37 has a large extent of about  $1^\circ$ , therefore it overlaps with several SNRs, HII regions, WR stars, high-energy  $\gamma$ -ray ( $> 100$  MeV) sources, and the hard X-ray transient IGR J20188+3647. A young energetic radio and  $\gamma$ -ray pulsar PSR

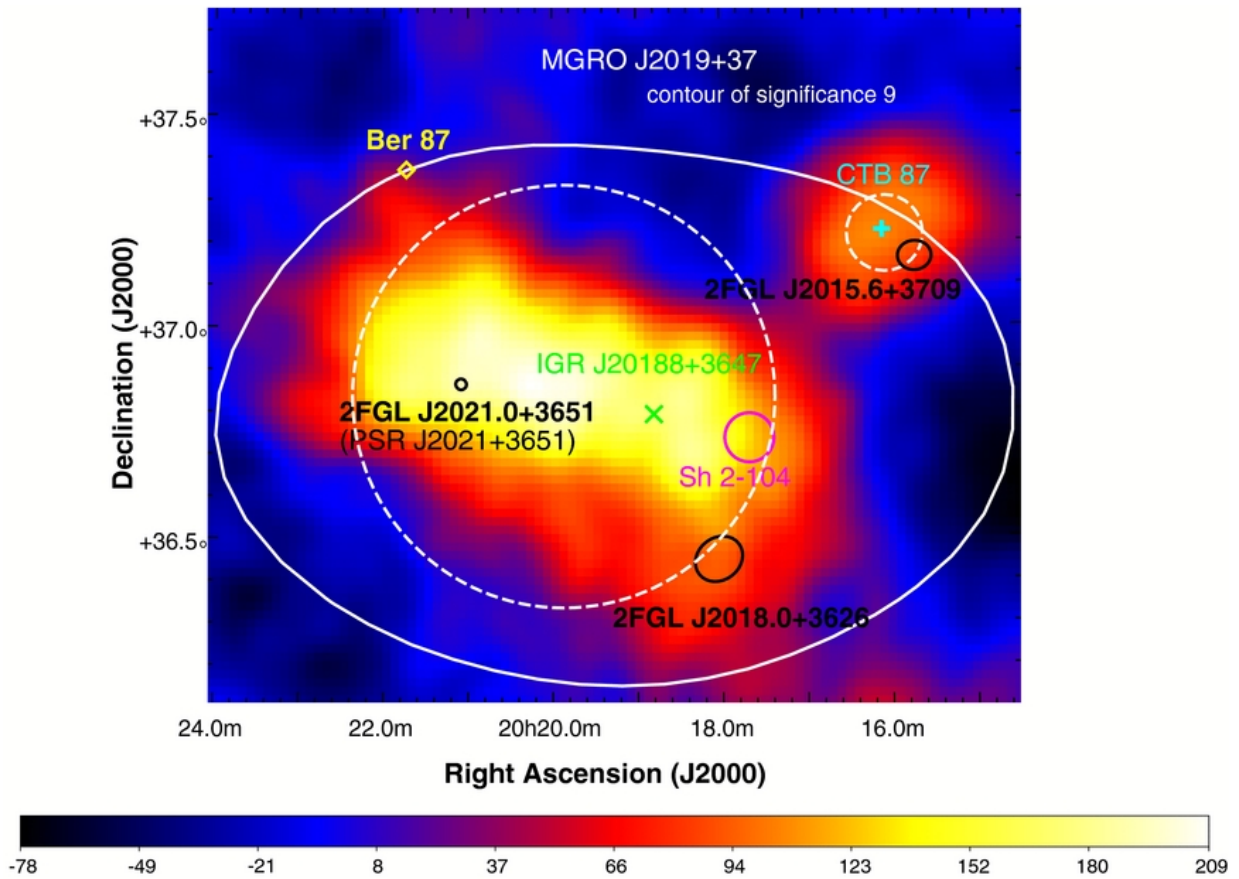


**Figure 6.1:** The excess count map of MGRO J2019+37 region observed by VERITAS above 600 GeV. The shift from blue to red colour occurs at a  $3\sigma$  level. Two sources, VER J2019+368 the bulk of the emission and VER J2016+371 are clearly resolved. The possible counterparts for both the sources are marked. The  $9\sigma$  contour of MGRO J2019+37 is also overlaid. Two circles with dashed lines show the regions used for the spectral analysis. The Figure is taken from (Aliu et al. 2014).

J2021+3651 (Roberts et al. 2002; Halpern et al. 2008) and its nebula, SNR G75.1+0.2 is also in the vicinity (Abdo et al. 2007b). PSR J2021+3651 is proposed to be the main contributor to the extended TeV emission seen by MILAGRO. However, (Paredes et al. 2009) suggested that PSR J2021+3651 cannot power the whole MGRO J2019+37 region alone, and proposed

other counterparts to be massive star-forming region associated with HII region Sharpless 104 (Sh 2-104). Another proposed scenario for the VHE emission was the winds from WR stars in the young cluster Ber 87 in the Cyg OB1 association (Bednarek 2007). The MGRO J2019+37 region was later observed by MAGIC and VERITAS for short durations, collecting 15 and 10 hours of data respectively, which led to upper limits consistent with MILAGRO (Bartko et al. 2008; Kieda 2008). Soon after, the Tibet Air Shower array confirmed the VHE extended source detection with  $5.8 \sigma$  (Amenomori et al. 2008). However, ARGO-YBJ reported a non-detection and reported the upper limits and proposed that the source is variable (Bartoli et al. 2012).

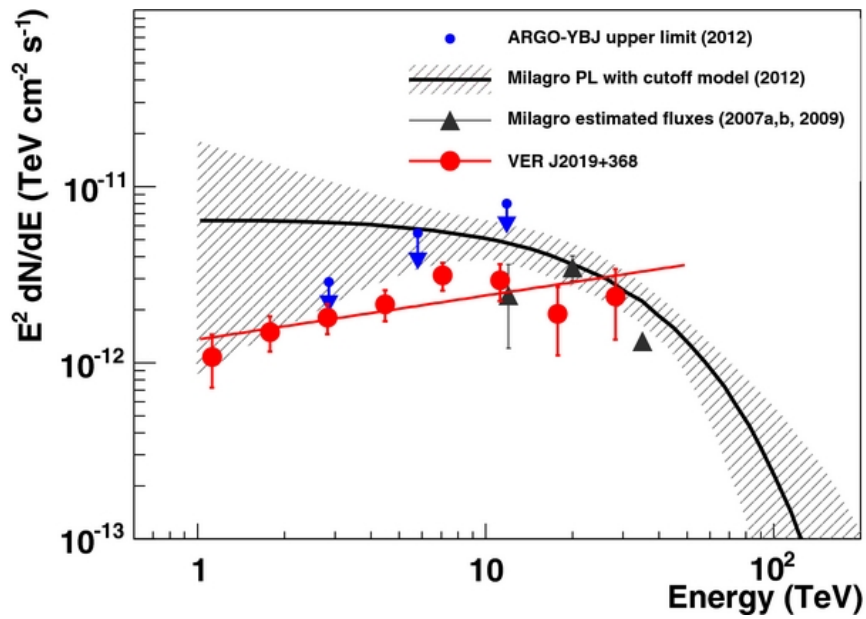


**Figure 6.2:** The spectrum of VER J2019+368 measured by VERITAS from 1 to almost 30 TeV. Spectral measurements from MILAGRO are shown in black with flux points at 12, 20 and 35 TeV and their best fit with  $1 \sigma$  band. 90 % confidence level upper limits from ARGO-YBJ are shown in blue. The Figure is taken from (Aliu et al. 2014).

A major development in the study of MGRO J2019+37 was the follow-up observation by VERITAS in (Aliu et al. 2014), a deep observation of MGRO J2019+37 of 70 hours duration spatially resolved it into two sources. In Figure 6.1, the observation of MGRO J2019+37 by VERITAS is shown. VER J2019+368 is the brighter extended source, which accounts for the bulk of the emission from MGRO J2019+37. VER J2016+371 is the other source, which is a point-like source to VERITAS. It was pointed out that the most likely counterpart of VER J2016+371 is a PWN in the SNR CTB 87. Because of the co-location of the VHE and X-ray emission as well as the X-ray/VHE luminosity. In the case of VER J2019+368, the picture still seems to be complicated. However, a PWN scenario of PSR J2021+3651 seems to be more favourable, because the X-ray morphology favours in this direction (Aliu et al. 2014; Mizuno et al. 2017a). In Figure 6.2, the spectrum measured by VERITAS and MILAGRO and the upper limits from ARGO-YBJ are shown. The hard spectral index measured by VERITAS for VER J2019+368 of  $\Gamma = 1.75$  resembling that of Vela X, another PWN system also favours this



scenario.

The region of VER J2019+368 was observed in X-rays using Chandra ACIS-S and led to the detection of an X-ray PWN G75.0.1 associated with the PSR J2021+3651 (Hessels et al. 2004). It was observed that the peak of TeV emission is offset by  $\sim 20'$ , and the measured size of X-ray PWN is  $\leq 15'$ . Due to the significantly smaller size of the X-ray PWN emission in comparison to the TeV emission of size  $\sim 1^\circ$ , it was difficult to draw any conclusion on their association. In a recent detailed spectral and morphological study of the X-ray PWN using the data from Suzaku-XIS and XMM-Newton, there is an indication that X-ray PWN and TeV emission are associated, and PSR J2021+3651 is a major contributor to the TeV emission, explaining about 80% of the emission (Mizuno et al. 2017b).

The location of the peak TeV  $\gamma$ -ray emission in VER J2019+368 is off-set from the pulsar location (Aliu et al. 2014), which is a typical behaviour in similar age PWNe systems. Addi-

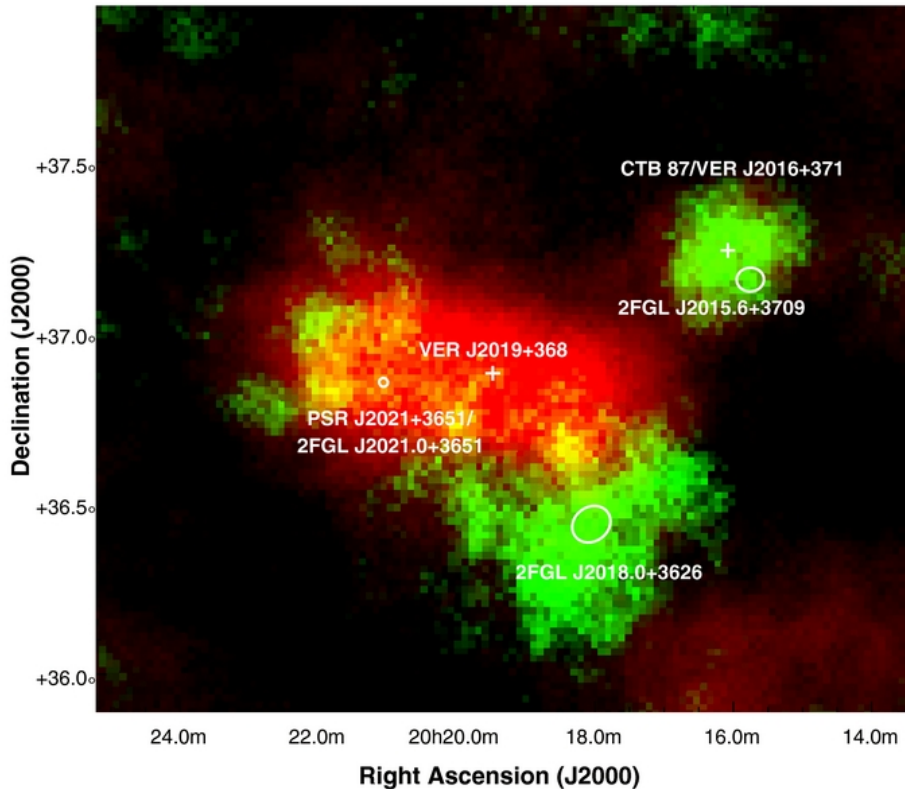


**Figure 6.3:** MGRO J2019+37 region observed by VERITAS in two energy bands, 600 GeV to 1 TeV shown in green and above 1 TeV shown in red. The Figure is taken from (Aliu et al. 2014).

tionally, the hint of energy-dependent morphology in the emission region of VER J2019+368 can be seen in Figure 6.3, where the VHE excess map of MGRO J2019+37 region observed by VERITAS is shown in two energy bands, low energy 600 GeV to 1 TeV in green and above 1 TeV in red. The higher energy emission seems to be close to the peak TeV emission of VER J2019+368, which is offset from the location of the pulsar. This behaviour can be explained as the electrons travel away from the pulsar they cool down and therefore lose energy, and/or to



energy-dependent diffusion or advection.

The Cygnus region is prominently visible in the HAWC sky-maps. 2HWC J2019+367 is the HAWC associated source to MGRO J2019+37 and VER J2019+368. The high-energy sensitivity of HAWC enables us to detect the emission in the energy range, which exceeds that of the VERITAS observations. The wide field of view of HAWC, about  $\sim 2$  sr, is very suitable for the observation of the extended sources such as 2HWC J2019+367. Therefore, in Section 6.6, we will look for the energy-dependent morphology in the TeV emission of 2HWC J2019+367. This is possible now because of the energy sky-maps available for the HAWC data, as explained in Section 6.2. The study of the energy-dependent morphology, in the wide energy range of HAWC, will contribute towards establishing the nature of the TeV emission. Additionally, the high energy sensitivity enables us to probe spectral feature such as a cut-off. Therefore in Section 6.7, we will probe the spectrum of 2HWC J2019+367. A cut-off below  $\sim 100$  TeV in  $\gamma$ -ray energies point towards a leptonic scenario, because of the suppression of the  $\gamma$ -ray emission due to KN effect (Moderksi et al. 2005).

## 6.2 Reconstructed Datasets

The previously published HAWC results (Abeysekara et al. 2017; Abeysekara et al. 2017b) up to now used the fraction of PMTs hit ( $f_{\text{hit}}$ ) for an air shower event as a proxy for the energy. More details on that can be found in Section 2.8 and in (Abeysekara et al. 2017). HAWC data were divided into so-called analysis bins ( $\mathcal{B}$ ) depending on the  $f_{\text{hit}}$  of the array which observed a non-zero signal. Although  $f_{\text{hit}}$  is in general a good parameter to know the shower size, as  $f_{\text{hit}}$  increases with increasing shower size, however, it is poorly correlated with energy. This is because of mainly two reasons: first, the observed  $f_{\text{hit}}$  for a given air shower event depends on zenith angle; second, due to the finite size of the detector array the partially contained air shower events will have a lower value of observed  $f_{\text{hit}}$  than their true size. The problem becomes more prominent at the highest energy, where the whole array is hit and also the showers are partially contained. For HAWC array, the energy is about 20 TeV where the whole array is hit. Therefore it becomes nearly impossible to distinguish a more than 20 TeV shower on the array, from a partially contained higher energy shower.

To resolve this, HAWC collaboration has recently developed energy estimation techniques. In Chapter 4 of this thesis, one of the approaches is demonstrated to perform the event-by-event energy reconstruction. In parallel, two other independent approaches, namely the Ground Parameter (GP) and Neural Network (NN) have been developed (Stephens Marinelli & Goodman 2017). The approach discussed in this thesis was motivated by a desire to improve the overall reconstruction and also merge the outrigger and main array reconstruction. Therefore this technique might be used for energy reconstruction, while performing the combined reconstruction of outrigger and main array data. For this analysis, I will be using the reconstructed data from the other two mentioned techniques, by taking into account their reconstructed energy information.

### 6.2.1 Energy Estimators

The two energy estimator approaches used in this study are Ground Parameter (GP) and Neural Network (NN). The GP algorithm does the energy estimation utilising the charge density at an optimum distance from the shower axis. It is primarily based on the method developed for the Pierre Auger Observatory as described in (Newton et al. 2007), with required modifications due to the smaller size of the HAWC array.

The NN algorithm is based on an artificial neural network. It estimates the energy of the primary  $\gamma$ -ray photon utilising the several quantities computed as a part of standard HAWC event reconstruction. It employs the Toolkit for Multivariate Analysis (TWVA) NN implementation as described in (Hoecker et al. 2007). The detailed description of the energy estimators and their performance will be described in an imminent publication by HAWC collaboration.

The energy estimation technique described in Chapter 4 could not be used due to ongoing developments, to take into account the recently collected data using the trigger array. Additionally, the air shower reconstruction chain of HAWC will be upgraded soon, to utilise the different newly developed reconstruction techniques. Afterwards, the optimisation and validation of analysis cuts will be performed, taking into account all the different reconstruction algorithms. It is pragmatic to perform the optimisation only once, after making the final decision on all the different reconstruction techniques to be taken into account.

### 6.2.2 Quality Cuts

As a result of the studies performed on the energy estimation techniques, the dataset used for GP and NN might differ from the standard  $f_{\text{hit}}$  dataset. The  $f_{\text{hit}}$  dataset used in this analysis is similar to the 2HWC catalogue as described in (Abeysekara et al. 2017b), except now it has been extended to 1017 days (33.3 months) taken between 26-11-2014 and 20-12-2017. Whereas in 2HWC catalogue it was for 17 months. The applied quality cuts are the standard HAWC quality cuts described in Section 2.8.

The full HAWC observatory was inaugurated in March 2015, however, HAWC took data prior to the inauguration with variable WCDs raging from 250 to 300. The dataset used for the energy estimators were collected between June 2015 and December 2017. It has a total live-time of 837 days ( $> 90\%$  uptime). In contrast to the  $f_{\text{hit}}$  dataset, the partial array dataset was not used. Another loss of live-time is due to the days when the detector was not operational due to maintenance or operational difficulties. A small amount of dataset was also removed where a large variation was observed in the zenith angle distribution, indicating that the detector was unstable.

Only the showers reconstructed inside the array are taken into account. This is because, for the off-array events the performance of the energy-estimators degrades. Removing the off-array events also leads to better angular resolution. Additionally, only events with reconstructed zenith angle  $< 45^\circ$  were taken into account. In contrast to  $f_{\text{hit}}$  dataset, to determine the shower size, only those non-zero PMT hits were taken into account which were within 20 ns window of the shower plane (for more details see Section 2.7). This reduced the number of noise hits in the shower size of a given event. The  $\gamma$ /hadron separation parameters are the same as for  $f_{\text{hit}}$  as

described in Section 2.6.3. However, they have been optimised for datasets obtained for GP and NN separately. The optimisation scheme is same as for  $f_{\text{hit}}$  as described in Section 2.8. The optimisation is done on the 2D binning scheme, in which, the dataset for NN and GP is binned in reconstructed energy bins together with the  $\mathcal{B}$  bins.

### 6.2.3 Binning

To include the reconstructed energy, a 2D binning scheme of energy bins in combination with the  $\mathcal{B}$  bins is used. 2D binning was used instead of only binning in reconstructed energy, mainly because the  $\gamma$ /hadron separation is very much dependent on the event shower size. As shown in Figure 6.4, similar to previous standard  $f_{\text{hit}}$  binning, 9  $\mathcal{B}$  bins were used in combination with 12 bins in reconstructed energy, which makes a 2D grid of total 108 bins. The energy bins are defined over an energy range of 316 GeV to 316 TeV. The bins are equispaced in  $\log_{10}(\text{Energy}/\text{GeV})$ , with each bin spanning over a quarter decade. Not all the 108 bins are occupied, therefore in practice the GP has 54 and NN has 50 bins in total.

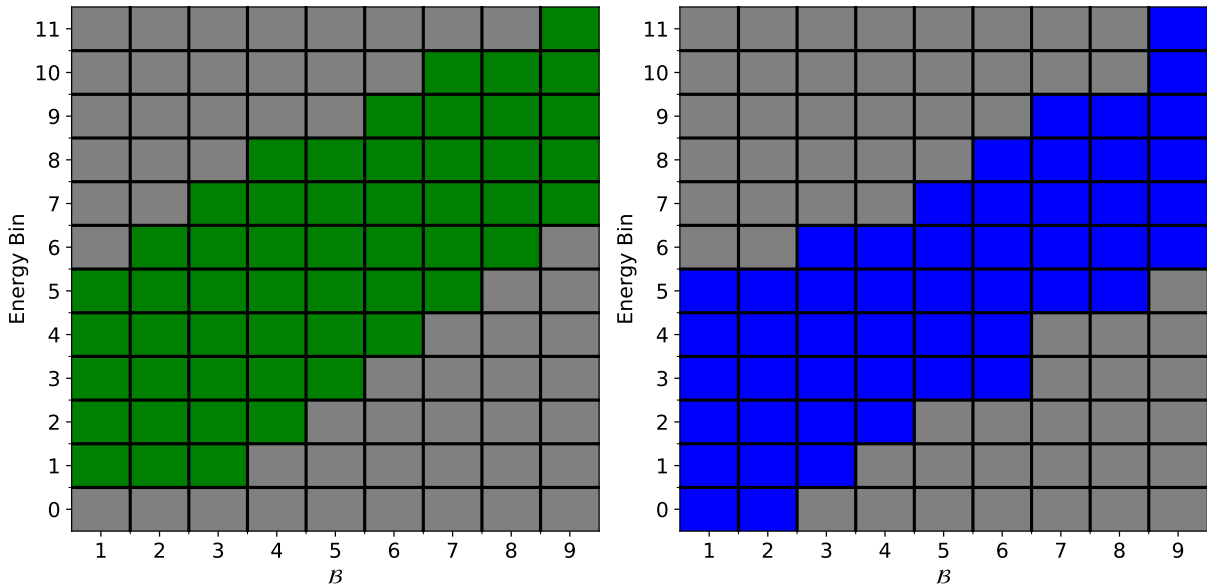


**Figure 6.4:** Occupied bins for GP and NN energy sky-maps are shown in the left and right panels in green and blue respectively. Out of 108 total number of bins, the number of occupied bins was 54 and 50 for GP and NN respectively. The empty bins are shown in grey.

Similar to  $f_{\text{hit}}$  sky-maps, where nine data and background maps are produced following the procedure described in Section 2.11, sky-maps for GP and NN dataset are produced for all the occupied bins. Therefore, for clarity, I will refer to the sky-maps using the  $f_{\text{hit}}$  dataset and binned in only  $\mathcal{B}$  bins, as  $f_{\text{hit}}$  sky-maps. To make a distinction, from hereafter, the sky-maps produced using the energy estimators will be called as energy sky-maps, while referring to both of them together, otherwise with GP and NN sky-maps separately.

The PSF is calculated for each 2D bin corresponding to GP and NN dataset, following the same procedure as described in Section 2.9. Similarly, using the simulation the detector response

function is obtained for both the energy estimator datasets. The detector response function (see Section 2.10) will be used to simulate the desired source with given properties together with the estimated background (see Section 2.11). Same procedure will be applied to obtain a model source to perform the spectral and morphological fit against the obtained data using a binned-likelihood technique for 2HWC J2019+367, as described in Section 6.7.

### 6.3 Slice Profiling Tool

To make the slice profiles on the sky-maps, I developed a tool within the HAWC framework. In Figure 6.5, an example is shown for a slice profile, which is centred at the location of Crab Nebula with a position angle of  $30^\circ$ . For brevity, from hereafter I will refer to the Crab Nebula as Crab. Although the orientation does not matter for the point sources, however, for other sources

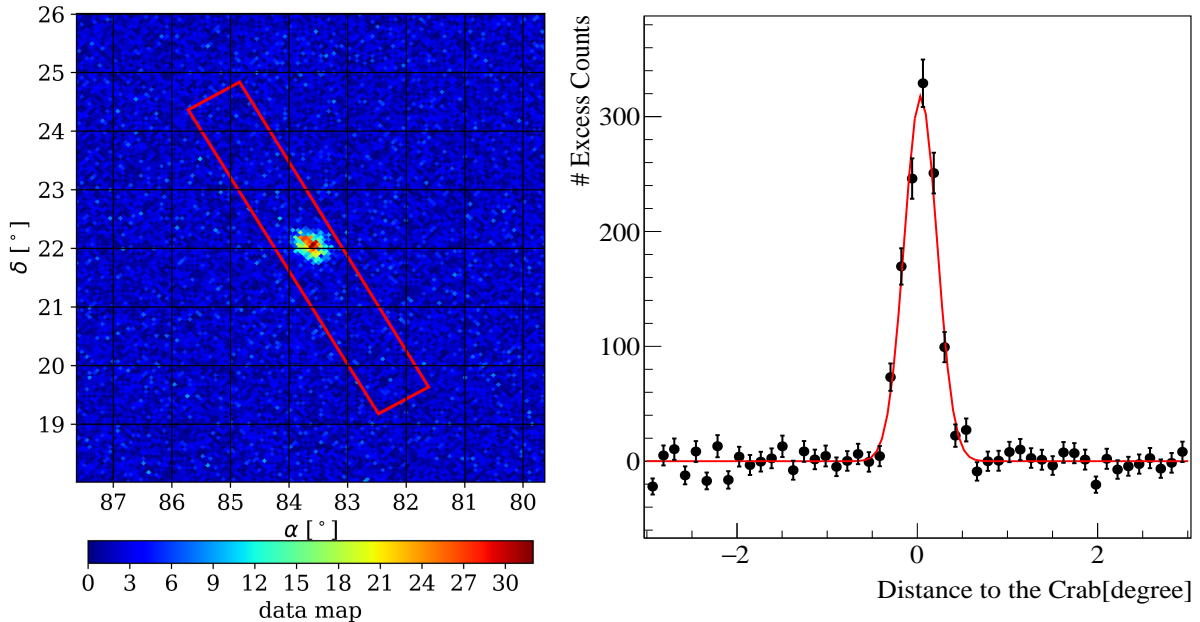


**Figure 6.5:** Example of slice profiling for the HAWC Crab data. In the left panel, the sky-map corresponding to  $\mathcal{B} = 7$  bin is shown with the slice definition drawn in red. In the right panel, the excess count profile extracted from the slice along the direction parallel to the length is shown. The excess counts profile is fitted with a Gaussian, shown in the red curve.

where a desired direction in the source morphology is required (for 2HWC J2019+367), it is possible to do that by using this slice profiling tool. One can get the excess counts profile over the background by using the slice profiles as shown in Figure 6.5 (right panel). For a point source, the excess counts profile can be fit with a Gaussian, the one sigma width of the fitted Gaussian is an equivalent measure of the PSF, which will be denoted as  $\text{PSF}'$  from hereafter.

For this example, the length of the slice is  $6^\circ$  which is divided into 50 equispaced equal solid angle bins, so that, the width at the Crab location is  $1^\circ$  and the bins are perpendicular to the direction of rotation. The slice characteristics such as length, width, and number of bins can be

changed. However, it is to be noted that the bin size should be larger than the resolution of the sky-map pixels, to avoid the binning effects. The sky-maps properties used in this analysis are the same as described in Section 2.11. These sky-maps are made using the HEALPix scheme of  $N = 1028$ , which corresponds to the mean pixel spacing of  $0.05^\circ$ . In this example, the bin size and spacing is  $0.12^\circ$ , which is larger than the mean pixel spacing of the used sky-map. From hereafter unless it is mentioned otherwise, I will use the same slice characteristics for point sources, except the position angle will be zero, therefore the slice will be parallel to the equal longitude lines.

## 6.4 Systematic Studies

In principle, the slice profiles can be made on each of the energy bins to study the spacial changes of a source morphology, however, there are following features that need careful considerations:

- ⊙ The PSF changes with the shower size in a given energy bin.
- ⊙ For a given source and energy bin, not all the  $\mathcal{B}$  bins contribute equally to the significance.

When studying morphology, it is desirable to obtain the best PSF possible, without notably reducing the significance in a given energy range. In order to do so, in a given energy bin the  $\mathcal{B}$  bins are excluded which do not contribute significantly to the significance, and have the worse PSF. To decide on which 2D (energy/ $\mathcal{B}$ ) bins to be excluded, one could make the selection study on a bright source such as Crab. However, the PSF of HAWC is declination dependent as described in Section 2.9. Therefore the selection on the 2D bins to be valid in other declinations the comparison of PSF is required at different declinations. As we do not have a bright source like Crab at different declinations, the simulation of sources is required. This also brings the necessity to check the consistency of PSF between data and simulations. Therefore, the problem in hand can be divided into the following segments:

- ⊙ Check the consistency between the data and the simulated source in different declinations.
- ⊙ Verify that the selection made on excluding the 2D bins is valid at different declinations.

### 6.4.1 Data and Simulation Comparison

First to check the consistency of PSF in data and simulation at different declinations, point sources, the Crab Nebula and Markarian 421 (Mrk 421) are used. The latitude of HAWC Observatory is about  $19^\circ$  and the Crab has a declination of about  $22^\circ$ , therefore the Crab passes almost through the zenith. Crab is a very bright point source to HAWC and is therefore an excellent source to check the consistency between the data and simulation. Mrk 421 is another point source to HAWC at a declination of about  $38^\circ$ , which is similar to the declination of 2HWC J2019+367 of about  $37^\circ$ . I have simulated point sources at different declinations, using the detector-response function (see Section 2.10) and the background information from the data maps as described before in Section 6.2.3. Point sources at declinations of Crab and Mrk 421 from data and simulation

are utilised to compare the consistency between data and simulations. This study is performed for both of the energy-estimator datasets, the GP and NN. To avoid overcrowding of plots, I will

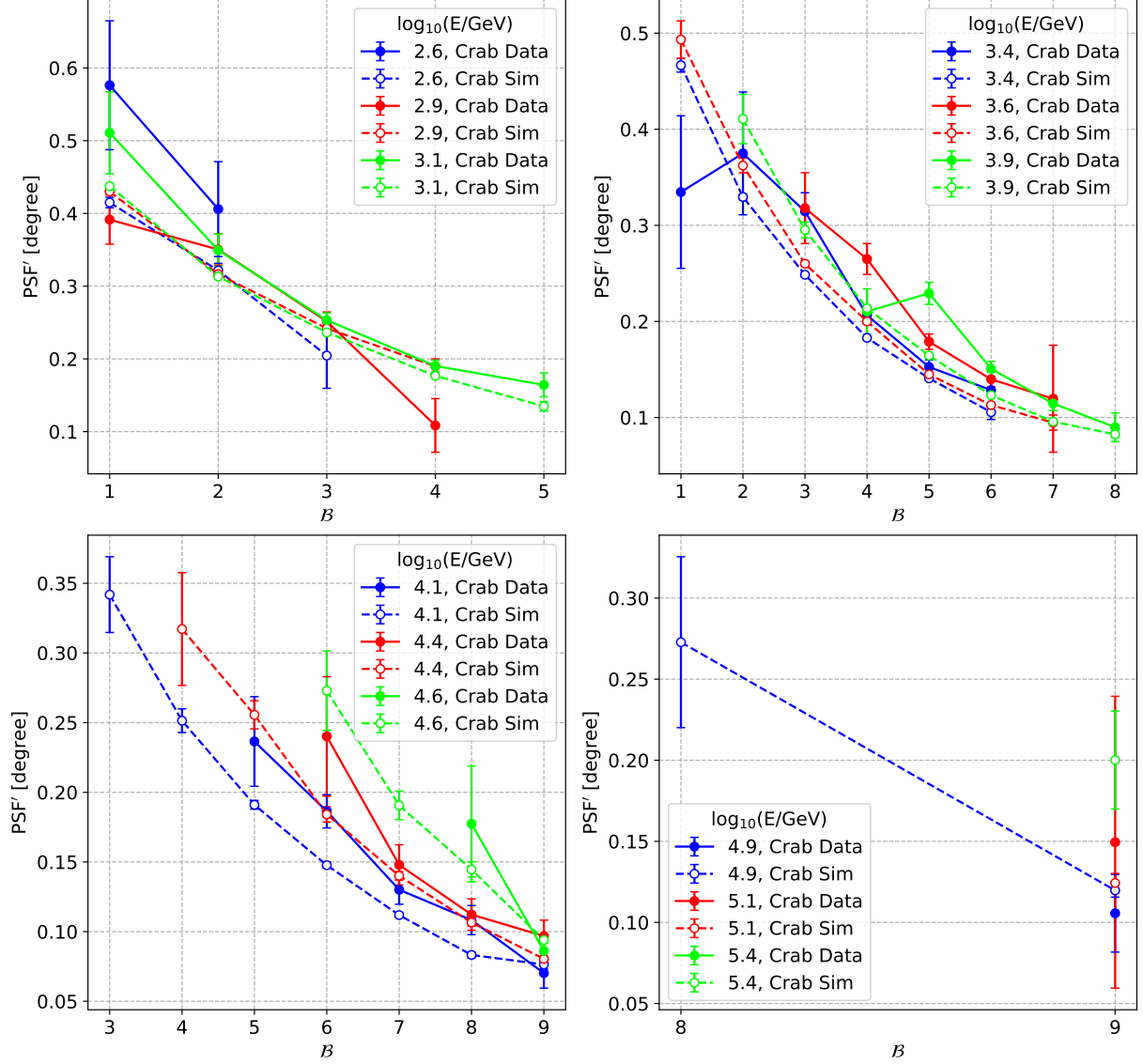


**Figure 6.6:** PSF' as a function of  $\mathcal{B}$  bins for a given energy bin. The mean energy ( $E$ ) in  $\log_{10}(E/\text{GeV})$  is denoted for each energy bin. The comparison in PSF', obtained between Crab data and simulated Crab is shown for all energy bins, 3 energy bins per plot with increasing energy. PSF' is obtained using the slice profile tool as described in Section 6.3. To ensure a sensible fit of the Gaussian a condition of the number of background counts  $>0$  and number of excess counts  $>3$  in the  $1\sigma$  width of the fitted Gaussian was imposed. The results are shown for GP. The corresponding plots for NN are shown in Figure A.3.

show some of the results for only the GP, however, corresponding plots for NN are in Appendix A and will be mentioned accordingly in the text. The main results will be shown for both the datasets.

For the simulated Crab, a point source is simulated with a power law spectrum of index 2.58. Power law was used, to not limit the number of events at the highest energy bins. The spectral index of 2.58 for the simulated power law was the same as the Crab data fitted to a power law. In Figure 6.6, the PSF' comparison for Crab data and simulated Crab is shown for GP dataset (for NN see Figure A.3). The slice profiling tool is used to obtain the excess count profile and fitted with a Gaussian as described in Section 6.3. The PSF' as a function of the  $\mathcal{B}$  bins (shower size dependence) is shown in a given energy bin for the Crab data and for the simulated Crab. Each of the plots covers 3 energy bins in increasing order. In all the energy bins, there is systematically

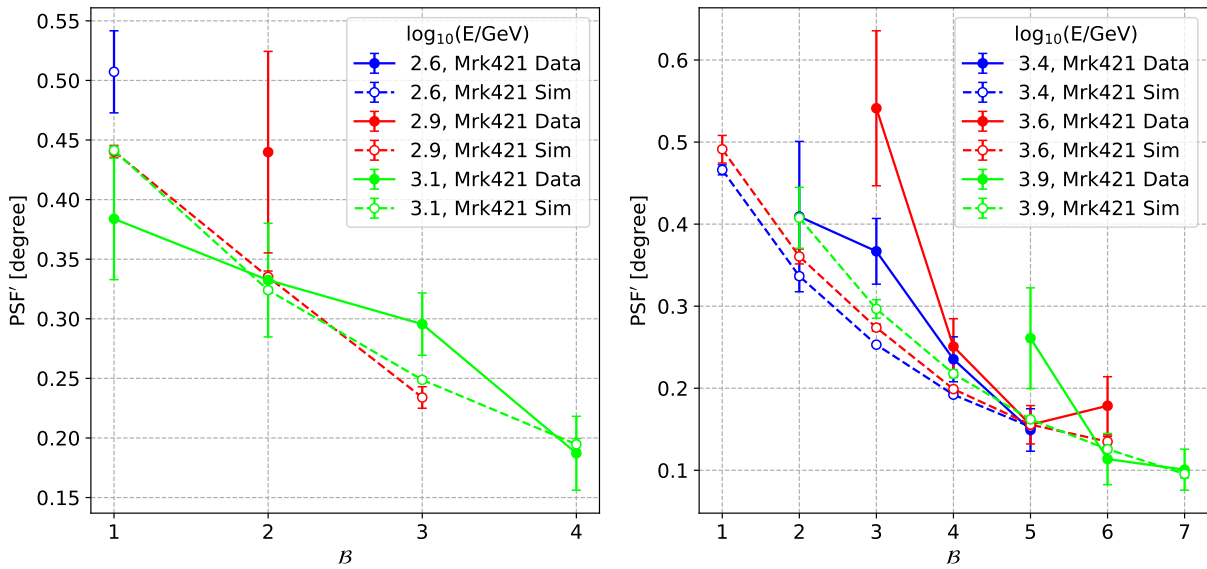


**Figure 6.7:** The description is the same as of Figure 6.6, for Mrk 421 between data and simulations. Only first 6 energy bins are shown, the last 6 energy bins for Mrk421 data were empty. The results are shown for GP. The corresponding plots for NN are shown in Figure A.4.

smaller PSF' in simulation compared to data. In most of the  $\mathcal{B}$  bins the difference is about  $\sim 0.05^\circ$ , however, in some cases, it can be higher or lower. In the last 3 energy bins (bottom left plot) there is not enough data, therefore, there are very few data points for Crab data. To verify the behaviour holds at other declinations the same comparison for Mrk 421 data and simulation is shown in Figure 6.7 for GP (for NN see Figure A.4). The Mrk 421 is simulated as a point source with power law spectrum of index 3.04. The index is obtained by fitting the data to a power law. The last 6 energy bins are not shown because there was not enough data at those energies. However, the systematic difference in PSF' similar to observed for Crab data and simulation can be seen and holds for both the energy estimators GP and NN.

## 6.4.2 Declination Dependence

In Figure 6.8, the comparison between the simulated point source at the location of the Crab and at the location of 2HWC J2019+367 is shown for GP (for NN see Figure A.5). To check the possibility of the change in PSF' because of the different simulated spectral index, I have

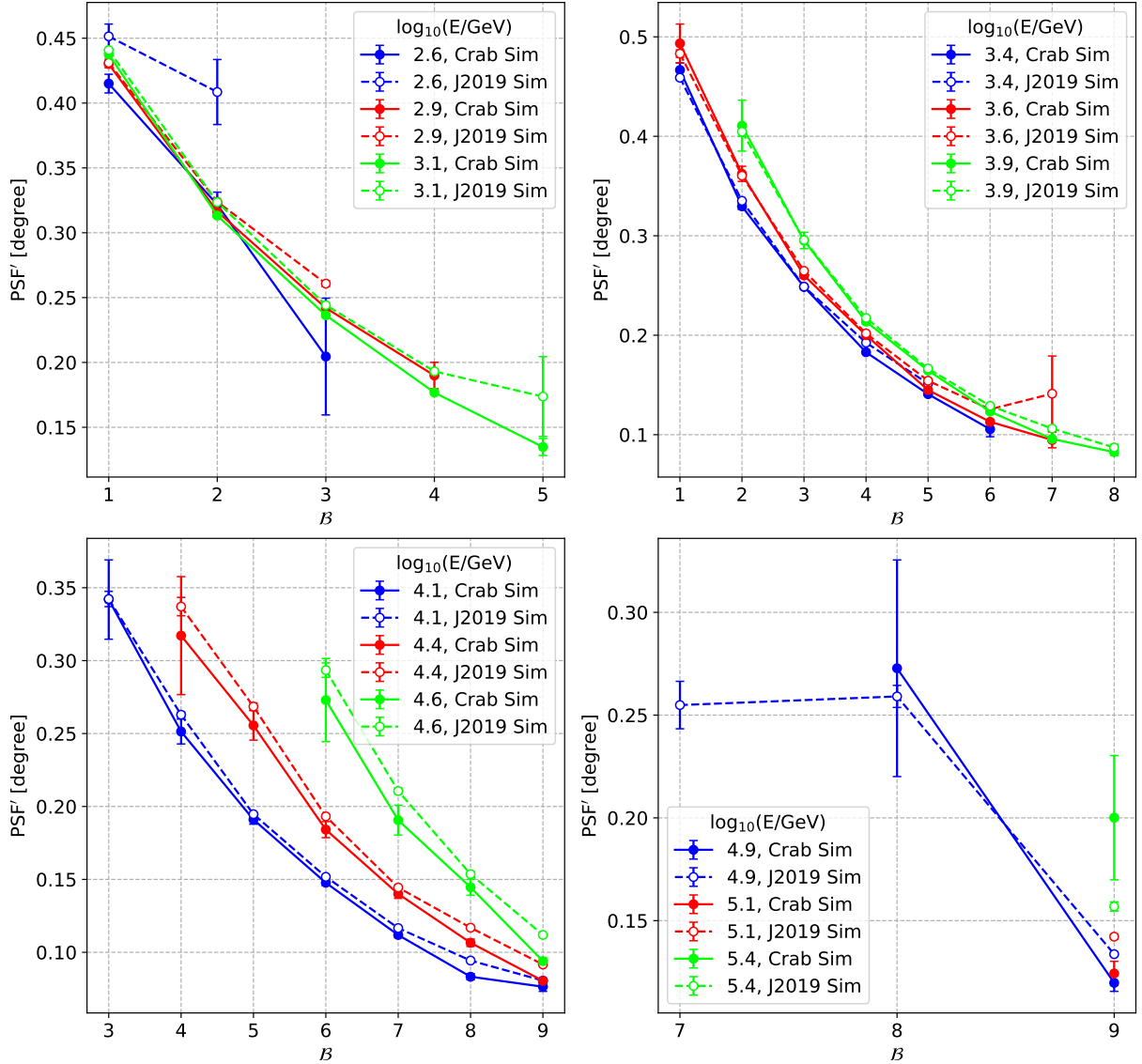


**Figure 6.8:** The description is the same as of Figure 6.6, for a simulated point source at the location of Crab and at the location of 2HWC J2019+367. The spectral index for the simulated Crab is the same as before, for 2HWC J2019+367 the spectral index is 2.2 with a simple power law. The results are shown for GP. The corresponding plots for NN are shown in Figure A.5.

simulated a spectrum index of 2.2 at the location of 2HWC J2019+367, whereas the simulated spectral index for source simulated at the location of the Crab is 2.58. Only small deviations in PSF' at two different declinations is evident in all the energy bins. Therefore, it is concluded that apart from the systematic difference between the data and simulations (see Section 6.4.1) the PSF' is not affected by the declination or the different source spectrum considerably. The results were shown only for GP, however, similar results were obtained for NN (see Figure A.5).



### 6.4.3 Energy Band Definition

It can be seen from Figure 6.6, even for data on the Crab nebula, not all the energy bins have enough excess counts, which in turn, make the uncertainties on the PSF' larger. Therefore it is not feasible to perform the slice profile analysis for other sources (dimmer than the Crab nebula) in separate energy bins in order to draw conclusions on the change in their size with energy. The grouping of energy bins in energy bands is necessary to avoid the large uncertainties in the fitted size by increasing the number of excess counts. The energy bins are grouped in a set of 3 energy bins, making four energy bands in total. The definition of energy bands with their corresponding energy ranges is given in Table 6.1.

Energy band	Combined energy bins	Energy range (TeV)
1	1, 2 and 3	0.316 to 1.77
2	4, 5 and 6	1.77 to 10
3	7, 8 and 9	10 to 56.23
4	10, 11 and 12	56.23 to 316.22

**Table 6.1:** Definition of energy bands with their corresponding energy ranges.

The first two energy bands can be understood as the soft energy bands, where most of the sources with a soft spectrum will have enough data. The last two energy bands are the hard energy bands, where we expect to see data from sources with hard spectrum.

Next, the selection of the 2D bins is done in each energy band, so that the best PSF possible is retained without losing considerably in significance. Performing this study is easier in simulated sources because of no limitations of statistics. Therefore the simulated Crab is used. Instead of making the slices and obtaining the PSF' in individual energy bins, energy bins are now combined to make energy bands. In Figure 6.9 (top panel), the PSF' as a function of the  $\mathcal{B}$  bins in different energy bands is shown. On the bottom panel, the significance (signal to noise ratio) is shown. It can be seen that the PSF' improves with increasing  $\mathcal{B}$  bin, however, the signal to noise ratio (significance) peaks at a given  $\mathcal{B}$  bin in a given energy band. Therefore it is desirable to at least retain the  $\mathcal{B}$  bins higher than the best significance  $\mathcal{B}$  bin. Which also decides the best PSF' attainable without losing notably in significance. However, for  $\mathcal{B}$  bins lower than the best significance  $\mathcal{B}$  bin, only those bins were retained which do not worsen the PSF' more than 25% than best PSF'. Although because of irregular behaviour in different energy bands, the condition was not stringent, in some cases the 25% condition can be slightly higher. The selection made is summarised in Table 6.2 and the remaining bins are depicted in Figure 6.10 (for comparison see Figure 6.4).

To access the quality of our selection the improvement in the PSF' and the amount of significance lost due to those excluded bins is shown in Figure 6.11. In the left panel, it can be seen that the PSF' reduced by  $\sim 40\%$  in all the energy bands. The lost significance was only  $\sim 15\%$ . The results are consistent in both data and simulated Crab.

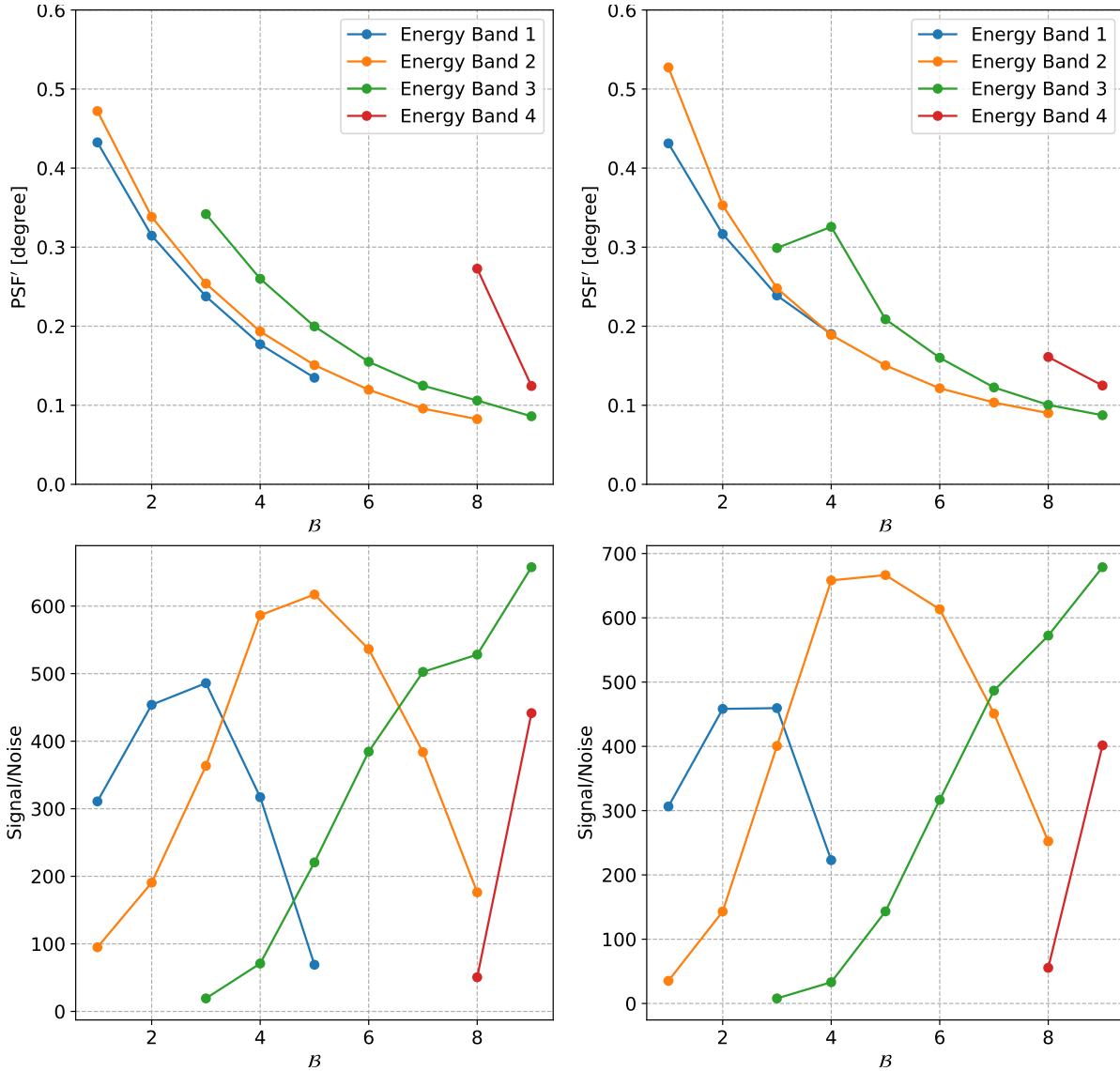


**Figure 6.9:** Top panel: The PSF' as a function of  $\mathcal{B}$  bins in different energy bands. Bottom panel: Similar to the top panel instead of PSF' signal to noise ratio is shown. The legends in top and bottom panel are the same. PSF' is obtained using the slice profile tool as described in Section 6.3. To ensure a sensible fit of the Gaussian a condition of the number of background counts  $>0$  and number of excess counts  $>3$  in the  $1\sigma$  width of the fitted Gaussian was imposed. The results are shown for simulated Crab. The plots on the left and right panel are for GP and NN respectively.

From the systematic studies, the following can be concluded. The PSF' is systematically smaller in simulations than compared to data with an order of  $\sim 0.05^\circ$ . The PSF' is only marginally affected by declination and spectrum of the source in consideration. The grouping of energy bins into energy bands is required to study the change in size with energy due to the scarcity of data in separate energy bins, therefore to reduce the uncertainty of the size measurement. The 12 energy

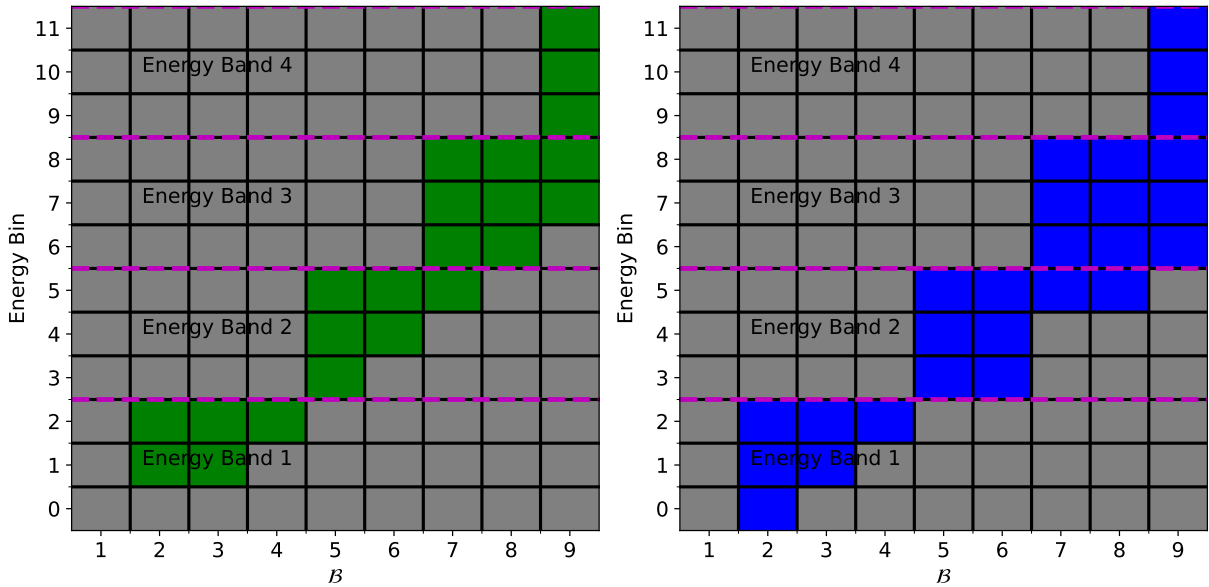


**Figure 6.10:** Out of the total number of occupied bins shown in Figure 6.4 the selected bins in energy bands for GP and NN energy sky-maps are shown in left and right panels in green and blue respectively. The energy band definition is shown in magenta dashed line. It can be seen that the number of bins are reduced in both the energy-skymaps. The definition and selection in energy bands in summarised in Tables 6.1 and 6.2.

Energy band	Excluded $\mathcal{B}$
1	1
2	1 to 4
3	1 to 6
4	1 to 8

**Table 6.2:** Selection of  $\mathcal{B}$  bins in energy bands.

bins are grouped in 4 energy bands and a selection on 2D (energy/ $\mathcal{B}$ ) bins is made to attain the best PSF possible without notably reducing the significance. The criterion of excluding 2D bins is assessed on Crab data and simulations with positive results as discussed before. As the PSF' does not depend significantly on declination and spectrum of the source in consideration, the selected 2D bins criterion in energy bands can be applied to other sources. Therefore in Section 6.6, I will investigate the energy-dependent morphology of 2HWC J2019+369 using the energy band definition.

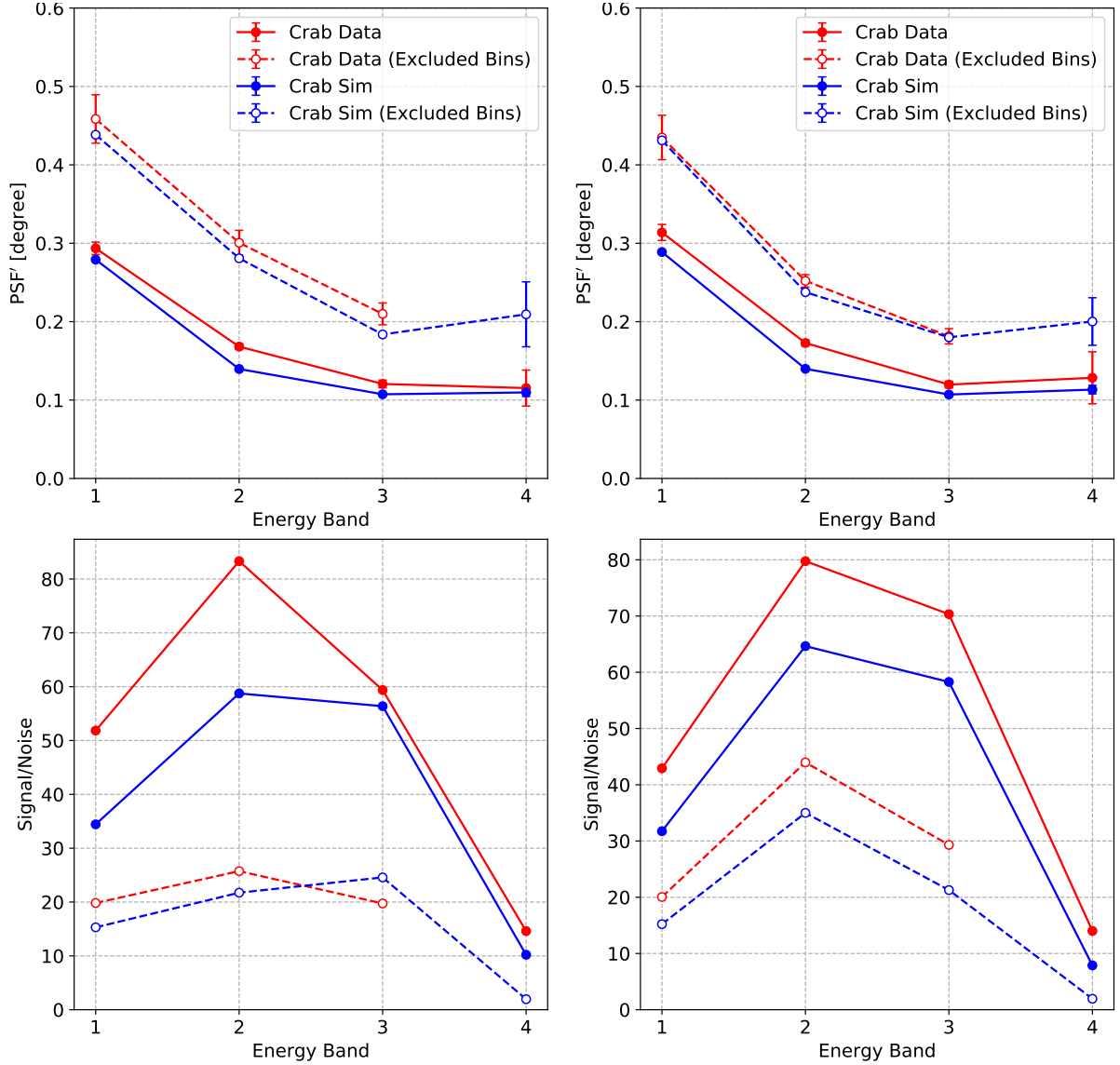


**Figure 6.11:** Top panel: PSF' obtained in energy bands in the excluded and selected 2D energy and  $\mathcal{B}$  bins in different energy bands for Crab data and simulated Crab. Bottom panel: Similar as the Top panel instead of PSF' signal to noise ratio is shown. In energy band 4 for Crab data, the excluded bins were empty, therefore the data point is not there. The plots on the left and right panel are for GP and NN respectively.

## 6.5 2HWC J2019+367 and its Field of View

The region of 2HWC J2019+367 is shown in Figure 6.12 (top panel: left, GP, right, NN, bottom panel:  $f_{\text{hit}}$ ) for both the energy estimators and for  $f_{\text{hit}}$ . It can be seen that in  $f_{\text{hit}}$  sky-map it appears more extended, this is because the event selection is different (discussed in Section 6.2.2) and therefore in  $f_{\text{hit}}$  sky-map the PSF is worse compared to the energy sky-maps. A simple power law

## 6. SPECTRAL AND MORPHOLOGICAL STUDIES OF 2HWC J2019+367

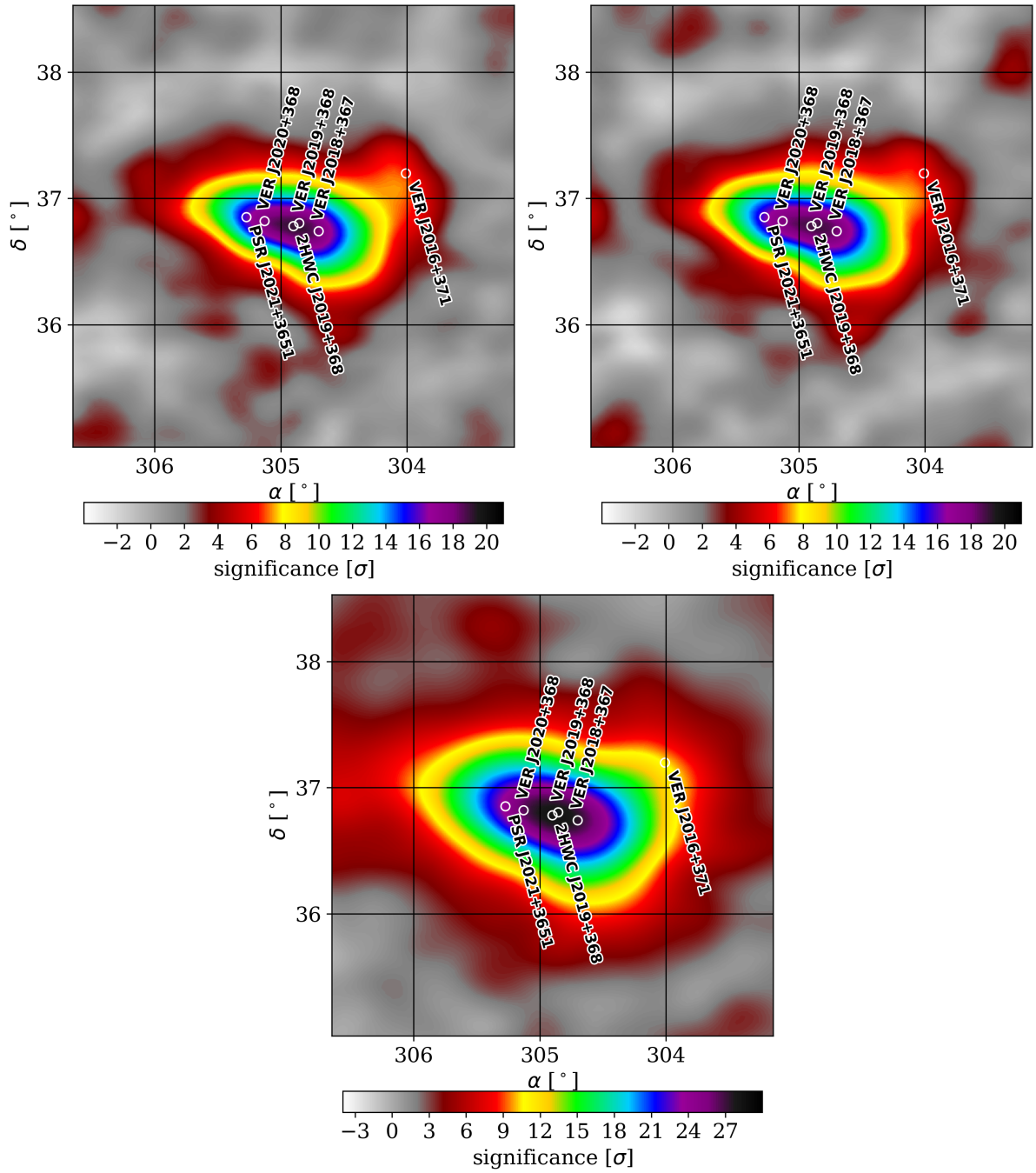


**Figure 6.12:** 2HWC J2019+367 in HAWC sky-maps. GP and NN are shown in the top panel: left and right panel respectively. In the bottom panel, it is shown for the  $f_{\text{hit}}$  sky-map. It is to be noted that the dataset for energy sky-maps and  $f_{\text{hit}}$  sky-map are different (see Section 6.2). A simple power law with an index of -2.7 and point source assumption was made to calculate the significance. The maps are smoothed using interpolation to the nearest pixels.

of index  $-2.7$  and point source is assumed to obtain the significance maps. More details on the significance calculation are described in Section 6.7. In all three sky-maps, 2HWC J2019+367 is observed with ample significance. The difference in significance in energy sky-maps and in  $f_{\text{hit}}$  sky-map is mainly due to difference in corresponding datasets and event selection schemes as described in Sections 6.2.2. The locations of the two VERITAS sources, VER J2019+368 and VER J2016+371 are indicated. Two recently proposed candidates hotspots by VERITAS, namely VER J2020+368 and VER J2018+367, are also shown for the sake of completeness (Abeysekara et al. 2018). The location of the PSR J2021+3651 is also indicated, this pulsar has been proposed to be the main contributor for the TeV emission.

## 6.6 Energy-Dependent Morphology

In Figure 6.13, the GP and NN energy-skymaps are shown for  $>56$  TeV reconstructed  $\gamma$ -ray energies. By comparing them to the corresponding maps in the top panel of the Figure 6.12, it can be seen that the size of the source decreases with increasing energy. There is also a hint that the peak significance in the 2HWC J2019+367 region moves towards the pulsar. The emission around VER J2016+371 location is not visible in  $>56$  TeV reconstructed  $\gamma$ -ray energies.

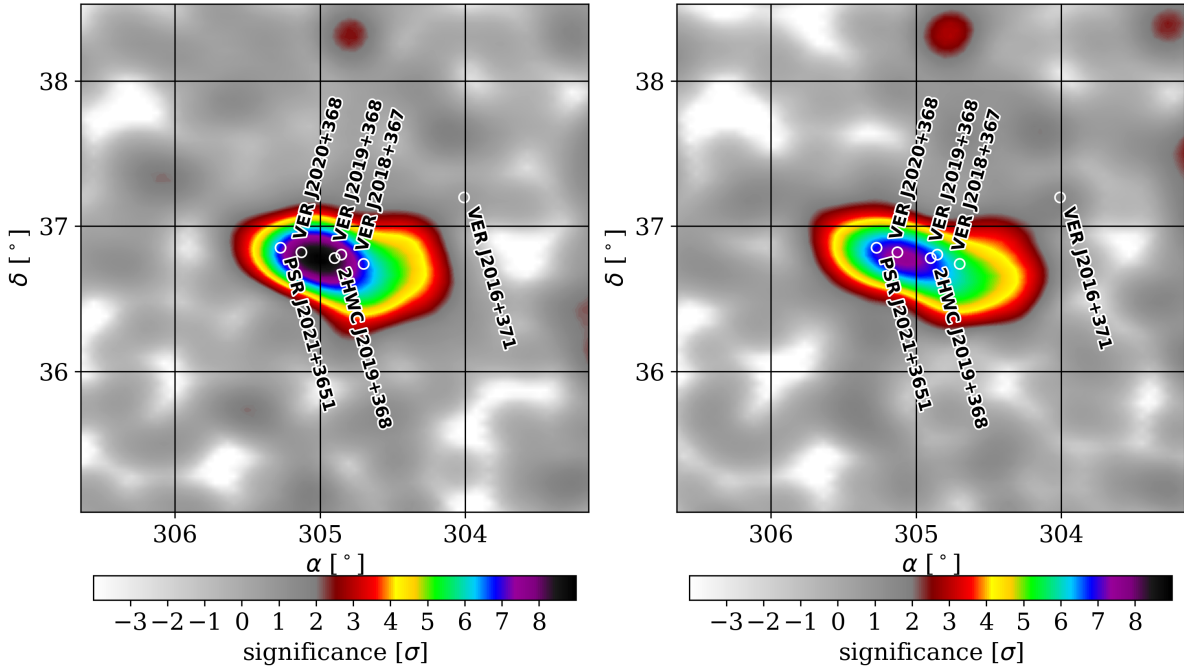


**Figure 6.13:** 2HWC J2019+367 in energy sky-maps  $>56$  TeV reconstructed  $\gamma$ -ray energy. GP and NN are shown in the left and right panel respectively. For comparison to the whole energy range see the top panel of Figure 6.12.

To study the energy-dependent morphology of 2HWC J2019+367, slice profiling of the energy sky-maps is performed using the slice profiling tool defined in Section 6.3. The profile of

the excess counts over the background is obtained within a region of a slice. The idea is to study the change in the morphology of the source in different energy ranges.

In Section 6.4, I explained the systematic studies necessary to perform the slice profile analysis and gave the definition of energy bands using the selected bins from the HAWC energy sky-maps. As shown in Figure 6.14 the slice is drawn in a preferred direction on 2HWC J2019+367. The orientation of the slice is the direction of the line joining the location of PSR J2021+3651

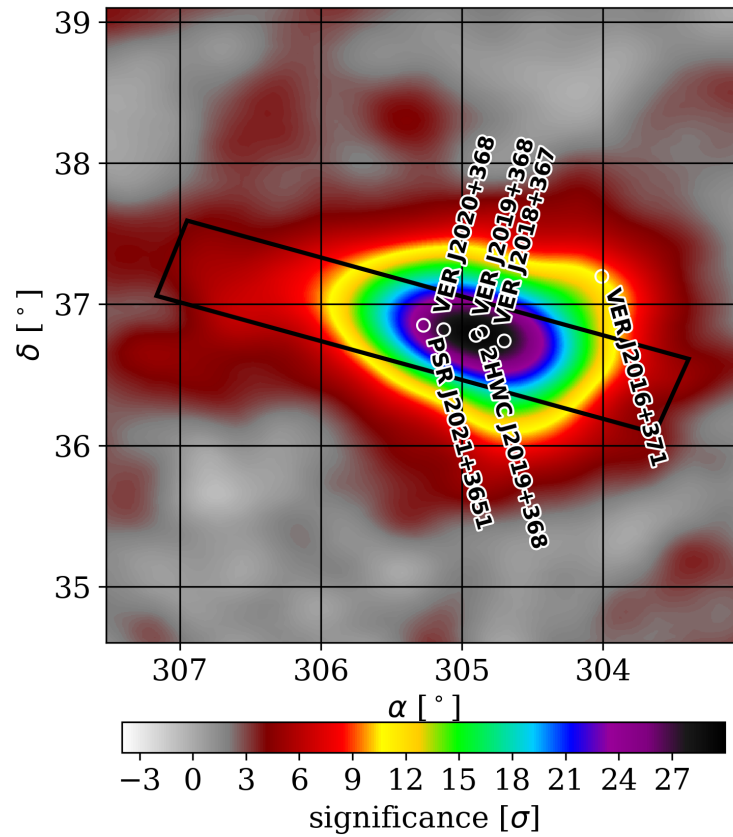


**Figure 6.14:** Schematic of the slice overlaid on 2HWC J2019+367. For details see Section 6.3.

and the location of VER J2019+368. This gives a position angle of  $71^\circ$ . The slice is centred at the location of PSR J2021+3651. It has a width of  $0.7^\circ$  and a length of  $6^\circ$ . The length is divided into 40 bins of  $0.15^\circ$  each. This bin size was chosen to be bigger than the resolution of the pixel binning (mean spacing of  $0.05^\circ$ ) in the used sky-map to avoid the binning effects. The width of  $0.7^\circ$  was chosen in order to exclude the contamination from VER J2016+371.

In Figure 6.15, the excess count profiles obtained in different energy bands are shown, GP on the left and NN on the right. The obtained PSF' using a simulated point source at the location of PSR J2021+3651 with a power law of spectral index 2.2 (keeping in mind the hard spectrum of VER J2019+368) is shown on the right. Although it is to be noted that the PSF' does not change significantly with the spectrum of the point source, therefore a slight change in the spectral index will not change the results significantly (see discussion in Section 6.4.2). There was no significant emission observed in the first energy band, which might be due to the hard spectrum



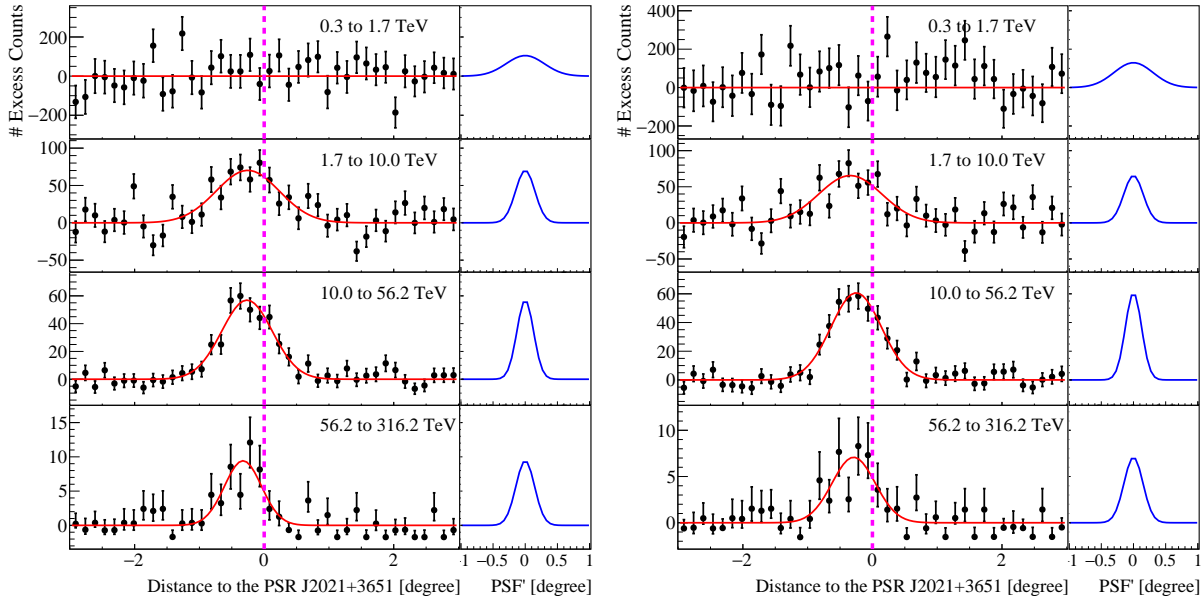


**Figure 6.15:** The slice profiles on the excess counts maps for 2HWC J2019+367 in different energy bands. The corresponding PSF' obtained using a simulated point source with power law assumption of spectral index of 2.2 at the location of 2HWC J2019+367 is shown on the right of each plot in blue. The excess profiles are fitted with a Gaussian shown in red. The location of the pulsar PSR J2021+3651 is shown with the magenta dashed line. The profiles for GP are shown on the left panel and for NN are shown in the right panel.

of VER J2019+368 as we know from the previous observations (Aliu et al. 2014). We see significant excess in energy bands 2, 3 and 4, which corresponds to energy range above 1.77 TeV. The excess profiles were fitted with a Gaussian in all these energy bands. The shrink in size of the Gaussian can be seen with increasing energy in both the energy sky-maps (GP and NN).

In Figure 6.16, the size of 2HWC J2019+367 along the axis of the slice is shown in energy bands 2, 3 and 4. It was obtained by subtracting 1 sigma width of the PSF' in quadrature from the 1 sigma fit size of the excess profiles in each energy bands. The 1 sigma width of the PSF' was corrected for  $0.05^\circ$  systematic difference between simulations and data, as shown in Section 6.4.1.

In Figure 6.17 the obtained size of 2HWC J2019+367, as explained above, is shown as a function of distance to the pulsar location in energy bands 2, 3 and 4. The distance to the pulsar was calculated from the mean position of the excess profile fit. There is an indication of the decrease in size with energy bands of increasing energy. However, the error bars on the measured size are large, therefore to conclude it significantly, more data with future observations is required. There is no significant shift towards the pulsar position with increasing energy.

The results are similar in both the cases for GP and NN. However, it is to be noted that there are certain differences in the obtained results from these two datasets. For NN the decrease in size while going from energy band 3 to 4 is less significant in comparison to GP. Which might be because of the differences in the performance of these two methods for the highest energy



## 6. SPECTRAL AND MORPHOLOGICAL STUDIES OF 2HWC J2019+367

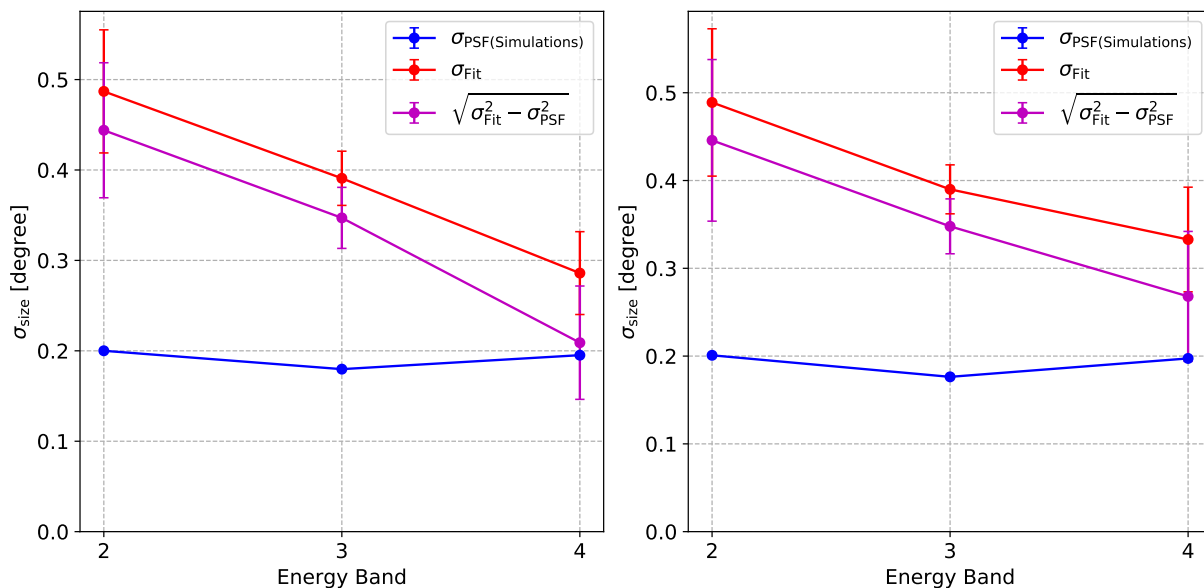


**Figure 6.16:** In red the fitted size and in blue the PSF' is shown from Figure 6.15 in energy bands 2, 3 and 4. The PSF' is corrected for the systematic difference of  $0.05^\circ$  between data and simulations as described in Section 6.4.1. The size of 2HWC J2019+367 in different energy bands is shown with the magenta color line and is calculated as shown in legends. The results are shown for GP and NN in the left and right panel respectively.

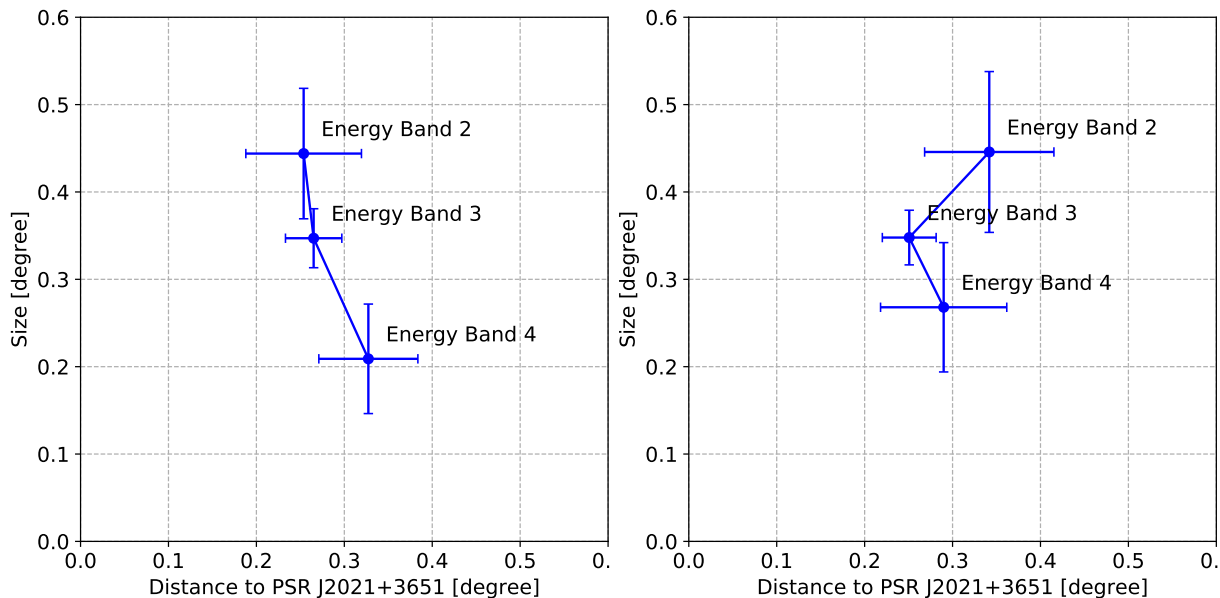


**Figure 6.17:** The size vs. distance to the pulsar PSR J2021+3651 in different energy bands for 2HWC J2019+367. The size is the same as explained in Figure 6.16. The mean position of the fitted Gaussian from Figure 6.15 is used to calculate the distance from the pulsar location. The left panel and right panel are showing the results for the GP and for the NN respectively.

showers.

Currently, efforts are being made to better understand the systematic differences in the performance of these two energy estimators. Therefore the results might change with further developments in the understanding of the energy estimators. It is to be noted that with the recent upgrade of HAWC with the outrigger array (see Chapter 3) the instrumented area of HAWC observatory is increased by a factor of 4 to 5. The outrigger array will be very helpful in acquiring more data at the highest energies and will be crucial to significantly verify the results on energy-dependent morphology of 2HWC J2019+367.

## 6.7 Morphological and Spectral Fit

For morphology and spectral fit of 2HWC J2019+367, the better energy reconstruction and PSF of energy estimators (GP and NN) is not the major focus anymore. Therefore, in addition to the energy sky-maps, I will show the results from the  $f_{\text{hit}}$  sky-map as well. To study morphology and the spectral behaviour of 2HWC J2019+367, I have used the standard HAWC source analysis framework. In which, a likelihood framework (Younk et al. 2015) is used to obtain the significance of an assumed source hypothesis. The same approach was used to create the 2HWC catalog (Abeysekara et al. 2017b). A fixed spectrum and source extension are assumed and the hypothesis of test source is moved across the Region of Interest (ROI) in the sky-map. By applying the Wilk's theorem (Wilks 1938), so that  $\sqrt{\text{TS}} = \sigma$ , the significance maps are created, where the TS is calculated as in equation (6.1).

$$\text{TS} = 2 \ln \frac{L(\text{source hypothesis})}{L(\text{null hypothesis})} \quad (6.1)$$

Where  $L$  denotes the likelihood of the hypothesis being tested. For the source model the likelihood is calculated by comparing the event counts in observed data to the expected data calculated using the detector response function (see Section 2.10) for an assumed source model in the ROI. For the null model, the expected counts are obtained using the background maps (see Section 2.11). To perform the detailed morphological and spectral analysis The Multi-Mission Maximum Likelihood framework (3ML) (Vianello et al. 2015) is used with a HAWC plug-in, which contains the information of the detector response function together with the source analysis framework. 3ML uses the sky-maps and the HAWC plug-in information to perform the morphology and spectral fits.

### 6.7.1 Single Source Fit

To find the best describing model for morphology and spectral shape of 2HWC J2019+367, different morphologies in combination with different spectral shapes are tested. For morphology, symmetric and asymmetric 2D Gaussian were tested, which are motivated by the previous studies by VERITAS and the excess profiles obtained using the slice profile analysis. Similarly, three assumptions for spectral shape, a power law, power law with an exponential cut-off and a log-parabola were tested. All the associated parameters depending on the morphology and spectral

## 6. SPECTRAL AND MORPHOLOGICAL STUDIES OF 2HWC J2019+367

shape are the free parameters of the fit (including location: right ascension (RA) and declination), except the pivot energy of the spectrum. The pivot energy was fixed to a value where the other spectral parameters are least correlated.

The result value of the fit TS for different morphology and spectral shape combinations are summarised in Table 6.3. It can be seen that, although, the result TS values differ for different sky-maps for a given morphology and spectral shape assumption, for all the three sky-maps the best fit model obtained was an asymmetric 2D Gaussian with a cut-off power law. Although it is to be noted that the fit TS for log-parabola spectral shape assumption is very similar to the cut-off power law, however, it is lower in all the cases. Therefore to make a distinction between the fit results between cut-off power law and log-parabola spectral shape more data from the future observations will be required.

Sky-map type	Morphology (2D Gaussian)	Spectral assumption	TS
GP	Symmetric	Cut-off power law	831.27
GP	Asymmetric	Cut-off power law	877.11
GP	Asymmetric	Simple power law	832.05
GP	Asymmetric	Log-parabola	876.47
NN	Symmetric	Cut-off power law	901.07
NN	Asymmetric	Cut-off power law	941.10
NN	Asymmetric	Simple power law	891.28
NN	Asymmetric	Log-parabola	934.18
$f_{\text{hit}}$	Symmetric	Cut-off power law	1273.31
$f_{\text{hit}}$	Asymmetric	Cut-off power law	1324.53
$f_{\text{hit}}$	Asymmetric	Simple power law	1292.23
$f_{\text{hit}}$	Asymmetric	Log-parabola	1322.13

**Table 6.3:** Comparison of different morphology and spectral assumptions for 2HWC J2019+367.

In Figure 6.18 the residual maps compared to the original maps shown in Figure 6.12 of the fit are shown (top panel: left, GP, right, NN and bottom panel:  $f_{\text{hit}}$ ). The residual maps were obtained by subtracting the best fit model for a given source assumption from the data maps. The significance in the residual maps is calculated with point source search of a spectral index -2.7 in the ROI following the procedure described earlier for TS calculation. It can be seen that most of the emission from the 2HWC J2019+367 has been modelled reasonably well. One can also see the clear residual at the location of VER J2016+371, which stands out significantly in the top right corner of each residual map.

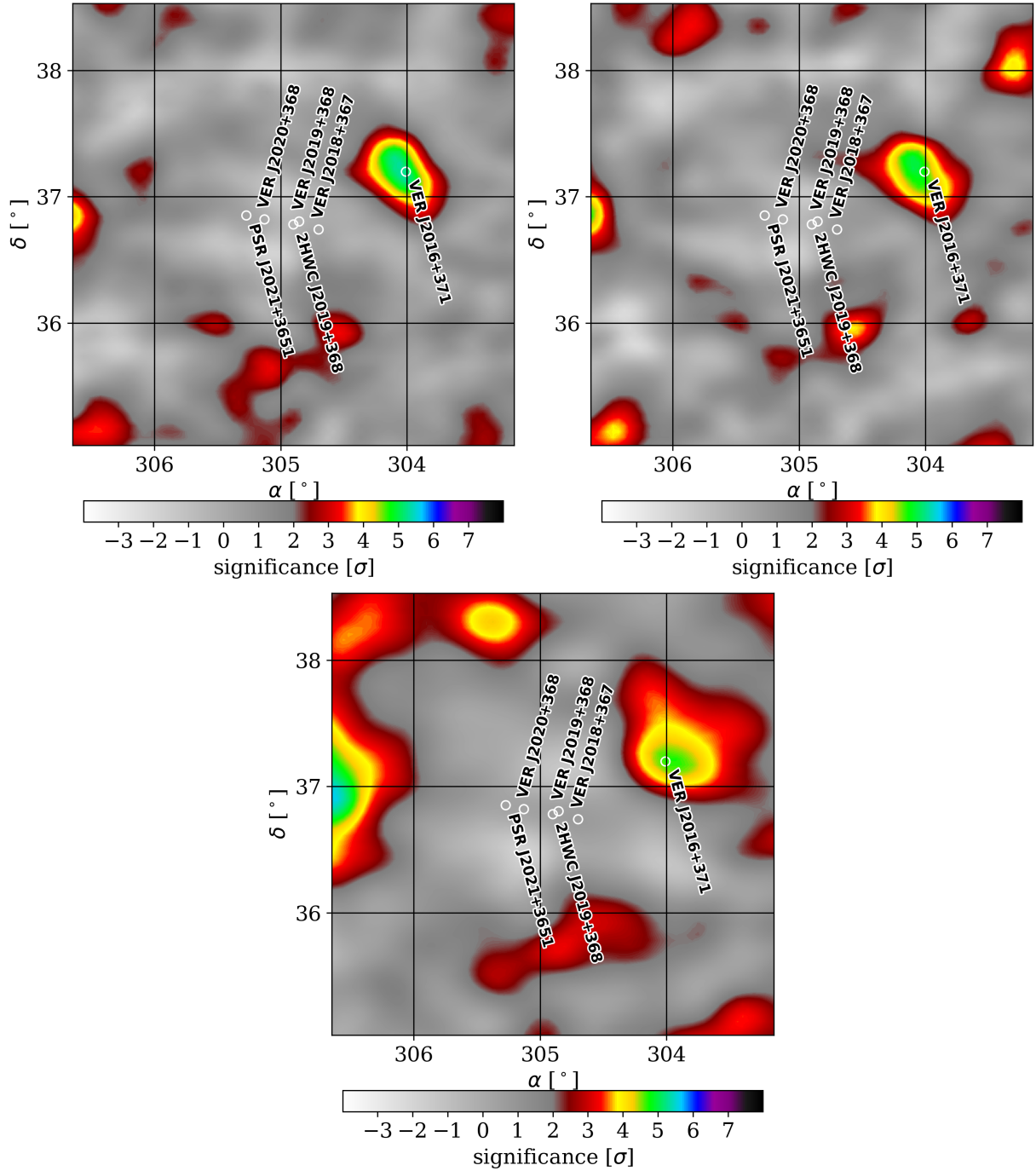


**Figure 6.18:** Residual maps after the fitting a 2D Gaussian morphology for 2HWC J2019+367 with a cut-off power law. The procedure to obtain the maps is the same as explained in Figure 6.12. The bulk of the emission is modelled reasonably well, leaving the residual of VER J2016+371 is clearly visible. The results for GP, NN and  $f_{\text{hit}}$  sky-maps are shown in the top left, top right and bottom panel respectively.

### 6.7.2 Joint Source Fit

A joint fit for 2HWC J2019+367 is performed with the same morphological and spectral assumption as before, in addition to that, a fixed point source assumption with a power law spectral shape at the location of VER J2016+371 (RA = 304.0083°, declination = 37.197°) is added. The results are summarised in Table 6.4. The fitted location of 2HWC J2019+367 is slightly shifted from the location reported by VERITAS for VER J2019+368 with a value of 0.043°. However, it is to be noted that the uncertainty on RA obtained by VERITAS is large (0.29°). Additionally, the obtained shift is of the order the pixel spacing (0.0573°) used in HAWC sky-maps, therefore it just might be a binning effect.

On the morphology side of J2019+368, it is crucial to mention an asymmetric 2D Gaussian morphology was also preferred by VERITAS, similar to the HAWC observations. The extension observed by HAWC is similar to the one observed by VERITAS for GP and NN sky-maps, which can be seen by looking at the fit values of the semi-major and minor axis. However, the extension observed in  $f_{\text{hit}}$  sky-maps is slightly bigger which might be due to the difference in dataset and event selection as described in Section 6.2.2. The observed position angle of the semi-major axis by VERITAS of 71° is also very similar to the HAWC observations. In the case of GP and NN it is about ~68° and ~69° respectively and for  $f_{\text{hit}}$  it is slightly less ~60°. The similarities in the fit results of morphology in VERITAS and HAWC strongly supports the association of the emission seen by both observations.

The Spectral Energy Distributions (SEDs) obtained from the joint fit of 2HWC J2019+367 are shown in Figure 6.19. The SED obtained by VERITAS is also shown. It can be seen that, in the case of GP and NN sky-maps, the normalisation of the SEDs is higher than the one obtained by VERITAS. For  $f_{\text{hit}}$  sky-map, it seems to align considerably well with the VERITAS observation. However, it is to be noted that for  $f_{\text{hit}}$  sky-map, in the joint fit the normalisation of VER J2016+371 is higher than the one obtained for 2HWC J2019+367. This might be due to some of the emission of 2HWC J2019+367 is stolen by VER J2016+371.

The spectral index of VER J2019+368 measured by VERITAS is 1.75, which was obtained for a power law. However, in HAWC observation, a cut-off power law is preferred. The spectral index measured by VERITAS is very similar to the ones obtained for HAWC energy-skymaps, with a value of about ~1.68 for GP and ~1.61 for NN. However, it is considerably different for  $f_{\text{hit}}$  sky-map where it has a value of 1.14. The observed cut-off in the spectrum also differs considerably in the case of  $f_{\text{hit}}$  sky-map and the energy estimator sky-maps (GP and NN). For  $f_{\text{hit}}$  sky-map the cut-off is around ~22 TeV, however for GP and NN sky-maps it is around ~45 TeV. The cut-off occurs around the same energy where VERITAS observations have its last data points. The reason behind the mismatch in HAWC observation between the energy (GP and NN) sky-maps and the  $f_{\text{hit}}$  sky-map is unclear, and it is under investigation. Regardless, it is to be noted that for the observation of extended sources, HAWC is well suited than VERITAS, because of better background estimation. There might be a possibility that in the VERITAS observation some flux might be missing and the normalisation can be affected by the difference in background estimation. Therefore once the mismatch between the HAWC energy-skymaps and  $f_{\text{hit}}$  maps is resolved the results can be better investigated together with the VERITAS observations.

For VER J2016+371, the fit results indicate that it is fitted with more than  $5\sigma$  significance

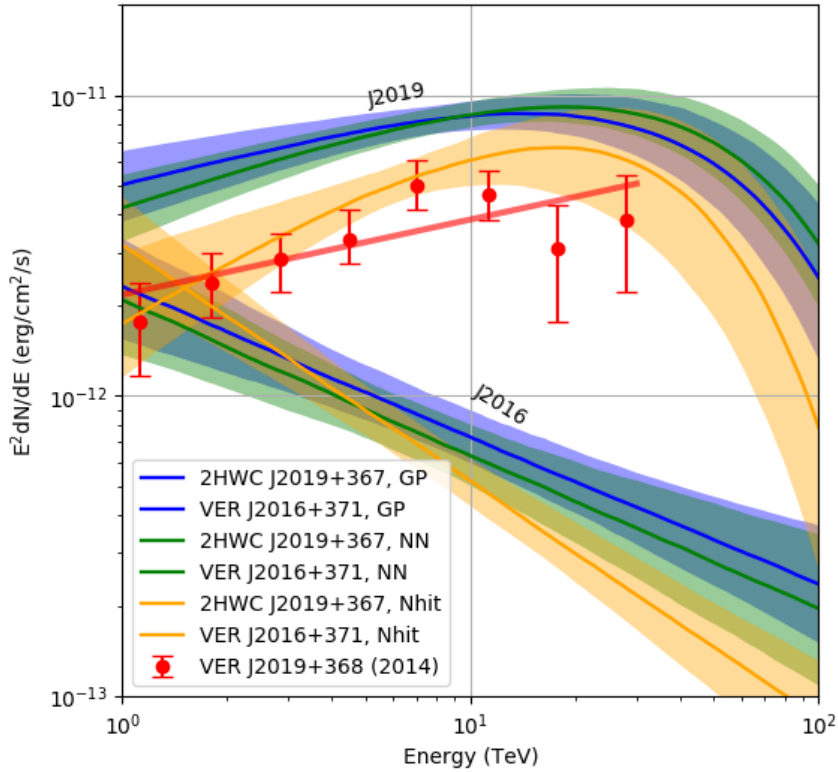


**Figure 6.19:** SEDs obtained using a power-law with an exponential cut-off assumption for 2HWC J2019+367 and a simple power law assumption for VER J2016+371 in a joint fit of the emission region. A cut-off is clearly visible around  $\sim 45$  TeV for GP and NN reconstructed energy. Whereas for  $f_{\text{hit}}$  it is around  $\sim 22$  TeV. The obtained SEDs for both energy sky-maps of HAWC have a higher normalisation than the one observed by VERITAS. However, the SED obtained from the  $f_{\text{hit}}$  sky-map is consistent with the one from VERITAS.

for all the three sky-maps. This means the discovery of a new HAWC source associated to VER J2016+371. By looking at Table 6.4 it can be seen that the spectral index obtained also matches reasonably well with the VERITAS observations. However, It seems to a bit lower in the case of  $f_{\text{hit}}$  sky-map. In Figure 6.20 the residual maps after performing the joint fit (top panel: left, GP, right, NN and bottom panel:  $f_{\text{hit}}$ ) are shown. It is clearly visible that most of the emission from the 2HWC J2019+367 is modelled reasonably well with the joint fit.

However, there is still some residual emission and can be seen at the middle left part of each residual maps. The reason for this emission is unclear. I looked for a possible candidate in the existing TeV and pulsar catalogues, no candidate was found in the vicinity. To better understand this residual a more detailed investigation is needed. However, it is to be noted that the centroid of TeV emission for 2HWC J2019+367 is about  $\sim 1.5^\circ$  away from the centroid of this remaining residual, therefore even if there is any overlap between them, it should be marginal, and therefore should not affect the results obtained for 2HWC J2019+367 significantly.

J2019+367:			
Fit Parameter	GP	NN	VERITAS
RA (deg)	$304.9 \pm 0.027$	$304.9 \pm 0.026$	$304.9 \pm 0.026$
Declination (deg)	$36.78 \pm 0.014$	$36.78 \pm 0.014$	$36.78 \pm 0.016$
Semi major axis (deg)	$0.365 \pm 0.024$	$0.367 \pm 0.023$	$0.435 \pm 0.025$
Semi minor axis (deg)	$0.139 \pm 0.023$	$0.155 \pm 0.024$	$0.193 \pm 0.0238$
Position angle (deg)	$68 \pm 3.3$	$69.1 \pm 3.4$	$60 \pm 4.0$
Spectral index	$-1.68 \pm 0.11$	$-1.61 \pm 0.10$	$-1.14 \pm 0.35$
Cut-off energy (TeV)	$46_{-9}^{+12}$	$48_{-9}^{+11}$	$22_{-7}^{+9}$
Fixed pivot (TeV)	10.0	11.0	7.0
Norm (1/TeV/cm <sup>2</sup> /s)	$6.7_{-0.6}^{+0.7} \times 10^{-14}$	$5.7 \pm 0.5 \times 10^{-14}$	$9.3_{-1.3}^{+1.5} \times 10^{-14}$
TS	862.77	929.42	1240.63
J2016+371:			
Spectral index	$-2.48 \pm 0.16$	$-2.5 \pm 0.19$	$-2.81 \pm 0.16$
Fixed pivot (TeV)	8.9	7.0	4.5
Flux (1/TeV/cm <sup>2</sup> /s)	$6.1_{-1.1}^{+1.4} \times 10^{-15}$	$9.7_{-2.0}^{+2.5} \times 10^{-15}$	$8.9_{-1.5}^{+1.8} \times 10^{-15}$
TS	30.65	25.21	30.75
			N/A
			N/A
			$1.75 \pm 0.38$ (Power law)
			N/A
			5.0
			$8.1 \pm 0.7_{\text{stat}} \pm 1.6_{\text{sys}} \times 10^{-14}$
			N/A

**Table 6.4:** Results from the joint fit of 2HWC J2019+367 with an asymmetric 2D Gaussian with a spectral assumption of a cut-off power law and a point source with spectral assumption of a simple power law at the location of VER J2016+371. The top part is showing the results for J2019+367 and the bottom part is for VER J2016+371. The results from previous VERITAS observations (Aliu et al. 2014) are also included for comparison. The position angle is given for the semi-major axis of an asymmetric 2D Gaussian. The flux is the differential flux at the pivot energy. The location of VER J2019+371 is fixed in the joint fit to the location obtained by VERITAS observations (RA = 304.0083°, declination = 37.197°).

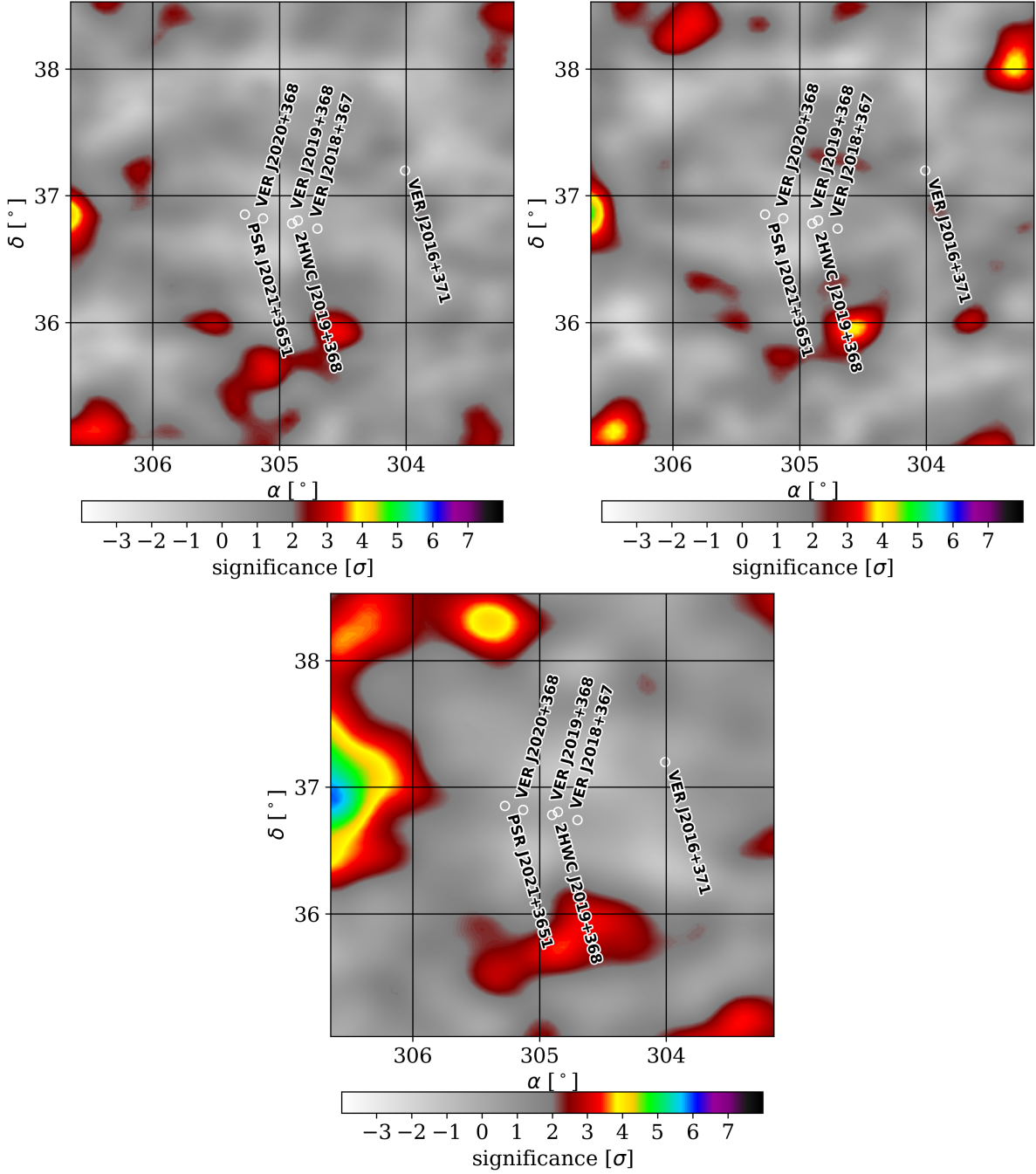


**Figure 6.20:** Residual maps after the joint fitting of 2HWC J2019+367 with an extended 2D source with 2D Gaussian morphology and a point source at the location of VER J2016+371. The procedure to obtain the maps is the same as explained in Figure 6.12. Most of the emission has been reasonably well. The results for GP, NN and  $f_{\text{hit}}$  sky-maps are shown in the top left, top right and bottom panel respectively. However, there is still some residual emission which can be seen in the middle left part of each plot for which the reasons are unclear (see text for discussion).



## 6.8 Multi-wavelength Data

The region of 2HWC J2019+367 has been observed in essentially all wavelengths and these data can be utilised to constrain various aspects of the source nature. For example, the X-ray and radio emission point towards the parent particle population being leptonic in nature. The IR emission can give information about the dominant radiation field density in the region etc. The studies by (Paredes et al. 2009) reported extended radio emission in the vicinity of 2HWC J2019+367, however, the position and extension were not reported. Fermi-LAT observation in GeV  $\gamma$ -rays only resulted in upper-limits (Abdo et al. 2009). Nevertheless, there are detailed studies of the X-ray data obtained using XMM-Newton and Suzaku (Mizuno et al. 2017a). In Figure 6.21, the

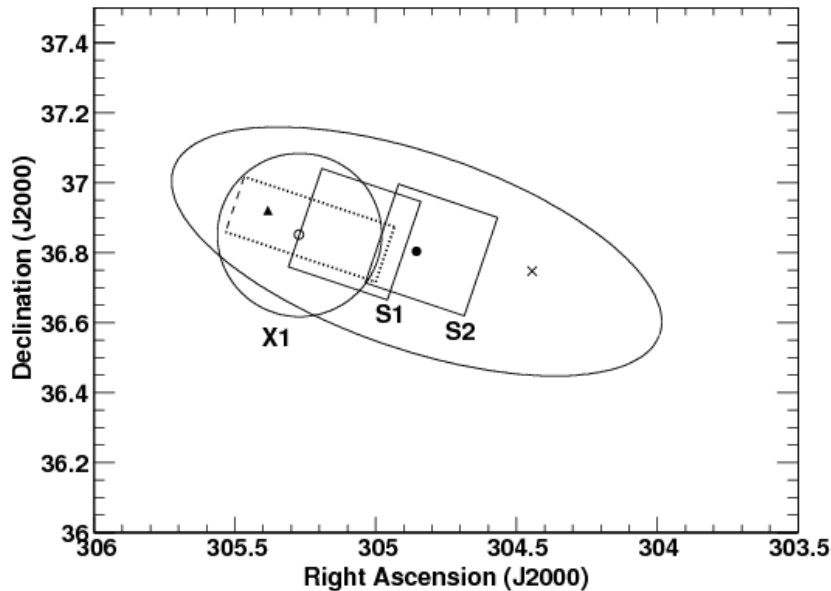


**Figure 6.21:** Schematic of the observations and objects tangled in the study performed by Suzaku (Mizuno et al. 2017a). The  $2.5\sigma$  emission for 2D Gaussian morphology of VER J2019+368 is shown with an ellipse. The two squares show the Suzaku-XIS FOV for the two observations. The circle shows the XMM-Newton FOV. The rectangle is the measured size of the X-ray PWN. The open circle, filled circle, triangle, and cross show the location of PSR J2021+3651, the peak position of the VERITAS TeV emission, WR 141 and Sh 2-104 respectively.

schematic of the observations performed using Suzaku and XMM-Newton are shown together with the  $2.5\sigma$  of measured extension (using a 2D Gaussian morphology) of VER J2019+368 is drawn. The measured extent of the X-ray PWN is also depicted.

In Figure 6.22, the combined observations S1 and S2 (see Figure 6.21) are shown in two energy bands. The images and corresponding count rates on the left and right are shown for the soft-band (0.7 to 2 keV) and hard-band (2 to 10 keV) of the X-ray emission respectively. It can be seen that the emission region shrinks while going from soft to the hard band. The measured absorption corrected spectrum is well described by a power law and has a hard spectral index  $\Gamma = 2.05 \pm 0.12$ . The position angle of the semi-major axis of the X-ray PWN is  $\sim 71.4^\circ$ . The similar

orientation of the X-ray and TeV emission (see Table 6.4 position angle HAWC and VERITAS) strongly supports their association.

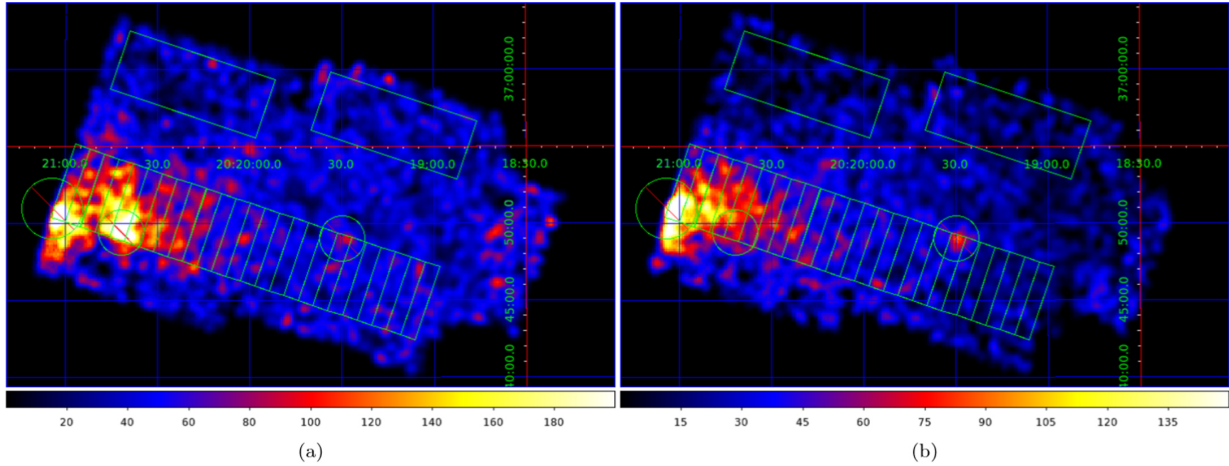


**Figure 6.22:** Suzaku emission in two energy bands. Left panel: soft-band, 0.7 to 2 keV. Right panel: hard-band, 2-10 keV. X-ray intensity maps combining the observations in S1 and S2 regions (see Figure 6.21) in equatorial coordinates. The colour scale shows the photon flux in the units of  $\text{s}^{-1}\text{cm}^{-2}\text{sr}^{-1}$ . Rectangles are drawn along the major axis of the X-ray PWN. The Figure is taken from (Mizuno et al. 2017a).

The X-ray data is crucial to constrain the ambient magnetic field present in the emission region, and also provides information on the morphology and on the nature of the particle population. I will use this information while performing the source modelling and in the interpretation of the analysis in Section 6.9.

## 6.9 Spectral Modelling

Amongst the different scenarios that can explain the multi-wavelength emission from 2HWC J2019+367, the observed spatial association between the X-ray and TeV emission, and the hint of shrink in size of the TeV emission with increasing energy seem to point towards a leptonic origin. A young energetic pulsar, PSR J2021+3651, is in the vicinity. Therefore, in this section, I present the combined modelling using a leptonic scenario where the emission is originated by a PWN. In the following, I will start by describing the model in Section 6.9.1 and then move to two scenarios where the model will be used to describe the observed X-ray and TeV emission together.

In the first scenario, dubbed as the one zone model (see Section 6.9.2), the observed X-ray and the whole range of TeV emission are described together. However, it is not ideal to model the X-ray emission between 2 and 10 keV (hard X-ray emission) together with TeV emission between 1 TeV and at least 56 TeV reconstructed  $\gamma$ -ray energy because of different parent electron populations. The size of the X-ray emission is very small compared to the TeV emission. The electron population emitting the hard X-rays at 2-10 keV must be the one emitting the highest

energy  $\gamma$  rays at several tens of TeV. This electron population must be of higher energy than compared to the one responsible for the extended TeV emission. The lower energy electrons have longer cooling timescales and can still produce TeV emission by travelling farther, whereas the opposite is true for the higher energy electrons.

In the second scenario, dubbed as the two zone model (see Section 6.9.3), where the X-ray emission will be compared with the highest energy TeV emission. Only the recently injected electrons will be used to describe the X-ray emission together with the whole history of injected electrons to describe the TeV emission. The possibility of the missing X-ray emission, comparable to the size of the TeV emission will be taken into account to describe the whole history of the system. The two zone model scenario is preferred for the interpretation over the one zone model. In the end, the obtained PWN properties using the two zone model will be discussed.

### 6.9.1 Model Considerations

I have used the ‘‘GAMERA’’ package to perform the spectral modelling (Hahn 2016). In which one can define a time-dependent model of injection and cooling of relativistic electrons to produce associated photon emission. To devise the spectral model in a PWN scenario, an electron spectrum of power law with an exponential cut-off is injected. A cut-off is set because the injected particles ( $e^\pm$ ) can only be accelerated up to a certain maximum energy ( $E_{\max}$ ) (Zhang et al. 2008; Gaensler & Slane 2006). The spectral index is assumed to be -2 and  $E_{\max}$  is treated as a free parameter.

To decide the evolution of the injected electron spectrum and hence to derive the photon spectrum, there are several unknown parameters which must be constrained. One could use the known parameters of the pulsar in order to derive the values of the unknown parameters that can describe the observed photon emission spectrum.

For PSR J2021+3651, the observed period ( $P$ ) and its time derivative ( $\dot{P}$ ) are 104 ms and  $9.57 \times 10^{-14} \text{ s}^{-2}$  respectively. Therefore the spin-down power is  $\dot{E} = 3.4 \times 10^{36} \text{ erg/s}$ . For the distance to the pulsar, the dispersion-based measurement is quite large  $\geq 10 \text{ kpc}$  (Roberts et al. 2002), which is in dispute with distance derived considering the X-ray measurements (Van Etten et al. 2008) of  $\sim 4 \text{ kpc}$ . The latest detailed study of Chandra archival X-ray data by taking into account an extinction-distance relation using the red-clump stars as standard candles in the line of sight by (Kirichenko et al. 2015) suggest a distance of  $\sim 1.8 \text{ kpc}$ . In this analysis, I will be using the distance of 1.8 kpc.

The characteristic age  $\tau_c$  of the pulsar is 17.2 kyr. However, it is to be noted that the  $\tau_c$  is only a good measure of the pulsar age for older systems, while the assumption of the birth period  $P_0 \ll P$  is true (see equation (5.4)). Therefore, in this model calculation, the  $\tau_c$  will not be used. True age ( $\tau$ ) of the system can be calculated using equation (5.3), where the initial birth period ( $P_0$ ) is unknown. Another, unknown parameter which is used in the calculation of time evolution of spin down luminosity and magnetic field (B-field) (see equations (5.8), (5.9)) is the spin-down time-scale ( $\tau_0$ ), which is expressed in terms of  $P_0$ ,  $P$ ,  $\dot{P}$ , and  $n$  as:

$$\tau_0 = \frac{P_0^{n-1} P^{2-n}}{(n-1)\dot{P}}, \quad (6.2)$$

where  $n$  is the pulsar braking index and it is assumed to be  $n = 3$ . Making  $P_0$  an unknown parameter instead of  $\tau_0$ , one could use the  $\tau$  of the system instead of the approximation  $\tau_c$ .  $P_0$  is constrained for a given system as it cannot be bigger than the observed  $P$ .

To obtain the time-dependent normalisation of the injected electron spectrum, one could use the value of  $\dot{E}$  to calculate the initial spin-down luminosity  $\dot{E}_0$  by solving the equation (5.8) for  $\dot{E}_0$  as the following:

$$\dot{E}_0 = \dot{E} \left( 1 + \frac{\tau}{\tau_0} \right)^{\frac{n+1}{n-1}} \quad (6.3)$$

where  $\dot{E}$  is the present spin-down luminosity, therefore in equation (5.8)  $t = \tau$ .

The injected particles continuously interact with the ambient B-field and radiation fields and cool down while producing photons. The time evolution of the B-field is taken into account. First calculating the initial value of the B-field ( $B_0$ ) similar to how it is done for  $\dot{E}_0$  and after using equation (5.9).

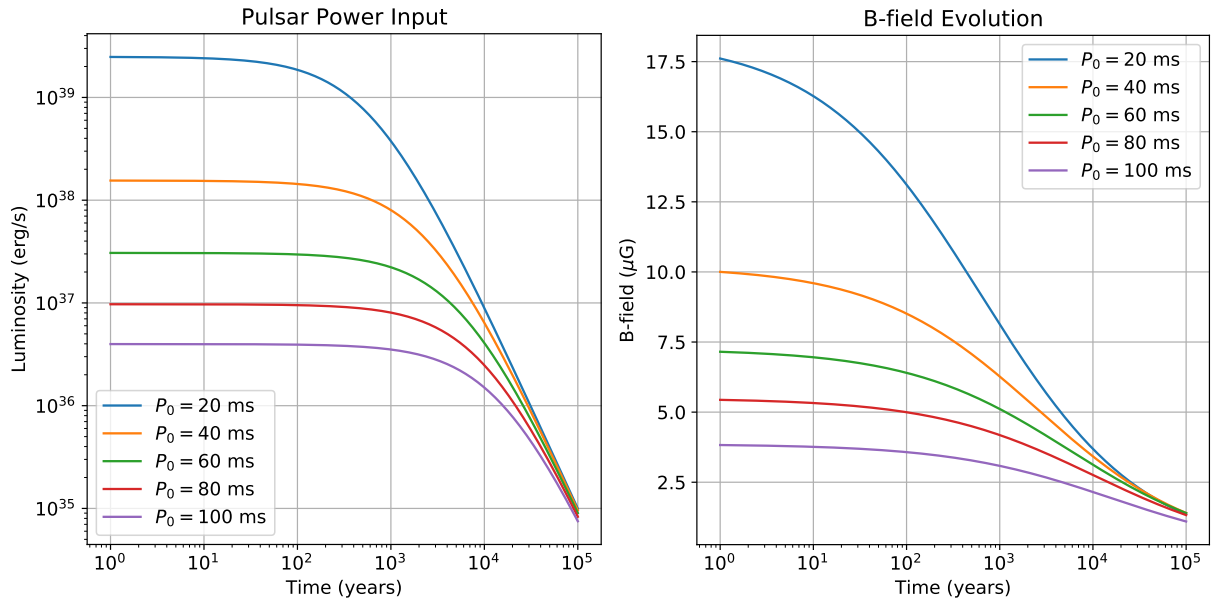


**Figure 6.23:** For different values of the initial birth period ( $P_0$ ), left panel: time evolution of the spin-down luminosity of the pulsar PSR J2021+3651, right panel: time evolution of the B-field.

Both the spin-down luminosity and the B-field are time-dependent and depend on the value of  $\tau_0$ , which is dependent on  $P_0$  (see Equation (6.2)). In Figure 6.23, the time-dependent evolution of  $\dot{E}$  and B-field are shown in the left and right panel respectively for different values of  $P_0$ . By construction, to infer the initial values of spin-down luminosity and B-field, the present values of them are used respectively (see Equation (6.3)). The illustration shown in Figure 6.23 is by using the values of  $\dot{E}$  and B-field of  $3 \mu\text{G}$  (at least equal to local ISM) at an age of  $\sim 7$  kyr (shown later as the true age of the system). It can be seen that both the spin down luminosity and B-field increases with decreasing age of the system for a given value of  $P_0$ . The values of the  $P_0$  mainly affects the initial injected spin-down power to the system. The higher value of spin-down

power corresponds to higher kinetic power in the particles present in the system and therefore also results in higher values of the B-Field.

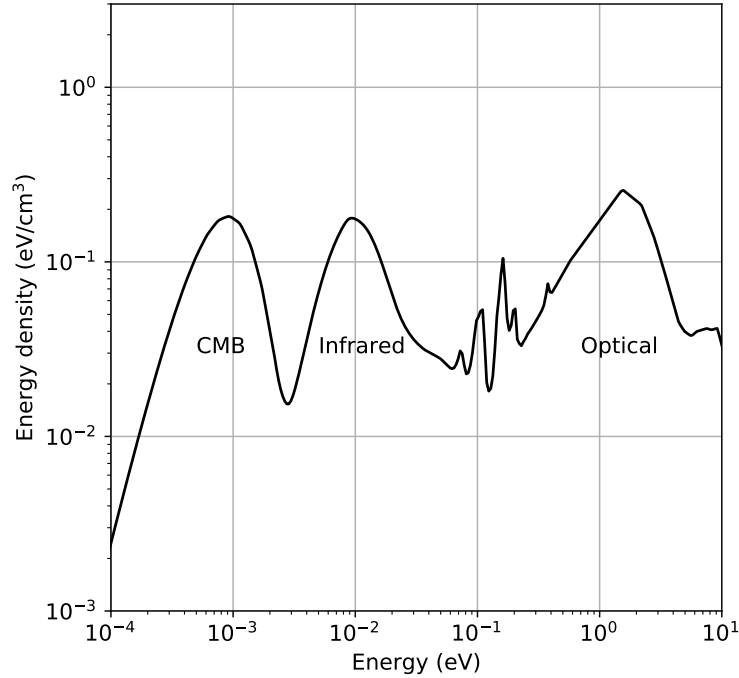


**Figure 6.24:** The calculated radiation fields at the location of 2HWC J2019+367. The radiation field model used is (Popescu et al. 2017).

To take into account the ambient radiation fields present at the location of 2HWC J2019+367, the radiation field model from (Popescu et al. 2017) is used. In the right panel of Figure 6.24, the obtained radiation field densities are shown as a function of photon energy. All the three main components CMB, IR and optical are taken into account.

Only a certain fraction of the total spin-down power goes into the  $e^\pm$  production, therefore a conversion efficiency ( $\epsilon$ ) needed to be multiplied to equation (5.8) to obtain the injected particle spectrum. The  $\epsilon$  is treated as an unknown parameter.

To summarise, I assumed the injected particle spectrum of index -2 and pulsar braking index  $n = 3$ . The cut-off energy ( $E_{max}$ ), the birth period ( $P_0$ ) and the conversion efficiency ( $\epsilon$ ) are treated as unknown parameters to describe the injected particle spectrum. The injected particle spectrum and B-field are time-dependent. The radiation fields are calculated from the model (Popescu et al. 2017) at the location of 2HWC J2019+367. After obtaining the injected particle spectrum for given values of assumed and unknown parameters, one can evolve it in the presence of B-field and radiation fields to calculate the evolved particle spectrum. The evolved particle spectrum is then utilised to calculate the emitted photon spectrum. The model emitted photon spectrum is tuned to the observed X-ray and TeV emission to obtain the values of the unknown parameters.

## 6.9.2 One Zone Model

Using the devised model described in the previous Section, one can obtain the emitted photon SED as shown in Figure 6.25. The corresponding plots describing the model are shown in Figures A.6 (injected spin-down power evolution and injected electron spectrum), A.7 (B-field evolution) and A.8 (evolved particle spectrum). The model synchrotron (dashed lines) and IC (solid lines) emission are manually tuned to match the observed X-ray and  $\gamma$ -ray emissions. For the consistency of the results with the energy dependent morphology study presented earlier in Section 6.6, only SEDs obtained using GP and NN sky-maps are shown. It can be seen that the model synchrotron and IC emission is reasonably consistent with the observed X-ray and  $\gamma$ -ray data SEDs. The obtained values of the model parameters are listed in Table 6.5.

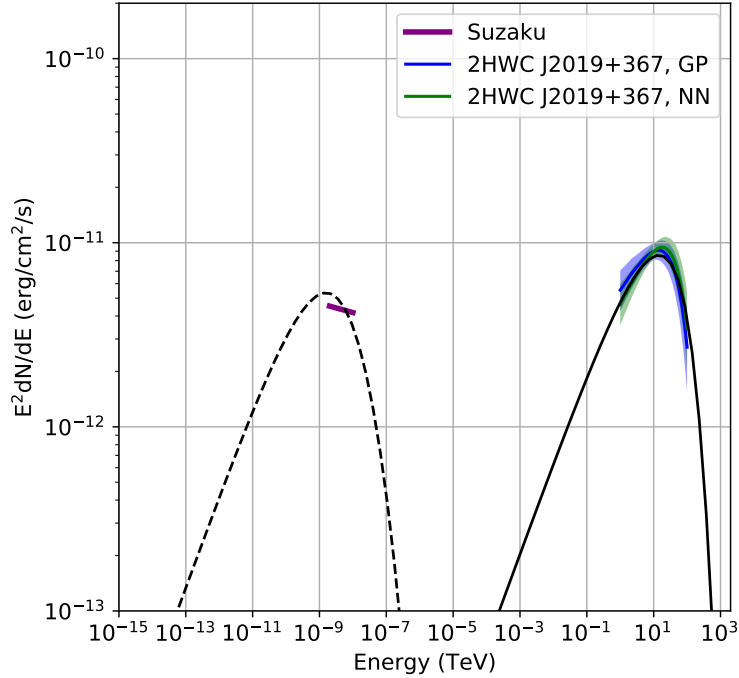


**Figure 6.25:** Model SED for synchrotron and IC are shown with dashed and solid lines respectively. The X-ray SED obtained by Suzaku and  $\gamma$ -ray SEDs obtained from using HAWC energy estimators are shown. The model SED is tuned by hand to provide an approximate match to the X-ray and HAWC TeV emission in the whole energy range. The required B-field is low with a value of  $1.8 \mu\text{G}$ .

The obtained low B-field of  $1.8 \mu\text{G}$  is not surprising as it depends on the relative normalisation of the peak synchrotron and IC emission. The peak of the X-ray (synchrotron) emission is lower compared to the TeV (IC) emission, therefore, a lower B-field is expected. The parent electron energy to produce X-ray of a given energy can be calculated as (Longair 2011):

$$E_e \approx 132 \text{ TeV} \left( \frac{E_{\text{X-ray}}}{1 \text{ keV}} \right)^{0.5} \left( \frac{B}{3 \mu\text{G}} \right)^{-0.5}. \quad (6.4)$$

To produce at least 2 keV X-rays, the required electron energy in  $1.8 \mu\text{G}$  B-field is about  $\sim 240$

Parameter	Value
Injected $e^\pm$ spectrum index (fixed)	-2.0
Exponential cut-off energy	$\sim 270$ TeV
Conversion efficiency ( $\epsilon$ )	15%
Pulsar braking index ( $n$ ) (fixed)	3
Initial birth period ( $P_0$ )	80 ms
True age ( $\tau$ )	7 kyr

**Table 6.5:** Parameters of the model presented in Figure 6.25.

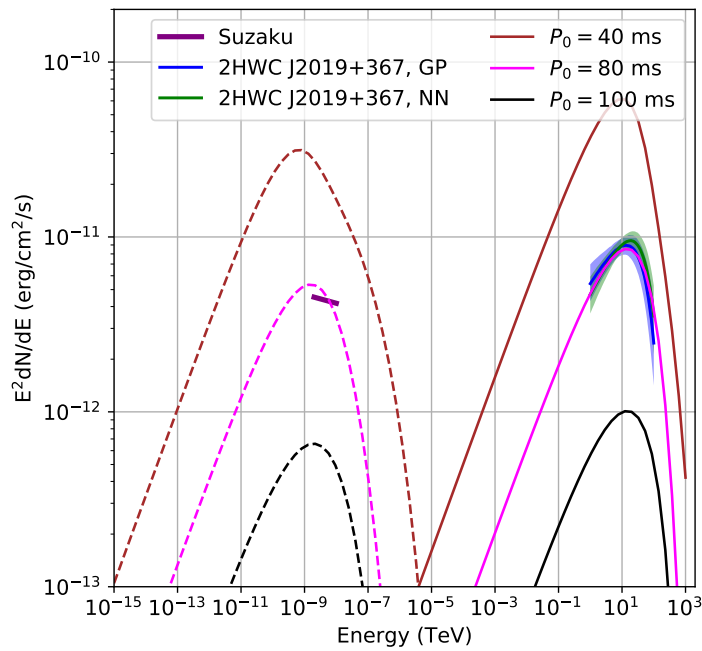


**Figure 6.26:** The effect of birth period ( $P_0$ ) in the devised model while fixing the other parameters of the model to the values shown in Table 6.5. With decreasing  $P_0$  the peak of model synchrotron and IC shift towards the lower energies. The normalisation of the model photon emission increases with decreasing  $P_0$  which corresponds to lower conversion efficiency ( $\epsilon$ ) in order to obtain the normalisation of the observed data.

TeV. X-rays above 2 keV energy would require even higher parent electron energies. Therefore the obtained cut-off in the injected electron spectrum at 270 TeV is reasonable.

After deciding the relative normalisation of the model synchrotron and IC peaks using the B-field of  $1.8 \mu\text{G}$ . The overall normalisation of the model synchrotron and IC emission can be decided by the injected power into the system, decided by  $P_0$  (see left panel of Figure 6.23), and by the conversion efficiency ( $\epsilon$ ). In Figure 6.26, the effect of birth period ( $P_0$ ) on the model photon emission SED is investigated while fixing the other model parameters to the values shown in Table 6.5. It can be seen that the model synchrotron and IC peak shifts towards lower energies with decreasing  $P_0$ .

To match the model synchrotron and IC peaks to the corresponding observed data peaks, the value of  $P_0$  should be 80 ms. The value of  $P_0$  also decides the true age ( $\tau$ ) of the system, which is calculated to be 7 kyr. Therefore the normalisation of the model synchrotron and IC peak is matched to the corresponding data peaks by a value of  $\epsilon = 15\%$ , which is reasonable value for a typical PWN scenario (Zhang et al. 2008). The obtained values of the parameters will be discussed in more details in Section 6.10.

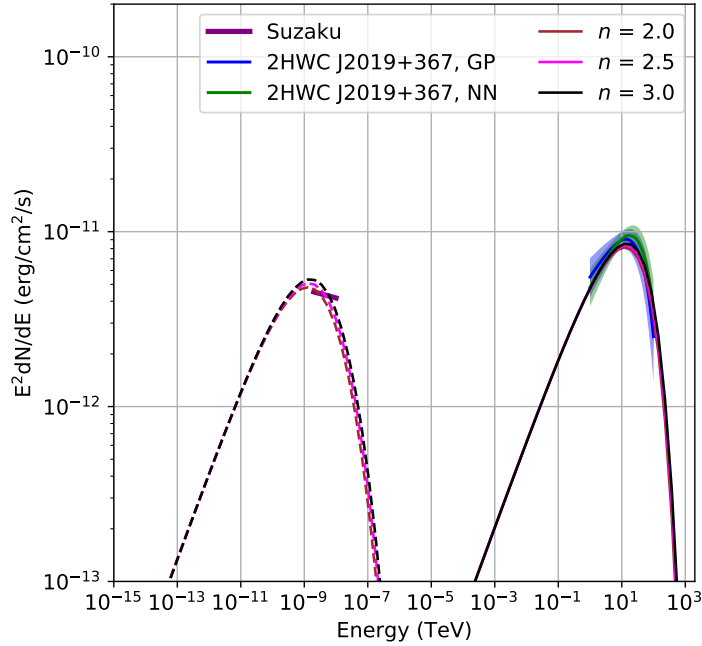


**Figure 6.27:** The effect of pulsar braking index ( $n$ ) in the devised model, while fixing the other parameters of the model to the values shown in Table 6.5.

Although the braking index of the pulsar is assumed to be  $n = 3$ , I also investigated its effect on the obtained model spectrum. In Figure 6.27, it can be seen that the effect of different values of  $n$  is very small and does not considerably change the model photon emission SED. Therefore fixing it to a value of  $n = 3$  will not change the obtained results significantly.

There are certain limitations of the outcomes of the one zone model mainly pertaining to the obtained B-field of  $1.8 \mu\text{G}$ . The estimated value of the B-field is very low in comparison to all expectations for a PWN and to the mean B-field of local ISM. This model would predict identical X-ray and  $\gamma$ -ray morphology, which is in contradiction with the observations, as the observed size of the X-ray PWN is significantly smaller than that of the TeV emission.

### 6.9.3 Two Zone Model

The low magnetic field derived in the One-zone model denote that the choice of describing the TeV emission together with the hard X-ray one, using the same population of electrons is not optimal. The limitations of the one zone model discussed in the previous Section 6.9.2 can be



resolved by considering that the electron population emitting in hard X-rays (2-10 keV) is only a component of the one emitting in the TeV  $\gamma$ -ray energies.

Using Equation (6.4) and just assuming minimum B-field of  $3 \mu\text{G}$  (equal to the local ISM) the corresponding parent electron population should be of energy  $\sim 300 \text{ TeV}$  for 5 keV X-rays. Given the radiation fields from the model described in Figure 6.24, at 300 TeV electron energies, the most relevant radiation field is CMB, the relevant cooling timescales are of the order of  $\sim 1 \text{ kyr}$ . Therefore, after picking the relevant timescales for the hard X-ray emitting electrons as last 1 kyr, I manually tuned the B-field to match the observed normalisation of X-ray emission. The required B-field is  $4 \mu\text{G}$ . As described before in Section 6.9.2, to match the model synchrotron

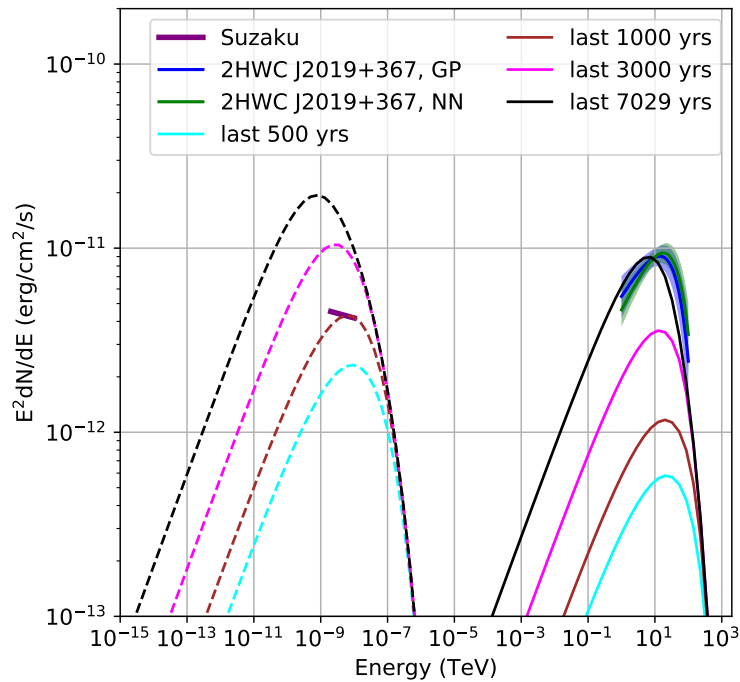


**Figure 6.28:** Model SED for synchrotron and IC are shown with dashed and solid lines respectively. Model SEDs due to electron population injected in last 0.5, 1, and 3 kyr is also drawn together with the total history (7 kyr). The X-ray SED obtained by Suzaku and  $\gamma$ -ray SEDs obtained from using HAWC energy estimators are shown. The model SED is tuned by hand to provide an approximate match to the X-ray emission by electron population injected in last 1 kyr, and TeV emission in the whole energy range by the total injection history (7 kyr). The required B-field is  $4 \mu\text{G}$ .

and IC peak to the observed X-ray and TeV emission peak a birth period of 80 ms is required. Therefore the true age of the system also remains the same with a value of 7 kyr. However, due to the increased B-field, the conversion efficiency is increased to a value of 20% in this case. The corresponding plots describing the model are shown in Figures A.9 (injected spin-down power evolution and injected electron spectrum), A.10 (B-field evolution) and A.11 (evolved particle spectrum). The other parameters of the one zone model described in Section 6.9.2 such as  $n$ , injected electron spectrum index and cut-off energy are the same as shown in Table 6.5.

In Figure 6.28 the model SED lines for electrons injected in last 0.5, 1 and 3 kyr are also

shown with the total injection history of  $\sim 7$  kyr. In this case, the total history synchrotron emission overshoots the observed X-ray SED by a factor of 4-5 at 2 keV. Which is not surprising because it is likely that due to the smaller region of the X-ray observations some of the emission might be missing. It is also mentioned by the authors in (Mizuno et al. 2017a) that the observed X-ray emission should be taken as the lower limit.

The X-ray emission seen by Suzaku is  $\sim 4' \times 10'$  in full width at half maximum (FWHM) (Mizuno et al. 2017a) and HAWC emission is about  $\sim 20' \times 50'$  in the same measure. Therefore the TeV emission seen by HAWC is a factor of 25 in solid angle compared to Suzaku emission. Taking the hard X-ray emission seen by Suzaku as a corresponding component of TeV emission with the same parent electron population. The Suzaku study might have missed more extended emission with a factor of  $\sim 5$  lower in surface brightness. The peak of the X-ray SED at 2 keV is about  $\sim 4 \times 10^{-12}$  erg/cm<sup>2</sup>/s, therefore by taking into account the expected missing emission it would be around  $\sim 2 \times 10^{-11}$  erg/cm<sup>2</sup>/s. It can be seen that for the total history the synchrotron model peak is around the value of  $\sim 2 \times 10^{-11}$  erg/cm<sup>2</sup>/s. For the total history of the system, the expected X-ray emission and observed HAWC TeV emission is compared to the model emission, it can be seen that the model total IC emission is reasonably consistent with the observed TeV emission.

## 6.10 Discussion

To motivate the obtained birth period ( $P_0$ ) of 80 ms and true age ( $\tau$ ) of 7 kyr, one can compare it with the behaviour of HESS J1825-137, which is a similar system to 2HWC J2019+367. Both of these sources are bright extended TeV sources with similar associated pulsars. The associated pulsar of HESS J1825-137 is PSR B1823-13. The comparison of the pulsar properties of PSR J2021-3651 and PSR B1823-13 are shown in Table 6.6. It can be seen that both the pulsars have

Sources	2HWC J2019+367	HESS J1825-137
Associated pulsar	PSR J2021+3651	PSR B1823-13
Present period ( $P$ )	104 ms	102 ms
$\dot{P}$	$9.57 \times 10^{-14} s^{-2}$	$7.5 \times 10^{-14} s^{-2}$
$\dot{E}$	$3.4 \times 10^{36}$ erg/s	$2.8 \times 10^{36}$ erg/s
Characteristic Age ( $\tau_c$ )	17.2 kyr	21.4 kyr
Distance $d$	$\sim 1.8$ kpc	$\sim 4$ kpc

**Table 6.6:** Comparison of the pulsar associated pulsar properties of 2HWC J2019+367 and HESS J1825-137 (Manchester et al. 2005).

similar  $P$ ,  $\dot{P}$ ,  $\dot{E}$ , and  $\tau_c$ . However, the main difference lies in the observed  $\gamma$ -ray luminosities of these two systems. For a given distance of 1.8 kpc and 4 kpc for 2HWC J2019+367 and HESS J1825-137, the integrated  $\gamma$ -ray luminosities of the observed TeV emission are  $\sim 10^{33}$  and  $\sim 10^{35}$  erg/s respectively. In order to match the  $\gamma$ -ray luminosity of 2HWC J2019+367 to the one for HESS J1825-137, the distance of 2HWC J2019+367 system has to be  $\sim 18$  kpc. However,

with the previous distance measurements as explained before this seems to be very unlikely. In both the systems, the assumed conversion efficiency of spin down power of the pulsar to  $e^\pm$  are  $\sim 15\text{-}20\%$  (Aharonian et al. 2006) (Zhang et al. 2008). If the radiation fields in both the systems do not differ drastically, and with a similar B-fields of few  $\mu\text{G}$ , the efficiency of  $e^\pm$  to  $\gamma$ -ray production should be similar. Therefore, one of the plausible explanation then would be that the PSR J2021+3651 has a larger  $P_0$  compared to PSR B1823-13 ( $\sim 1$  ms) (Khangulyan et al. 2018). Due to the similar  $P$  and  $\dot{P}$  of the two systems and assuming  $\dot{P}$  did not change rapidly in the past, PSR B1823-13 must have injected more power into the system compared to PSR J2021+3651.

The larger  $P_0$  of PSR J2021+3651, in turn, makes the 2HWC J2019+367 system younger ( $\sim 7$  kyr) compared to its characteristic age of  $\sim 17$  kyr. It is also favoured by comparing the peak TeV emission of HESS J1825-137 and 2HWC J2019+367, which are at  $\sim 0.1$  TeV and  $\sim 20$  TeV respectively. For HESS J1825-137, assuming that the true age of the system is close to its characteristic age, the 2HWC J2019+367 system should be younger to explain the higher peak TeV emission and hard spectral index of  $\sim 1.6$ . One can estimate the parent electron population energy for a given  $\gamma$ -ray photon energy in the Thompson regime (only assuming CMB) (Longair 2011) as:

$$E_e \simeq 17.2 \text{ TeV} \left( \frac{E_{\gamma\text{-ray}}}{1 \text{ TeV}} \right)^{0.5}. \quad (6.5)$$

For 20 TeV  $\gamma$ -ray photon the parent electron population would be of energy  $\sim 80$  TeV. The KN effect only starts to dominate above a  $\sim 300$  TeV electron energies with only CMB (Hinton & Hofmann 2009). The cooling timescales for electrons of energy  $E_e$  in given radiation and magnetic fields can be calculated as:

$$\tau_{\text{cool}} \approx 3.1 \times 10^5 \left( \frac{U}{\text{eVcm}^{-3}} \right)^{-1} \left( \frac{E_e}{\text{TeV}} \right)^{-1} \text{ yr}, \quad (6.6)$$

where  $U = f_{\text{KN}} \times U_{\text{ph}} + 0.025(B/\mu\text{G})^2 \text{ eV/cm}^3$ , is the total energy density in the radiation ( $U_{\text{ph}}$ ) and magnetic fields respectively and  $f_{\text{KN}}$  is the normalisation factor to take into the suppression of IC losses due to KN effect.  $f_{\text{KN}}$  can be calculated as:

$$f_{\text{KN}} \approx \left( 1 + 15 \frac{E_e}{\text{TeV}} \frac{E_T}{\text{eV}} \right)^{-1.5} \quad (6.7)$$

Where  $E_T$  is the target photon energy (Hinton & Hofmann 2009). Using equation 6.6, the corresponding cooling timescale for 80 TeV electrons in 4  $\mu\text{G}$  B-field and CMB are of the order of  $\sim 8$  kyr, which is similar to the estimated age of the system of  $\sim 7$  kyr. The electrons  $> 80$  TeV energies are already cooled, making the TeV spectrum softer after  $\sim 20$  TeV  $\gamma$ -ray energies. The lower energy electron population  $< 80$  TeV has not cooled yet, making the spectral index hard upto 20 TeV in  $\gamma$ -ray energies.

In Figure 6.29, a zoomed in version of the 2HWC J2019+367 region at several wavelengths is shown, with radio in green, X-ray in blue and infrared in red. It can be seen that the extension of the X-ray emission is very small compared to the whole TeV emission region. The X-ray emission is mostly coincident with the pulsar position as discussed before. The cone-shaped radio emission starting at the pulsar location and extending towards the west region give us the

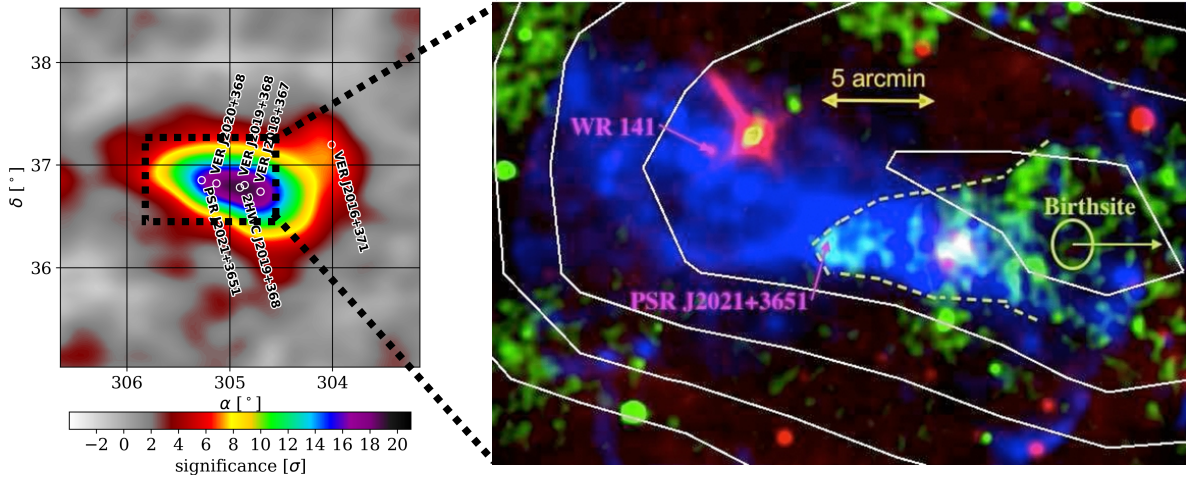


**Figure 6.29:** Left: 2HWC J2019+367 in GP sky-maps, the dashed rectangle is shown to highlight the region corresponding to the image shown in the right side. Right: Composite image (corresponding to the region highlighted with dashed rectangle) in false colors of radio (green), X-ray (blue) and infrared (red) emission observed in the vicinity of PSR J2021+3651 by VLA 20 cm, XMM 18 keV and MSX 8.3  $\mu$ m respectively. Solid lines show 3, 4, 5, 6, and 7 $\sigma$  contours of VERITAS observation. The ellipse shows the closest birth-site of PSR J2021+3651 suggested by the radio morphology shown with the dashed line. The arrow indicates the direction of the birth-site of the pulsar if it happened to be farther away. The Figure is taken from (Aliu et al. 2014).

insight about the likely birth location of the pulsar. It can be seen that the suggested birth location of the pulsar is close to the peak TeV emission. Which further supports the peak emission in TeV energies being offset from the pulsar location, because the lower energy electrons can still emit in TeV energies via IC due to their longer cooling timescales and by that time the pulsar should have moved towards the other location. On the other hand, due to the higher energies of the X-ray emitting electrons and therefore smaller cooling timescales, the X-ray emission is closer to the pulsar position. If we assume that the pulsar was born at the location of the peak TeV emission the corresponding angular distance is  $\sim 0.3^\circ$ . Given the distance to pulsar as  $\sim 1.8$  kpc and with estimated age of the system is  $\sim 7$  kyr. With the assumption that the current location of the pulsar is due to only its proper motion, the transverse velocity would be  $\sim 1300$  km/sec. The obtained transverse velocity is certainly at the higher end of the pulsar transverse velocity distribution (Faucher-Giguere & Kaspi 2006), however it would not unrealistic.

The measured extension of 2HWC J2019+367 is about  $0.36^\circ$  along the major axis obtained from the morphology fit using an asymmetric 2D Gaussian as described in Section 6.7, which would correspond to a projected size of  $\sim 11$  pc with a given distance of  $\sim 1.8$  kpc to the pulsar. In the energy dependent morphology study (see Section 6.6), the measured extension has smallest error bars in energy band 3 (see Figure 6.15), where the measured extension is about the same with a value of  $\sim 0.35^\circ$  in both the energy-skymaps. The energy band 3 corresponds to the energy range between 10 and 56 TeV. Using equation (6.5), the corresponding parent population of electrons would be in the energy range between  $\sim 50$  and  $\sim 130$  TeV. The size of the TeV emission in

energy band 3 is about  $\sim 11$  pc. The median energy of energy band 3 is  $\sim 23$  TeV in the reconstructed  $\gamma$ -ray energy, which corresponds to electron energy of about  $\sim 80$  TeV (using equation (6.5)). At this energy, one can calculate the cooling timescale to be  $\sim 7$  kyr using equation (6.6), by taking into account B-field of  $4 \mu\text{G}$  and the CMB. Therefore, the corresponding transport speed of electrons is about  $\sim 1500$  km/s or a diffusion coefficient of about  $\sim 2.5 \times 10^{27}$  cm<sup>2</sup>/s. In the case of Bohm diffusion, the diffusion coefficient in  $4 \mu\text{G}$  B-field would be  $\sim 6 \times 10^{26}$  cm<sup>2</sup>/s (Aharonian 2004) (page number 209). Typical value for diffusion coefficient at  $\sim 80$  TeV electron energy for the ISM would be  $\sim 9 \times 10^{29}$  cm<sup>2</sup>/s (Aharonian 2004) (page number 151). Therefore, we see that the obtained value of diffusion coefficient is close to the Bohm diffusion. If this is the mechanism dominating the transport for this source, it would imply that the magnetic field is much more turbulent than averages on the ISM, which is not surprising taking into account that we are in a region heavily dominated by the pulsar wind. Hence, the advection velocity or diffusion coefficient is constrained by the morphology of the TeV emission region. However, it is to be noted that for a detailed study of transport mechanisms (diffusion/advection) would require a better measurement of energy dependent morphology with more data from future observations.

## 6.11 Conclusions

Despite the previous studies performed on the 2HWC J2019+367 region, it is still classified as unidentified owing to its extended complex emission region. The previous studies suggest it to be a Pulsar Wind Nebula (PWN) powered by the pulsar PSR J2021+3651. This pulsar has an X-ray PWN but its association with observed TeV emission is suggested but not confirmed yet. VERITAS has observed the emission region and resolved it into two sources. VER J2019+368 is responsible for the bulk of the emission, and VER J2016+371 which is a point source. VERITAS reported a hard spectral index of 1.7 and extended morphology for the TeV emission. However, no spectral cut-off was observed upto 30 TeV energy.

In HAWC data, 2HWC J2019+367 is observed with ample significance as a bright extended source. 2HWC J2019+367 is significantly observed  $>56$  TeV reconstructed  $\gamma$ -ray energy in the HAWC energy sky-maps. Recently developed energy estimation techniques for HAWC provide the opportunity to examine the energy-dependent morphology of the source. A detailed systematic study is performed, which is required to look for the energy dependent morphology of 2HWC J2019+367. The idea here is to retain the best PSF possible without a significant loss in sensitivity, which is desirable to study the energy dependent morphology of a given source. Therefore, a selection prescription for the energy-skymaps was given and energy bands were defined. It is shown that the selection prescription improves the PSF by 40% with only a 15% loss in significance in all the energy bands. It is to be noted that the prescription for energy bands is not limited to the analysis of 2HWC J2019+367 only, as it can be applied to any other source to probe its energy dependent morphology in the HAWC analysis framework.

A slice profiling tool is developed to make excess count profiles of the HAWC sky-maps with preferred slice characteristics. The developed tool is applied in energy bands to study the energy dependent morphology of 2HWC J2019+367. It is found that 2HWC J2019+367 shows a hint of energy dependent morphology, where its size seems to decrease with increasing energy. The

significance of the results is limited due to lack of data. Therefore more data from future observations is required to draw a firm conclusion on the energy dependent morphology of 2HWC J2019+367. The recent upgrade with the outrigger array will be very helpful, as it increases the instrumented area by 4 to 5 times and will greatly enhance the currently limited data, especially at energies above 10 TeV. It is to be noted that this is the first study in HAWC to investigate the energy dependent morphology of a source.

To obtain the general morphological features and spectrum of 2HWC J2019+367, different source morphologies and spectral hypotheses were tested in different HAWC datasets. The best source hypothesis for 2HWC J2019+367, is an asymmetric two-dimensional (2D) Gaussian for morphology with a cut-off power law spectrum. A clear residual of VER J2016+371 is obtained. Therefore in a next step, a joint fit of 2HWC J2019+367 with VER J2016+371 is performed. Both the sources are observed with more than  $5\sigma$  significance. This means the discovery of a new HAWC source.

The morphology of 2HWC J2019+367 in energy sky-maps is very similar to the one observed by VERITAS observations. The position angle of the semi-major major axes in the TeV emission is about  $\sim 70^\circ$ . The X-ray emission observed using Suzaku also has a preferred semi-major axis. The position angle of the X-ray emission is about  $\sim 71^\circ$ . The consistency of similar position angles show a preferred direction of emission both in X-ray PWN and TeV emission and therefore strongly supports their association.

The spectrum of 2HWC J2019+367 is measured with a cut-off around  $\sim 45$  TeV reconstructed energy in HAWC energy-skymaps. VERITAS observations do not see any cut-off upto 30 TeV photon energy. Similar spectral indices were obtained with a value of  $1.68 \pm 0.11$  for GP and  $1.61 \pm 0.10$  for NN energy-skymaps and  $1.7 \pm 0.38$  for VERITAS. However, a higher flux normalisation was observed in HAWC energy-skymaps compared to VERITAS observations, reasons for which are still unclear and are under investigation.

Finally, spectral modelling of the HAWC emission together with X-ray emission observed by Suzaku is performed, in a leptonic scenario of PWN of PSR J2021+3651. A leptonic scenario is preferred because of the hint of shrink in size of 2HWC J2019+367 with increasing energy and suggested association of X-ray PWN with the TeV emission. The results of spectral analysis are found to be consistent with a PWN scenario. A mean B-field of  $1.8 \mu\text{G}$  is obtained in the vicinity of the emission region, which is very low compared to all expectations for a PWN and to the mean B-field of local ISM. However, considering the different electron populations responsible for 2-10 keV X-ray emission and for the whole TeV emission a higher mean B-field of  $4 \mu\text{G}$  is obtained.

The obtained results suggest that the pulsar should have a birth period of 80 ms, which also corresponds to an age of  $\sim 7$  kyr, whereas the characteristic age of the pulsar is  $\sim 17$  kyr. By comparing the obtained PWN system properties for 2HWC J2019+367 to the similar system of HESS J1825-137, it is argued that the low  $\gamma$ -ray luminosity of 2HWC J2019+367 ( $\sim 10^{33}$  erg/s) in comparison to HESS J1825-137 ( $\sim 10^{35}$  erg/s) is due to its larger birth period. The larger birth period and a younger age are also favoured to explain the peak TeV emission at 20 TeV and a hard spectrum of 2HWC J2019+367. The peak of the TeV emission of 2HWC J2019+367 is offset from the location of the pulsar, which is a very well known behaviour of PWNe of similar age. The radio emission observed in the vicinity also suggest the birth site of the pulsar being

## 6. SPECTRAL AND MORPHOLOGICAL STUDIES OF 2HWC J2019+367

---

close to peak TeV emission, which further supports the leptonic scenario of a PWN.

Therefore, with the results obtained in this analysis of 2HWC J2019+367, on the energy dependent morphology study, morphology and spectral studies and modelling of the TeV emission together with the X-ray data, it can be concluded that 2HWC J2019+367 is likely to be TeV PWN of PSR J2021+3651. In the future analysis, with more data, the energy dependent morphology of 2HWC J2019+367 can be concluded and with a better understanding of the newly developed energy estimators the obtained spectrum of 2HWC J2019+367 can be better understood.





# 7

## Conclusion

In this thesis, a number of contributions are made to improve the performance of the High Altitude Water Cherenkov (HAWC)  $\gamma$ -ray observatory, especially at the highest energies. A detailed analysis of a prominent high energy source, 2HWC J2019+367, is presented to investigate its nature. HAWC detects cosmic- and  $\gamma$ -rays in the energy range of 1-100 TeV using an array of Water Cherenkov Detectors (WCDs) (see Chapter 1 and 2). To improve the air shower reconstruction at the energies above 10 TeV, HAWC was recently upgraded with a sparse array of smaller WCDs, the outrigger array. The footprint of the air shower at 10 TeV energy becomes comparable to the size of the HAWC array. The outrigger array will improve the core estimation for events falling outside the HAWC array and therefore will improve the reconstruction of those events. Simulation studies to decide on the different components of the outrigger array are presented. The results are to use an 8" PMT and black wall color tanks with a separation of at least 10 m between two outriggers. The results presented in this study are incorporated in the final outrigger array design (see Chapter 3).

To combine the shower reconstruction of the outrigger array with the main array, and to improve the shower reconstruction, a new Monte Carlo (MC) template-based air shower reconstruction method is developed. The developed algorithm estimates the core location and energy of the primary  $\gamma$ -ray. The goodness of fit (GoF) of the method is used as a  $\gamma$ /hadron separator. It is to be noted that the newly developed method is described on HAWC, however, it can be applied to particle detector arrays in general. The new method improves the core resolution by three-fold for the energies  $< 10$  TeV for showers falling on the array. Similar three-fold improvement is obtained for showers falling outside the array for the energies  $> 10$  TeV. The performance obtained on energy reconstruction is promising for air shower arrays, with a  $\sim 50\%$  energy resolution in the energy range  $< 10$  TeV and for higher energies, the energy resolution improves to  $\sim 25\%$ . On the

significance of the Crab Nebula observation, an improvement of  $>20\%$  is achieved in the HAWC analysis bins 4 to 9 over the standard reconstruction. It is shown that the LH method already performs significantly better compared to the standard HAWC reconstruction, however, it is to be noted that further improvement in its performance is expected with corresponding improvements in detector simulations.

The method is applied to the combined reconstruction of HAWC and the outrigger array. It is shown that air showers are reconstructed successfully for this mixed type particle detector array. The obtained core resolution including outriggers (for the events falling on the outrigger array) is similar to the core resolution of the main array (for the events falling on the main array) at energies greater than 10 TeV. The developed method is in consideration for the reconstruction of the archival data together with the combined reconstruction of the main array and outrigger data. In principle, this method can be applied to perform the reconstruction of the CRs as well, however, the generation of the MC templates for the different particle species will be comparatively more challenging. Additionally, a similar procedure for producing the MC templates can be followed in order to perform the direction reconstruction. The reconstruction of CR events together with  $\gamma$ -ray events and the reconstruction of particle arrival direction would be the future avenues to explore. This method is an excellent candidate for present particle air shower arrays such as Tibet AS- $\gamma$  Experiment (Amenomori et al. 2015) and ARGO-YBJ (Bartoli et al. 2015) and future observatories such as LHAASO (Di Sciascio 2016) and a next-generation observatory to be built in the Southern Hemisphere (Ohnishi et al. 2017; Becherini et al. 2017; Conceição et al. 2017; Di Sciascio et al. 2017; Schoorlemmer et al. 2017) (see Chapter 4).

The HAWC  $\gamma$ -ray observatory has shown its effectiveness by detecting several  $\gamma$ -ray sources presented in the 2HWC catalogue (Abeysekara et al. 2017b). 2HWC J2019+367 is one of the most prominent high energy source in the Cygnus region. 2HWC J2019+367 shows significant emission above 56 TeV in  $\gamma$ -ray reconstructed energies. Previous studies have suggested it to be the Pulsar Wind Nebula (PWN) of PSR J2021+3651. However, the nature of the source still remains unknown owing to its complicated extended emission region. In this thesis, I have presented detailed spectral and morphological studies of 2HWC J2019+367. The properties of a PWN system can be characterised using different pulsar models, some of which are used in the modelling of 2HWC J2019+367. The multi-wavelength emission from PWNe is modelled with different approaches, such as MHD and energy spectrum models (see Chapter 5). In the study of 2HWC J2019+367, the energy spectrum modelling approach is used.

The study of energy dependent morphology of 2HWC J2019+367 is performed using the datasets from the recently developed energy estimators (energy sky-maps). To study energy dependent morphology, the best PSF possible is desirable together with enough data in a given energy range. In order to achieve this, a detailed systematic study is performed on the energy sky-maps in which, energy bins are combined to give a new definition of energy bands. A selection prescription for the energy-skymaps is given and it is shown that it indeed improves the PSF by 40% with only a 15% loss in significance in all the energy bands. A slice profiling tool is developed within the HAWC analysis framework to obtain excess counts profiles with the desired slice characteristics, which is used on the energy band sky-maps, to look for the energy dependent morphology of 2HWC J2019+367. It is found that 2HWC J2019+367 shows a hint of energy dependent morphology with a decrease in its size with increasing energy. It is to be

## 7. CONCLUSION

---

noted that this is the first energy dependent morphology study of a source using the HAWC data. The procedure and tools developed for this analysis are not only limited to the study of 2HWC J2019+367, as they can be applied to probe the energy dependent morphology of any other source in the HAWC dataset.

A combined spectral and morphological fit of the 2HWC J2019+367 emission region is performed. A cut-off power law with an asymmetric 2D Gaussian morphology is found to be the best describing model. A clear residual of VER J2016+371, another point source resolved by previous VERITAS observation, is obtained. In a joint fit, together with VER J2016+371 as a point source and power law spectral shape, both the sources are observed with more than  $5\sigma$ . This means the discovery of a new HAWC source.

The morphology obtained in this analysis is very similar to the one obtained by VERITAS. The position angle of the semi-major axis in the TeV emission is very similar to the one in X-ray emission observed by Suzaku. The similar direction of the X-ray and TeV emission strongly supports their association. A cut-off in the spectrum of 2HWC J2019+367 is obtained at about  $\sim 45$  TeV in  $\gamma$ -ray reconstructed energy. However, it is to be noted there are certain systematic differences in the obtained spectrum using the different HAWC datasets. Currently, efforts are being made to resolve this issue. Therefore, it is possible that the presented results might change slightly with future developments, however, a drastic change in the shown results is unlikely.

Modelling of the TeV emission of 2HWC J2019+367 together with observed X-ray emission using Suzaku is performed in a PWN scenario. A low B-field of  $1.8 \mu\text{G}$  is obtained while modelling the whole range of TeV emission together with hard X-ray emission of 2 to 10 keV. The B-field of  $1.8 \mu\text{G}$  is very low to all the expectations of a PWN and to the local ISM. Additionally, in this case, the size of the X-ray emission would be identical to the size of the TeV emission, which is in contradiction with the observations. Therefore, considering the hard X-ray emission seen by Suzaku as a corresponding component of TeV emission with the same parent electron population. The 2-10 keV X-ray emission is modelled with a recently injected electron population of  $\sim 1$  kyr, together the TeV emission is described with the total history of  $\sim 7$  kyr. In this case, a mean magnetic field of  $4 \mu\text{G}$  is obtained.

The obtained birth period of the pulsar is  $\sim 80$  ms, which corresponds to an age of  $\sim 7$  kyr. The obtained age suggest than the system is younger than its characteristic age of  $\sim 17$  kyr. The behaviour of the system is compared to the similar system of PWN HESS J1825-137, which supports that the 2HWC J2019+367 is a younger system with a larger birth period. The peak TeV emission at 20 TeV and a hard spectral index of 2HWC J2019+367 can also be explained with the obtained birth period and age of the system. The results of the spectral modelling of 2HWC J2019+367 are consistent with a typical PWN scenario. Additionally, the strong association of X-ray PWN of PSR J2021+3651 and TeV emission further supports that 2HWC J2019+367 is likely to be the TeV PWN of PSR J2021+3651 (see Chapter 6).

More data from future observations with HAWC and its outrigger array will help in better understanding the 2HWC J2019+367. To draw firm conclusions on the energy dependent morphology, the outrigger array will play a crucial role, as its 4-5 times bigger instrumented area compared to the main array will greatly enhance the statistics of observed events specifically at the highest energies. Further development of the reconstruction techniques such as shown in Chapter 4, will be very crucial in improving the PSF of the HAWC observatory and for bet-

ter measurement of spectrum and morphology. The three-fold better angular resolution above 10 TeV  $\gamma$ -ray energies of the CTA north (<http://www.cta-observatory.org/science/cta-performance/>) will be helpful to study the overall morphology in greater details.



# Appendix

$\mathcal{B}$	$f_{\text{hit}}$	PINC ( $\mathcal{P}$ ) Maximum	Compactness ( $\mathcal{C}$ ) Minimum	GoF Maximum
1	6.7 - 10.5%	<2.2	>7.0	4.6
2	10.5 - 16.2%	1.8	12.59	3.1
3	16.2 - 24.7%	1.3	15.85	2.5
4	24.7 - 35.6%	1.4	12.59	2.7
5	35.6 - 48.5%	1.4	15.85	1.5
6	48.5 - 61.8%	1.3	10.00	1.1
7	61.8 - 74.0%	1.2	19.95	5.0
8	74.0 - 84.0%	1.3	12.59	1.8
9	84.0 - 100.0%	1.3	5.01	5.0

**Table A.1:** The analysis cuts for LH method, defined over analysis bins ( $\mathcal{B}$ ), which correspond to a certain fraction of the available PMTs that observed a non-zero signal ( $f_{\text{hit}}$ ). The PINC, Compactness and GoF cuts determine the background rejection and are optimised on the Crab data for highest statistical significance. The results corresponds to “including the off-array events” as described in the text.

Parameter	Value	Description
RUNNR	1	run number
SEED	20994 0 0	seed for 1. random number sequence
SEED	19976 0 0	seed for 2. random number sequence
SEED	3638 0 0	seed for 3. random number sequence
NSHOW	100	number of showers to generate
PRMPAR	1	article type of prim. particle
<b>ERANGE</b>	30000 30000	energy range of primary particle (GeV)
ESLOPE	0	slope of primary energy spectrum
<b>THETAP</b>	0. 0.	range of zenith angle (degree)
<b>PHIP</b>	0. 360.	range of azimuth angle (degree)
FIXHEI	0. 0	first interaction height and target
FIXCHI	0.	starting altitude (g/cm <sup>2</sup> )
ATMOD	22	Atmospheric model
<b>MAGNET</b>	27.717 29.907	magnetic field at the HAWC site
ELMFLG	F T	em. interaction flags (NKG,EGS)
STEPFC	1.0	mult. scattering step length fact.
HADFLG	0 0 0 0 2	flags hadr. interact. and fragmentation
ECUTS	0.05 0.05 0.0003 0.0003	energy cuts in GeV for particles
MUADDI	F	additional info for muons
MUMULT	T	muon multiple scattering angle
ELMFLG	F T	em. interaction flags (NKG,EGS)
STEPFC	1.0	mult. scattering step length fact.
RADNKG	200.E2	outer radius for NKG elect. distrib.
<b>OBSLEV</b>	4100.E2	observation level (in cm)
ARRANG	0.	rotation of array to north
LONGI	T 20. T F	longit.distr. and step size and fit and out
MAXPRT	0	max. number of printed events
ECTMAP	1.E4	cut on gamma factor for printout
DIRECT	location of output directory	output data directory
DATDIR	location of data files	Directory with CORSIKA data files
DATBAS	T	write .dbase file
PAROUT	T F	
DEBUG	F 6 F 1000000	debug flag and log.unit for out
EXIT		terminates input

**Table A.2:** CORSIKA simulation input card, for outrigger simulations.

A. APPENDIX

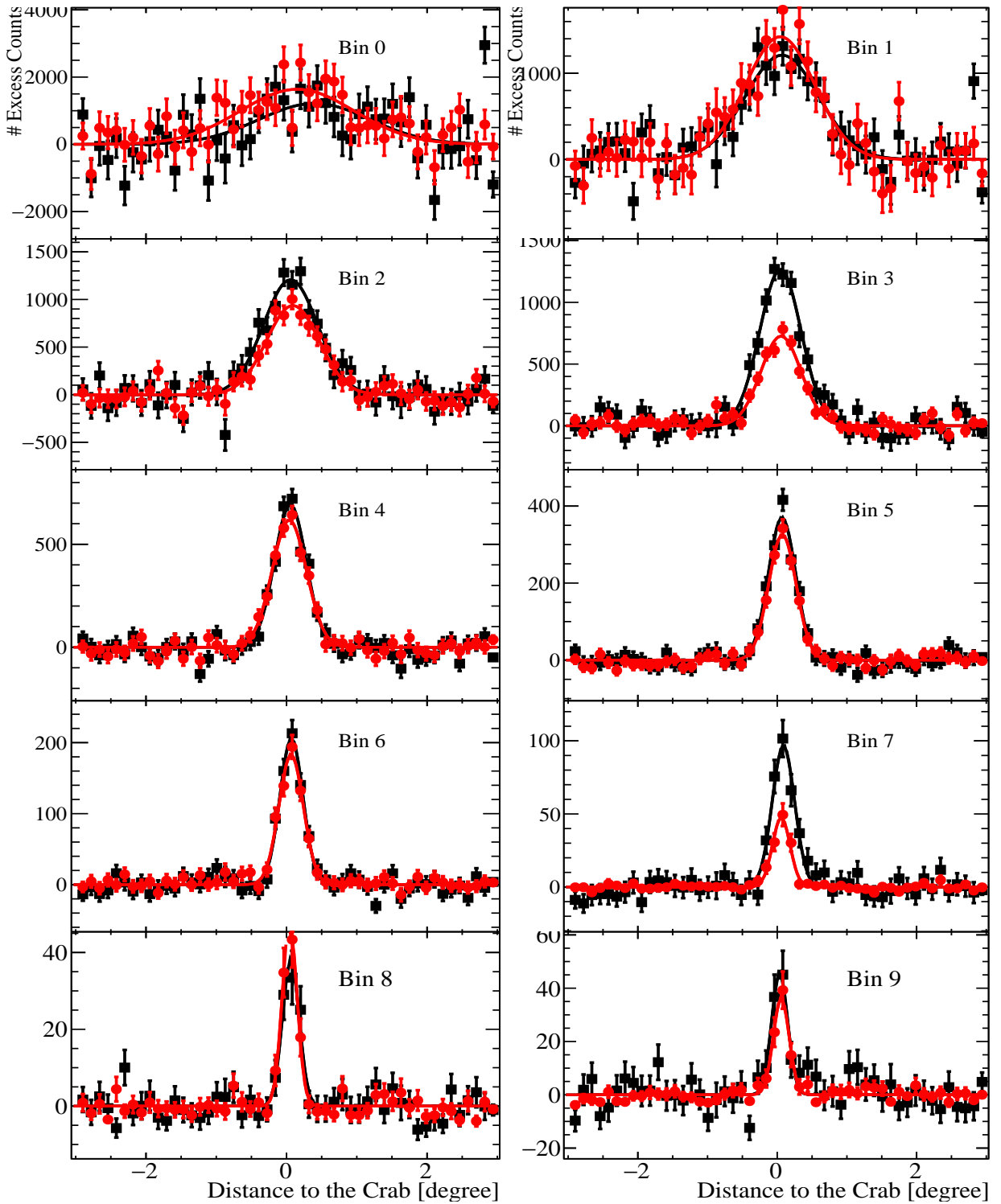


**Figure A.1:** Excess count profiles in  $\mathcal{B}$  0 to 9 on Crab data. The reconstructed data using LH and SFCF methods are shown in red and black colours respectively. The excess count profiles are fitted with a Gaussian in both the cases. The location of the Crab is at 0 on the X-axis. The results corresponds to “including the off-array events” as described in the text.

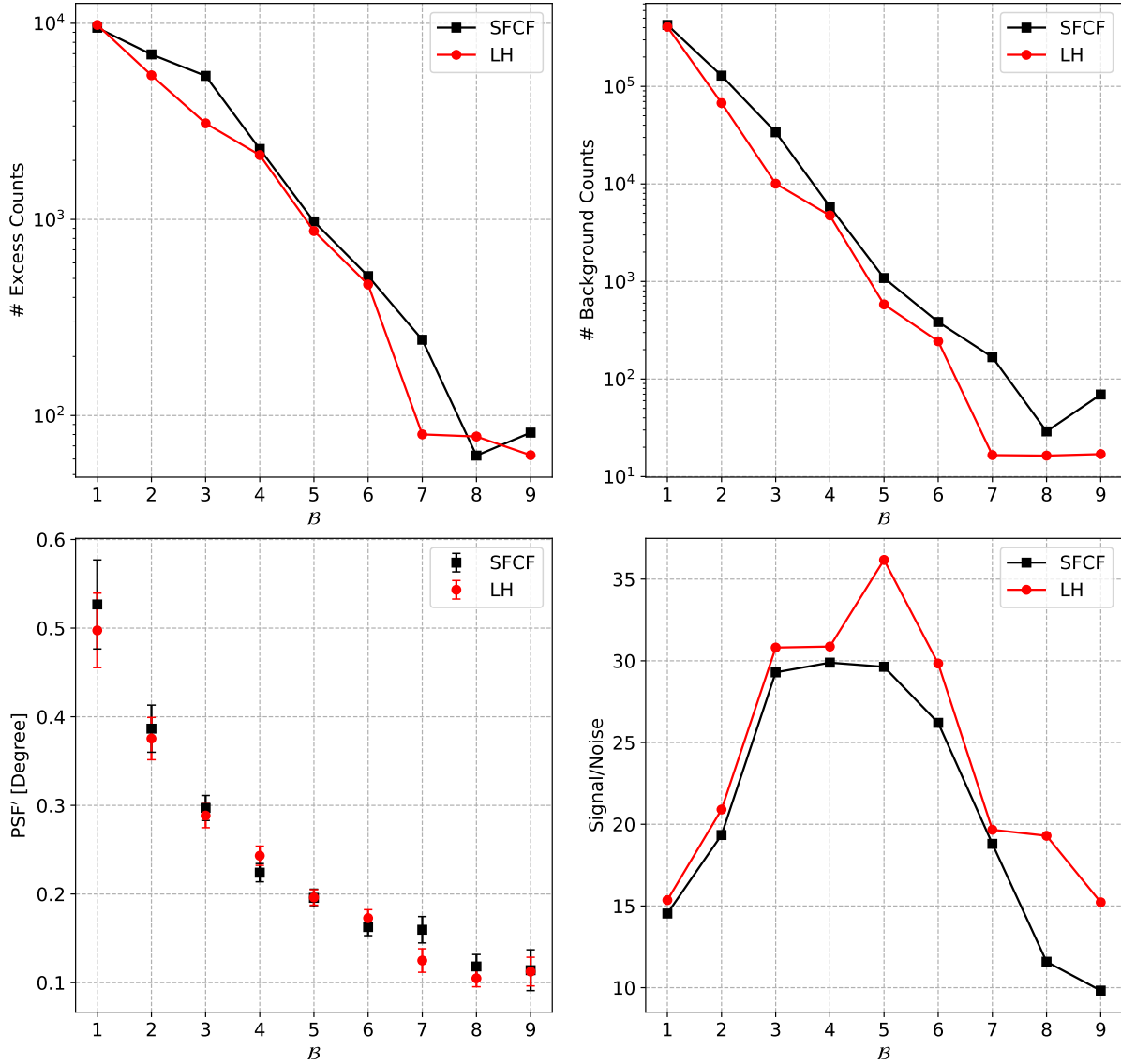


**Figure A.2:** The results are shown for the Crab data using the slice profile analysis as described in the text. SFCF is the standard core fit method used in HAWC and LH stands for the new likelihood method. Top panel: excess counts (left) and background counts (right) as a function of  $B$  in  $1\sigma$  region of the fitted Gaussian to the slice profiles. Bottom panel: PSF' (left),  $1\sigma$  width of the fitted Gaussian and signal to noise ratio (right) in that region (right) as a function of  $B$  bin. The results corresponds to “including the off-array events” as described in the text.



## A. APPENDIX

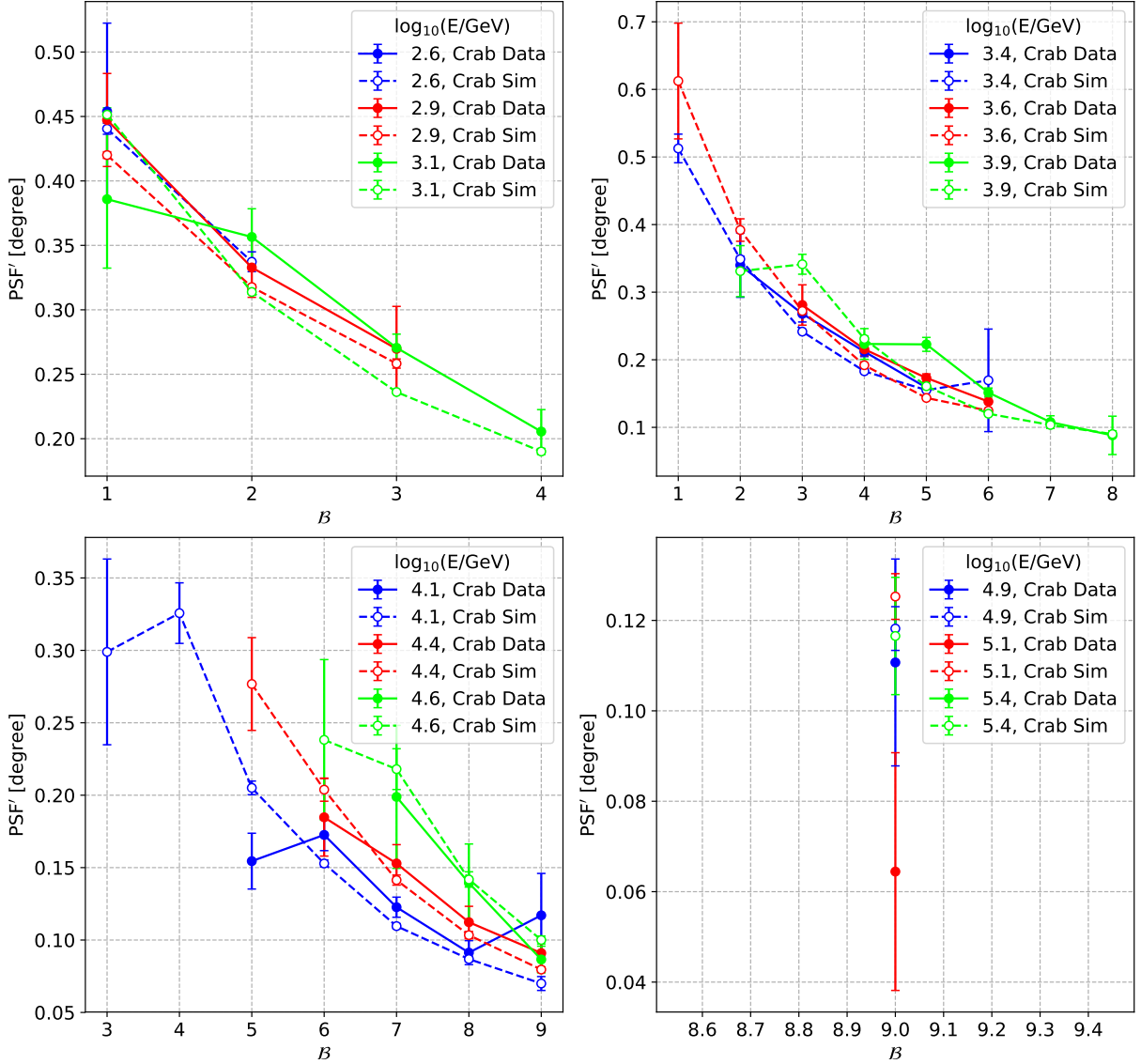


**Figure A.3:** PSF' as a function of  $B$  bins for a given energy bin. The mean energy ( $E$ ) in  $\log_{10}(E/\text{GeV})$  is denoted for each energy bin. The comparison in PSF' obtained between the Crab data and simulated Crab is shown for all energy bins, 3 energy bins per plot with increasing energy. PSF' is obtained using the slice profile tool as described in Section 6.3. To ensure a sensible fit of the Gaussian a condition of number of background counts  $>0$  and number of excess counts  $>3$  in the  $1\sigma$  width of the fitted Gaussian was imposed. The results are shown for NN.

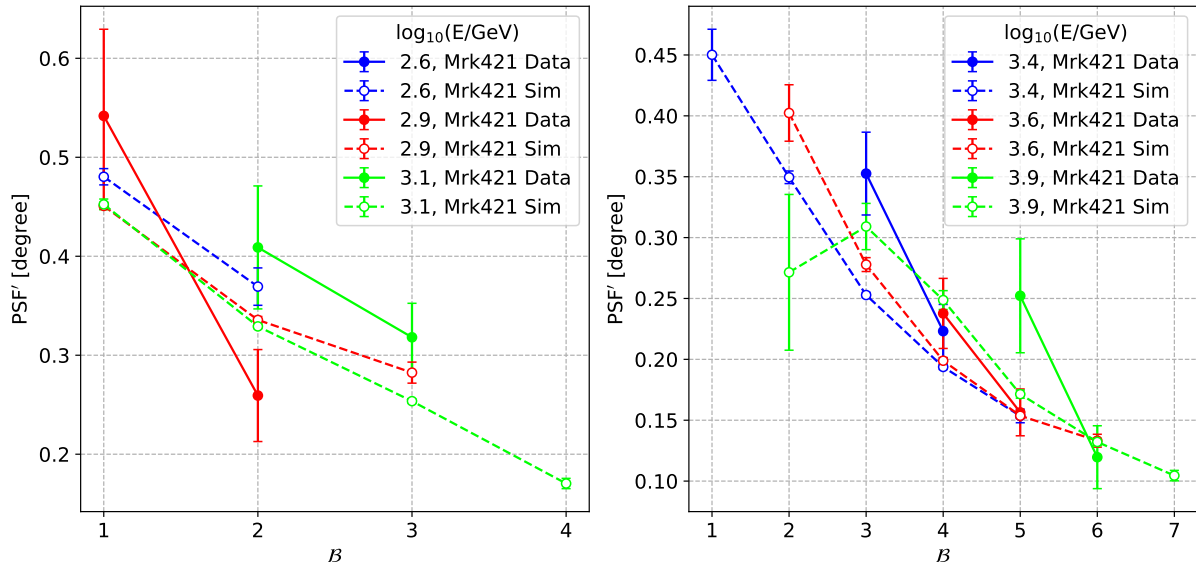


**Figure A.4:** The description is the same as of Figure A.3, for Mrk 421 between data and simulations. Only first 6 energy bins are shown, the last 6 energy bins did not have data. The results are shown for NN.

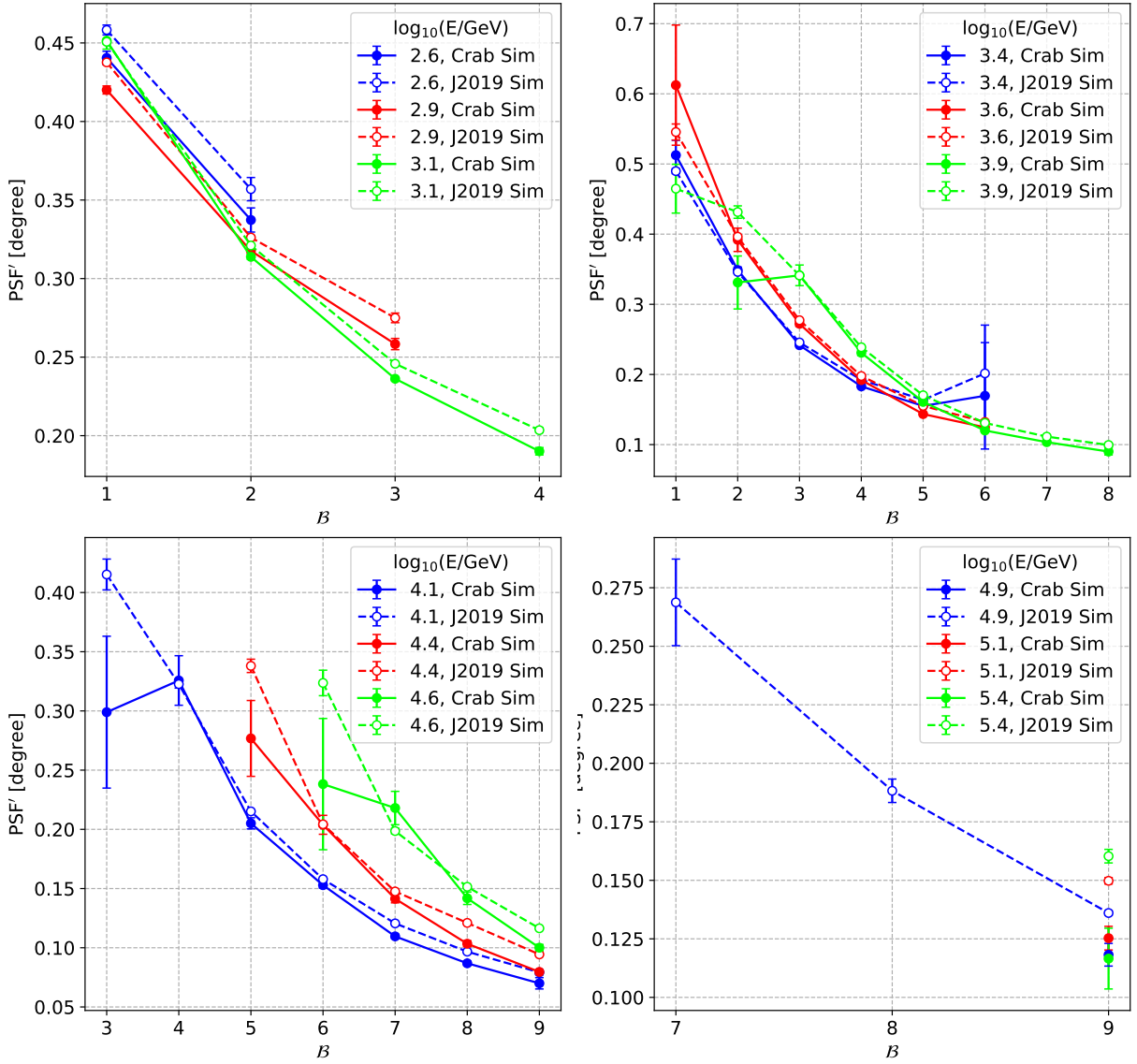


**Figure A.5:** The description is the same as of Figure A.3, for a simulated point source at the location of Crab and at the location of 2HWC J2019+367. The spectral index for the simulated Crab is the same as before, for 2HWC J2019+367 the spectral index is 2.2 with a simple power law. The results are shown for NN.

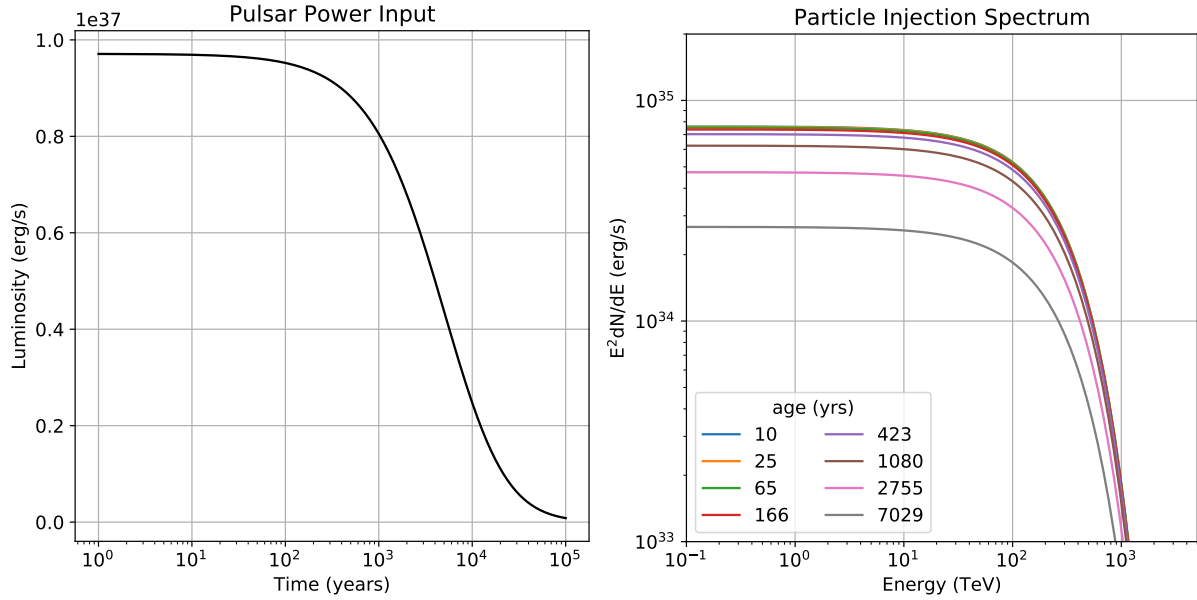


**Figure A.6:** Left panel: time evolution of the spin-down power of the pulsar PSR J2021+3651 corresponding to the birth period ( $P_0$ ) of 80 ms. Right panel: Injected particle spectrum at different ages with conversion efficiency ( $\epsilon$ ) of 15%. The evolution of the injected particle spectrum is continuous in time, it is to be noted that only few ages are shown. The values shown in the plots correspond to the one zone model shown in Section 6.9.2.

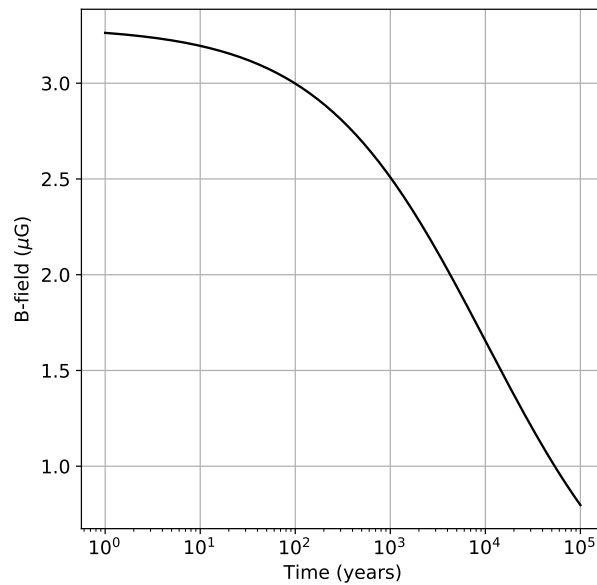


**Figure A.7:** Time evolution of ambient B-field for spectral modelling of 2HWC J2019+367 system. The values shown correspond to the one zone model shown in Section 6.9.2.

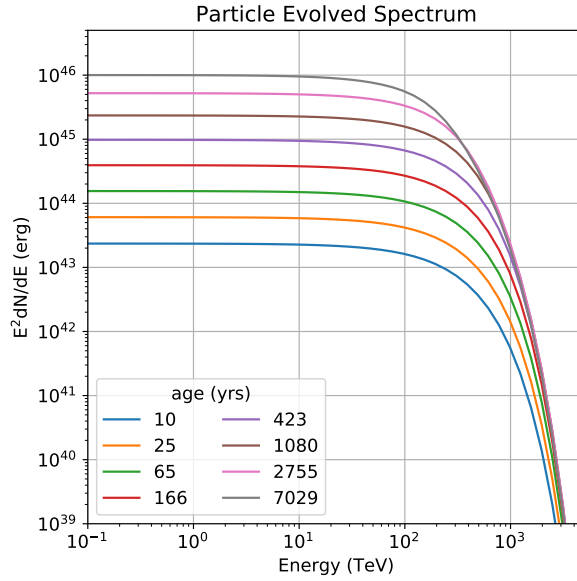


**Figure A.8:** Evolved particle  $e^\pm$  spectrum in the presence of ambient B-field shown in A.7 and radiation fields shown in 6.24 for different ages of the system. The values shown in the plot correspond to the one zone model shown in Section 6.9.2.

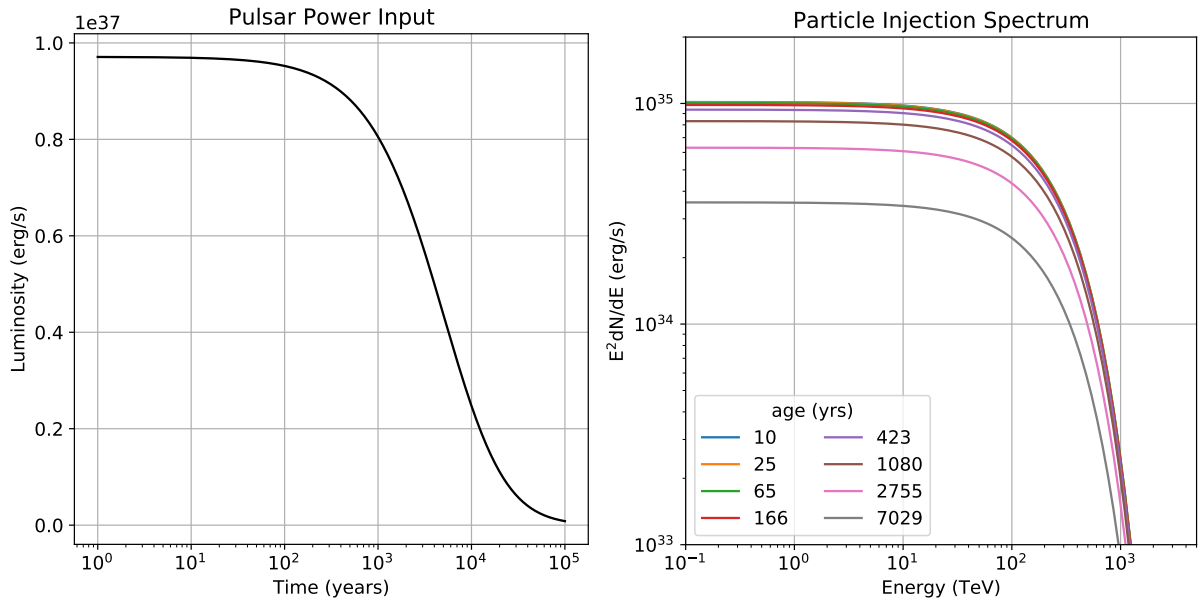


**Figure A.9:** Left panel: time evolution of the spin-down power of the pulsar PSR J2021+3651 corresponding to the birth period ( $P_0$ ) of 80 ms. Right panel: Injected particle spectrum at different ages with conversion efficiency ( $\epsilon$ ) of 20%. The evolution of the injected particle spectrum is continuous in time, it is to be noted that only few ages are shown. The values shown in the plots correspond to the two zone model shown in Section 6.9.3.

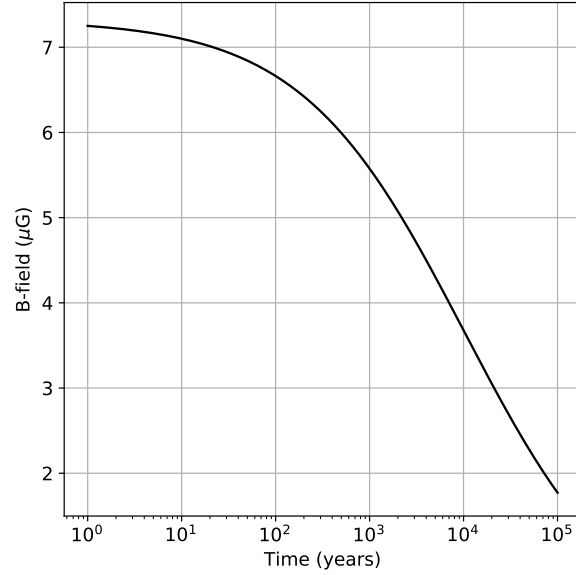


**Figure A.10:** Time evolution of ambient B-field for spectral modelling of 2HWC J2019+367 system. The values shown correspond to the two zone model shown in Section 6.9.3.

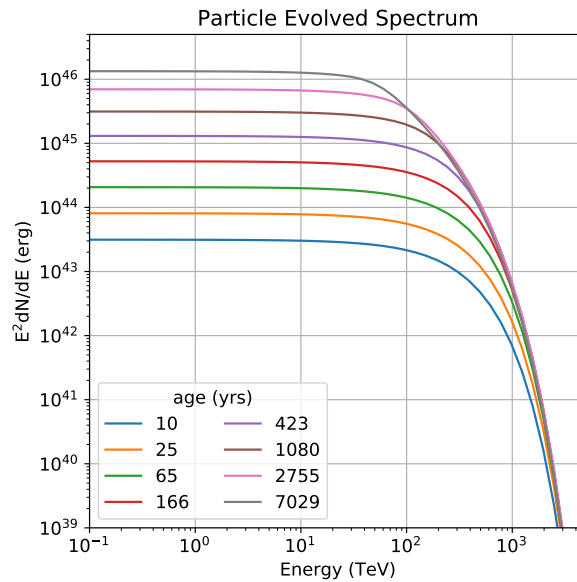


**Figure A.11:** Evolved particle  $e^\pm$  spectrum in the presence of ambient B-field shown in A.10 and radiation fields shown in 6.24 for different ages of the system. The values shown in the plot correspond to the two zone model shown in Section 6.9.3.

## References

- Weekes, T. C., et al. 1989, *ApJ*, 342, 379
- Aartsen, M. G., et al. 2017, *ApJ*, 849, 67
- Abdo, A. A., et al. 2007a, *ApJ*, 658, L33
- Abdo, A. A., et al. 2007b, *ApJ*, 664, L91
- Abdo, A. A. et al. 2009, *Astrophys. J.*, 700, 1059
- Abdo, A. A., et al. 2012, *ApJ*, 753, 159
- Abeysekara, A. U. et al. 2013, *Astropart. Phys.*, 50-52, 26
- Abeysekara, A. U., et al. 2017, *ApJ*, 841, 100
- Abeysekara, A. U. et al. 2017, *Astrophys. J.*, 843, 39
- Abeysekara, A. U., et al. 2017a, *ApJ*, 842, 85
- Abeysekara, A. U., et al. 2017b, *ApJ*, 843, 40
- Abeysekara, A. U., et al. 2018, *ApJ*, 861, 134
- Abeysekara, A. U. et al. 2018a, *Astrophys. J.*, 865, 57
- Abeysekara, A. U. et al. 2018b, *Nature*, 562, 82
- Acero, F., et al. 2015, *ApJS*, 218, 23
- Acharya, B. S., et al. 2013, *Astroparticle Physics*, 43, 3
- Agostinelli, S. et al. 2003, *Nucl. Instrum. Meth.*, A506, 250
- Aharonian, F., et al. 2004, *Nature*, 432, 75
- Aharonian, F. et al. 2006, *Astron. Astrophys.*, 460, 365
- Aharonian, F., et al. 2008, *Rept. Prog. Phys.*, 71, 096901
- Aharonian, F., et al. 2012, *Nature*, 482, 507
- Aharonian, F. A., et al. 2000, *ApJ*, 539, 317
- Aharonian, F. A. 2004, *Very high energy cosmic gamma radiation : a crucial window on the extreme Universe* (World Scientific Publishing Co)
- Ahlers, M. et al. 2018, *Progress in Particle and Nuclear Physics*, 102, 73
- Albert, A., et al. 2018a, *ApJ*, 853, 154
- Albert, A., et al. 2018b, *ArXiv e-prints*
- Alfaro, R. et al. 2017, *Phys. Rev.*, D96, 122001
- Alfaro, R., et al. 2017, *ApJ*, 843, 88
- Aliu, E. et al. 2008, *Science*, 322, 1221
- Aliu, E., et al. 2014, *ApJ*, 788, 78
- Amenomori, M., et al. 2008, *International Cosmic Ray Conference*, 2, 695
- Amenomori, M., et al. 2015, *The Astrophysical Journal*, 813, 98
- Arons, J. et al. 1979, *ApJ*, 231, 854
- Arons, J. 1983, *ApJ*, 266, 215
- Atkins, R. W. et al. 2003, *Astrophys. J.*, 595, 803
- Ave, M., et al. 2003, *Astroparticle Physics*, 19, 61

- Ayala Solares, H. A. 2017, PhD thesis, Michigan Technological University
- Baade, W. et al. 1934, *Physical Review*, 46, 76
- Barrau, A., et al. 1997, *ArXiv Astrophysics e-prints*
- Barrau, A. et al. 1998, *Nucl. Instrum. Meth.*, A416, 278
- Bartko, H., et al. 2008, *International Cosmic Ray Conference*, 2, 649
- Bartoli, B., et al. 2012, *ApJ*, 745, L22
- Bartoli, B., et al. 2013, *ApJ*, 779, 27
- Bartoli, B. et al. 2015, *Astrophys. J.*, 798, 119
- Bauleo, P. M. et al. 2009, *Nature*, 458N7240, 847
- Becherini, Y. et al. 2017, *Proceedings of Science: 35th International Cosmic Ray Conference*, 782
- Becker, W. et al. 1997, *A&A*, 326, 682
- Bednarek, W. 2007, *MNRAS*, 382, 367
- BenZvi, S. 2018
- Bhabha, H. J. et al. 1937, *Proceedings of the Royal Society of London Series A*, 159, 432
- Blumenthal, G. R. et al. 1970, *Rev. Mod. Phys.*, 42, 237
- Bothe, W. et al. 1929, *Zeitschrift fur Physik*, 56, 751
- Braun, J. 2016, *Internal HAWC Memo*
- Bucciantini, N. 2008, in *American Institute of Physics Conference Series*, Vol. 983, *40 Years of Pulsars: Millisecond Pulsars, Magnetars and More*, ed. C. Bassa, Z. Wang, A. Cumming, & V. M. Kaspi, 186–194
- Camilo, F., et al. 2006, *Astrophys. J.*, 637, 456
- Carroll, B. W. et al. 2006, *An introduction to modern astrophysics and cosmology*
- Chandrasekhar, S. 1931, *ApJ*, 74, 81
- Cheng, K. S., et al. 1986, *ApJ*, 300, 500
- Cherenkov, P. 1934, *C. R. (Doklady) Akad. Sci. URSS*, 2, 451
- Chevalier, R. A. 1977, *ARA&A*, 15, 175
- Cocke, W. J., et al. 1969, *Nature*, 221, 525
- Conceição, R. et al. 2017, *Proceedings of Science: 35th International Cosmic Ray Conference*, 784
- Cortina, J. 2005, *Ap&SS*, 297, 245
- de Naurois, M. et al. 2009, *Astroparticle Physics*, 32, 231
- Di Sciascio, G. 2016, *Nucl. Part. Phys. Proc.*, 279-281, 166
- Di Sciascio, G. et al. 2017, *Proceedings of Science: 35th International Cosmic Ray Conference*, 781
- Dingus, B. L., et al. 2000, in *American Institute of Physics Conference Series*, Vol. 510, *American Institute of Physics Conference Series*, ed. M. L. McConnell & J. M. Ryan, 642–645
- Dubus, G. 2013, *A&A Rev.*, 21, 64



## REFERENCES

---

- Fabian, A. C. 2012, *ARA&A*, 50, 455
- Faucher-Giguere, C.-A. et al. 2006, *Astrophys. J.*, 643, 332
- Fermi, E. 1949, *Physical Review*, 75, 1169
- Frail, D. A. et al. 1997, *ApJ*, 480, 364
- Fraschetti, F. 2008, *Phil. Trans. Roy. Soc. Lond.*, A366, 4417
- Funk, S. 2005
- Gaensler, B. M. et al. 2006, *ARA&A*, 44, 17
- Gaisser, T. K., et al. 1998, *The Astrophysical Journal*, 492, 219
- Ginzburg, V. L. et al. 1964, *The Origin of Cosmic Rays*
- Ginzburg, V. L. et al. 1965, *ARA&A*, 3, 297
- Goldreich, P. et al. 1969, *ApJ*, 157, 869
- Górski, K. M., et al. 2005, *ApJ*, 622, 759
- Greisen, K. 1960, *Annual Review of Nuclear and Particle Science*, 10, 63
- Greisen, K. 1966, *Physical Review Letters*, 16, 748
- Grieder, P. K. F. 2010, *Extensive Air Showers: High Energy Phenomena and Astrophysical Aspects - A Tutorial*, Reference Manual and Data Book
- Grupen, C. 2005, *Astroparticle Physics* (Springer)
- Gupta, Y., et al. 2005, *Curr. Sci.*, 89, 853
- Hahn, J. 2016, *PoS, ICRC2015*, 917
- Halpern, J. P., et al. 2008, *ApJ*, 688, L33
- Hempel-Arias, Z. 2017, PhD thesis, The University of Wisconsin - Madison
- Hartman, R. C., et al. 1999, *ApJS*, 123, 79
- Heck, D., et al. 1998, *CORSIKA: a Monte Carlo code to simulate extensive air showers*.
- Heger, A., et al. 2003, *ApJ*, 591, 288
- Hess, V. F. 1912, *Z. Phys.*, 13, 1084
- Hessels, J. W. T., et al. 2004, *ApJ*, 612, 389
- Hewish, A., et al. 1968, *Nature*, 217, 709
- Hillas, A. M. 1984, *Ann. Rev. Astron. Astrophys.*, 22, 425
- Hinton, J. A. 2004, *New Astron. Rev.*, 48, 331
- Hinton, J. A. et al. 2009, *Annual Review of Astronomy and Astrophysics*, 47, 523
- Hirovani, K. 2011, *ApJ*, 733, L49
- Hirovani, K. 2013, *ApJ*, 766, 98
- Hoecker, A., et al. 2007, *ArXiv Physics e-prints*
- Hunter, S. D., et al. 1997, *ApJ*, 481, 205
- James, F. et al. 1975, *Computer Physics Communications*, 10, 343
- Joshi, V. 2017, in *European Physical Journal Web of Conferences*, Vol. 136, European Physical Journal Web of Conferences, 03006
- Joshi, V. et al. 2017, *ArXiv e-prints*
- Joshi, V., et al. 2018, *ArXiv e-prints*
- Kamata, K. et al. 1958, *Progress of Theoretical Physics Supplement*, 6, 93
- Kennel, C. F. et al. 1984, *ApJ*, 283, 710

- Khangulyan, D., et al. 2018, *Astrophys. J.*, 860, 59
- Kieda, D. B. 2008, *International Cosmic Ray Conference*, 2, 843
- Kirichenko, A., et al. 2015, *Astrophys. J.*, 802, 17
- Kirk, J. G., et al. 2002, *A&A*, 388, L29
- Kirk, J. G., et al. 2009, in *Astrophysics and Space Science Library*, Vol. 357, *Astrophysics and Space Science Library*, ed. W. Becker, 421
- Kraushaar, W. L. et al. 1962, *Physical Review Letters*, 8, 106
- Krennrich, F., et al. 2004, *New A Rev.*, 48, 345
- Kumar, P. et al. 2015, *Phys. Rep.*, 561, 1
- Le Bohec, S. et al. 1998, *Nucl. Instrum. Meth.*, A416, 425
- Lemoine-Goumard, M., et al. 2011, *Mem. Soc. Astron. Italiana*, 82, 739
- Longair, M. S. 2011, *High Energy Astrophysics*
- Lopez-Coto, R. 2015, PhD thesis, *Universitat Autònoma de Barcelona*
- Manchester, R. N. et al. 1977, *Pulsars* (W. H. Freeman and Co.)
- Manchester, R. N., et al. 2005, *AJ*, 129, 1993
- Matheson, H. et al. 2010, *ApJ*, 724, 572
- Matthews, J. 2005, *Astropart. Phys.*, 22, 387
- Meyer, M., et al. 2010, *A&A*, 523, A2
- Minkowski, R. 1942, *ApJ*, 96, 199
- Mitchell, A. M. W. 2016
- Mizuno, T., et al. 2017a, *ApJ*, 841, 104
- Mizuno, T., et al. 2017b, *ApJ*, 841, 104
- Moderksi, R., et al. 2005, *Mon. Not. Roy. Astron. Soc.*, 364, 1488, [*Mon. Not. Roy. Astron. Soc.*363,no.3,954(2005)]
- Naito, T. et al. 1994, *Journal of Physics G: Nuclear and Particle Physics*, 20, 477
- Nakamura, K. et al. 2010, *J. Phys.*, G37, 075021
- Netzer, H. 2015, *ARA&A*, 53, 365
- Neugebauer, G., et al. 1984, *ApJ*, 278, L1
- Newton, D., et al. 2007, *Astroparticle Physics*, 26, 414
- Ohm, S. 2016, *Comptes Rendus Physique*, 17, 585
- Ohnishi, M. et al. 2017, *Proceedings of Science: 35th International Cosmic Ray Conference*, 437
- Pacini, F. 1967, *Nature*, 216, 567
- Pacini, F. 1968, *Nature*, 219, 145
- Pacini, F. et al. 1973a, *ApJ*, 186, 249
- Pacini, F. et al. 1973b, *ApJ*, 186, 249
- Paredes, J. M., et al. 2009, *A&A*, 507, 241
- Parsons, R. D. et al. 2014, *Astroparticle Physics*, 56, 26
- Piddington, J. H. et al. 1952, *Australian Journal of Scientific Research A Physical Sciences*, 5, 17
- Piran, T. 2004, *Reviews of Modern Physics*, 76, 1143

## REFERENCES

---

- Popescu, C. C., et al. 2017, MNRAS, 470, 2539
- Rees, M. J. et al. 1974, MNRAS, 167, 1
- Reynolds, S. P. et al. 1984, ApJ, 278, 630
- Richards, D. W. et al. 1969, Nature, 222, 551
- Roberts, M. S. E., et al. 2002, ApJ, 577, L19
- Roberts, M. S. E., et al. 2002, Astrophys. J., 577, L19
- Scharlemann, E. T., et al. 1978, ApJ, 222, 297
- Schoorlemmer, H. et al. 2017, Proceedings of Science: 35th International Cosmic Ray Conference, 819
- Staelin, D. H. et al. 1968, Science, 162, 1481
- Stephens Marinelli, S. et al. 2017, ArXiv e-prints
- Sturrock, P. A. 1971, ApJ, 164, 529
- Swanenburg, B. N. 1981, Annals of the New York Academy of Sciences, 375, 381
- Syrovatskii, S. I. 1959, Soviet Ast., 3, 22
- Tanabashi, M. et al. 2018, Phys. Rev., D98, 030001
- Tanimori, T., et al. 1998, The Astrophysical Journal Letters, 492, L33
- Truelove, J. K. et al. 1999, ApJS, 120, 299
- Uyaniker, B., et al. 2001, A&A, 371, 675
- Van Etten, A., et al. 2008, Astrophys. J., 680, 1417
- Venter, C. et al. 2007, in WE-Heraeus Seminar on Neutron Stars and Pulsars 40 years after the Discovery, ed. W. Becker & H. H. Huang, 40
- Vianello, G., et al. 2015, ArXiv e-prints
- Wagner, R. 2006, Measurement of VHE  $\gamma$ -ray emission from four blazars using the MAGIC telescope and a comparative blazar study., PhD. thesis
- Wakely, S. P. et al. 2008, International Cosmic Ray Conference, 3, 1341
- Warren, J., Wayne H. 1990
- Wilks, S. S. 1938, Annals Math. Statist., 9, 60
- Wisher, I. G. 2016, PhD thesis, The University of Wisconsin - Madison
- Wood, J. 2018, ArXiv e-prints
- Younk, P. W., et al. 2015, ArXiv e-prints
- Zanin, R. 2011, PhD thesis, Barcelona, Autònoma U.
- Zatsepin, G. T. et al. 1966, Journal of Experimental and Theoretical Physics Letters, 4, 0
- Zhang, L., et al. 2008, The Astrophysical Journal, 676, 1210
- Zhou, H. 2015, PhD thesis, Michigan Technological University



# Acronyms

$X$	depth in the atmosphere.
$f_{\text{hit}}$	fraction of PMTs hit.
$r$	distance from the shower axis (impact distance).
<b>2D</b>	two-dimensional.
<b>3ML</b>	The Multi-Mission Maximum Likelihood framework.
<b>a.s.l.</b>	above sea level.
<b>AGN</b>	Active Galactic Nuclei.
<b>BH</b>	Black Hole.
<b>C</b>	Carbon.
<b>CANGAROO</b>	Collaboration of Australia and Nippon for a Gamma-Ray Observatory in the Outback.
<b>CAT</b>	Cherenkov Array at Themis.
<b>CGRO</b>	Compton Gamma-Ray Observatory.
<b>CMB</b>	Cosmic Microwave Background.
<b>COM</b>	center of mass.
<b>CORSIKA</b>	COsmic Ray SIMulations for KAscade.
<b>CR</b>	Cosmic-Ray.
<b>CTA</b>	Cherenkov Telescope Array.
<b>DAQ</b>	data acquisition system.
<b>EAS</b>	Extensive Air Shower.
<b>EGRET</b>	Energetic Gamma-Ray Experiment Telescope.
<b>EM</b>	Electromagnetic.
<b>Fe</b>	Iron.
<b>FEB</b>	front-end board.
<b>FIR</b>	Far Infrared.
<b>FOV</b>	Field of View.

<b>FWHM</b>	full width at half maximum.
<b>GBM</b>	Gamma-ray Burst Monitor.
<b>GoF</b>	goodness of fit.
<b>GP</b>	Ground Parameter.
<b>GRB</b>	Gamma-Ray Burst.
<b>GZK</b>	Greisen-Zatsepin-Kuzmin.
<b>H</b>	Hydrogen.
<b>HAWC</b>	High Altitude Water Cherenkov.
<b>He</b>	Helium.
<b>HEALPix</b>	Hierarchical Equal Area isoLatitude Pixelization of a sphere.
<b>HEGRA</b>	High Energy Gamma-Ray Astronomy.
<b>HESS</b>	High Energy Stereoscopic System.
<b>HV</b>	high voltage.
<b>IACT</b>	Imaging Atmospheric Cherenkov Telescope.
<b>IC</b>	Inverse Compton.
<b>ImPACT</b>	Image Pixel-wise Fit for Atmospheric Cherenkov Telescopes.
<b>IR</b>	Infrared.
<b>ISM</b>	Interstellar Medium.
<b>KN</b>	Klein-Nishina.
<b>LAT</b>	Large Area Telescope.
<b>LDF</b>	lateral distribution function.
<b>LH</b>	likelihood.
<b>MAGIC</b>	Major Atmospheric Gamma Imaging Cherenkov Telescopes.
<b>MC</b>	Monte Carlo.
<b>MHD</b>	Magnetohydrodynamic.
<b>MILAGRO</b>	Multiple Institution Los Alamos Gamma Ray Observatory.
<b><math>N_{pe}</math></b>	number of photo-electrons.
<b>NKG</b>	Nishimura-Kamata-Greisen.
<b>NN</b>	Neural Network.
<b>NS</b>	Neutron Star.
<b>O</b>	Oxygen.

## ACRONYMS

---

<b>PDF</b>	probability distribution function.
<b>PE</b>	photo-electron.
<b>PINC</b>	Parameter for Identifying Nuclear Cosmic-rays.
<b>PMT</b>	Photo-Multiplier Tube.
<b>PSF</b>	Point Spread Function.
<b>PWN</b>	Pulsar Wind Nebula.
<b>QE</b>	quantum efficiency.
<b>RA</b>	right ascension.
<b>RMS</b>	Root Mean Square.
<b>ROI</b>	Region of Interest.
<b>RPC</b>	Resistive Plate Chamber.
<b>SAS-2</b>	Small Astronomy Satellite 2.
<b>SED</b>	Spectral Energy Distribution.
<b>SFCF</b>	Super Fast Core Fit.
<b>SMBH</b>	Super Massive Black Hole.
<b>SN</b>	Supernova.
<b>SNR</b>	Supernova Remnant.
<b>SSC</b>	Synchrotron Self Compton.
<b>TDC</b>	time-to-digital-converter.
<b>ToT</b>	time-over-threshold.
<b>TS</b>	test statistics.
<b>TWVA</b>	Toolkit for Multivariate Analysis.
<b>UV</b>	Ultraviolet.
<b>VERITAS</b>	Very Energetic Radiation Imaging Telescope Array System.
<b>VHE</b>	Very High Energy.
<b>WCD</b>	Water Cherenkov Detector.
<b>WD</b>	White Dwarf.
<b>WR</b>	Wolf-Rayet.
<b><math>X_{\max}</math></b>	depth of the shower maximum.





## Units

Abbreviation	Name	Equivalence
m	meter	
s	second	
V	volt	
kg	kilogram	
eV	electronvolt	$1.60 \times 10^{-19} \text{ kg m}^2 \text{ s}^{-2}$
erg	ergio	0.62415 TeV
Hz	hertz	$1 \text{ s}^{-1}$
pc	parsec	$3.086 \times 10^{16} \text{ m}$
yr	year	$3.154 \times 10^7 \text{ s}$

## Prefixes

Abbreviation	Prefix	Equivalence
Z	Zeta	$10^{21}$
E	Exa	$10^{18}$
P	Peta	$10^{15}$
T	Tera	$10^{12}$
G	Giga	$10^9$
M	Mega	$10^6$
k	kilo	$10^3$
-	-	$10^0$
c	centi	$10^{-2}$
m	mili	$10^{-3}$
$\mu$	micro	$10^{-6}$
n	nano	$10^{-9}$
p	pico	$10^{-12}$



## Acknowledgements

First and foremost, I gratefully thank Prof. Dr. Jim Hinton for the opportunity to pursue my Ph.D. in MPIK Heidelberg and for all the throughout guidance and support. Prof. Dr. Werner Hofmann for the supervision in the thesis committee. Prof. Dr. Stefan Wagner for the thesis committee supervision and for refereeing this work.

I sincerely thank Dr. Harm Schoorlemmer for the supervision throughout my Ph.D. and helping me out with uncountable problems. Dr. Rubén López-Coto for answering endless questions and for being a great office mate. Dr. Vincent Marandon and Dr. Dan Parsons for all the spontaneous help in countless occasions. Dr. Joachim Hahn for the help with GAMERA package and guidance on PWNe analysis. Dr. Hans Dembinski for the help with python.

I thank all my past and present colleagues in MPIK for creating an excellent work environment. Sabina Puerckhauer, Simon Sailor and Johannes King for being my German support system. Armelle Jardin-Blicq, Pooja Surjballi, and Edna L. Ruiz Velasco for being a great HAWC team in MPIK. A big thank you to Ruth Crespo for all the help and support.

I thank all my colleagues from the HAWC collaboration. I especially thank Dr. John Pretz, Dr. Colas Rivière and Dr. Segev BenZvi for their help in software development issues. I also thank Prof. Brenda Dingus and Prof. Petra Hütemeyer for the discussion on different aspects of my Ph.D. work.

I gratefully acknowledge the funding and support from International Max Planck Research School for Astronomy and Cosmic Physics at the University of Heidelberg (IMPRS-HD). I big thank you to Dr. Christian Fendt for his support during my stay in Heidelberg. I thank all the fellow IMPRS-HD students for socialising and for all the joyful occasions.

I thank all my friends in Heidelberg, in India and abroad. Especially Rishabh, Nir-mal, Aseem, Rajwinder, Tamasi, Thomas, Rajorshi, Samir and Angshuman for staying in touch. A special thank you to Leo for all the support, motivation and for being there.

Mammi, Didi, Jijaji aur Joti: ab kya hi main kahu? Sabhi ko pair chu ke pranam, akhirkar lagta hai PhD ho hi jayegi. Sabhi ka dhanyawad, Mammi aur Didi tum dono ka khoob sare vrat rakhne ke liye bahut bahut dhanyawad.

My sincere apologies to those whom I may have forgotten by mistake. Please consider yourself remembered here. Again thank you all.

